SLAC-R-503
UC-414

Precision Measurement of the Neutron Spin Dependent Structure Functions

Yury G. Kolomensky

Stanford Linear Accelerator Center
Stanford University
Stanford, CA 94309

SLAC-Report- 503
February 1997

MASTER

Prepared for the Department of Energy
under contract number DE-AC03-76SF00515

DISTRIBUTION OF THIS DOCUMENT IS UNLIMITED

Printed in the United States of America. Available from the National Technical Information Service, U.S. Department of Commerce, 5285 Port Royal Road, Springfield, VA 22161.

PRECISION MEASUREMENT OF THE NEUTRON SPIN DEPENDENT STRUCTURE FUNCTIONS

A Dissertation Presented

by

YURY G. KOLOMENSKY

Submitted to the Graduate School of the
University of Massachusetts Amherst in partial fulfillment
of the requirements for the degree of

DOCTOR OF PHILOSOPHY

February 1997

Department of Physics and Astronomy

Оле, Мише и Саше

ACKNOWLEDGMENTS

First and foremost, I would like to express my gratitude to my adviser Professor Gerald A. Peterson for giving me the opportunity to work on this experiment from its very beginning in 1994. I am deeply indebted to him for his attention, help, and advice I value very much. I would like to thank the members of my committee for taking the time to read and correct the manuscript.

The experiment was a collaborative effort of many physicists. I would like to thank the spokesperson, Professor Emlyn W. Hughes, for the time and energy he put into the project, and for being such an enthusiastic and motivating person he is. I had a privilege to work with many fine physicists, and I appreciate help, support, and many discussions with Ray Arnold, Cristina Berisso, Gordon Cates, Roger Gearhart, Krishna Kumar, Zein-Eddine Meziani, Makis Petratos, Rainer Pitthan, Richard Prepost, Paul Souder, and Charlie Young. This work would not be possible without the effort of my fellow graduate students. Many thanks to Piotr, MO, Mike, Franck, Dave, Todd, Greg, Steve, Sebastien, and Jason for sharing this exciting experience with me, and for making the project succeed.

My physics education started at St. Petersburg Technical University in Russia, and I am thankful to the faculty of the Department of Physics and Mechanics for giving me the basis for a successful career in physics. I was fortunate to continue my education at UMass and interact with Professors Eugene Golowich, John Donoghue, and Barry Holstein.

Finally, I would like to thank Alexey Petrov for his friendship and help, and my parents for their support and understanding. But most of all, I am indebted to my dearest wife Olga for her love, patience, and support through all these years.

ABSTRACT

PRECISION MEASUREMENT OF THE NEUTRON SPIN DEPENDENT STRUCTURE FUNCTIONS

FEBRUARY 1997

YURY G. KOLOMENSKY, B.S., ST. PETERSBURG TECHNICAL UNIVERSITY, RUSSIA

M.S., UNIVERSITY OF MASSACHUSETTS AMHERST

PH.D., UNIVERSITY OF MASSACHUSETTS AMHERST

Directed by: Professor Gerald A. Peterson

In experiment E154 at the Stanford Linear Accelerator Center the spin dependent structure function $g_1^n(x, Q^2)$ of the neutron was measured by scattering longitudinally polarized 48.3 GeV electrons off a longitudinally polarized ^{3}He target. The high beam energy allowed us to extend the kinematic coverage compared to the previous SLAC experiments to $0.014 \leq x \leq 0.7$ with an average Q^2 of 5 GeV^2. We report the integral of the spin dependent structure function in the measured range to be $\int_{0.014}^{0.7} dx\ g_1^n(x, 5\ \text{GeV}^2) = -0.036 \pm 0.004(\text{stat.}) \pm 0.005(\text{syst.})$. We observe relatively large values of g_1^n at low x that call into question the reliability of data extrapolation to $x \to 0$. Such divergent behavior disagrees with predictions of the conventional Regge theory, but is qualitatively explained by perturbative QCD. We perform a Next-to-Leading Order perturbative QCD analysis of the world data on the nucleon spin dependent structure functions g_1^p and g_1^n paying careful attention to the experimental and theoretical uncertainties. Using the parameterizations of the helicity-dependent parton distributions obtained in the analysis, we evolve the data to $Q^2 = 5$ GeV^2, determine the first moments of the polarized structure functions of the proton and neutron, and find agreement with the Bjorken sum rule.

TABLE OF CONTENTS

APPENDICES

LIST OF TABLES

LIST OF FIGURES

CHAPTER 1

MOTIVATION

1.1 Introduction

The mystery of the structure of the nucleon is one of the most fascinating challenges facing modern physics. Deep inelastic scattering data helps us to meet the challenge. Like a powerful microscope, it allows us to look inside the sub-nuclear particles at a much deeper level and check our ideas of what nucleons consist of and how they behave.

Deep-inelastic scattering (DIS) experiments provide perhaps our cleanest window on hadron structure at large momentum transfer squared Q^2. The original DIS experiments in End Station A at the Stanford Linear Accelerator Center (SLAC) in the 1960s showed that the form factors in *ep* scattering exhibit approximate *scaling* at large Q^2.[1] This remarkable observation was celebrated when the 1990 Nobel Prize in Physics was awarded to the experimenters Friedman, Kendall, and Taylor.[2] It gave rise to the original parton ideas of Feynman[3] and of Bjorken and Paschos.[4,5] Precise data revealed the logarithmic scaling violations and also the gluon distribution that were predicted by QCD.

While the theoretical grounds for understanding unpolarized deep inelastic scattering are well established and surprises are rare, experimental polarization data have often challenged the theory. It is more than two decades since the first polarized deep inelastic scattering experiments were done at SLAC.[6,7] This work became the subject of renewed interest when EMC[8] extended the SLAC measurements to smaller x and announced their results on the spin-dependent proton structure function g_1. The naive parton model interpretation of their data is that the quarks contribute very little to the proton's spin – in contradiction with quark models.

Since that measurement, much more data have become available from SLAC[9–11] and CERN.[12,13] The work described in these pages is a further step in studying the dynamics of quarks and gluons inside the nucleon. In experiment E154,[14] we have measured the spin structure functions of the neutron $g_1^n(x, Q^2)$ and $g_2^n(x, Q^2)$ by scattering longitudinally polarized electrons off longitudinally or transversely polarized ^{3}He nuclei. High statistical precision and broad kinematic coverage of the experiment gives us a stronger basis for understanding the structure of the nucleon.

The experiment was carried out in October-November of 1995 by a collaboration of 80 physicists from 23 institutions in End Station A at SLAC.

1.2 Structure functions

1.2.1 Definitions

Our primary concern is with deep-inelastic scattering from polarized targets. Experiments at SLAC and DESY use polarized electrons while experiments at CERN by the European Muon Collaboration (EMC) and the Spin Muon Collaboration (SMC) utilize naturally polarized muon beams. Consider a DIS experiment where a lepton beam with definite polarization and momentum $k^\mu = (E, \vec{k})$ scatters from a polarized proton target. This is shown in the one photon exchange diagram of Fig. 1.1 to leading order in the electromagnetic interaction. We work in the laboratory frame so that the proton target P has momentum $p^\mu = (M, 0)$ and polarization S^μ. The lepton L is scattered through an angle θ and emerges with momentum $k'^\mu = (E', \vec{k}')$. The exchanged photon carries four-momentum $q^\mu = (k - k')^\mu$. The scattering process is then characterized by the two invariants $Q^2 = -q^2$ and $\nu = p \cdot q / M$ [$\nu = (E - E')$ in the LAB frame] or, equivalently, by Q^2 and the Bjorken variable $x = \frac{Q^2}{2M\nu}$. We measure the inclusive hadronic cross section so that hadronic final states X with

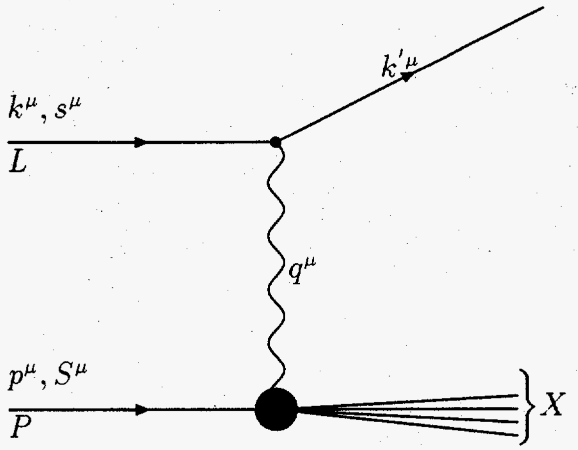

Fig. 1.1. Deep inelastic scattering.

the same invariant mass squared, $W^2 = (p+q)^2$, are not separated. The kinematic variables are summarized in Table 1.1.

The differential cross section for the one photon exchange process (Fig. 1.1) is given by[15]

$$\frac{d^2\sigma}{d\Omega dE'} = \frac{\alpha^2}{Q^4}\frac{E'}{E} L_{\mu\nu} W^{\mu\nu}. \tag{1.1}$$

Here, α is the fine structure constant and $L_{\mu\nu}$ and $W_{\mu\nu}$ describe the leptonic and hadronic vertices respectively. Since the lepton is elementary we can write down an exact expression for $L_{\mu\nu}$ from the Feynman rules,

$$L_{\mu\nu} \equiv L^S_{\mu\nu} + iL^A_{\mu\nu} = 2\left[k_\mu k'_\nu + k'_\mu k_\nu - g_{\mu\nu}(k\cdot k' - m^2) + im\epsilon_{\mu\nu\rho\sigma}q^\rho s^\sigma\right] \tag{1.2}$$

where we split the leptonic tensor in two parts: $L^S_{\mu\nu}$ is symmetric under $\mu \Leftrightarrow \nu$, and $L^A_{\mu\nu}$ is antisymmetric and contains the lepton spin.

The hadronic tensor $W^{\mu\nu}$ contains all of the information about the hadronic target that one can extract from such inclusive measurements. Its form is constrained by symmetry arguments. Again, we write $W_{\mu\nu}$ as a sum of symmetric and antisym-

Table 1.1. Kinematic variables and invariants of lepton-nucleon scattering.

Variable	Expression	Lab Frame	Meaning
E			Incident lepton energy
E'			Scattered lepton energy
$\vec{k}$			Incident lepton momentum
$\vec{k}'$			Scattered lepton momentum
ϑ	$\arccos\left(\frac{\vec{k}\cdot\vec{k}'}{\lvert\vec{k}\rvert\lvert\vec{k}'\rvert}\right)$		Lepton scattering angle
m			Lepton mass
k^μ	$(E,\vec{k})$		Incident lepton 4-momentum
k'^μ	$(E',\vec{k}')$		Scattered lepton 4-momentum
s^μ			Incident lepton polarization vector
M			Nucleon mass
P^μ		$(M,\vec{0})$	Nucleon 4-momentum
S^μ			Nucleon polarization vector
q^μ	$(k-k')^\mu$		4-momentum transfer
Q^2	$-q^2$	$4EE'sin^2\vartheta/2$	4-momentum transfer squared
ν	$P\cdot q/2M$	$(E-E')$	Energy transfer
x	$Q^2/2M\nu$	$\frac{4EE'sin^2(\vartheta/2)}{2M(E-E')}$	Bjorken x; the fraction of nucleon momentum carried by a struck parton

metric contributions; $W_{\mu\nu} = W^S_{\mu\nu} + iW^A_{\mu\nu}$. Then the requirements of covariance, parity, charge conjugation, and current conservation ($q^\mu W_{\mu\nu} = 0$) imply the form

$$W^S_{\mu\nu} = \frac{1}{M}(-g_{\mu\nu} + \frac{q_\mu q_\nu}{q^2})F_1(x,Q^2) + \frac{1}{M^2\nu}(p_\mu - \frac{p\cdot q}{q^2}q_\mu)(p_\nu - \frac{p\cdot q}{q^2}q_\nu)F_2(x,Q^2) \quad (1.3)$$

and

$$W^A_{\mu\nu} = \frac{\epsilon_{\mu\nu\lambda\sigma}q^\lambda S^\sigma}{M\nu}g_1(x,Q^2) + \frac{\epsilon_{\mu\nu\lambda\sigma}q^\lambda(M\nu S^\sigma - q\cdot Sp^\sigma)}{M^2\nu^2}g_2(x,Q^2) \quad (1.4)$$

The form factors in Equations 1.3 and 1.4 contain all of the target dependent information.

One has to use both polarized beam and polarized target in order to measure spin-dependent structure functions g_1 and g_2 since combinations with mixed symmetry vanish $L^S_{\mu\nu}W^{\mu\nu}_A = L^A_{\mu\nu}W^{\mu\nu}_S = 0$ and only combinations $L^S_{\mu\nu}W^{\mu\nu}_S$ and $L^A_{\mu\nu}W^{\mu\nu}_A$

survive. For this experiment, the unpolarized structure functions F_1 and F_2 are considered to be known.

Deep inelastic scattering is defined by the kinematic limit where both $Q^2 \gg M^2$ and $W^2 \gg M^2$, so that we are beyond the resonance region (where W^2 may coincide with the mass squared of one of the excited nucleon resonances). In the DIS limit the form factors F_i and g_i in $W_{\mu\nu}$ exhibit approximate *scaling.* That is, they behave as structure functions of the single variable x - modulo a slow logarithmic variation in Q^2, which is described by perturbative QCD. The scaling property reveals a local interaction between the hard photon and charged elementary partons (quarks) inside the proton. It is the same effect as in Rutherford's α particle scattering experiments which revealed the nucleus inside the atom.[16]

We now turn to the measurement of the spin dependent structure functions. We will consider leptons longitudinally polarized and targets longitudinally or transversely polarized with respect to the incident beam direction. We will let $\uparrow\downarrow$ denote the longitudinal lepton polarization and $\Uparrow\Downarrow$ ($\Leftarrow$) denote longitudinal (transverse) polarization of the target nucleon. Then the differential cross sections are

$$\frac{d^2\sigma}{d\Omega dE'}^{\downarrow\Uparrow} + \frac{d^2\sigma}{d\Omega dE'}^{\uparrow\Uparrow} = \frac{8\alpha^2(E')^2}{MQ^4}\left[2\sin^2\frac{\vartheta}{2}\; F_1(x,Q^2) + \frac{M}{\nu}\cos^2\frac{\vartheta}{2}\; F_2(x,Q^2)\right] \quad (1.5)$$

and

$$\frac{d^2\sigma}{d\Omega dE'}^{\downarrow\Uparrow} - \frac{d^2\sigma}{d\Omega dE'}^{\uparrow\Uparrow} = \frac{4\alpha^2 E'}{Q^2 EM\nu}\left[(E + E'\cos\vartheta)\; g_1(x,Q^2) - 2xM\; g_2(x,Q^2)\right] \quad (1.6)$$

for longitudinally polarized leptons and nucleons, and

$$\frac{d^2\sigma}{d\Omega dE'}^{\downarrow\Leftarrow} - \frac{d^2\sigma}{d\Omega dE'}^{\uparrow\Leftarrow} = \frac{4\alpha^2 E'}{Q^2 EM\nu} E'\sin\vartheta\left[\; g_1(x,Q^2) + \frac{4xEM}{Q^2}\; g_2(x,Q^2)\right] \quad (1.7)$$

for longitudinally polarized leptons and transversely polarized targets.

The structure function g_2 is suppressed in Eq. (1.6) with respect to g_1 by a factor $\frac{M}{E} \approx 0.02$, for the beam energy of 50 GeV. The transverse asymmetry in Eq. (1.7) primarily measures g_2.

The experiments usually do not measure cross section differences of Equations (1.6) and (1.7) directly, but measure longitudinal and transverse asymmetries

$$A_{\|} = \frac{\frac{d^2\sigma}{d\Omega dE'}^{\downarrow\Uparrow} - \frac{d^2\sigma}{d\Omega dE'}^{\uparrow\Uparrow}}{\frac{d^2\sigma}{d\Omega dE'}^{\downarrow\Uparrow} + \frac{d^2\sigma}{d\Omega dE'}^{\uparrow\Uparrow}} \tag{1.8}$$

and

$$A_{\perp} = \frac{\frac{d^2\sigma}{d\Omega dE'}^{\downarrow\Leftarrow} - \frac{d^2\sigma}{d\Omega dE'}^{\uparrow\Leftarrow}}{\frac{d^2\sigma}{d\Omega dE'}^{\downarrow\Leftarrow} + \frac{d^2\sigma}{d\Omega dE'}^{\uparrow\Leftarrow}}. \tag{1.9}$$

Then, if the beam and/or target polarizations are reversed frequently, all slow-varying factors (beam properties, detector efficiencies and acceptance, etc.) cancel between different polarization states, and one can write the asymmetries in terms of detector counting rates:

$$A_{\|} = \frac{1}{fP_bP_t}\frac{(N/Q)^{\downarrow\Uparrow} - (N/Q)^{\uparrow\Uparrow}}{(N/Q)^{\downarrow\Uparrow} + (N/Q)^{\uparrow\Uparrow}} \tag{1.10}$$

and

$$A_{\perp} = \frac{1}{fP_bP_t}\frac{(N/Q)^{\downarrow\Leftarrow} - (N/Q)^{\uparrow\Leftarrow}}{(N/Q)^{\downarrow\Leftarrow} + (N/Q)^{\uparrow\Leftarrow}}\ . \tag{1.11}$$

Here N and Q are the number of events and beam charge for each helicity state, respectively, P_b and P_t are the beam and target polarizations, and the factor f is the dilution factor, the ratio of scattering rates from the polarized nuclei to the total number of target nuclei:

$$f(x, Q^2) = \frac{n_P\sigma_P(x, Q^2)}{n_P\sigma_P(x, Q^2) + n_U\sigma_U(x, Q^2)}. \tag{1.12}$$

The polarized nucleus (^{3}He, H, or D) is denoted by P, and U stands for unpolarized material. The scattering cross sections are $\sigma_i(x, Q^2)$, and n_i are the nucleon densities.

1.2.2 The virtual photon-nucleon asymmetries

Deep inelastic scattering is composed of two processes. One, represented by the top vertex in Fig. 1.1, is the emission of the virtual photon by the incident lepton, and is completely calculable in QED. The bottom vertex represents the absorption of the photon by the target nucleon. The optical theorem relates the total photoabsorption cross section to the imaginary ("absorptive") part of the forward ($t = 0$) virtual photon-nucleon Compton scattering amplitude (where t is the momentum transfer Mandelstam variable).

Let us denote the Compton amplitudes $\mathcal{M}_{ab\to cd}$ where a and b are the incident photon and nucleon, and c and d are the final photon and nucleon helicities, respectively. These amplitudes are derived from the hadronic tensor $W_{\mu\nu}$ through

$$\mathcal{M}_{ab\to cd} = \epsilon^{\mu\dagger}(\lambda_a)\epsilon^{\nu}(\lambda_c)W_{\mu\nu} \ , \tag{1.13}$$

where $\epsilon^{\mu}(\lambda)$ is the polarization vector of the virtual photon.

There are four independent helicity amplitudes (just as there are four independent structure functions defined in Section 1.2.1):[17]

$$\mathcal{M}_{1\frac{1}{2}\to 1\frac{1}{2}},\ \mathcal{M}_{1-\frac{1}{2}\to 1-\frac{1}{2}},\ \mathcal{M}_{0\frac{1}{2}\to 0\frac{1}{2}},\ \mathcal{M}_{0\frac{1}{2}\to 1-\frac{1}{2}}. \tag{1.14}$$

Using Equations (1.3) and (1.4), we get for the virtual photoabsorption cross sections:

$$\begin{aligned}
\sigma_{1/2} &= \frac{4\pi^2\alpha}{K}\mathcal{M}_{1-\frac{1}{2}\to 1-\frac{1}{2}} = \frac{4\pi^2\alpha}{MK}\left[F_1 + g_1 - \frac{2Mx}{\nu}g_2\right] \\
\sigma_{3/2} &= \frac{4\pi^2\alpha}{K}\mathcal{M}_{1\frac{1}{2}\to 1\frac{1}{2}} = \frac{4\pi^2\alpha}{MK}\left[F_1 - g_1 + \frac{2Mx}{\nu}g_2\right] \\
\sigma_L &= \frac{4\pi^2\alpha}{K}\mathcal{M}_{0\frac{1}{2}\to 0\frac{1}{2}} = \frac{4\pi^2\alpha}{K}\left[\frac{F_2}{\nu}\left(1 + \frac{\nu^2}{Q^2}\right) - \frac{1}{M}F_1\right] \\
\sigma_{TL} &= \frac{4\pi^2\alpha}{K}\mathcal{M}_{0\frac{1}{2}\to 1-\frac{1}{2}} = \frac{4\pi^2\alpha}{K}\frac{\sqrt{Q^2}}{M\nu}\left[g_1 + g_2\right]
\end{aligned} \tag{1.15}$$

where the photon flux K is defined according to Hand's convention as

$$K = \frac{W^2 - M^2}{2M} = \nu - \frac{Q^2}{2M}. \tag{1.16}$$

The quantities $\sigma_{1/2}$ and $\sigma_{3/2}$ are the virtual photoabsorption cross sections when the total photon-nucleon spin along the photon direction is 1/2 and 3/2 respectively. The total transverse photoabsorption cross section is defined by

$$\sigma_T = \frac{1}{2}\left(\sigma_{1/2} + \sigma_{3/2}\right) = \frac{4\pi^2\alpha}{MK}F_1. \tag{1.17}$$

The cross section for the longitudinally polarized photon is σ_L, and the interference term between transverse and longitudinal amplitudes is σ_{TL}.

The virtual photon-nucleon asymmetries are defined by

$$A_1(x,Q^2) \equiv \frac{\sigma_{1/2} - \sigma_{3/2}}{\sigma_{1/2} + \sigma_{3/2}} = \frac{g_1(x,Q^2) - \gamma^2 g_2(x,Q^2)}{F_1(x,Q^2)} \tag{1.18}$$

and

$$A_2(x,Q^2) \equiv \frac{\sigma_{TL}}{\sigma_T} = \frac{\gamma\left(g_1(x,Q^2) + g_2(x,Q^2)\right)}{F_1(x,Q^2)}, \tag{1.19}$$

where $\gamma = \sqrt{Q^2/\nu^2}$. We can also define the ratio of the longitudinal to transverse cross sections

$$R(x,Q^2) \equiv \frac{\sigma_L}{\sigma_T} = \frac{1+\gamma^2}{2xF_1(x,Q^2)} F_2(x,Q^2) - 1 \tag{1.20}$$

which links two unpolarized structure functions

$$F_1(x,Q^2) = \frac{1+\gamma^2}{2x\left(1 + R(x,Q^2)\right)} F_2(x,Q^2). \tag{1.21}$$

The virtual asymmetries satisfy the unitarity conditions[18]

$$|A_1(x,Q^2)| \leq 1, \quad |A_2(x,Q^2)| \leq \sqrt{R(x,Q^2)}. \tag{1.22}$$

1.2.3 Structure functions and experimental asymmetries

Finally, we can express the structure functions and virtual photon-nucleon asymmetries in terms of the experimentally measured asymmetries

$$g_1(x,Q^2) = \frac{F_1(x,Q^2)}{D'}\left[A_{||}(x,Q^2) + A_{\perp}(x,Q^2)\tan(\vartheta/2)\right], \tag{1.23}$$

$$g_2(x,Q^2) = \frac{F_1(x,Q^2)}{D'}\frac{y}{2\sin\vartheta}\left[-A_{||}(x,Q^2)\sin\vartheta + A_{\perp}(x,Q^2)\frac{E + E'\cos\vartheta}{E'}\right] \tag{1.24}$$

and

$$A_1(x,Q^2) = \frac{A_{||}(x,Q^2)}{D(1+\zeta\eta)} - \frac{\eta A_{\perp}(x,Q^2)}{d(1+\zeta\eta)}, \tag{1.25}$$

$$A_2(x,Q^2) = \frac{\zeta A_{||}(x,Q^2)}{D(1+\zeta\nu)} + \frac{A_\perp(x,Q^2)}{d(1+\zeta\nu)} . \tag{1.26}$$

The kinematic factors used above are

$$\begin{aligned}
\epsilon &= \frac{1}{1+2(1+(\nu^2/Q^2))\tan^2(\vartheta/2)} , \\
D' &= \frac{(1-\epsilon)(2-y)}{y(1+\epsilon R(x,Q^2))} , \\
D &= \frac{1-E'\epsilon/E}{1+\epsilon R(x,Q^2)} , \\
d &= D\sqrt{\frac{2\epsilon}{1+\epsilon}} , \\
\eta &= \frac{\epsilon\sqrt{Q^2}}{E-E'\epsilon} , \quad \text{and} \\
\zeta &= \eta\frac{1+\epsilon}{2\epsilon} ,
\end{aligned} \tag{1.27}$$

where $y = (E-E')/E$ is the fractional energy transfer from the electron to hadrons.

1.2.4 The parton model and polarized parton distributions

The parton model began with Feynman who showed that the early SLAC deep inelastic scattering experiments could be explained in terms of the hard photon scattering incoherently from elementary *parton* constituents in the proton. The structure functions measure the probability for finding a quark with momentum fraction $x = p^+_{parton}/p^+_{proton}$[1] in the proton and which is polarized either in the same or the opposite direction to the proton's polarization. This is usually called the naive parton model; it has no gauge degrees of freedom.

In the naive parton model the structure functions are described by the four linearly independent parton distributions. There are two spin-independent distribu-

---

[1] Here, p^+ denotes the light-cone momentum; see Appendix A for details

tions (one for a quark and one for an anti-quark), and two spin-dependent distributions. The charge conjugation even combination [2]

$$(q+\bar{q})^{\uparrow}(x)+(q+\bar{q})^{\downarrow}(x) \tag{1.28}$$

occurs in the structure functions $F_1(x,Q^2)$ and $F_2(x,Q^2)$. It is measured in the unpolarized lepton-nucleon scattering. In the naive parton model one finds

$$F_2(x)=2xF_1(x)=x\sum_q e_q^2\Big[(q+\bar{q})^{\uparrow}(x)+(q+\bar{q})^{\downarrow}(x)\Big], \tag{1.29}$$

where e_q denotes the quark charge. The relationship between F_1 and F_2 is called the Callan-Gross relation.

The polarized (spin-dependent) quark and anti-quark distributions occur in the spin-dependent structure function $g_1(x)$, which in the naive parton model is written as:

$$g_1(x)=\frac{1}{2}\sum_q e_q^2\Delta q(x)\ , \tag{1.30}$$

where

$$\Delta q(x)\equiv\delta q(x)+\delta\bar{q}(x)=(q^{\uparrow}-q^{\downarrow})(x)+(\bar{q}^{\uparrow}-\bar{q}^{\downarrow})(x) \tag{1.31}$$

is the polarized quark distribution. It is helpful to rewrite $g_1(x)$ in terms of the SU(3) flavor combinations:

$$\begin{aligned}\Delta q_3(x) &\equiv \Delta u(x)-\Delta d(x),\\ \Delta q_8(x) &\equiv \Delta u(x)+\Delta d(x)-2\Delta s(x),\\ \Delta\Sigma(x) &\equiv \Delta u(x)+\Delta d(x)+\Delta s(x).\end{aligned} \tag{1.32}$$

Combination $\Delta\Sigma$ (also refered to as Δq_0) is a singlet distribution whereas Δq_3 and Δq_8 are non-singlet.

---

[2] In Eq. (1.28), $q^{\uparrow}(x)$ ($\bar{q}^{\uparrow}(x)$) denotes the distribution for helicity aligned quark (anti-quark), and $q^{\downarrow}(x)$ ($\bar{q}^{\downarrow}(x)$) stands for helicity anti-aligned distributions. By convention, the parton distributions are given for the proton, and one can get the corresponding neutron distribution functions using isospin symmetry. These distributions are often written in the literature as $G_{p/H}(x,\lambda,Q)$ where p denotes the parton (quark or gluon), H stands for the hadron, and λ is the parton helicity.

Calculation of the x-dependence of the structure functions requires precise knowledge of the nucleon wave function. The moments of structure functions, on the other hand, can be calculated and provide a testing ground for our understanding of nucleon structure in QCD. The first piece of experimental evidence that showed that we needed to go beyond the naive parton model came when it was observed that quarks contribute only 50% of the proton's momentum. This was naturally accommodated with the advent of QCD where the gluons in the limit of infinite Q^2 carry the momentum fraction

$$\langle xG_{g/p}(x,Q^2)\rangle \to \frac{16}{16+3N_f}\,, \tag{1.33}$$

where N_f is the number of quark flavors.[19]

In the naive parton model,

$$\Delta q = \int_0^1 dx\ \Delta q(x) \tag{1.34}$$

determines the fraction of the proton's helicity which is carried by quarks (and anti-quarks) of flavor q. Thus, we write

$$\Gamma_1^p \equiv \int_0^1 dx\ g_1^p(x) = \frac{1}{12}(\Delta u - \Delta d) + \frac{1}{36}(\Delta u + \Delta d - 2\Delta s) + \frac{1}{9}(\Delta u + \Delta d + \Delta s) + \frac{2}{9}\Delta c. \tag{1.35}$$

Assuming isospin symmetry, the neutron integral is obtained by interchanging u and d quarks in Eq. (1.35). The singlet term $\Delta\Sigma = \Delta u + \Delta d + \Delta s$ denotes the light-quark spin, or more strictly speaking, helicity content of the nucleon[3]

In operator language, Δq is defined by the proton matrix element of the axial current. We write

$$2MS_\mu \Delta q_a =< p, S|\bar{q}\gamma_\mu\gamma_5\frac{\lambda^a}{2}q|p, S > \tag{1.36}$$

for $a = 3, 8, 0$. The non-singlet matrix elements also arise in the neutron and hyperon beta decays. Current algebra relates the spin dependent (strong interaction) struc-

---

[3] In Eq. (1.35), we have explicitly written a contribution from charm quarks Δc, which is present above the charm threshold. It is usually ignored in the numerical analysis.

ture of the proton measured in polarized deep inelastic scattering at high energies to the quantities needed in low-energy weak-interaction physics. The currents which measure Δq_3 and Δq_8 do not renormalize, so these quantities are scale independent. They are determined as $\Delta q_3 = g_A = F + D$ and $\Delta q_8 = \frac{1}{\sqrt{3}}(3F - D)$ within SU(3). The axial coupling constant of the neutron beta-decay is g_A, and F and D are the antisymmetric and symmetric SU(3) couplings. One finds[20,21]

$$\Delta u - \Delta d = g_A = 1.2601 \pm 0.0025 \tag{1.37}$$

and

$$\Delta u + \Delta d - 2\Delta s = \frac{1}{\sqrt{3}}(3F - D) = 0.688 \pm 0.035. \tag{1.38}$$

Since Δq_3 and Δq_8 are determined from other experiments, by measuring the integral Γ_1^p or Γ_1^n, we can extract the singlet "spin content" of the proton $\Delta\Sigma$ as well as individual quark contributions Δu, Δd, and Δs (this assumes that there is a negligible charm component Δc in the data.)

1.2.5 Sum rules

The angular momentum of a fast-moving nucleon has three sources, the angular momentum carried by the quarks, the angular momentum carried by the gluons, and the orbital angular momentum carried by any of the constituents. Angular momentum conservation for J_z at a fixed light-cone time implies the sum rule[24][4]

$$\frac{1}{2}(\Delta u + \Delta d + \Delta s) + \Delta G + < L_z >= \frac{1}{2}. \tag{1.39}$$

The sum $\Delta\Sigma = \Delta u + \Delta d + \Delta s$ is interpreted as the proton helicity carried by quarks, and $\Delta G \equiv \int_0^1 dx \Delta G(x)$ is the helicity carried by the gluon where $\Delta G(x)$ is the difference between the helicity-aligned and anti-aligned gluon distributions

---

[4] Such interpretation is not gauge- or Lorenz-invariant[25], so one commonly assumes the infinite-momentum frame (in which the nucleon moves with an infinite momentum along the z direction), and the light-cone gauge (see Appendix A). A gauge-invariant treatment of the spin sum rule has been derived in Ref. [25].

$G^+(x)$ and $G^-(x)$. The unpolarized gluon distribution $G(x)$ is the sum of these two functions, $G(x) \equiv G^+(x) + G^-(x)$. By definition, the anti-quark contributions are included in $\Delta q(x)$ and $q(x)$.

There are two sum rules for g_1 which can be tested in spin dependent deep inelastic scattering. The Bjorken sum rule[26] gives a relation for the difference between the first moment of g_1 for a proton and neutron target. In the scaling limit, it reads:

$$\int_0^1 dx\, \left(g_1^p(x) - g_1^n(x)\right) = \frac{1}{6} g_A \,. \tag{1.40}$$

The Bjorken sum rule was derived using current algebra before the advent of QCD and is a test of isospin symmetry.

At the finite Q^2 of an experiment one must include perturbative QCD (pQCD) Wilson coefficients. Including corrections to order α_S^3, the Bjorken sum rule becomes

$$\int_0^1 dx\, \left(g_1^p(x) - g_1^n(x)\right) = \frac{1}{6} g_A \left[1 - \frac{\alpha_S(Q^2)}{\pi} + C_2 \left(\frac{\alpha_S(Q^2)}{\pi}\right)^2 + C_3 \left(\frac{\alpha_S(Q^2)}{\pi}\right)^3\right], \tag{1.41}$$

where $C_2 = -3.5833$ and $C_3 = -20.2153$ in the three-flavor theory.[28] The corresponding expansion for the first moment of the proton spin structure function reads

$$\int_0^1 dx\, g_1^p(x, Q^2) = \frac{1}{6}\left[\left(\Delta q_3 + \frac{1}{\sqrt{3}}\Delta q_8\right)\left(1 - \frac{\alpha_S}{\pi}\right) + 2\sqrt{\frac{2}{3}}\Delta\Sigma\left(1 - \frac{\alpha_S}{\pi}\frac{33 - 8N_f}{33 - 2N_f}\right)\right], \tag{1.42}$$

where the perturbative coefficients are quoted to $O(\alpha_S)$.[27]

The second sum rule for g_1 is the Ellis-Jaffe sum rule[29] and is a test of Zweig's (or OZI after Okuba, Zweig, and Iizuka) rule in the flavor singlet channel. If we assume that strange (and heavy) quarks do not play a significant role and set $\Delta s = 0$, then the quark "spin content" would be determined by the hyperon beta decays. In this scenario we would have $\Delta\Sigma = \Delta q_8 = 0.688 \pm 0.035$, where the rest of the proton's spin would be carried by the gluons and also by quark and gluon orbital angular momentum. Substituting this value into Eq. (1.42) we find

$$\int_0^1 dx\ g_1^p(x) = 0.189 \pm 0.005 \tag{1.43}$$

(at 10 GeV^2). The Ellis-Jaffe sum rule involves a model-dependent assumption that the OZI rule is obeyed, whereas the Bjorken sum rule should hold exactly in QCD. Experiments up to now have found Ellis-Jaffe sum rule to be violated by more than two standard deviations[8,10–13] and confirmed the Bjorken sum rule.[11,13,30]

1.2.6 Transverse spin-dependent structure function g_2

The nucleon transverse spin-dependent structure function $g_2(x, Q^2)$ has only recently been measured,[22,23] and there have been few theoretical studies of it. As we mentioned above, it is strongly suppressed in the longitudinal asymmetry measurements and has been customarily neglected in the analysis of the early experiments. However, precise measurements of g_1, like the one described in this thesis, require taking into account all associated corrections.

One of the first theoretical observations was the Burkhardt-Cottingham sum rule[31]

$$\int_0^1 dx\ g_2(x, Q^2) = 0\ . \tag{1.44}$$

It was originally derived using Regge theory and dispersion relations,[32] raised many questions and induced a lively theoretical discussion.[32–34] The experimental measurement of the sum rule could provide a test of Regge theory in DIS.

A reliable method for exploring the properties of structure functions in the DIS limit is the operator product expansion (OPE) on the light-cone, *i.e.* in the space-time region $x_\mu x^\mu \leq Q^{-2} \to 0$ in the Bjorken limit.[32] Using OPE, the product of two electromagnetic currents forming the hadronic tensor

$$W_{\mu\nu}(q,p,S) = \frac{1}{4\pi} \int d^4x e^{iqx} \langle pS|[J_\mu(x), J_\nu(0)]|pS\rangle \tag{1.45}$$

can be expanded in terms of the renormalized local operators with singular coefficients. In the Bjorken limit the importance of an operator is determined by its twist, or light-cone singularity of the coefficient function (see Section 1.3.2.2). As it is shown in Ref. [35], while higher-twist operators (for instance, twist-three operators that reflect finite quark masses and quark-gluon interactions in the nucleon) have only correcting impact on g_1, their contribution to g_2 is rather big and can be measured experimentally. In general, g_2 can be written as

$$g_2(x,Q^2) = g_2^{WW}(x,Q^2) + g_2^{HT}(x,Q^2)\ , \tag{1.46}$$

where the first term proposed by Wandzura and Wilczek[36] contains only twist-2 matrix elements and is determined entirely by g_1 :

$$g_2^{WW}(x,Q^2) = -g_1(x,Q^2) + \int_0^1 \frac{dy}{y} g_1(y,Q^2). \tag{1.47}$$

The second term, g_2^{HT}, receives contributions from the quark-gluon interactions inside the nucleon and non-zero values of quark masses (twist-3 operators). In principle, twist-3 contributions can be big because of the strong confining interaction and the appreciable value of the s-quark mass. Bag model calculations support such an assumption.[35] If so, experimental measurements of g_2 directly measure the interaction-dependent higher twist matrix elements and could provide us with important information about nucleon structure.

1.3 QCD-improved parton model

1.3.1 Spin structure functions in QCD

In the "naive" parton model, the nucleon spin structure function g_1 defined by Eq. (1.30) is a weighted sum of the quark helicity distributions that depend only on the scaling variable x. In the QCD-improved parton model, quark distributions, and hence g_1 evolve with Q^2 due to gluon bremsstrahlung and gluon-induced quark-antiquark pair creation. In the leading order (LO) in the strong coupling constant α_S Eq. (1.30) simply becomes

$$g_1(x, Q^2) = \frac{1}{2} \sum_q e_q^2 \Delta q(x, Q^2). \tag{1.48}$$

The spin structure function g_1 is again defined by the quark contributions, and gluons couple to it only indirectly via the evolution of the quark distributions. In higher orders, g_1 is defined as

$$g_1(x, Q^2) = \frac{1}{2} \sum_q^{N_f} e_q^2 \left[C_q \otimes \Delta q + \frac{1}{N_f} C_G \otimes \Delta G \right] , \tag{1.49}$$

where again both quark and antiquark contributions are included into definition of $\Delta q \equiv \delta q + \delta \bar{q}$. The sum is over all active flavors ($N_f = 3$ is only light and strange quarks are taken into account), and the symbol $\otimes$ in Eq. (1.49) denotes the convolution integral

$$(f \otimes g)(x) = \int_x^1 \frac{dy}{y} f(y) g(\frac{x}{y}). \tag{1.50}$$

The perturbative Wilson coefficients $C_{q,G}$ represent QCD radiative corrections, and are written as series in powers of α_S

$$C_{q,G} = C_{q,G}^{(0)} + \frac{\alpha_S}{2\pi} C_{q,G}^{(1)} + \ldots . \tag{1.51}$$

The leading order expression Eq. (1.48) is obtained by dropping higher-order $C_{q,G}^{(1)}$ terms and having $C_q^{(0)}(x) = \delta(1-x)$ and $C_q^{(0)}(x) = 0$. The next-to-leading (NLO) spin-dependent coefficients $C_q^{(1)}$ and $C_G^{(1)}$ in the modified minimal subtraction ($\overline{\text{MS}}$) renormalization scheme are given[37] by

$$\begin{aligned} C_q^{(1)}(x) \;\; = \;\; & C_F \left[(1+x^2) \left(\frac{\ln(1-x)}{1-x} \right)_+ - \frac{3}{2} \frac{1}{(1-x)_+} - \frac{1+x^2}{1-x} \ln x + \right. \\ & \left. + 2 + x - \left(\frac{9}{2} + \frac{\pi^2}{3} \right) \delta(1-x) \right] \end{aligned} \tag{1.52}$$

$$\text{and} \quad C_G^{(1)}(x) = 2T_f\left[(2x-1)\left(\ln\frac{1-x}{x}-1\right)+2(1-x)\right], \tag{1.53}$$

and their moments are given in Appendix B. Here $C_F = 4/3$ and $T_f = N_f/2$ are Casimir invariants for the quark representation of $SU(3)_{flavor}$, and $(1-z)_+$ is defined by

$$\int_0^1 dz\frac{f(z)}{(1-z)_+} \equiv \int_0^1 dz\frac{f(z)-f(1)}{(1-z)}. \tag{1.54}$$

The charm contribution is usually ignored, so the number of flavors $N_f = 3$.

As it follows from Eq. (1.49), in the NLO analysis, the gluon density directly affects the spin structure function g_1. Precision measurements of g_1 can therefore reveal information about the gluon contribution to the nucleon helicity.

1.3.2 Q^2 dependence of the polarized parton distributions

In the simple "naive" parton model with no gauge degrees of freedom, the quark distributions are functions of only one variable – Bjorken x. This is not the case in QCD which predicts systematic deviations from this simple picture.

There are several sources of scaling violations. At high values of Q^2 quarks are likely to radiate gluons (Fig. 1.2[5]), and gluons, in turn, create quark-antiquark pairs. The gluon emission reduces the momentum of the quark effectively shifting the quark distribution to lower values of x. At high x the structure functions should then decrease with increasing Q^2, whereas at low x they are expected to increase. Thus, QCD predicts the *evolution* of the parton distributions with Q^2 that produces the logarithmic Q^2 dependence of the structure functions.

Another source of the scaling breaking is the effect of "higher twist" contributions, or corrections that arise from the subprocesses which involve more than the minimal number of interacting fields, such as the processes of Fig. 1.3. Although

---

[5] The figure shows virtual Compton scattering since its amplitude is related to the deep inelastic cross section via the optical theorem.

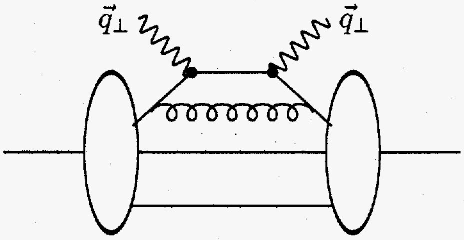

Fig. 1.2. Gluon emission results in logarithmic deviations from Bjorken scaling, as described by the DGLAP equations.

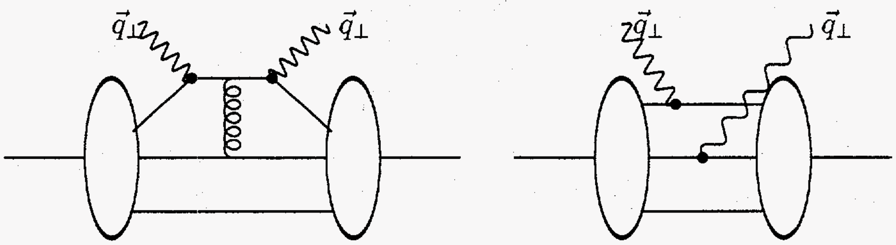

Fig. 1.3. Examples of higher twist corrections to the virtual Compton scattering amplitude.

these corrections are suppressed by powers of Q^2, they turn out to be significant at fixed $(1-x)Q^2$.[40]

1.3.2.1 *Evolution of the parton distributions*

Having the initial distributions at some value of $Q^2 = Q_0^2$ as the boundary conditions, one can obtain the distributions at higher Q^2 using the Dokshitzer-Gribov-Lipatov-Altarelli-Parisi (DGLAP) evolution equations[41–43] that read:

$$\begin{aligned} \frac{d\delta q_i(x,Q^2)}{d\ln Q^2} &= \frac{\alpha_S(Q^2)}{2\pi}\left[\delta q_i \otimes \Delta P_{qq} + \Delta G \otimes \Delta P_{qG}\right] \quad \text{and} \\ \frac{d\Delta G(x,Q^2)}{d\ln Q^2} &= \frac{\alpha_S(Q^2)}{2\pi}\left[\sum_{i=1}^{2N_f} \delta q_i \otimes \Delta P_{Gq} + \Delta G \otimes \Delta P_{GG}\right] , \end{aligned} \tag{1.55}$$

where (unlike the definition of Δ in Eq. (1.31)), $\delta q_i = q_i^{\uparrow}(x, Q^2) - q_i^{\downarrow}(x, Q^2)$ is the spin distribution for a quark (antiquark), $\Delta G = G^{\uparrow}(x, Q^2) - G^{\downarrow}(x, Q^2)$ is the gluon distribution, N_f is the number of active quark flavors, and $\otimes$ denotes the convolution integral of Eq. (1.50).

Like the perturbative Wilson coefficients of Eq. (1.51), the splitting functions are calculated as a series in the strong coupling constant

$$\Delta P_{ij} = \Delta P_{ij}^{(0)} + \frac{\alpha_S}{2\pi} \Delta P_{ij}^{(1)} + \dots . \tag{1.56}$$

The leading order spin-dependent splitting functions are[41,43]

$$\begin{aligned}
\Delta P_{qq}^{(0)}(z) &= \frac{4}{3}\left[\frac{1+z^2}{(1-z)_+} + \frac{3}{2}\delta(z-1)\right] , \\
\Delta P_{qG}^{(0)}(z) &= \frac{1}{2}\left[z^2 - (1-z)^2\right] , \\
\Delta P_{Gq}^{(0)}(z) &= \frac{4}{3}\left[\frac{1-(1-z)^2}{z}\right] , \quad \text{and} \\
\Delta P_{GG}^{(0)}(z) &= 3\left[(1+z^4)\left(\frac{1}{z} + \frac{1}{(1-z)_+}\right) - \frac{(1-z)^3}{z} + \left(\frac{11}{6} - \frac{N_f}{9}\right)\delta(1-z)\right] .
\end{aligned} \tag{1.57}$$

The next-to-leading order spin-dependent splitting functions have been calculated in Ref. [37], and their moments are given in Appendix B. The evolution equations for the unpolarized distributions can be easily obtained by changing $\delta q_i \to q_i$, $\Delta G \to G$, $\Delta P_{ij} \to P_{ij}$, and the unpolarized splitting functions $P_{ij}^{(0)}$ given in References [41,43] (LO), and References [38,39] (NLO).

It is not possible to find an exact analytic solution to the Equations (1.55). However, numerical calculations and approximations are feasible.[44] It is clear from Eqs. (1.55) that the evolution of the quark distributions is sensitive to the gluon polarization; thus studying the Q^2 dependence of the polarized structure functions can provide us with the experimental constraints on the polarized gluon distribution functions. For the presently available experimental data, such a program is carried out in Chapter 5.

It should be noted that in the leading order, qq elements of the evolution matrix are equal in both polarized and unpolarized cases: $\Delta P_{qq}^{(0)} = P_{qq}^{(0)}$. Thus, if the gluon contribution is small (such is the case at high x), the evolution of the unpolarized and polarized structure functions is similar, and the ratio g_1/F_1 (or the asymmetry A_1) is approximately independent of Q^2. This observation, supported within the precision of the data, has been used by the experimental collaborations to evolve data taken at different values of Q^2 to a common scale. This assumption is clearly unjustified at low x where the gluon densities, both unpolarized and polarized, rise sharply. As the quality of the data improves, the Q^2-coverage increases, and even lower values of x are probed, a consistent pQCD-based approach should be used.

1.3.2.2 Higher twist effects

The diagrams involving interference terms between different quark currents as well as the quark-gluon correlations (Fig. 1.3) are responsible for the contributions to the structure functions that are suppressed relative to the leading contributions by the powers of Q^2. These corrections, however, become important at fixed values of W^2. Taking the *higher twist* corrections into account leads to the following series expression for the unpolarized structure functions[40]

$$F_2(x, Q^2) = F_2(x, Q^2)_{\text{leading twist}} \left[1 + \frac{A}{Q^2(1-x)} + \frac{B}{Q^4(1-x)^2} + \cdots \right] , \qquad (1.58)$$

where the coefficient $A \approx O(m_\rho^2)$ is set by the wavefunction scale. Unpolarized data from SLAC show substantial higher twist contributions at high x.[79] One can therefore assume that higher twist contributions to the polarized structure functions are not negligible at low W^2.

Higher twist corrections modify the structure function sum rules as follows:

$$\Gamma(Q^2) = \Gamma_\infty \left[1 + \sum_n C_n \left(\frac{\alpha_S(Q^2)}{\pi} \right)^n \right] + \sum_m \frac{D_m}{(Q^2)^m} , \qquad (1.59)$$

where D_m are the higher twist coefficients. There is no firm agreement on the size of the correction for the Bjorken sum rule; the recent estimate[78] is

$$D_1 = -0.02 \pm 0.01 \text{ GeV}^2 \tag{1.60}$$

so the effect is quite small but comparable to the size of the current experimental errors.

1.4 Shape of the polarized parton distributions

1.4.1 Helicity-dependent quark distributions

The Q^2-evolution of structure functions is well predicted by perturbative QCD DGLAP equations.[41–43] The initial shape of these distributions, however, is not directly calculable and reflects the non-perturbative dynamics of quarks and gluons inside the nucleon. Nevertheless, the end-point behavior of the structure functions can be accurately predicted from perturbative arguments. In this section, we will constrain the behavior of the structure functions in the regions of $x \approx 0$ and $x \approx 1$. The predicted forms can be combined to form a parameterization of the polarized structure functions.

The polarized quark and gluon distribution functions $G_{q/H}(x, \lambda, Q)$ and $G_{g/H}(x, \lambda, Q)$ of a hadron are most conveniently represented as overlaps of the light-cone wave functions $\psi_n(x_i, k_\perp, \lambda_i)$, where[6] $\sum_{i=1}^{n} x_i = 1$, and $\sum_{i=1}^{n} k_\perp = 0$. As shown in Appendix A, the region of $x \to 1$ represents a very far off-shell configuration of the bound state wave function. Assuming that the bound state wave function is dominated by the lowest invariant mass Fock state, one can conclude that a constituent can get $x \approx 1$ only by exchanging hard gluons. Thus, the leading behavior of the amplitudes in the region of $x \approx 1$ can be computed from the simple minimally connected gluon-exchange diagrams (Fig. 1.4) calculable in perturbative QCD.

---

[6] see Appendix A

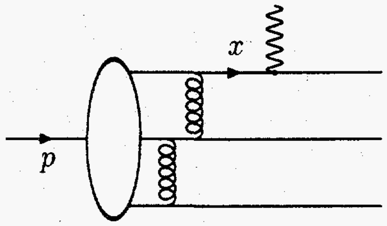

Fig. 1.4. Leading-order diagram for $G_{q/H}(x, \lambda, Q)$ at $x \approx 1$.

The limiting power-law behavior at $x \to 1$ of helicity-dependent distributions is

$$G_{q/H} \sim (1-x)^{2n-1+2\Delta S_z}. \tag{1.61}$$

Here n is the minimal number of spectator quark lines, and $\Delta S_z = | S_z^q - S_z^H | = 0, 1$ for parallel or anti-parallel quark and proton helicities, respectively.[50] This counting rule (*cf.* Eqs. (A.13), (A.14), and (A.15)) reflects the fact that the valence Fock states with the minimum number of constituents give the leading contribution to structure functions when one quark carries nearly all of the light-cone momentum; contributions from Fock states with a higher number of partons fall off faster at $x \to 1$.[49] The helicity dependence of the counting rule also reflects the helicity retention properties of the gauge couplings; a quark with a large momentum fraction of the hadron also tends to carry its helicity. The anti-aligned helicity quark is suppressed by a relative factor $(1-x)^2$. Similarly, in the case of splitting functions such as $q \to qg$ or $g \to \bar{q}q$, the sign of the helicity of the parent parton is transferred to the constituent with the largest momentum fraction.[51] The counting rule for valence quarks can be combined with the splitting functions to predict the $x \to 1$ behavior of gluon and non-valence quark distributions of non-exotic hadrons; they fall off faster by at least one power of $(1-x)$ than the respective quark distributions.

The counting rules for the end-point-behavior of quark and gluon helicity distributions can also be derived from duality, *i.e.* a direct relationship between the physics of exclusive and inclusive channels at fixed invariant mass.[52] As shown by Drell and Yan,[52] a quark distribution function behaves as

$$G_{q/H} \sim (1-x)^{2n-1} \tag{1.62}$$

at $x \to 1$ if the corresponding form factor falls off as

$$F(Q^2) \sim (1/Q^2)^n \tag{1.63}$$

at large Q^2. Measurements of elastic electron-proton scattering at SLAC[53] are compatible with the perturbative QCD predictions[54] for both the helicity-conserving $F_1(Q^2)$ and helicity-changing $F_2(Q^2)$ form factors: $Q^4F_1(Q^2)$ and $Q^6F_2(Q^2)$ become approximately constant at large Q^2. This behavior corresponds to the threshold behavior of helicity-parallel and helicity anti-parallel quark distributions: $(1-x)^3$ and $(1-x)^5$ as $x \to 1$, respectively, in agreement with the counting rules. The leading exponent for quark distributions is odd in the case of baryons and even for mesons in agreement with the Gribov-Lipatov crossing rule.[41]

The counting rule predictions for the quark and gluon distributions are relevant at low momentum transfer scales $Q_0 \approx \Lambda_{QCD}$ in which the controlling physics is that of the hadronic bound state rather than the radiative corrections associated with structure function evolution.

At high Q^2 the radiation from the struck quark line increases the effective power law fall-off $(1-x)^p$ of structure functions relative to the underlying quark distributions[49]:

$$\Delta p = (4C_F/\beta_1)\ln\left(\frac{\ln(Q^2/\Lambda^2)}{\ln(Q_0^2/\Lambda^2)}\right), \tag{1.64}$$

where $C_F = 4/3$ and $\beta_1 = 11 - (2/3)N_f$. Thus, the counting rule predictions for the power p provide a *lower bound* for the effective exponent of quark structure functions at high $Q^2 > Q_0^2$. However, in the end-point region $x \approx 1$, the struck quark is far off-shell and the radiation is quenched since one cannot evolve Q^2 below

$Q_0^2 \simeq k_F^2 = -(\mu^2/(1-x))$, the Feynman virtuality of the struck parton[40] (here, μ is the invariant mass of the spectator quarks).

Thus pQCD can give useful predictions for the power law fall-off of helicity-aligned and anti-aligned structure functions at $x \approx 1$. Higher order contributions involving additional hard gluon exchange are suppressed by powers of $\alpha_S(k_F^2)$. Further iterations of the interaction kernel will give factors of fractional powers of $\log(1-x)$ analogous to the anomalous dimensions $\log^{\lambda_n} Q^2$ which appear in the pQCD treatment of form factors at large momentum transfer.[54]

The fact that one has a definite prediction for the $x \approx 1$ behavior of leading twist structure functions is a powerful tool in QCD phenomenology, since any contribution that does not decrease sufficiently fast at large x is most likely due to coherent multi-quark and quark-gluon correlations. As discussed in Ref. [55], such contributions are higher twist, and they are significant at fixed $(1-x)Q^2 \approx M^2$.

1.4.2 Helicity-dependent gluon distributions

At $x \to 1$ the gluon distribution function is constrained by the counting rule arguments (see Fig. 1.5) and obeys the Gribov-Lipatov crossing rule[41]:

$$G_{g/p} \sim (1-x)^4, \quad x \to 1. \tag{1.65}$$

It is known in QED[51] that in $e \to e\gamma^*$ processes the polarization of the initial electron is retained by the photon at high momentum transfer; the same behavior is expected for any gauge theory including QCD. Thus,

$$\frac{G^-(x)}{G^+(x)} = (1-x)^2, \quad x \to 1. \tag{1.66}$$

At low x quarks radiate coherently (Fig. 1.6), and one has to take into account interference terms. Brodsky, Burkardt, and Schmidt have obtained the following constraint on the gluon distribution functions at $x \approx 0$[49]:

$$\left(\frac{\Delta G(x)}{G(x)}\right)_{\text{proton}} \to \frac{x}{3}\left\langle\frac{1}{y}\right\rangle, \quad x \to 0. \tag{1.67}$$

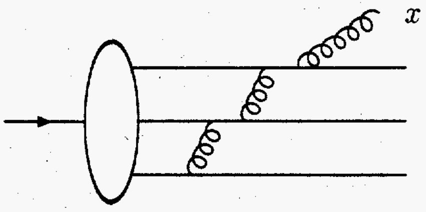

Fig. 1.5. The leading contribution to the gluon distribution function at high x.

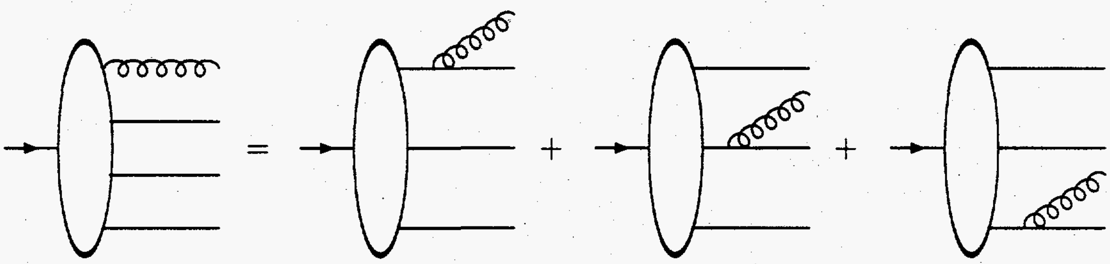

Fig. 1.6. The low-x behavior of the gluon distribution function is determined by coherence effects.

Here $\langle 1/y \rangle$ stands for the first inverse moment of the quark light-cone momentum fraction distribution in the lowest proton Fock state. For this state $\langle 1/y \rangle \approx 3$.

For baryons, a simple form of the gluon distributions, which incorporates the limiting behaviors presented above, is[49]

$$\Delta G(x) = \frac{N}{x}[1-(1-x)^2](1-x)^4, \tag{1.68}$$

$$G(x) = \frac{N}{x}[1+(1-x)^2](1-x)^4 \,, \tag{1.69}$$

where N is a normalization constant. In this model the momentum fraction carried by the gluons in the proton is

$$\langle x_g \rangle \equiv \int_0^1 dx \; xG(x) = \frac{12}{35}N, \tag{1.70}$$

and the helicity carried by the gluons is

$$\Delta G \equiv \int_0^1 dx \Delta G(x) = \frac{11}{30} N, \tag{1.71}$$

Taking the momentum fraction $\langle x_g \rangle$ to be 1/2 yields $\Delta G = 0.54$.

1.4.3 The axial anomaly

The prediction, found in the previous section, that $\Delta G \simeq 0.5$ is phenomenologically interesting. If one also accepts the experimental suggestion from EMC that the quark helicity sum $\Delta u + \Delta d$ is small, then this implies that gluons could carry a large part of the proton helicity $J_z = 1/2$. The angular momentum conservation requires then significant (and, most likely, negative) orbital angular momentum L_z which arises, for example, from the finite transverse momentum associated with the $q \to qg$ gluon emission matrix element.

Several authors have argued[56–58] that the gluon polarization may explain the small quark helicity content of the proton observed by EMC and rescue the Ellis-Jaffe assumption of $\Delta s = 0$.[59] Gluons could contribute to proton helicity via the γ_5-triangle anomaly that breaks, at the quantum level, the conservation of the axial current $\bar{q}\gamma_\mu\gamma_5 q$:

$$\partial^\mu A^0_\mu = \frac{\alpha_s}{\pi} N_f \text{ tr } F_{\mu\nu}\tilde{F}^{\mu\nu} \ , \quad \tilde{F}^{\mu\nu} \equiv \epsilon^{\mu\nu\alpha\beta} F_{\alpha\beta} \tag{1.72}$$

where $F_{\mu\nu}$ is the gauge field strength tensor in QCD. The intuitive meaning of Eq. (1.72) is that the anomaly induces a mixing between gluons and the flavor-singlet axial current of quarks. One can then redefine the quark helicities measured in the experiment to be

$$\Delta q \to \Delta q - \frac{\alpha_S}{2\pi} \Delta G. \tag{1.73}$$

The authors of Ref. [60] have calculated, based on the recent experimental data,that the $\Delta s = 0$ assumption requires $\Delta G \approx 2$. This number is not as big as claimed in Ref. [59], but still requires a large negative orbital angular momentum contribution.

Equation (1.73) demonstrates the intrinsic ambiguity associated with the interpretation of the quark distribution function. This is the manifestation of the *factorization scheme dependence* of the parton distributions.[61–63] Although the structure functions measured in the experiment are unambiguous, their factorization in Eq. (1.49) into non-perturbative parton distributions Δf_i and hard cross sections ΔC_i is definition-dependent. One therefore always has to specify a particular prescription (*scheme*) according to which the factorization is performed. In fact, if the calculation is done using the dimensional regularization in the conventional $\overline{\mathrm{MS}}$ scheme, the gluon contribution to the first moment of g_1 vanishes[61] (due to the fact that $\int_0^1 dx C_G(x) = 0$ in Eq. (1.49)[37]). We will discuss more details of the scheme dependence as well as other theoretical uncertainties in extracting the parton distributions in Chapter 5.

1.5 Low and high x phenomenology

No experiment can measure the full range $0 \leq x \leq 1$, and every experiment must make some assumption in order to extrapolate to the full x range. The contribution from the high x is typically small since the structure functions decrease rapidly. From the perturbative QCD arguments outlined in Section 1.4.1, the valence quark contribution to g_1 falls off at least as $(1-x)^3$ at $x \to 1$, and the sea and gluon contributions are suppressed by additional powers of $(1-x)$. The helicity-antialigned quark distribution is suppressed by $(1-x)^2$ relative to the helicity-aligned distribution, so one can write on general grounds for the virtual photon-nucleon asymmetry

$$A_1 \sim \frac{\Delta q}{q} \to 1, \; x \to 1. \tag{1.74}$$

Experiments commonly use Eq. (1.74) to extrapolate data to $x = 1$, or extrapolate g_1 directly assuming the pQCD predicted power fall off

$$g_1 \sim \Delta q \sim (1-x)^3, \; x \to 1. \tag{1.75}$$

Both extrapolations are consistent with the data within experimental errors.

The situation is much less clear for the small x extrapolation. At fixed Q^2, the $x \to 0$ limit corresponds to the infinite photon energy $\nu \to \infty$, or, equivalently,

$$s \equiv (P+q)^2 \equiv W^2 = M^2 - Q^2 + 2M\nu = M^2 + Q^2\frac{1-x}{x} \to \infty \tag{1.76}$$

for the photon-nucleon center-of-mass energy s. This limit has been traditionally described by the theory of complex angular momentum (Regge theory). In Regge theory, one assumes that the high energy limit of the s-channel amplitude for the scattering $ab \to cd$ is determined by the singularities of the t-channel amplitude in the complex angular momentum plane; in the case of a simple pole (associated with an exchange of a particle – *"Reggeon"*[7]), the corresponding contribution to the amplitude can be written as

$$\mathcal{A}^{ab\to cd}(s,t) = \beta(t)s^{\alpha(t)},\ s \to \infty\ , \tag{1.77}$$

where $\alpha(t)$ is the Regge *trajectory.* The optical theorem relates the total cross section to the imaginary part of the forward ($t=0$) amplitude:

$$Im\mathcal{A}^{ab\to cd}(s,t=0) = s\sigma_{tot}^{ab\to cd}(s), \tag{1.78}$$

and we have

$$\sigma_{tot}^{ab\to cd}(s) \sim s^{\alpha(0)-1}. \tag{1.79}$$

The Regge *intercept* $\alpha(0)$ is determined experimentally, for instance, in πN or NN scattering.

Regge theory has been very successful in describing a wide variety of high energy *unpolarized* cross sections.[64] Since it provides a simple and economical (in terms of free parameters) description of the total cross sections, Donnachie and Landshoff conclude that[64] *"Regge theory remains one of the great truths of particle physics".*

---

[7] Such a particle can possess quantum numbers of a real meson, or vacuum, in which case it is called a Pomeron[32].

In Section 1.2.2 we have shown the relationship between the virtual nucleon photoabsorption cross sections and the spin structure functions. For $\nu \to \infty$ and a fixed Q^2, the leading expression for g_1 is

$$g_1 \approx \nu(\sigma^T_{1/2} - \sigma^T_{3/2})/2 \tag{1.80}$$

(ignoring terms constant or decreasing with ν). Since $s \approx 2M\nu$ at large ν and fixed Q^2,

$$g_1 \sim \beta(Q^2)\nu^\alpha \sim x^{-\alpha},\ x \to 0\ , \tag{1.81}$$

where α is the dominant Regge intercept and $\beta(Q^2)$ is the pole residue. It is believed[65] that the leading behavior of g_1 is controlled by the a_1 meson trajectory with the intercept $\alpha_{a_1} = -0.14 \pm 0.20$.[65,66] Thus g_1 converges at low x according to the traditional Regge picture. Experiments so far have used the upper limit $\alpha_{a_1} = 0$ to extrapolate data to $x = 0$ and evaluate sum rules; the variation in α_{a_1} is used to estimate the extrapolation error.

There are several problems with this simple description. It is not certain at which values of x, and at what Q^2 the Regge theory is applicable. Strictly speaking, it works at the low hadron scales, *i.e.* Q^2 below 1 GeV^2. At high ν and Q^2 and finite x the structure functions are, in general, not determined by the rightmost singularities in the complex angular momentum plane; one has to include all relevant contributions. One therefore has to assume[32] that there is a smooth transition from the scaling regime ($\nu \to \infty$, $Q^2 \to \infty$, x fixed) to the Regge regime ($\nu \to \infty$, $Q^2 = const$) at small x. This is an additional hypothesis. In the unpolarized case, it has been shown[32] that the residues of the dominating Regge poles $\beta(Q^2)$ have to have a special Q^2 dependence. Even if the Regge regime is not truly set in, the unpolarized analysis benefits from the fact that the residues of different poles are generally of the same sign (positive), whereas in the polarized case this may not be the case and one cannot ignore possible "interference effects" that could mask the true asymptotic behavior.

Several authors argued[67,68] that the double-Pomeron cut contributes to g_1 at low x; it then induces a singular behavior[8]

$$g_1 \sim \frac{1}{x \log^2 x}, \; x \to 0. \tag{1.82}$$

Again, the kinematic domain where such behavior applies is not specified; moreover, it has not been observed in the unpolarized data.[69]

A model of the Pomeron based on the non-perturbative gluon exchange[70] gives a softer, but still singular behavior:

$$g_1 \sim 1 + 2\log x, \; x \to 0. \tag{1.83}$$

The coherence arguments based on perturbative QCD and outlined in Section 1.4.2 imply that at some low hadron scale the polarized gluon distribution $\Delta G(x)$ is related to the unpolarized one $G(x)$ according to the Eq. (1.67), *i.e.*

$$\Delta G(x) \sim x G(x), \; x \to 0. \tag{1.84}$$

Since the evolution mixes quark singlet and gluon distributions (see Section 1.3.2.1), the most singular of the two controls the behavior of the structure functions at low x and moderately high Q^2. Thus, if the behavior of $G(x)$ is harder than $1/x$, $\Delta G(x)$ and consequently $g_1(x)$ is singular at low x.

Finally, instead of relying in the theoretical predictions, one can fit the data to a phenomenological model. A power-law dependence similar to Eq. (1.81) but with power α varying freely is a reasonable choice. On general grounds, one should distinguish between isospin 1 and isospin 0 states (or, in QCD language, between non-singlet and singlet contributions to g_1). In this case, the fit of the following form is performed:

$$g_1 = b_{NS} x^{-a_{NS}} + b_S x^{-a_S} \; , \tag{1.85}$$

where S stands for singlet and NS for non-singlet quark distributions.

---

[8] There are also counter-arguments, see, for example Ref. [32] and Ref. [66].

There exists a theoretical estimate[71] of the powers a_{NS} and a_S based on the summation of the contributions of the form $\alpha_S \log^2(1/x)$. It was shown to produce a very divergent behavior

$$g_1^{NS} \sim \frac{1}{x^{0.4}},\ g_1^S \sim \frac{1}{x^{1.01}\log^{3/2}(1/x)},\ x \to 0. \tag{1.86}$$

This is much more singular than the dependence induced by the GLAP evolution.

Clearly, precise experimental data at high energies are needed to determine the low x behavior of the polarized structure functions. So far the data have not been able to constrain it well, which poses certain problems in evaluating the polarized sum rules. We will return to this issue in Section 4.4.3.

1.6 Extracting g_1^n from ^{3}He data

In the experiment E154, we scattered polarized electrons off a polarized ^{3}He target. To a very good approximation, ^{3}He nucleons are in the spatially symmetric S state. The two protons are in a symmetric isospin state, and therefore, due to the Pauli principle, they are in the antisymmetric spin state. The total spin of ^{3}He is thus carried by the neutron in this approximation, and asymmetries measured on a ^{3}He target are directly proportional to the neutron structure functions.

In a more realistic model, other components of the ^{3}He wave function are included. Besides the S-wave, the three-body wavefunction contains percentages of the S' wave, arising from the differences in the tensor $T = 0$ and $T = 1$ forces distorting the primary S state, and the D wave.[72] The P-wave is suppressed due to its opposite parity. The admixture of S' and D partial waves reduces the net neutron polarization p_n in ^{3}He and introduces finite proton polarization p_p. The proton and neutron polarizations can be calculated by considering the quantities $P^{(\pm)}_{p(n)}$, representing the probability to have a proton (neutron) with spin parallel (+) or antiparallel (−) to the ^{3}He spin. In a pure S wave state $P_n^{(+)} = 1$, $P_n^{(-)} = 0$ and

$P_p^{(+)} = P_p^{(-)} = \frac{1}{2}$, whereas for a three-body wave function containing S, S' and D waves, one has[72,73]

$$\begin{aligned} P_n^{(+)} &= 1 - \Delta \\ P_n^{(-)} &= \Delta \\ P_p^{(\pm)} &= \frac{1}{2} \mp \Delta', \end{aligned} \qquad (1.87)$$

where $\Delta = \frac{1}{3}[P_{S'} + 2P_D]$ and $\Delta' = \frac{1}{6}[P_D - P_{S'}]$. Here we introduced $P_{S'}$ and P_D as probabilities of S' and D state, respectively.

From published calculations on the three body system one obtains, in correspondence of the experimental value of the binding energy of ^{3}He, $\Delta = 0.07 \pm 0.01$ and $\Delta' = 0.014 \pm 0.002$.[72] In the approximation of *independent scattering* off unbound nucleons, one can write:

$$g_{1^3\mathrm{He}}(x) = 2p_p g_1^p(x) + p_n g_1^n(x) \qquad (1.88)$$

and

$$A_{^3\mathrm{He}} = (2f_p p_p A_p + f_n p_n A_n) \ , \qquad (1.89)$$

where A is the measured asymmetry $A_{||}$ or $A_\perp$, and $f_{p(n)} = F_2^{p(n)}/[(2F_2^p + F_2^n) f_{\mathrm{EMC}}]$ is the proton (neutron) dilution factor. The nuclear effects in the unpolarized scattering are taken into account by the EMC effect factor.[74] Taking into account the S' and D state probabilities, the effective nucleon polarizations are:

$$\begin{aligned} p_p &= P_p^{(+)} - P_p^{(-)} = -0.028 \pm 0.004 \quad \text{and} \\ p_n &= P_n^{(+)} - P_n^{(-)} = 0.87 \pm 0.02. \end{aligned} \qquad (1.90)$$

In the assumption of independent scattering, one neglects nuclear binding effects and effects of Fermi motion and nuclear shadowing. It was shown by the authors of Ref. [73] that for the polarization observables these effects are only noticeable for $x > 0.9$ and $x \approx 0$ in the deep inelastic scattering regime $Q^2 > 1$. We use Eq. (1.89) to extract neutron asymmetries from the ^{3}He data. Thus, polarized ^{3}He is good model of polarized neutron.

1.7 Experimental status

The deep inelastic scattering program at SLAC was started in the late 1960's with the SLAC-MIT experiment that led to the discovery of the quark-parton model.[2–5] The first experiment on spin-dependent deep inelastic scattering was E80 at SLAC in 1976.[6] The experiment used a polarized electron beam with energies of 9.7 and 12.9 GeV and a polarized butanol target to measure the photon-nucleon asymmetry A_1^p. The technique of Dynamical Nuclear Polarization[75] was used to polarize protons to $\approx$ 50%. The experiment was repeated in 1980 by the same SLAC-Yale collaboration (SLAC E130)[7] with higher electron energies (16.2 and 22.7 GeV). Both experiments used fixed-angle magnetic spectrometers to detect scattered electrons, centered at 9° (E80) and 10° (E130). They found good agreement with the quark-parton expectations over the covered x range. The main parameters of E80 and E130, as well as of other experiments to be described in this Section, are summarized in Table 1.2.

After the early series of the experiments on the spin-dependent deep inelastic scattering ended at SLAC in early 1980's, the experimental program was continued at CERN. The EMC experiment took data in 1984/5, and the first results became available in 1988.[8] EMC scattered a μ^+ beam with energies between 120 and 200 GeV off a polarized ammonia target. The muon beam is naturally polarized to $\approx$ 80% since it is produced in the π^+ decay. The high muon energy allowed the measurement to extend to much lower x than in original SLAC experiment, *i.e.* values of $x \approx 0.01$. The EMC results was in good agreement with the naive quark model expectations and SLAC results for $x > 0.1$, but the data lay significantly below the prediction at lower values of x. Consequently, combining EMC and SLAC

Table 1.2. Parameters of polarized deep-inelastic scattering experiments.

Experiment	years	target	E_b (GeV)	P_b	P_t	Events (10^6)
SLAC E80	1976	butanol	9 – 12	50%	50% (p)	2
SLAC E130	1980	butanol	16 – 22	80%	60% (p)	1
CERN EMC	1988	ammonia	190	80%	75%	1
SLAC E142	1992	^{3}He	23	35%	33%	300
SLAC E143	1993	ammonia (p)	29	80%	80%	200
		ammonia (d)			40%	
CERN SMC	1992–	butanol (d)	190	80%	40%	≈20
	1996	ammonia (p)			80%	
DESY HERMES	1995–	atomic	27	60%	40% (^{3}He)	≈6
		^{3}He, ^{1}H, ^{2}D				
SLAC E154	1995	^{3}He	48	80%	38%	100
SLAC E155	1997	ammonia (p)	48	80%	80%	???
		^{6}LiD (d)			50%	

data and using a smooth Regge extrapolation $g_1^p \sim x^{0.12}$, $x \to 0$, EMC obtained for the first moment of g_1^p

$$\Gamma_1^p(\mathrm{EMC}) = 0.126 \pm 0.010 \text{ (stat.) } \pm 0.015 \text{ (syst.)} \tag{1.91}$$

at an average $Q^2 = 10$ GeV^2, about a three standard deviation disagreement with the Ellis-Jaffe prediction. Assuming $SU(3)_{\mathrm{flavor}}$ symmetry and using Eq. (1.42), one can find that the total quark contribution to the proton spin is small:

$$\Delta\Sigma = 0.12 \pm 0.17. \tag{1.92}$$

This result came as a surprise, and the effect was even dubbed "the proton spin crisis" in the community. It has inspired a large amount of theoretical work aimed at understanding the spin structure of the proton. It has also been the genesis of a new experimental program in polarized DIS. The interest shifted towards experimental tests of the Bjorken sum rule, and precision determinations of the spin structure of the nucleon.

The SLAC spin structure program restarted in the Fall of 1992 with the experiment E142.[9] The experiment used a AlGaAs polarized electron source developed for the SLC which produced a high-intensity beam of 40% polarization. The beam was delivered to the End Station A with energies of 19, 22, and 25 GeV. A high-density polarized ^{3}He target was developed for this experiment, for which ^{3}He gas was polarized using optical pumping and spin exchange techniques (see Section 2.5) to yield an average polarization of 33%. Scattered electrons were detected in two independent magnetic spectrometers centered at 4.5° and 7°.[76] The experiment collected approximately 300 million deep-inelastic events over the kinematic range $0.03 \leq x \leq 0.6$ at the average Q^2 of 2 GeV^2, which resulted in the most precise determination of the neutron structure function g_1^n, prior to E154. Unlike the original SLAC experiments, the transverse asymmetry $A_\perp$ was also measured to minimize the systematic error in extracting g_1^n. An additional advantage of the SLAC experiments was the ability to flip the electron helicity pseudo-randomly on the pulse-by-pulse basis. Combined with the regular reversals of the target spin orientation, this feature resulted in the strong suppression of the beam-related systematic effects.

Experiment E143 at SLAC ran in the winter of 1993/4.[10,11] The development of strained *GaAs* photocathodes resulted in high beam polarization (80%) available to E143. The beam energy was raised to 29 GeV; data were also taken at lower beam energies of 9 and 16 GeV to study the Q^2 dependence of the spin-dependent structure function g_1.[77] Polarized ammonia and deuterated ammonia targets were used to measure the spin dependent structure functions of the proton and deuteron. The spectrometer setup was essentially unchanged from E142. The experiment collected approximately 200 million deep inelastic events, and both the longitudinal[10,11] and the transverse[22] structure functions were measured over the range $0.03 \leq x \leq 0.7$ at an average Q^2 of 3 GeV^2.

The program at CERN continued with the SMC experiment[12,13] that took data with polarized deuteron targets in 1992, 1994, and 1995 (deuterated butanol was used as a target material), and with a proton target in 1993 and 1996. Like EMC, SMC used the highest energy 190 GeV muon beam, and the butanol target was superseded in 1996 by an ammonia target. Due to the high beam energy, the experiment reached lower values of x and higher Q^2 than the SLAC experiments. The measurements covered the x range of $0.003 \leq x \leq 0.7$ at an average Q^2 of 10 GeV^2. However, the muon intensity was low, and statistics limits the precision of the SMC measurements.

A new spin structure program was started recently at DESY. The HERMES experiment[80] operates in the HERA storage ring utilizing the 27 GeV positrons (electrons) and polarized internal gas targets. The novel technique is used to inject the polarized atoms into the windowless target chamber inside the storage ring, thus allowing to have the dilution factor very close to unity. The main feature

Table 1.3. Values of the first moments of g_1^p, g_1^n, and g_1^d reported by experiments at SLAC and CERN.

Experiment	Target	Q^2 (GeV^2)	Γ_1	Ref.
CERN EMC	p	10	0.126 ± 0.010 (stat.) ± 0.015 (syst.)	[8]
CERN SMC	p	10	0.136 ± 0.011 (stat.) ± 0.011 (syst.)	[12]
CERN SMC	d	10	0.041 ± 0.006 (stat.) ± 0.005 (syst.)	[13]
SLAC E142	n	2	0.031 ± 0.006 (stat.) ± 0.009 (syst.)	[9]
SLAC E143	p	3	0.129 ± 0.004 (stat.) ± 0.009 (syst.)	[10]
SLAC E143	d	3	0.042 ± 0.003 (stat.) ± 0.004 (syst.)	[11]

of the experiment is the ability to identify the final state hadrons simultaneously with scattered positrons. By tagging the flavor of the leading hadron (*i.e.* doing a *semi-inclusive* measurement), one is able to probe directly the valence and sea quark distributions inside the nucleon. The first inclusive results from the 1995 run with the ^{3}He target have been released in the preliminary form[81] and are expected to be published soon. The experiment will continue to run into the next century.

The summary of the data available prior to E154 is given in Table 1.3 and Figures 1.7 and 1.8. The consistency of the data taken in different experiments and at different kinematics, is outstanding. Not only the tests of sum rules are possible, but information about the shape of the structure functions, and the underlying parton distributions has begun to emerge.

Barring difficulties with the low-x extrapolation and the Q^2 evolution of the structure functions, the values of the moments in Table 1.3 can be used to test the Bjorken sum rule and extract the total quark contribution to the proton helicity $\Delta\Sigma$. Ellis and Karliner[82] performed a global fit to the data and obtained

$$\int_0^1 dx \left[g_1^p(x,Q^2) - g_1^n(x,Q^2)\right] = 0.164 \pm 0.011 \tag{1.93}$$

at $Q^2 = 3$ GeV^2, in perfect agreement with the prediction. They went even further, and assuming the validity of the Bjorken sum rule, extracted the value of α_S from the Q^2 dependence of the measured quantity (Eq. (1.41)):

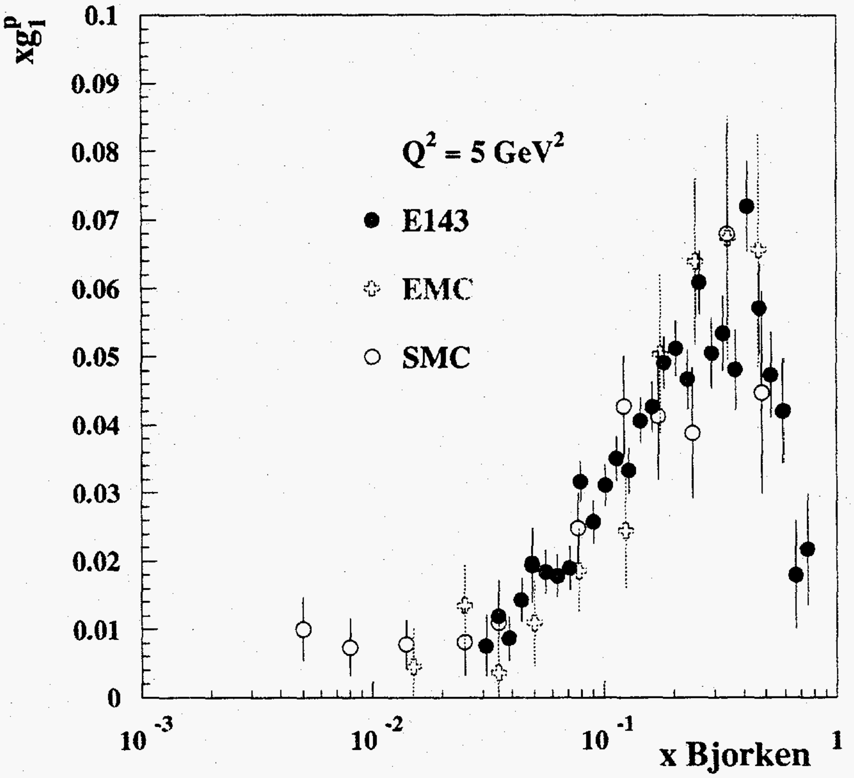

Fig. 1.7. World data on $xg_1^p(x)$.

$$\alpha_S(3\ \mathrm{GeV}^2) = 0.328^{+0.026}_{-0.037}\ , \tag{1.94}$$

which is quite competitive with other determinations which are available.[20] For the quark helicity contributions, Ellis and Karliner obtained[82]

$$\begin{aligned} \Delta u &= \quad 0.82 \pm 0.03 \\ \Delta d &= -0.44 \pm 0.03 \\ \Delta s &= -0.11 \pm 0.03 \end{aligned} \tag{1.95}$$

and

$$\Delta\Sigma = \Delta u + \Delta d + \Delta s = 0.27 \pm 0.04. \tag{1.96}$$

One has to keep in mind, of course, that the theoretical errors associated with the low x extrapolation, Q^2 dependence of asymmetries, higher twist effects, etc. have

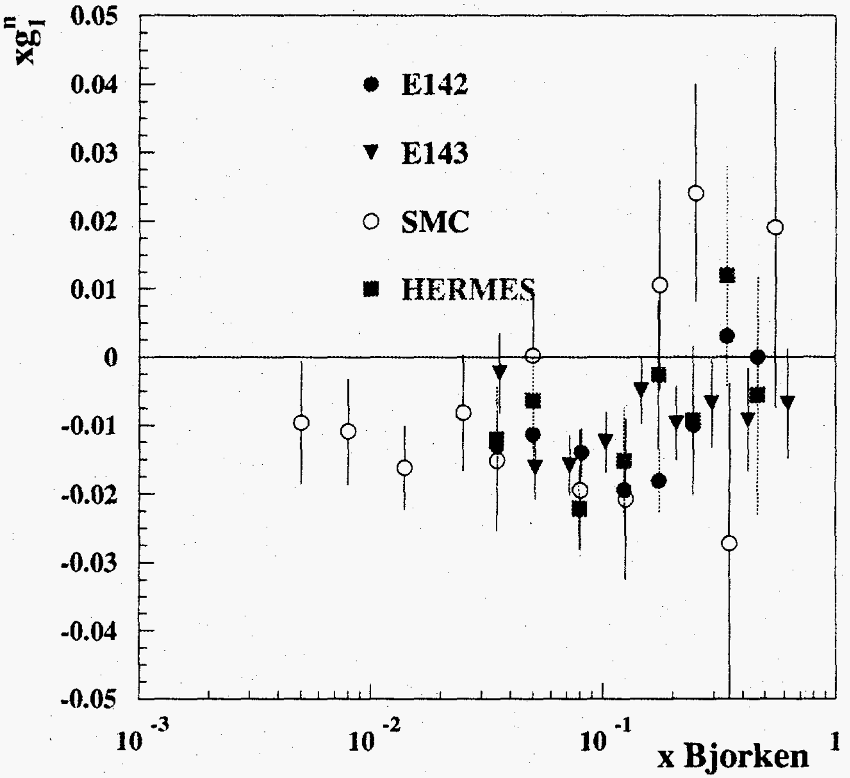

Fig. 1.8. World data on $xg_1^n(x)$.

not been included in Equations (1.96) and (1.96).

Several pQCD fits to the polarized deep inelastic data have been made in the leading[60,83–85] and next-to-leading[63,86,87] orders in α_S. The first information on the polarized parton distributions have become available. We will discuss this program in Chapter 5.

CHAPTER 2

EXPERIMENTAL APPARATUS

2.1 Overview

In SLAC experiment E154 the spin dependent structure functions $g_1^n(x, Q^2)$ and $g_2^n(x, Q^2)$ of the neutron were measured in the kinematic range $0.014 \leq x \leq 0.7$ and $1 \text{ GeV}^2 \leq Q^2 \leq 17 \text{ GeV}^2$ using a polarized, optically pumped ^{3}He gas target and a longitudinally polarized 48.3 GeV electron beam. The average target polarization of 38% was achieved in the longitudinal direction, and the average beam polarization was determined to be 82%. Scattered electrons were detected simultaneously in two independent large acceptance magnetic spectrometers centered around 2.75° and 5.5° relative to the beam line. Results for g_1^n were obtained by measuring the asymmetry between the cross sections in which the target and beam polarizations were parallel versus anti-parallel and using existing measurements of the unpolarized structure functions F_1 and F_2.

The experiment was a collective effort of 80 physicists from 22 institutions. It ran for two months in October-November, 1995. In this Chapter, we describe the apparatus used to perform the measurement.

2.2 Polarized electron source and beam transport

2.2.1 Polarized electron source

The polarized electrons were produced by photoemission from a strained GaAs photocathode.[88,89] The photocathode was illuminated by a flashlamp-pumped Ti:sapphire laser that produced ≈ 10 μs long pulses at a wavelength of 850 nm with a 120 Hz frequency. The pulses were then sliced by the Laser Pulse Chopper (LPC) to

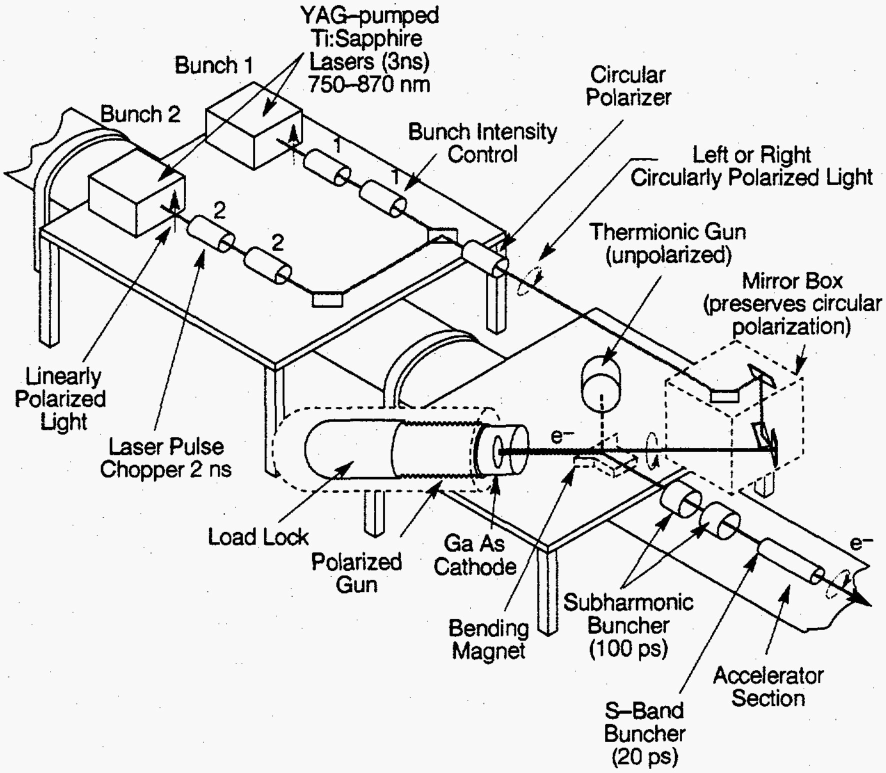

Fig. 2.1. A schematic of the polarized source at SLAC. The setup shown is for the SLC operation. The E154 setup was very similar with one of the lasers changed to flashlamp-pumped Ti:sapphire.

200 − 250 ns and shaped slightly non-uniformly to compensate for the beam loading effects in the accelerator and to obtain uniform pulses in the end of the linac. A schematic of the polarized source is presented in Fig. 2.1.

The laser light was polarized with a linear polarizer and a combination of two Pockels cells, the quarter-wave plates that can change the optical axes depending on the applied high voltage. The axes of one of the Pockels cells were rotated by 45% relative to the axes of the linear polarizer and the other cell. This cell (CP Pockels cell) was used to generate the circularly polarized light; the sign of the high voltage determined the helicity of the light incident on the photocathode (and hence the helicity of the electrons). The second cell (PS Pockels cell) was used to control the charge asymmetry of the beam.

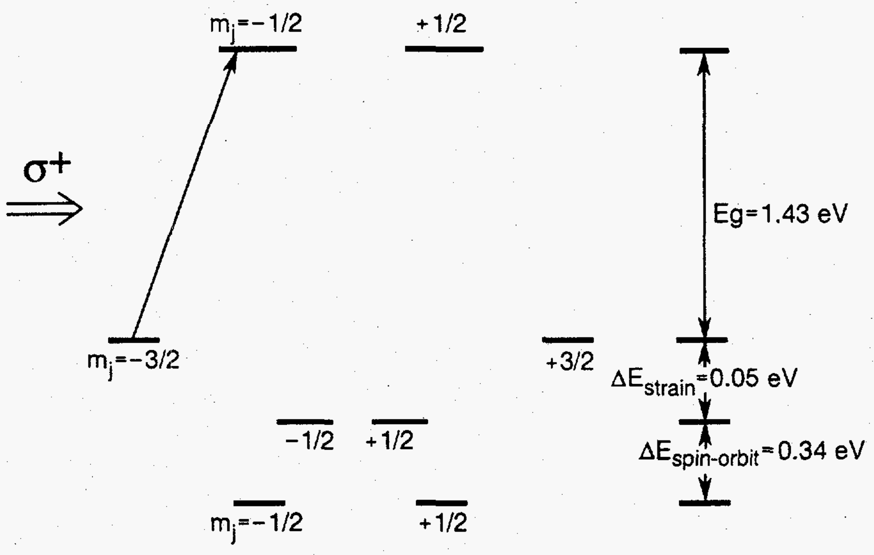

Fig. 2.2. Energy levels in strained GaAs.

The energy levels of a *strained* GaAs are illustrated in Fig. 2.2. The strain is induced by growing a 0.1 μm layer of GaAs on a substrate of GaAsP. The difference in the lattice constants of GaAs and GaAsP creates the compressive strain and splits the degeneracy of the $J = 3/2$ valence band by $\approx$ 50 meV. Photons with positive helicity and energy 1.43 eV $< E_\gamma <$ 1.48 eV excite the transition from the $m_j = -3/2$ valence band level to the $m_j = -1/2$ conduction band level. The electrons then diffuse from the conduction level into the vacuum. The quantum efficiency (QE) of the cathode is increased by growing a thin layer of Cesium that lowers the bulk conduction band.

The extracted electrons have the same helicity as the incident photons since they exit in the direction opposite to that of the photons. The maximum polarization of 100% could be achieved from a strained GaAs cathode, compared to regular GaAs which is limited to 50% polarization due to degeneracy of $J = 3/2$ state. In practice, polarizations of up to 85% were achieved from the strained cathode.

After photoemission the electrons were accelerated across the 60 kV potential of the gun, creating a 200$-$250 ns pulse of $\approx 0.5-2\times10^{11}$ electrons which were bunched and accelerated down the linac. The source operated at 120 Hz, but typically only 119 were used by E154. One in every 120 pulses was a short, high-intensity 3 ns pulse used for accelerator diagnostics and tuning. This *"witness" pulse* was deflected in the Beam Switchyard and did not enter the End Station A.

2.2.2 Beam acceleration and transport

The electrons created at the source entered the 3.2 km linear accelerator. The accelerator structure consists of 30 sectors, each containing eight klystrons, steering dipoles, a quadrupole, and additional elements for monitoring the beam position and current.

Each of the 240 klystrons feed microwave radiation at 2856 MHz into copper cavities. During E154 (and during the SLC running) a technique called SLAC Energy Doubling (SLED) was used that involves reversal of the microwave phase during the pulse. This results in a sharp increase in the accelerating voltage in the cavities at the expense of reducing the pulse length to 200 – 300 ns (compared to $\approx 2\ \mu$s in the normal, non-SLED mode). The maximum beam energy achievable in the SLED mode is ≈ 52 GeV.

At the end of the linac, the beam is deflected by 0.5° into the A-line by two magnets in the Beam Switchyard (BSY). The A-line consists of twelve identical 3 m long dipole magnets operated in series, each of which bends the beam by $\approx 2°$ from the linac towards End Station A (ESA). Twelve quadrupoles are used to control the beam divergence and the spot size at the target.

2.2.3 Spin precession and beam energy

The helicity of electrons entering the linac is the same as that of photons hitting the photocathode and it remains constant during acceleration to the end of the linac. Two dipole magnets located in the BSY deflect the beam by 0.5° north into the A-Line where the set of twelve dipole magnets bend it by 24.0° north into the End Station A. During deflection, the spin of the electrons precesses by an amount

$$\Delta\theta_{\text{precession}} = \gamma\Delta\theta_{\text{bend}}\left(\frac{g-2}{2}\right) \tag{2.1}$$

where $\gamma = E/m$, $\Delta\theta_{\text{bend}} = 24.5°$, and g is the gyromagnetic ratio of the electrons.[20] For beam energies which are even multiples of 3.2374 GeV, the electron helicity at the target in ESA is the same as it is at the source. E154 ran at the linac energy of 48.56 GeV which is an odd multiple, and the helicity of the electrons at the target was opposite to that at the source.

At high beam energies, synchrotron radiation becomes important. In general, the energy loss due to the synchrotron radiation is given by

$$\Delta E_{\text{synch}} = \frac{2\theta_{\text{bend}}}{3}\frac{e^2}{\rho}\left(\frac{E}{m}\right)^4 \tag{2.2}$$

where $\rho = 85.927$ m is the bending radius. Taking into account the synchrotron energy loss, the "magic energy" corresponding to 15π spin rotations is $E = 48.362$ GeV. Experiment E154 took polarized data at a beam energy $E = 48.325$ GeV with an uncertainty on the value of ≈ 0.05 GeV.[90] It was determined by measuring the energy dependence of the beam polarization in the Møller polarimeter.[91]

Synchrotron radiation also results in the growth of the beam emittance and therefore a larger spot size at the target. In order to reduce the spot size to the required ≈ 1 mm, a quadrupole (Q41) was placed in the alcove of the ESA. The focal point was at the target, and the beam gradually diverged after the target.

2.2.4 Electron beam helicity reversal

The ability to reverse the beam polarization on a pulse-to-pulse basis with the Pockels cell was very important for reducing systematic errors. Possible false asymmetries due to slow changes in spectrometer acceptance and detector efficiencies were averaged out by the rapid beam helicity reversals. Also, by changing the target polarization direction periodically, we could further reduce the effect of asymmetries induced by possible helicity-dependent differences in the beam properties. The absolute helicity of the light was determined by the sign of the asymmetry measured by the Møller polarimeter.

The beam helicity was chosen on a pulse-to-pulse basis using a pseudo-random bit generator. The sequence began when a 32 bit random number was chosen, with the last (32nd) bit determining the helicity of the beam. For the next pulse, the 19th and 32nd bit determined the new first bit via a logical XOR, and the remaining bits were shifted up. The new 32nd bit determined the helicity of this pulse, and the cycle was repeated. The sequence of the 33 consecutive polarization bits thus determined the polarization state of all consecutive spills. The generator was running continuously even when the source was off. Thus, we could predict the polarization state of each spill knowing the spill number and could test the integrity of the system.[92]

The polarization state of the beam was sent to the Data Acquisition System via four physically distinct pathways: the PMON line, Mach line, Pockels Cell High Voltage Line, and the Veto Bits. Each pathway delivered a two-bit combination, where the combination '01' referred to positive helicity photons and '10' meant that the photons incident on the photocathode were of negative helicity. Combination '00' in the PMON meant that the beam is unpolarized, and '11' marked an error condition. Typically, all five (four hardware signals and the predictor) methods of determining the polarization state of the spill agreed[92] and we discarded the pulses if a disagreement was detected. If the rate of mismatches exceeded a conservative limit of $5 \cdot 10^{-4}$, the entire run was discarded (see Section 3.7.2).

2.3 Beam monitoring

2.3.1 Beam energy

The energy of the beam was monitored continuously and recorded at every checkpoint (typically, three or four times per half an hour run). A flip-coil was located in an off-line dipole, identical to the twelve used in the A-line and placed in series with them. The current induced in this flip-coil is proportional to the magnetic field in the dipoles. In turn, the magnetic field strength determines the momentum of the electrons passing through the A-line to about 0.1%. The absolute energy scale was also determined independently by measuring the energy dependence of the beam polarization (see below). The energy spread of the beam, $\Delta E/E$, entering ESA was restricted to 1% full width by using three adjustable slits located in the A-line.

2.3.2 Beam current

On a pulse-to-pulse basis the beam charge was measured with two independent ferromagnetic toroids. One was located about 38 m upstream of the target, and the second a few meters upstream. As the beam passed through the ferrite core of the toroid, a signal was induced in loops of wire wrapped around the toroid, which in turn was sent to a resonant LC circuit. The induced current was amplified and integrated, and hence the total charge was proportional to the beam current. Each toroid was calibrated by discharging a precisely charged capacitor through the toroid and measuring the induced charge. The calibration coefficients were extracted several times a day for each toroid, and the total beam charge of each spill was measured to about 0.5%.

2.3.3 Beam position and steering

The beam position and width were monitored with a wire array positioned 10.5 m downstream of the target. Each of the 24 wires in both (x and y) projections were made of 0.127 mm diameter CuBe, with a spacing of 1.1 mm. The wire arrays were read out on a pulse-to-pulse basis by the beam branch of our Data Acquisition System (DAQ); this information was also available to linac operators at the Main Control Center (MCC) to perform minor steering corrections to the beam. Two mylar roller screens, coated with fluorescent ZnS and observed with television monitors, were placed periodically into the beam and allowed a coarse centering and focusing of the beam. The first screen was placed ≈ 25 m upstream from the target right after the quadrupole Q41. The second roller screen was in front of the target.

Additional information about the beam quality came from two scintillator counters. The first one (dubbed a *"bad spill monitor"*) was located upstream of the target in the End Station alcove and was sensitive to beam scraping. The second counter (a *"good spill monitor"*) was downstream of the target, several meters away from the beam pipe. It was sensitive primarily to particles created at the target and served as a good indicator of the time structure of the beam. Signals from both counters were displayed on oscilloscopes (both in the Counting House and MCC) and monitored continuously. The signals were also integrated by ADCs and stored on tape to be used in the data analysis.

Other monitors of the beam included two traveling wave beam position monitors (TWBPM) located in front of the target. One cavity produced an RF signal proportional to the deviation of the beam from the horizontal center of the cavity, the second was sensitive to vertical displacement. A final system used for the target protection was a secondary emission monitor (SEM) made of a thin aluminum foil with a circular aperture of 2 cm for the beam that matched the diameter of a target cell. It was placed immediately upstream of the target. Large signals from the SEM indicated a potentially destructive displacement of the beam, prompting an automatic beam shutdown. This prevented the beam from hitting the thick side walls of the target.

2.4 Møller polarimeter

The beam polarization was measured periodically by a single arm Møller polarimeter. The polarimeter was located upstream of the target, and consisted of the polarized iron foil target, momentum-analyzing magnet, and a set of finely-segmented silicon detectors. The polarimeter was also used to optimize the beam energy and the source laser wavelength with respect to the beam polarization.

2.4.1 Møller asymmetry

The cross section for polarized e^-e^- scattering is fully calculable in QED, and in the center-of-mass frame is given by[93]:

$$\frac{d\sigma}{d\Omega} = \frac{\alpha^2}{s}\frac{(3+\cos^2\theta)^2}{\sin^4\theta}[1 + P_z^B P_z^T A_{zz}(\theta)] \tag{2.3}$$

for longitudinally-polarized beam and target, where the asymmetry is

$$A_{zz}(\theta) = -\frac{(7+\cos^2\theta)\sin^2\theta}{(3+\cos^2\theta)^2}\ . \tag{2.4}$$

Here s and θ are the CM energy squared and the scattering angle, P_z^B and P_z^T are the beam and target foil longitudinal polarizations, respectively. By measuring the Møller scattering rate for the electron beam and target spins aligned, $\sigma^{\uparrow\uparrow}$, and anti-aligned, $\sigma^{\uparrow\downarrow}$, we can form the asymmetry

$$A = \frac{\sigma^{\uparrow\uparrow} - \sigma^{\uparrow\downarrow}}{\sigma^{\uparrow\uparrow} + \sigma^{\uparrow\downarrow}} = P_z^B P_z^T A_{zz}(\theta). \tag{2.5}$$

If the target polarization is independently known, a measurement of the Møller asymmetry determines the beam polarization.

The asymmetry maximum is at $\theta_{CM} = 90°$ where the unpolarized laboratory cross section is 0.179 b/sr and $A_{zz} = -7/9$. With a typical foil polarization of 0.08 (that corresponds to 2 outer-shell electrons of Fe aligned with the external magnetic field) and beam polarization of 0.8, the expected asymmetry is roughly 0.05.[91]

2.4.2 Polarimeter apparatus

The polarimeter consisted of polarized target foils, a mask to define the azimuthal and vertical acceptance, a magnet to analyze the momentum of the scattered electrons, and detectors to measure the scattering rate. The mask selected Møller scattered electrons in the vertical plane and the magnet deflected them horizontally. The beam vacuum pipe went through the magnet and was enclosed in an iron septum to eliminate the field inside the beam pipe. The elastically-scattered Møller electrons have correlated momenta and scattering angles, and form a stripe at the plane of the detector. The top silicon detector contained 48 channels placed on two 4×6 cm^2 pads to produce a segmentation of 2.18 mm in the vertical (θ) direction. It was mounted on a remotely-controlled mover and could be positioned anywhere within the Møller acceptance. Four separate silicon detectors with coarser pitch were mounted side by side at fixed positions in the bottom aperture.

The E154 polarimeter was an evolution of the previous End Station A Møller Polarimeters[94] and utilizes many ideas and components of previous designs. The top and side views of the polarimeter are shown in Fig. 2.3.

2.4.3 Foil polarization

The foil polarization was determined by measuring its magnetization $\vec{\mathbf{M}}$.[95] Ramping the external field $\vec{\mathbf{H}}$, induces a voltage in a pickup coil wound around the foil $\int V dt = \Phi_f - \Phi_i$. The flux Φ has contributions from the foil and air:

$$\Phi = N_{\text{turns}} \left[\vec{\mathbf{B}}_{\text{foil}} \cdot \vec{\mathbf{A}}_{\text{foil}} + \vec{\mathbf{H}} \cdot (\vec{\mathbf{A}}_{\text{coil}} - \vec{\mathbf{A}}_{\text{foil}}) \right] , \tag{2.6}$$

where $N_{\text{turns}} = 500$ is the number of turns of the pickup coil. By integrating the induced voltage with and without the foil, and noting that $\vec{\mathbf{B}}_{\text{foil}} = \vec{\mathbf{H}} + 4\pi\vec{\mathbf{M}}$, we obtain

$$4\pi|\vec{\mathbf{M}}| = \frac{1}{N_{\text{turn}}|\vec{\mathbf{A}}_{\text{foil}}|} \left[\int_{\text{foil in}} V dt - \int_{\text{foil out}} V dt \right] \tag{2.7}$$

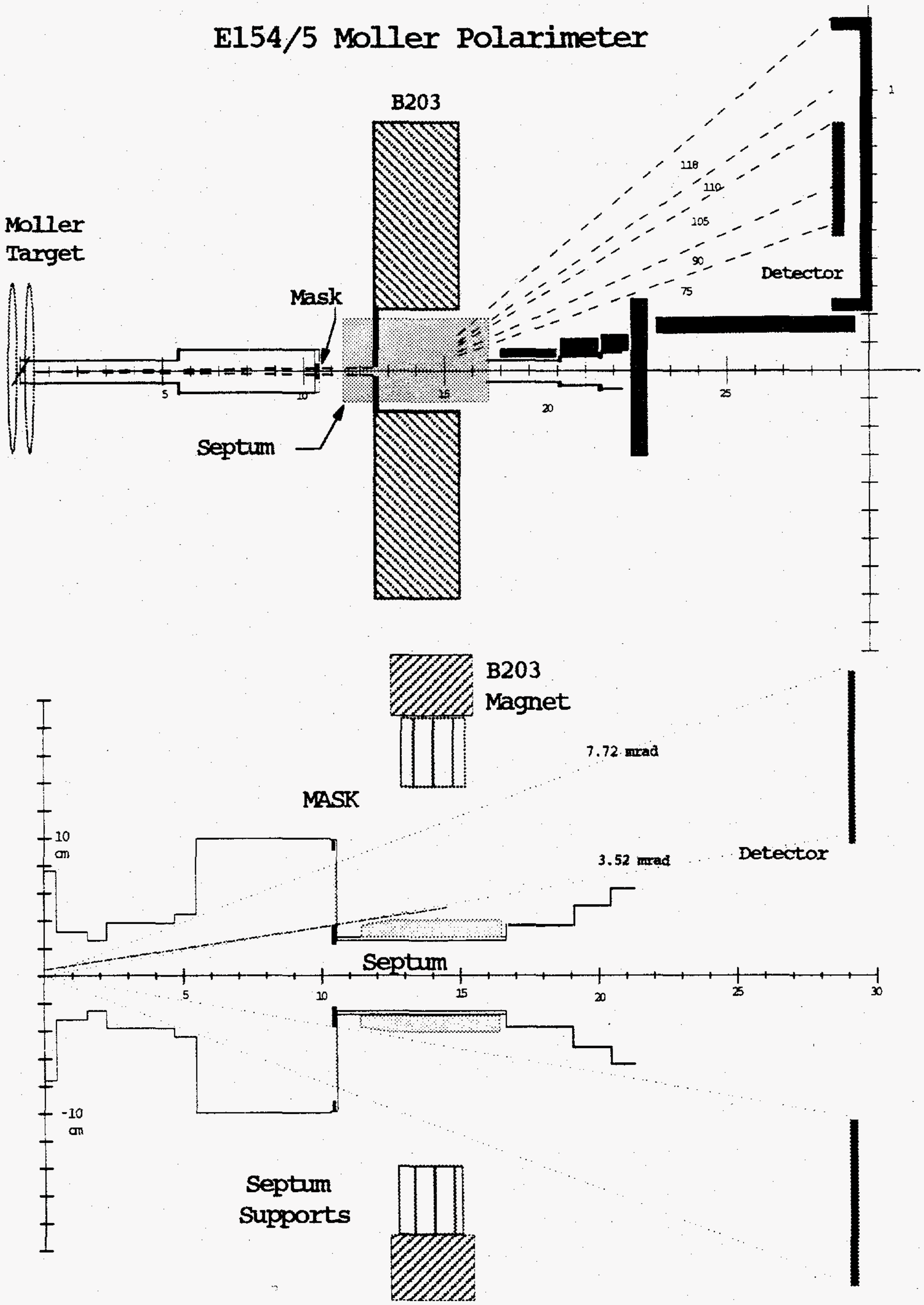

Fig. 2.3. Top (top picture) and side (bottom picture) views of the E154 Møller Polarimeter.

The magnetization is related to the foil polarization by

$$P_z^T = \left[\frac{g}{g-1}\frac{g'-1}{g'}\right]\frac{|\vec{\mathbf{M}}|}{n\mu_B} \tag{2.8}$$

where g is the gyromagnetic ratio of the electron,[20] $g' = 1.916 \pm 0.02$ is the gyromagnetic ratio of Permendur,[96] n is the number density of electrons, and μ_B is the Bohr magneton.

Six foils of approximate thicknesses 20, 20, 30, 40, 40, and 154 μm were installed at a 20.7° relative to the beam line. The majority of E154 Møller data were taken with a 40 μm foil. The foils were magnetized to saturation by $\approx$ 100 G field produced by Helmholtz coils. The polarity of the coils was typically reversed between the Møller runs to reduce systematic effects. The magnetization of the foils was measured before and after E154. Both measurements agreed within 0.6% with an average change of less than 0.1%. A relative systematic error of 1.9% was assigned to the foil polarization.

2.4.4 Beam polarization results of the Møller runs

Møller data were taken periodically throughout the experiment for a total of about 140 runs. The signals from the silicon detectors were pre-amplified and read out by the ADCs. In each run, the average pulse heights in every channel were recorded for the two beam helicities, from which the (R–L) and (R+L) line-shapes were formed. The background under the unpolarized (R+L) Møller line-shape was estimated by fitting the (R+L) line-shape to a quadratic polynomial plus the line-shape expected from unpolarized Møller scattering.[91] The unpolarized Møller line-shape was obtained by using the (R–L) shape with the corrections for the atomic motion of target electrons,[97] and was in a very good agreement with a Monte Carlo calculation. The (R–L) and (R+L) line-shapes were integrated and the Møller asymmetry was formed. The background subtraction increased the measured asymmetry by 17–24%. The statistical errors on the beam polarization were typically

Table 2.1. Measured longitudinal beam polarization for different running periods. The error is statistical only.

Run range	Polarization
1329–1411	0.759 ± 0.004
1456–1684	0.775 ± 0.005
1691–2311	0.814 ± 0.002
2316–3371	0.824 ± 0.001
3377–3788	0.826 ± 0.002

Table 2.2. Systematic error contributions to the beam polarization measurement.

Systematic error contribution	Value
Foil magnetization	1.9%
Kinematic acceptance	0.3%
Background correction	2.0%
Fit range	0.3%
TOTAL	2.8%

0.003 – 0.006 per run. The history of the beam polarization measured by the polarimeter is shown in Fig. 2.4 and is given in Table 2.1. The average beam polarization (weighted by statistics of $A_{||}$) was 81.8%.

2.4.5 Systematic errors

The overall systematic error has contributions from the foil polarization, uncertainties in the expected Møller asymmetry for each detector, and uncertainties in the background subtraction. The various contributions to the systematic error are summarized in Table 2.2.[91]

2.5 Polarized ^{3}He target

The polarized ^{3}He target was one of the major factors that determined the success of this experiment. It was very similar to the polarized target used in E142.[98] The target was a two-chambered 30 cm long glass cell containing ^{3}He at densities of

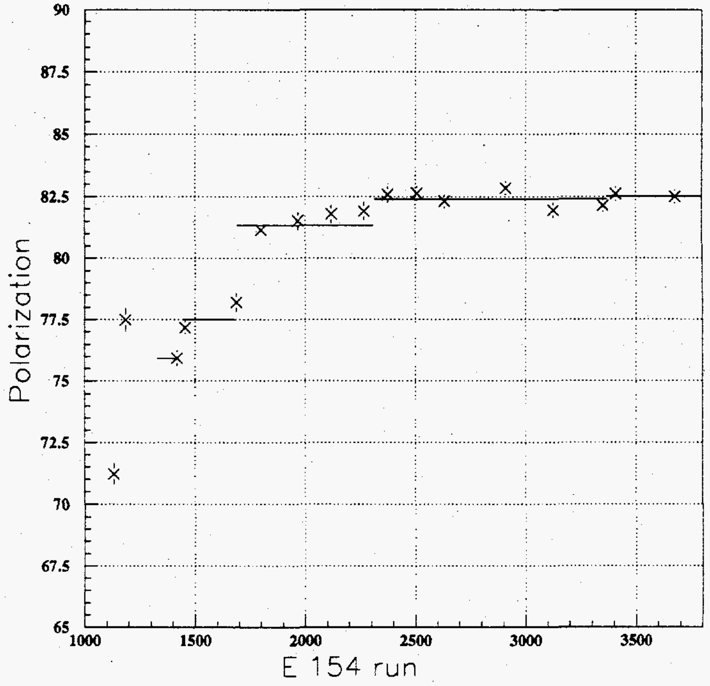

Fig. 2.4. Measured longitudinal beam polarization versus E154 run number. Errors are statistical only. "Jumps" in the measured value of polarization indicate various adjustments made to the source during the run.

2.6×10^{20} atoms/cm^3. The ^{3}He nuclei were polarized in the spin exchange collisions with optically pumped Rubidium atoms. Target polarizations of nearly 50% were achieved with an average polarization of 38%.

2.5.1 Optical pumping and spin exchange

Optical pumping is an effective technique for achieving high polarizations in a high density noble gas target.[99] The process is illustrated in Fig. 2.5. For example,for a positive helicity, circularly polarized laser light at 794.7 nm excites the $5S_{1/2}(M_J = -1/2)$ ground state to the $5P_{1/2}(M_J = +1/2)$ in Rubidium vapor (the D1 line). Radiative decays to the ground state favor the $5S_{1/2}(M_J = -1/2)$ state over $5S_{1/2}(M_J = +1/2)$ state by a factor two. By adding 65 torr of N_2, as

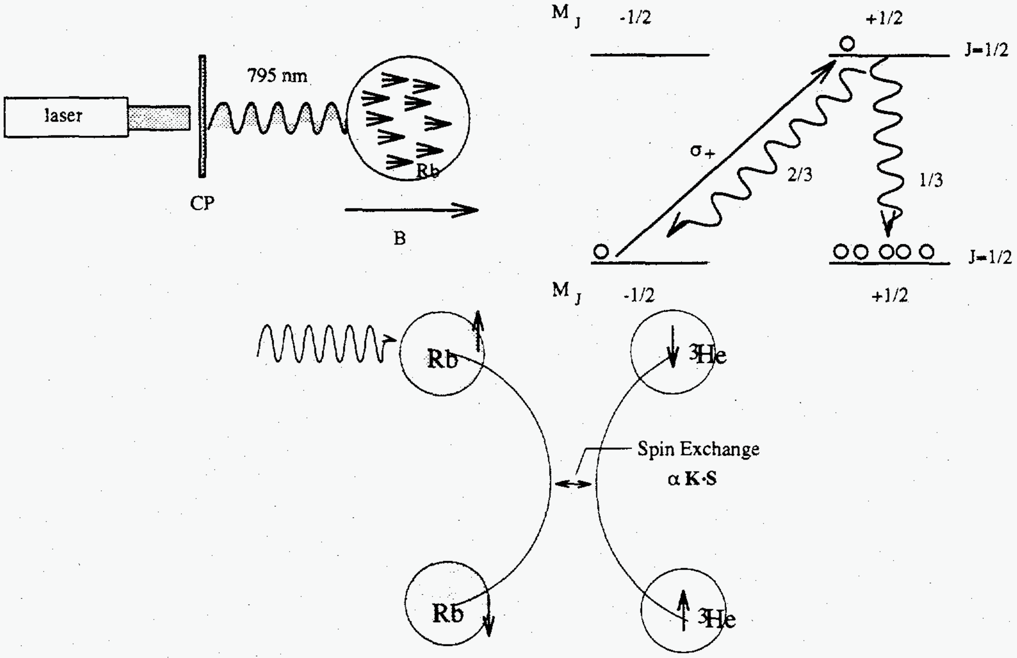

Fig. 2.5. Schematic of the optical pumping and spin exchange processes.

in our target cells, the $5P_{1/2}(M_J = \pm 1/2)$ states are collisionally mixed at a rate exceeding the radiative decay. The relaxation into the $5S_{1/2}$ ground states occurs equally into the two sub-states, and only two photons are required to increase the $5S_{1/2}(M_J = +1/2)$ population by one. The polarization of the valence electrons of Rb competes with several depolarizing mechanisms, the most of important of which are from Rb-Rb and Rb-^{3}He collisions (the latter is dominant at high pressures), as well as Rb-target cell wall interactions. However, with sufficiently high Rb vapor density (10^{14} atoms/cm^3) and high laser power, the optical pumping rate of $1/\gamma_{\text{pump}} \approx 10^{-6}$ s exceeds the $1/\gamma_{\text{relax}} \approx 10^{-3}$ s relaxation rate, and almost 100% Rubidium polarization could be achieved.

The polarization of the Rb atoms is transferred to the ^{3}He nuclei in the spin exchange collisions due to the hyperfine interaction of the Rb electron magnetic moment and the magnetic moment of the ^{3}He nucleus, as shown in Fig. 2.5. The spin exchange rate, γ_{SE}, is proportional to the relative velocity between the ^{3}He and Rb, v, and to the number density of Rb, [Rb]:

$$\gamma_{SE} \equiv < \sigma_{SE} v > [\mathrm{Rb}] \tag{2.9}$$

where the velocity averaged cross section is $\approx 1.2 \times 10^{-19}$ cm^2/s.[100] With [Rb] $\approx 10^{14}$ cm^{-3}, polarization times for ^{3}He are very long, $1/\gamma_{SE} \approx 25 - 40$ hours.

Various processes are responsible for depolarization of the ^{3}He atoms. Collisions between ^{3}He atoms can cause the exchange of the nuclear spin and orbital angular momentum. Paramagnetic impurities, both gaseous and embedded in the cell walls, contribute further to the spin relaxation. Factors external to the cell also play a role. Polarized ^{3}He diffusing through regions in which the holding field is inhomogeneous, precesses about the local field and the spin direction is randomized. This effect is usually minimized by keeping the gradients perpendicular to the alignment field small ($<$ 20 mG/cm). Nuclear relaxation is also induced by the ion production in the cell by the electron beam due to creation of non-zero electron spin states in the ionized ^{3}He atom.[101] The cumulative effect of these relaxation processes can be characterized by

$$\Gamma_R = \frac{1}{\tau_{\mathrm{cell}}} + \frac{1}{\tau_{\nabla B}} + \frac{1}{\tau_{\mathrm{beam}}} , \tag{2.10}$$

where τ_{cell}, $\tau_{\nabla B}$, and τ_{beam} are intrinsic cell relaxation time, and relaxation times induced by the magnetic field gradients and the electron beam. Typical relaxation times for our target cells were on the order of $40 - 60$ hours.

The time dependence of the ^{3}He polarization is given by a simple model of the competing spin exchange and relaxation processes

$$P_{^3\mathrm{He}}(t) = \frac{\gamma_{SE}}{\gamma_{SE} + \Gamma_R} P_{\mathrm{Rb}} \left[1 - \exp\left(-(\gamma_{SE} + \Gamma_R)t\right)\right] , \tag{2.11}$$

assuming $P_{^3\mathrm{He}}(t = 0) = 0$, and where P_{Rb} is the equilibrium polarization of Rb $\approx$ 100%. The polarization buildup ("spin-up") observed in one of the best cells, Picard, is shown in Fig. 2.6. The maximum polarization of 47.9% was achieved.

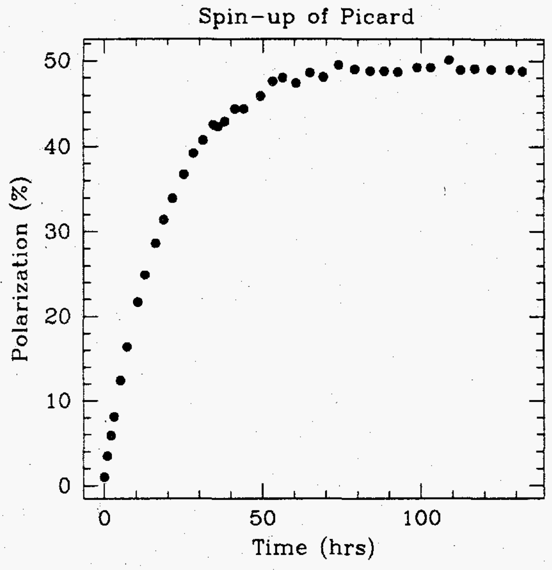

Fig. 2.6. The on-line plot of the polarization buildup in the target cell Picard. The calibration constant was reduced by $\approx 2\%$ in the post-run analysis.

2.5.2 Target apparatus

The target cell was made of Corning 1720 aluminosilicate glass, which has low ^{3}He permeability. It used a two chamber design where the upper, pumping cell with a volume of $70-80$ cm^3 contained ^{3}He and a few tens of mg of Rb. This chamber was enclosed in a plastic oven and heated to 170-200° C to create a Rb vapor density of about 10^{14} atoms/cm^3. Three 20 W diode lasers and four Argon-ion pumped Ti:sapphire lasers were located in a specially constructed laser hut near the target. The lasers pumped the target continuously, resulting in a total of almost 80 watts of power[1] on the pumping cell. The light from each laser passed through the various optical components including a quarter-wave plate to produce circularly polarized light, before reaching the pumping cell which was about 3 m away. A schematic of the target is shown in Fig. 2.7.

---

[1] The spectrum of the diode lasers is quite broad so the total power absorbed by Rb at 795 nm was somewhat smaller.

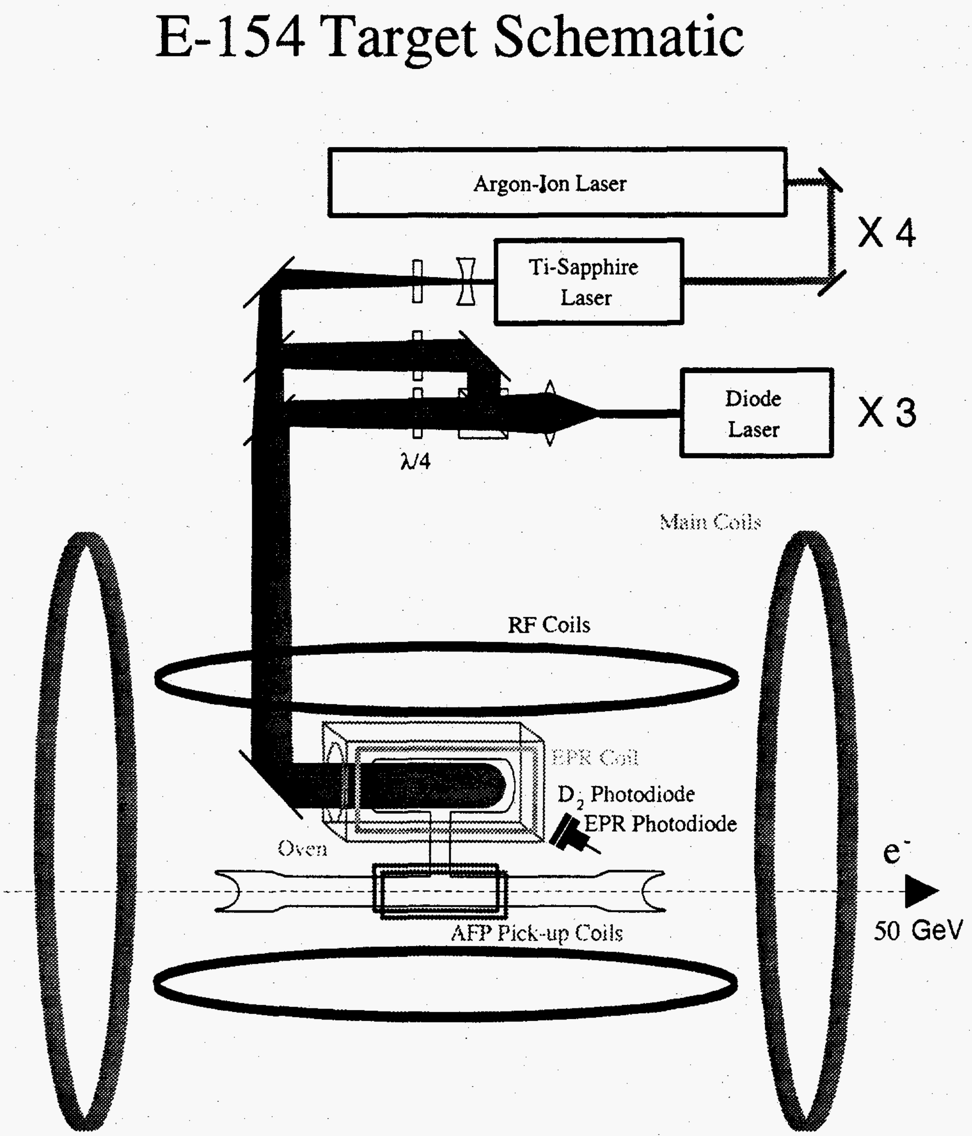

E-154 Target Schematic

Fig. 2.7. The schematic of the E154 polarized target setup.

The ^{3}He atoms polarized in the upper cell diffused through a 60 mm long transfer tube to the lower, target cell, with a time constant of about 10 minutes. This cell was a cylinder $\approx$ 30 cm long, 1 cm in radius, with $\approx$ 50 μm thick endcaps of concave shape. Since the glass is stronger under compression than under tension, the concave design allowed thinner windows than the traditional convex, shape for the same ^{3}He pressure. E154 benefited greatly from this feature since the dilution factor (the scattering rate from polarized ^{3}He relative to the total rate) was increased by almost a factor of 2 compared to E142. Cooling jets of ^{4}He were directed at the endcaps to relieve the heating caused by the beam. The target cell temperatures were monitored with 6 Resistive Thermal Devices (RTDs) mounted in various places on the target and pumping cells. The temperature throughout the target cell remained at $60 - 80$ °C (depending on the position). The residual Rb density was of the order 10^{11} atoms/cm^3, which is insignificant in comparison to the 2.6×10^{20} atoms/cm^3 of ^{3}He and the 2.4×10^{18} molecules/cm^3 of N_2 which were the primary components of the target cell. The target holder had three positions with the reference cell placed below the polarized cell (the third position was empty). The reference cell was used for the experimental studies of the dilution factor (see Section 3.10), and the "no target" runs were used to monitor the beam halo[2]. The precision mover placed either of two cells into the beam with a sub-millimeter accuracy. A large scattering chamber enclosed the target assembly, and was kept under vacuum of a few mtorr.

Outside of the scattering chamber was a set of 1.4 m diameter Helmholtz coils which produced a 10–30 G holding field to align the nuclear spins of ^{3}He. A similar set of coils perpendicular to the beam direction was used to achieve the transverse polarization for measurements of $A_\perp$.

---

[2] The initial estimates of the beam halo were obtained with a special "dummy" cell that had no windows. Since such a cell was not in the target holder during most of the run, results of the "no target" runs were used for monitoring the halo, and the "dummy" cell runs were used as a calibration.

2.5.3 Target cells

The thin target windows could not sustain the high intensity electron beam for more than a week. Several effects could be blamed for breaking of the windows, but the exact cause is unknown. A total of nine polarized target cells and four reference cells were used in the experiment. The catalog of the cells with the relevant dimensions is given in Table 2.3.[102]

The target windows thickness was measured by three independent methods: by a micrometer, by X-ray absorption (using ^{55}Fe source), and using the interference of the laser light reflected from two surfaces of a window. The optical method is the most precise and gives an uncertainty of 3%, limited by the non-uniformity of the windows. The windows that broke in the beam were not measured by the optical technique, and the uncertainty in their thicknesses is 5%.

The ^{3}He density was measured during the filling of the cell, and later using the pressure broadening of the Rb absorption line. The fill density was corrected for the difference in the pumping and target cell temperatures. The error on the density is 2%.

2.5.4 Target polarimetry and polarization results

The ^{3}He polarization was determined by two independent techniques.[103] The traditional method, the adiabatic fast passage (AFP) NMR, was used during the run.[104] A set of 42.75 cm diameter Helmholtz drive coils above and below the target provided a 72 mG RF field at 92 kHz, while the main holding field was swept from 18 G to 36 G, through the Larmor resonance at 28.4 G. The field sweep rate was optimized to minimize the polarization losses. The rate of 1.2 G/s was slow enough for the nuclear spins to follow the changing field, but fast enough to avoid the de-phasing of the spins while passing through the resonance. The resulting nuclear spin flip induced a signal in a set of 200 turn copper pickup coils, wound

Table 2.3. Target cells used in E154.

Cell Name	Runs	Windows (μm)	Length (mm)	^{3}He density (10^{20} cm^{-3})	N$_2$ density (10^{18} cm^{-3})	Fate
Dave	1201 – 1388	45.0, 53.5	291	2.70	2.3	Broke
Riker	1412 – 1757	66.5, 60.0	300	2.68	1.4	Broke
Bob	1777 – 2043	70.1, 69.7	299	2.68	2.3	Broke
SMC	2050 – 2311	68.8, 64.2	302	2.68	2.4	Survived
Generals	2316 – 2594	52.2, 56.7	297	2.63	2.4	Broke
Hermes	2597 – 2902	46.9, 56.6	295	2.64	2.4	Broke
Prelims	2903 – 3100	45.1, 42.2	300	2.68	2.3	Broke
Chance	3101 – 3371	83.0, 83.0	299	2.68	2.3	Survived
Picard	3377 – 3788	69.3, 61.6	299	2.64	2.3	Survived
Ref. Cell #1	733 – 1757	58.4, 46.5	304			Broke
Ref. Cell #2	1777 – 2047	73.5, 46.3	297			Survived
Ref. Cell #3	2050 – 2596	50.9, 48.5	304			Survived
Ref. Cell #4	2597 – 3788	70.8, 64.0	302			Survived

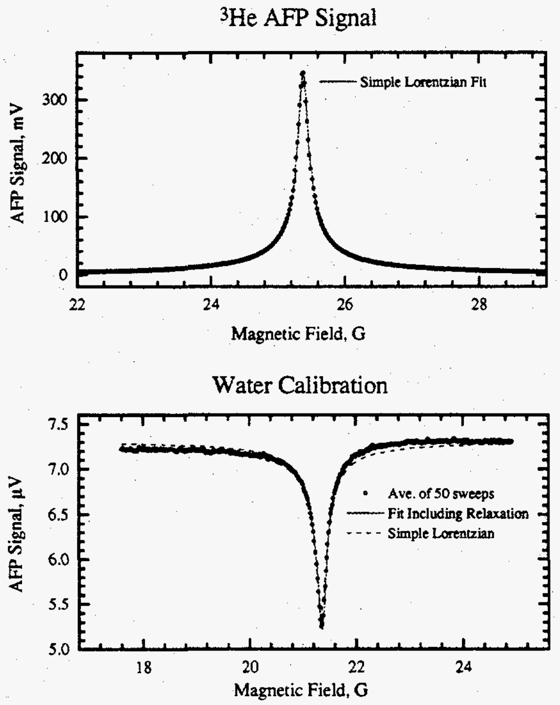

Fig. 2.8. Typical ^{3}He and water AFP-NMR signals.

on a 76.2 mm by 25.4 mm Teflon form and centered around the target cell. Using a 100 pF capacitor, an LC resonant circuit was formed. The signal was pre-amplified, then went through a lock-in amplifier that subtracted the 92 kHz modulation. The resulting NMR signal was proportional to the ^{3}He polarization. The proportionality constant was determined from the thermal equilibrium Boltzmann polarization of protons in a water sample. The water signals were 10^5 times smaller compared to the ^{3}He signals, so typically many sweeps were averaged. Typical ^{3}He and water signals are shown in Fig. 2.8.

The primary sources of the systematic uncertainty in the AFP-NMR polarimetry were the height of the water signal (1.8%), proton polarization in water (1.0%), and ^{3}He density (1.9%). The total systematic error of the AFP method is 3.4%.[103]

The second method, used to calibrate the AFP-NMR polarization measurement, was based on the Electron Paramagnetic Resonance (EPR) technique.[105] It used

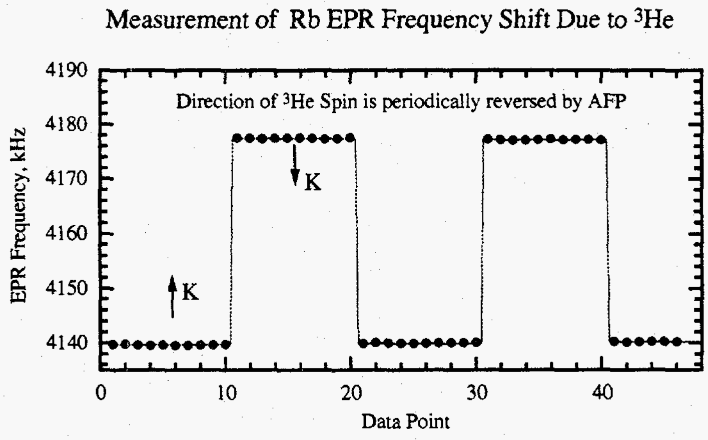

Fig. 2.9. EPR frequency shift due to reversal of ^{3}He polarization.

the shift of the Rb Zeeman resonance due to the magnetic field created by the polarized ^{3}He. The shift is quite substantial (about 20 kHz out of 8 MHz) and easy to measure. If the Rb polarization is very high, most of the atoms are in $F = 3$, $M = \pm 3$ state (where F and M are the total angular momentum and its projection for the nuclear and electron spins of ^{95}Rb). By applying the RF frequency, one can induce the transitions between neighboring M sublevels of the $F = 3$ manifold. The EPR resonance is observed by monitoring the rate of fluorescence at the D_2 Rubidium line as a function of RF frequency.[103] The RF field was created by a coil mounted on a side of the oven. The fluorescence was detected by a photodiode with a D_2-line filter. The magnetic field was measured to one part in 10^5 by a Flux-Gate magnetometer. The frequency shift due to ^{3}He polarization was detected by reversing the ^{3}He polarization. A typical EPR signal is shown in Fig. 2.9. The quality of the data is very good and the size of the frequency shift was extracted with an error of less than 0.5%.

The frequency shift is proportional to the ^{3}He polarization where the coefficient of the proportionality κ_0 is specific to the Rb-^{3}He system.[105] This coefficient was measured[103] with an uncertainty of 1.0%. The errors in the EPR measurement mostly came from κ_0, the polarization gradient between the pumping (where the polarization is measured by EPR) and the target cells (1.5%), and the spread of the data (1.3%). The total systematic error of the measurement is 3.0%.

The AFP and EPR polarization measurements disagreed by 5.4%. If the uncertainties of each measurement are treated as independent and the shapes of probability distributions are Gaussian, the probability of such a disagreement is 23%. However, an unknown systematic effect could alter one of the measurements. We therefore increase the polarimetry error so that it covers both measurements and their errors. The final error also includes a 1.7% drift in AFP calibration constants measured before and after the run. The final target polarimetry error is 4.8%.

2.5.5 ^{3}He polarization direction

The direction of the ^{3}He polarization relative to the magnetic field was determined in three ways.[106] The first method used the sign of the AFP-NMR signals. Protons and ^{3}He have magnetic moments of opposite sign, so if their spins are in the same directions initially and are swept through a resonance with $d|\mathbf{B}|/dt$ of the same sign, the NMR resonance signals are of opposite sign. This determines the ^{3}He polarization direction with respect to the proton, which is preferentially aligned parallel to the external fields. The second method relates the sign of the EPR frequency shift which is proportional to the ^{3}He polarization. The third method was based on the observation of the masing effect during AFP due to the coupling of ^{3}He spins to the pickup coils. All three methods were consistent.

The direction of the holding field was determined by a flux-gate magnetometer, by a Hall probe relative to the spectrometer magnets, by compass, and finally by the direction of the current in the Helmholtz coils. Again, all methods were consistent. In addition, liquid crystal circular polarizers determined the laser helicity, which determines the angular momentum transferred to the ^{3}He nuclei, and hence the polarization direction.

2.6 Magnetic spectrometers

2.6.1 Introduction

Design of the magnetic spectrometers for the 50 GeV spin structure program at End Station A was driven by the physics requirements. The goal of the experiments is to measure the spin structure functions of the neutron and proton down to the lowest possible x and over a more extensive Q^2 range than compared to the previous ESA experiments.[9–11] Design choices reflect the requirements of high counting rates, while keeping the ability to unambiguously identify scattered electrons and determine their energy in the presence of large background of charged hadrons and low energy neutral particles. An important factor is a short SLED beam pulse, which leads to a factor of $10-20$ increase in the instantaneous rates compared to E142 and E143 (if the rate per spill is kept the same).

The system consists of two independent magnetic spectrometers centered around 2.75° and 5.5° relative to the beam direction. The 48.3 GeV beam combined with the choice of angles allows the measurements in the kinematic range $0.014 \leq x \leq 0.8$ and $1\ \mathrm{GeV}^2 \leq Q^2 \leq 17\ \mathrm{GeV}^2$ (Fig. 2.10). This is the most extensive kinematic range ever achieved by polarized electron scattering experiments to date. The 2.75° spectrometer covers a momentum range from 10 to 44 GeV, and the 5.5° spectrometer covers a momentum range from 10 to 39 GeV. The low momentum cutoff is dictated by the requirement of $y = (E-E^{'})/E < 0.8$ imposed by radiative corrections (which increase rapidly at high y), and the desire to keep the charged hadron background at a tolerable level. The high momentum cutoff is set by the standard deep-inelastic cut $W^2 > 4\ \mathrm{GeV}^2$. The theoretically calculated differential cross sections $d^2\sigma/d\Omega dE$ for the two spectrometers are plotted in Fig. 2.11.

A system of two independent "closed-geometry" magnetic spectrometers has several advantages. First, the neutral background is highly suppressed with the so-called *"double-bounce"* geometry that prevents neutral particles from reaching the

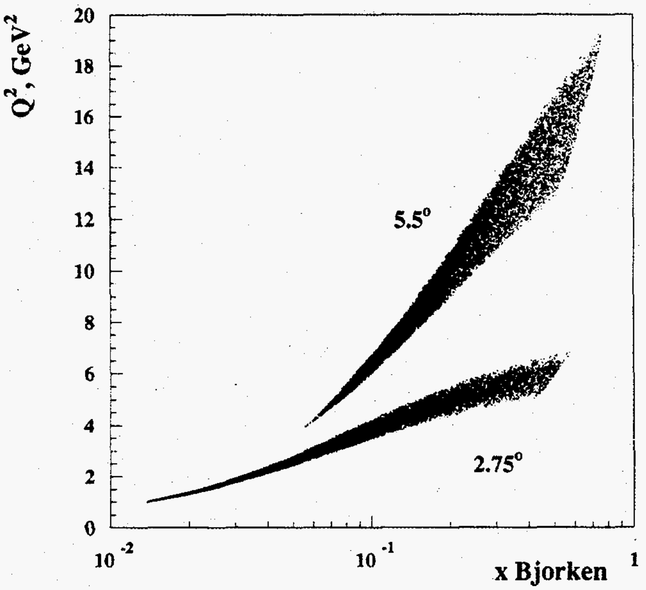

Fig. 2.10. Kinematic coverage in x and Q^2 of E154 spectrometers.

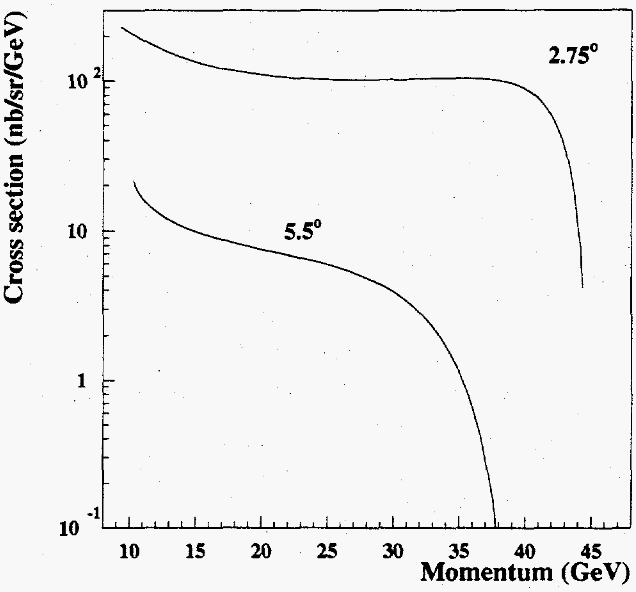

Fig. 2.11. Double differential cross section for 2.75° and 5.5° spectrometers at beam energy 48.3 GeV (^{3}He target, cross section per nucleon).

detectors without bouncing at least twice off the magnets and collimators. Second, unlike the typical open-geometry detectors used in particle physics experiments, we can choose the relative acceptances of two spectrometers in such a way that the electron rates, and therefore statistical errors, are comparable at low and high x. Two spectrometers also provide the lever arm essential for studies of the Q^2 dependence of deep-inelastic spin asymmetries.

The conceptual design of the spectrometer systems is described in Ref. [107,108]. The spectrometers are similar to the 4° and 7° spectrometers used in E142/E143.[76] Both spectrometers use two conventional dipole magnets bending in opposite directions achieving a so-called "S-bend", or "reverse-bend" configuration introduced for E142.[76] In addition, the 2.75° spectrometer features the quadrupole defocusing of scattered particles in the horizontal direction, thus reducing the instantaneous rates per detector element. It also provides focusing in the vertical (bend) plane. The detector system consists of a pair of gas Cherenkov detectors, planes of highly segmented plastic scintillators, and a lead glass calorimeter in a fly's eye configuration. The schematic plan of the spectrometers is shown in Fig. 2.12.

2.6.2 Optics model

In the following, we will use the "spectrometer" coordinate system. It is a right-handed coordinate system with the target as origin. The line along the 2.75° (or 5.5°) direction is taken as the $\hat{z}$ axis. The $\hat{y}$ axis is vertical, and the $\hat{x}$ axis is horizontal and perpendicular to the $\hat{z}$ direction ($\hat{x}$ points north in ESA). The dipole magnets bend electrons in the vertical direction, so we will call the $\hat{y} - \hat{z}$ plane a *bend* plane. The angles in the bend plane will be denoted as ϕ. The *non-bend* plane is horizontal $(\hat{x} - \hat{z})$, and the angles are defined as θ.

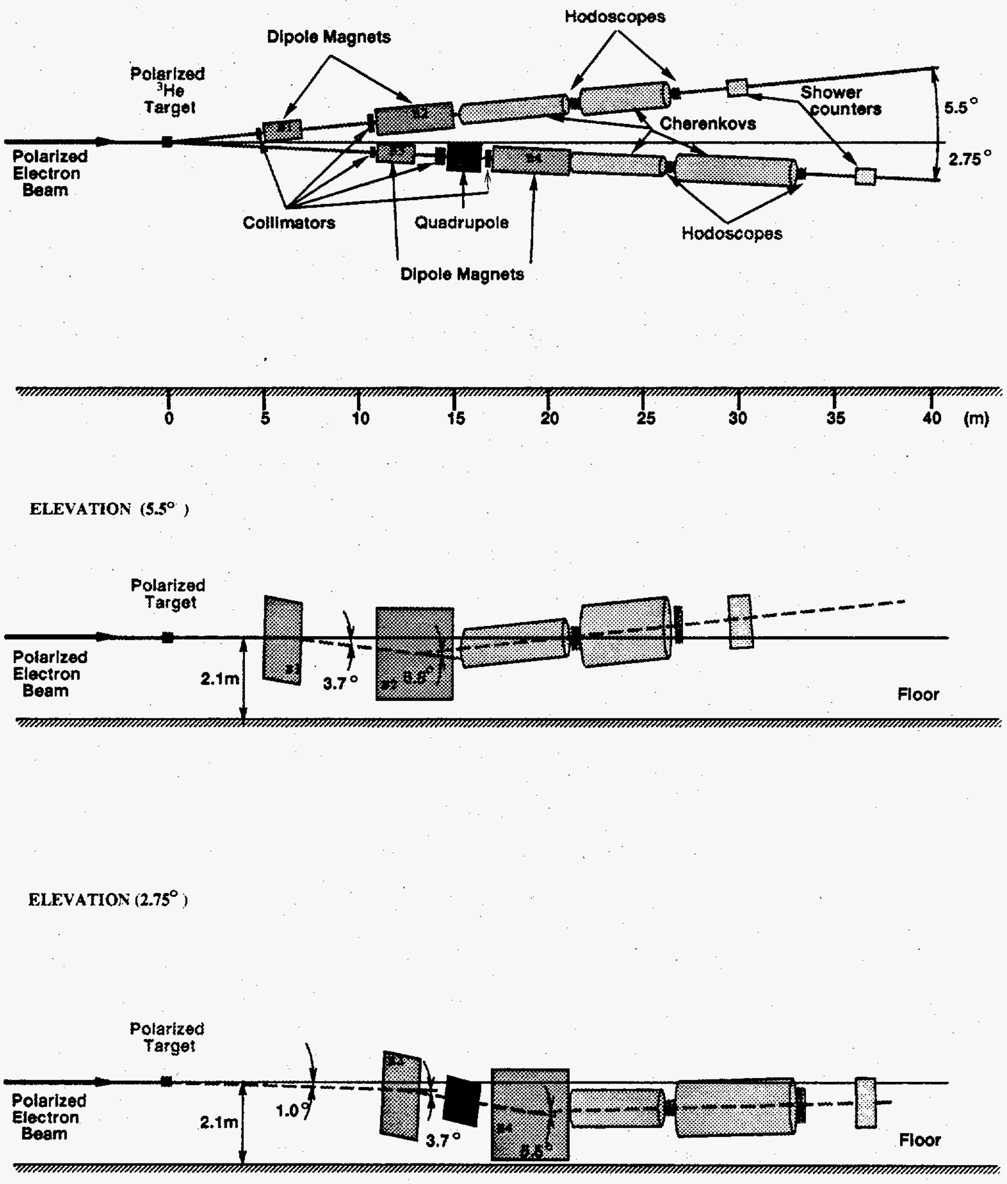

Fig. 2.12. Schematic plan of the E154 spectrometers.

2.6.2.1 Magnets

In order to cover the desired range in Bjorken x, the momentum acceptance of the spectrometers had to extend over the broad range of momenta with large solid angles to ensure a reasonable counting rate. An additional design consideration was to suppress the large neutral background, mainly photons from bremsstrahlung and π^0 decay. The momentum resolution was not a major constraint, it had to be good enough to ensure that the resolution in Bjorken x is much smaller then the bin width.

The "reverse-bend" spectrometer design, achieved with two dipole magnets bending in the opposite directions, has two main advantages. First, unlike conventional systems with bends in the same direction, it allows one to maintain a relatively large solid angle over the broad range of momenta, and hence extend the kinematic coverage of the experiment. A solid angle of $0.3 - 0.5$ msr for $10 - 40$ GeV particles was achieved for 5.5° spectrometer; the solid angle of the 2.75° spectrometer was variable from 0.05 to 0.1 msr for $9 < p < 40$ GeV. Second, a proper choice of bending strengths and detector geometry achieves a so-called "two-bounce" system where the photons from the target are not allowed to hit the detector elements without bouncing at least twice off the collimator or the magnet. Thus, the neutral background originating at the target is reduced to a tolerable level.

The optics of the magnetic spectrometers is usually related to an imaginary ray called the *"central trajectory"*. The trajectory of a charged particle is defined by specifying its position and momentum vector relative to this central trajectory. Since the curvature of a charged particle in a magnetic field is (inversely) proportional to its momentum, scaling the field of all magnets in the system scales the central momentum, but does not change the optics of the system *relative* to the central ray. It is convenient to choose the central trajectory in such a way that the optics of the spectrometer is approximately symmetric around it. For our spectrometers, the central trajectory is defined by ($\theta = 0, \phi = -1^\circ$) (2.75°) and ($\theta = 0, \phi = -0.48^\circ$) (5.5°) at the target and the central momentum $p_c = 20$ GeV.

The main characteristics of the spectrometer magnets are given in Table 2.4.The front dipoles of both spectrometers are almost identical[3], they are copper-coil beam line magnets 18D72. Both magnets bend the central ray downwards by 3.7°. The rear dipoles, also quite similar, are B81 and B82 magnets from the SLAC 8 GeV spectrometer. They bend the electrons upwards. In addition to the dipole magnets, a quadrupole placed between the dipoles in the 2.75° spectrometer defocuses electrons in the horizontal plane so as to reduce the instantaneous rate of particles per detector element. In the bend plane, it also results in focusing (at $p = 18$ GeV at the shower counter) and spreads the low momentum particles over the large range in $\hat{y}$. The latter fact is important in reducing the probability of electron-pion overlaps at the shower counter. The optics of two spectrometers is shown in Fig. 2.13.

The magnet currents were maintained to within 0.1% of the set point and monitored at every checkpoint (a few times a run). In addition, NMR probes were placed inside each dipole magnet and were read out every shift. The field in the quadrupole was monitored by a Hall probe.

2.6.2.2 Collimators and acceptance definition

The acceptance of the spectrometers is defined by the collimators and is matched by the active areas of the detectors. The front collimators, 2SC1 and 5SC1 in 2.75° and 5.5° respectively, are placed in front of the first dipoles B1 and B3. They define the horizontal and vertical entrance apertures. They are identical in design. Both consist of two sets of "jaws" which are movable independently in $\hat{x}$ and $\hat{y}$ directions. The aperture is defined by 1 inch thick tungsten "lips" succeeded by 4 inches of

---

[3] The only difference is in the amount of steel that was cut from the flux return plates in order to clear the beam line.

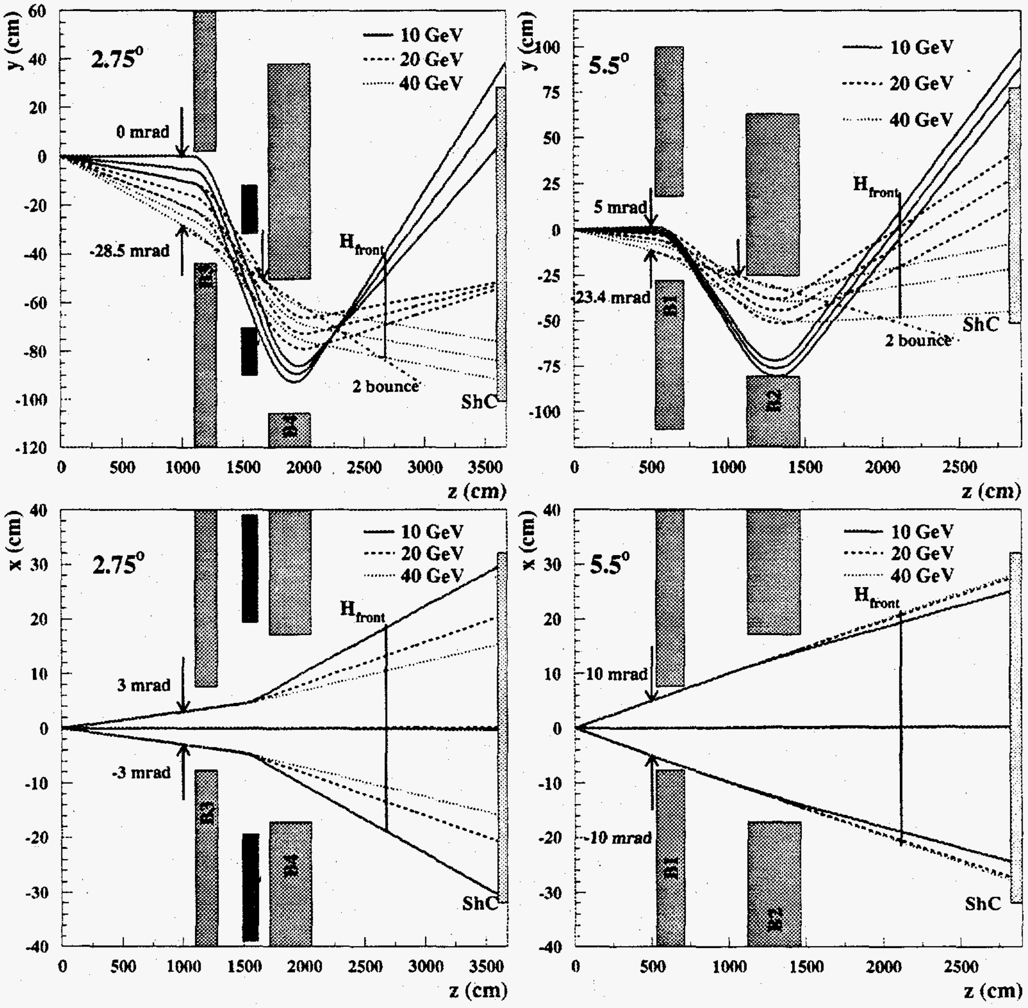

Fig. 2.13. Optics of the 2.75° (left) and 5.5° (right) spectrometers in the bend (top) and non-bend (bottom) planes.

Table 2.4. Characteristics of the spectrometer magnets used in E154.

	5.5°		2.75°		
Magnet	B1	B2	B3	Q1	B4
Type	Dipole	Dipole	Dipole	Quadrupole	Dipole
Name	18D72	B82	18D72	Q203	B81
Length (cm)	182.88	345.44	182.88	130.18	345.44
Aperture (cm) x:	15.24	34.29	15.24		34.29
y:	45.72	55.56	45.72		55.56
Pole radius (cm)				19.36	
Center x (cm)	1.16	−0.23	−0.53	0.01	0.04
Center y (cm)	−5.17	−53.32	20.77	−50.81	−78.09
Center z (cm)	620.75	1294.28	1190.91	1555.59	1887.91
Pitch (°)	−2.322	−0.009	−2.804	−4.713	0.006
Roll (°)	0.017	−0.017	−0.009	0.009	0.007
Yaw (°)	−0.761	0.056	0.347	−0.019	−0.003
$\int Bdl$ (pole, kG-m)	43.105	79.486	43.105	(1) 13.682 (2) 9.874	64.183
Bend angle (°)	−3.7	6.8	−3.7		5.5
Current (Amps)	2658.8	2538.9	2684.3	(1) 2190.4 (2) 1580.8	1960.8

(1) Runs 1 – 3383; (2) Runs 3384 – 3788 (Picard).

Table 2.5. Apertures and positions of the spectrometer collimators 2SC1 and 5SC1.

	2SC1	5SC1
z (cm)	1064.9	495.3
$\Delta\theta$ (mrad)	±3.0	±9.8
ϕ_{min} (mrad)	−28.5	−23.4
ϕ_{max} (mrad)	(1) 0.0 (2) 3.3	+5.0

(1) Runs 1 – 3383; (2) Runs 3384 – 3788 (Picard).

lead. The jaws move symmetrically in $\hat{x}$. In the vertical direction, the bottom lip is fixed and defines the double-bounce geometry; the top lip is movable and defines the low momentum acceptance. The apertures of these collimators are summarized in Table 2.5.

The second set of collimators that define the double-bounce geometry and affect the high momentum acceptance in both spectrometers is 2SC3 (2.75°) and 5SC2

Table 2.6. Apertures and positions of the spectrometer collimators 2SC3 and 5SC2.

	2SC3	5SC2
z (cm)	1662.1	1067.9
Width (cm)	31.5	31.4
Height (cm)	36.3	45.4
y_{top} (cm)	-50.3	-25.6
Pitch, °	-2.4	-2.2

(5.5°). They are positioned in front of B2 and B4. These are fixed lead collimators 4.25 inches thick. Both of them were used in E142/E143, and we adopted them without major modifications. The horizontal aperture is big and does not constrain the acceptance. The top lip is pitched by $-2.2°$ (2SC3) and $-2.4°$ (5SC2). The collimators are positioned in such a way that the acceptance is cleanly defined by their apertures, *i.e.* the accepted electrons do not go through the magnet coils. The double-bounce line is defined by the bottom lips of the front collimators (2SC1 and 5SC1) and the top lips of 2SC3 and 5SC2 (*cf.* Fig. 2.13). The hodoscopes are positioned above this line, so that neutral particles must bounce at least twice off the collimator (or magnet) apertures before hitting the detectors. The positions of 2SC1 and 5SC1 are given in Table 2.6.

The collimator 2SC2, positioned in front of the quadrupole Q1, is designed to control the peak electron acceptance of the 2.75° spectrometer. Its vertical jaws, which have 1 inch thick tungsten lips in front of 4 inches of lead, could be moved independently. Three fixed 4 inch thick lead collimators (old E142/3 collimators) are placed behind the jaws to help stop low energy pions. These collimators are always behind the "shadow" of the movable jaws and thus do not affect the electron acceptance. Placed between two dipoles in the region where the electron y position is almost insensitive to the momentum, the collimator 2SC2 provides effective means of tuning the peak electron acceptance. The acceptance could be adjusted from 0 to 0.1 msr at the peak without change in the momentum range. Starting with target

Table 2.7. Apertures and position of the adjustable collimator 2SC2 in the 2.75° spectrometer.

Runs	1304- 2311	2312 2643	2644- 3100	3101- 3121	3122- 3371	3372- 3788
z (cm)	1417.5					
y_{top} (cm)	-37.0	-33.0	-30.0	-33.2	-32.0	-25.8
y_{bottom} (cm)	-42.0	-44.0	-49.0	-43.9	-47.0	-53.9

cell Hermes, the aperture of 2SC2 was adjusted for every cell to compensate the differences in target window thickness and achieve roughly constant electron rate of 0.5 electrons per spill. Table 2.7 lists the vertical positions of the collimator lips for all run intervals.

The positions and sizes of the detectors were matched to the optics to achieve maximal acceptance while preserved the double-bounce system. The main constraints were a desire to have sufficiently long Cherenkov detectors (to keep high efficiency for electrons), the need to keep the separation between the rear hodoscope and the shower counter at least 2 meters (for efficient tracking), and the physical size of the End Station. Small scattering angles further complicated the design since the magnets had to clear the beam line and the detectors had to be sufficiently far from it to allow for adequate shielding. The positions and sizes of the detectors (typical) are listed in Table 2.8. The detector apertures do not limit the electron acceptance, except for the low momentum region (where the top of the shower counter defines the low-momentum cutoff). The acceptances of two spectrometers are shown in Fig. 2.14.

2.6.2.3 *Reconstruction of the kinematic variables.*

For a given set of magnetic fields, the trajectory of a charged particle in the spectrometer is determined by six variables: the vertex position at the target (x_0, y_0, z_0) and the initial momentum 3-vector (p_{0x}, p_{0y}, p_{0z}). Only four variables are measured

Table 2.8. Typical positions and apertures of the detectors. The smallest hodoscope apertures are quoted. For the shower counter, the quoted apertures exclude half of the edge block on each side. The quoted z position of the shower counter is 5 radiation length inside from the surface.

	2.75°	5.5°
Front hodoscope		
x_{center} (cm)	0.0	0.0
y_{center} (cm)	−62.0	−14.4
z_{center} (cm)	2673	2109
Width (cm)	36.0	43.0
Height (cm)	41.0	69.0
Rear hodoscope		
x_{center} (cm)	0.0	0.0
y_{center} (cm)	−41.5	4.0
z_{center} (cm)	3394	2618
Width (cm)	57.2	51.0
Height (cm)	122.6	107.0
Shower counter		
x_{center} (cm)	0.0	0.0
y_{center} (cm)	−36.2	13.1
z_{center} (cm)	3628	2902
Width (cm)	57.2	57.2
Height (cm)	122.6	122.6

in the detector hut: track slopes $\Theta = dx/dz$ and $\Phi = dy/dz$, and track intercepts with $z = 0$ (X_0 and Y_0)[4]. Coordinates x_0 and y_0 are the beam coordinates at the target and are measured by the wire array and the traveling wave beam position monitor (TWBPM). Moreover, since for E154 the magnetic field at the target is negligible, one of the variables (for instance, x_0) is not independent. Furthermore, the beam spot size was typically on the order of 1 mm and the fluctuations of the beam position were small, so we can neglect the dependence of the trajectories on y_0 and eliminate the second target coordinate. We now have four measured quantities, and four parameters we would like to extract: track momentum p_0, track angles θ and

---

[4] Tracks are straight in the detector hut since there are no magnetic fields. See Section 3.5 for the description of tracking algorithm and definition of variables.

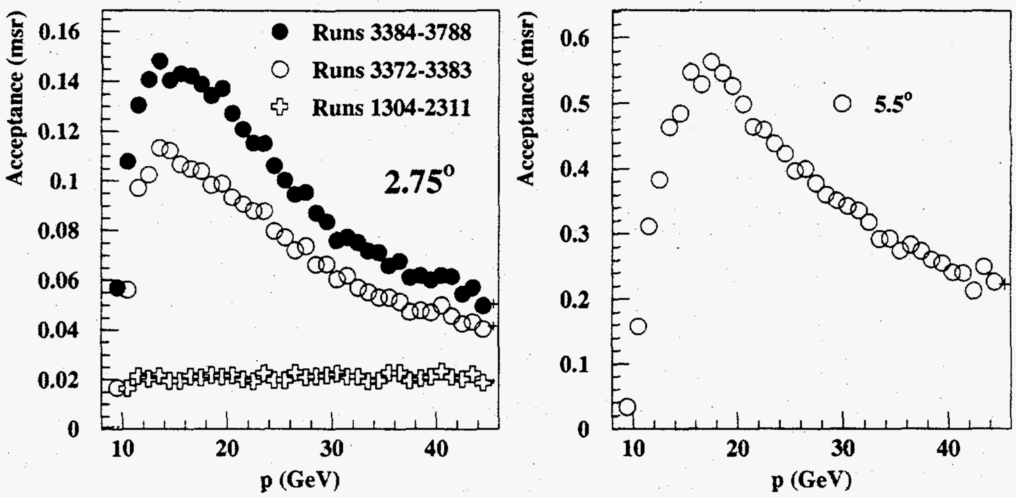

Fig. 2.14. The acceptances of the 2.75° (left) and 5.5° (right) spectrometers. The acceptance of the 2.75° spectrometer was adjusted several times during the run to maintained the rate of detected electrons approximately constant at different beam currents and target window thicknesses. We show the smallest acceptance (runs 1304–2311, current of $9 \cdot 10^{10}$ electrons/spill), the biggest acceptance with the standard setting of Q1 (runs 3372–3383, current of $5 \cdot 10^{10}$ electrons/spill), and the acceptance with the new setting of Q1 (runs 3384–3788, current of $3 \cdot 10^{10}$ electrons). See Table 2.4 and Table 2.7 for details of the magnet and collimator settings.

ϕ at the target, and the position z_0 (the latter is not actually used in reconstruction of the kinematics of the DIS event). The spectrometer can be thought of as an instrument that transforms the vector of initial variables (p_0, θ, ϕ, z_0) into the vector of track parameters (X_0, Θ, Y_0, Φ). The problem can thus be formulated with a matrix notation[109] where the coefficients that are used to calculate (p_0, θ, ϕ, z_0) from the track parameters in the spectrometer are called *inverse matrix elements* (as opposed to *direct* elements that do the forward transformation).

Since the sextupole components of the magnetic field are small (as will be shown below), the equations of motion are almost decoupled in the bend and non-bend planes. The dependence of the trajectories on z_0 is quite weak in the vertical plane, so we can reconstruct p_0 and ϕ using only two track parameters: Y_0 and Φ. Traditionally, this is done with a Taylor expansion

$$\begin{aligned} \frac{p_0}{p_c} &= \sum_{i,j=0}^{N_p} a_p^{ij} Y_0^i \Phi^j \quad \text{and} \\ \phi &= \sum_{i,j=0}^{N_\phi} a_\phi^{ij} Y_0^i \Phi^j \,, \end{aligned} \tag{2.12}$$

where p_c is the central momentum. Such expansion was used for E142 and E143,[76] and during the E154 run in the on-line analysis. It works well when the momentum bite of the spectrometer $\Delta p/p_c$ and the deviations from the central trajectory are small (and the expansion is justified). However, the convergence of the expansion is rather poor for spectrometers with a wide momentum acceptance such as ours, so the matrix elements have to be calculated up to the fourth or fifth order (we used $N_p = 5$ and $N_\phi = 4$ online). Even then, the bias in the momentum reconstruction on the edges of acceptance (*i.e.* at low and high momenta) was too big to be acceptable (up to 4%). For the analysis of the Data Summary Tapes (DST), we tabulated the dependence of p_0 and ϕ on the spectrometer coordinates (Y_0, Φ). We used a grid with 5 mm spacing in Y_0 and 1 mr spacing in Φ; the linear interpolation was used between the grid nodes. The comparison between the momentum obtained with the look-up table and the Taylor expansion of Eq. (2.12) is shown in Fig. 2.15. In order to further eliminate the bias in the momentum (which was due to the finite size of the grid) a small correction was applied to the reconstructed momentum.

The track parameters in the non-bend plane (X_0, Θ) are used to determine the angle θ and the target coordinate z_0. Again, we use the grid with the spacing of 10 mm in X_0 and 1 mr in Θ. We neglect a gentle momentum dependence of X_0 and Θ in the 2.75° spectrometer (introduced by the quadrupole[5]). This results in somewhat deteriorated angular resolution at low momentum (0.6 mrad compared

---

[5] The quadrupole effect in the 5.5° spectrometer due to the pole face rotations is even less important.

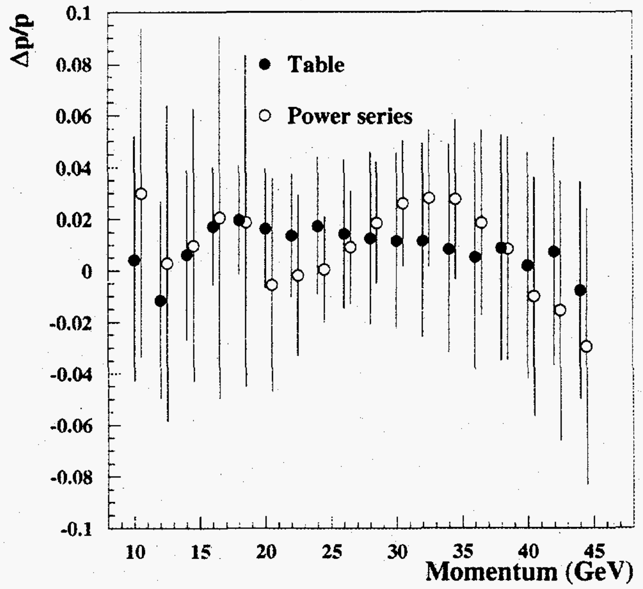

Fig. 2.15. The momentum bias for the tabulated matrix elements (closed circles) and the power series of Eq. (2.12) (open circles). The error bar represents the momentum resolution.

to 0.3 mrad at high momentum); it is however significantly better than what is required to measure the Bjorken x of the event.

2.6.2.4 Resolution

The reverse bend design results in a moderate momentum resolution that ranges from ≈ 2% at low momentum to ≈ 4% at high momentum. The resolution of the spectrometers was calculated by a Monte Carlo simulation (see Section 3.5) using a detailed optics model and taking into account multiple scattering and bremsstrahlung as well as background effects. The momentum resolution is plotted in Fig. 2.16 as a function of momentum. The average momentum resolution is 2.4% in the 2.75° spectrometer and 2.7% in the 5.5° spectrometer (weighted by acceptance). The average angular resolution is ≈ 0.4 mr in both spectrometers. For the original quadrupole setting in the 2.75° spectrometer (pre-Picard runs), the resolution in the bend plane (both momentum and angular) degrades rapidly at low momentum. This

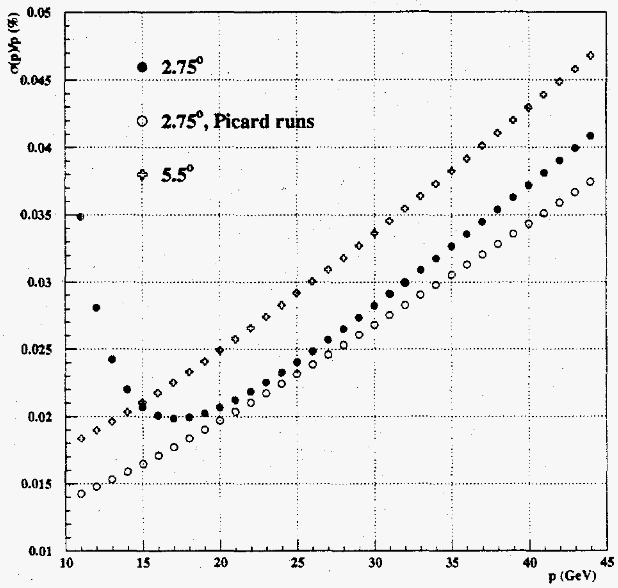

Fig. 2.16. Momentum dependence of the tracking momentum resolution. Standard optics configuration of the 2.75° spectrometer is shown by solid circles, Picard optics by open circles, and that of the 5.5° spectrometer by open crosses.

is due to a strong quadrupole focusing that results in almost ambiguous optics in the upper part of the spectrometer. Conversely, the angular resolution in the non-bend plane ($\sigma(\theta)$) is almost constant with momentum and is determined primarily by the segmentation of the front hodoscopes and shower counter spatial resolution. The parameterizations of the momentum and angular resolutions in the bend plane are given in Section 3.5.

2.6.3 Magnetic measurements

An optics model of the spectrometers can be constructed with the information given in Table 2.4 assuming pure dipole and quadrupole fields. However, in order to eliminate biases in momentum reconstruction, a detailed and accurate field map of the magnets is needed. Prior to E154, we have performed magnetic measurements in two of the magnets, B1 and B3. Part of the flux return plates had been removed in these magnets in order to place the magnets more closely to the beam line. The parts were not removed symmetrically, and certain non-uniformities were introduced to the fields. Such non-uniformities introduce sextupole (and higher order) components in addition to the pure dipole component of the field. The sextupole component induces mixing between the $\hat{x}$ and $\hat{y}$ projections of the particle trajectories which are otherwise decoupled. The effect could be potentially very important since the front magnets B1 and B3 have a long lever arm to affect the particle trajectories. The magnetic field was measured on a grid with 2 inch spacing in $\hat{z}$ direction and $0.5-1$ inch spacing in $\hat{x}$ and $\hat{y}$ directions. Total of 2720 points were measured in B1 (which is symmetric around the median $\hat{x}-\hat{z}$ plane), and 4320 points were taken in B3 (where the cut distorts the symmetry).

2.6.3.1 Magnetic maps

The horizontal component of the field $B_x(x,y,z)$ was measured by a Hall probe which was calibrated periodically against the NMR probe. The Hall probe reading was corrected for temperature effects by a feedback system and showed stability of better than 0.1%. The precision of individual measurements was $\approx 0.1\%$ at high fields and ≈ 3 G at low fields. The primary uncertainty was the position of the probe relative to the magnet which was estimated to be 1.6 mm in $\hat{x}$ and $\hat{y}$, and 3.2 mm in $\hat{z}$.

In the absence of field sources, the components of magnetic field are derived from a scalar potential function which obeys the Laplace equation

$$\Delta\Phi(x,y,z)=0\ , \tag{2.13}$$

where $\vec{\mathbf{B}}=\vec{\nabla}\Phi$. The components of the vector $\vec{\mathbf{B}}$ are coupled; by measuring the primary field component $B_x(x,y,z)$, we can determine the scalar potential (neglecting a trivial constant)

$$\Phi(x,y,z)=\int_0^x B_x(x',y,z)dx' \tag{2.14}$$

and thus obtain other components of $\vec{\mathbf{B}}$.

The components of the magnetic field are reconstructed in the following way. We assume that the solution of Eq. (2.14) has a separable form:

$$\Phi(x,y,z) = \Phi_1(z)\Phi_2(x,y)\ . \tag{2.15}$$

We use the standard multipole expansion (up to the sextupole component) in the $\hat{x} - \hat{y}$ plane for each measured z_i. The coefficients of the multipole expansion are fitted to the measured values of $B_x(x,y,z)$:

$$B_x(x,y,z_i) = \sum_{j=2,4,6} a_j(z_i) B_x^j(x,y)\ . \tag{2.16}$$

Coefficients $a_j(z)$ are interpolated between the nodes and their derivatives determine the $\hat{z}$ component of the field[6].

The primary and secondary field components B_x and B_y are shown as functions of x and y at the center of B3 in Fig. 2.17. The field map of B1 is very similar. The deviation from the pure dipole field ($B_x = \text{const}$, $B_y = 0$) is mainly due to the sextupole component and does not exceed 1% in both B1 and B3. The quadrupole component is highly suppressed. The z dependence of the dipole and sextupole components of the field is shown in Fig. 2.18.

The magnetic properties of the rear dipole magnets, B2 and B4, were measured prior to E142.[110] The higher-order components were found to be quite small ($\approx$ 0.1%), so we approximate the field in B2 and B4 to be dipole. The z dependence of the field was re-measured in both magnets to correct for the environmental effects (such as a mirror plate of Q1 that affects the fringe field of B4), and to check consistency of the two sets of measurements. In general, a good agreement with the data of Ref. [110] was found. The z dependence of the dipole field in B2 and B4 is shown in Fig. 2.19.

---

[6] Note that the effect of B_z on electron trajectory is suppressed due to a very small transverse component of electron momentum.

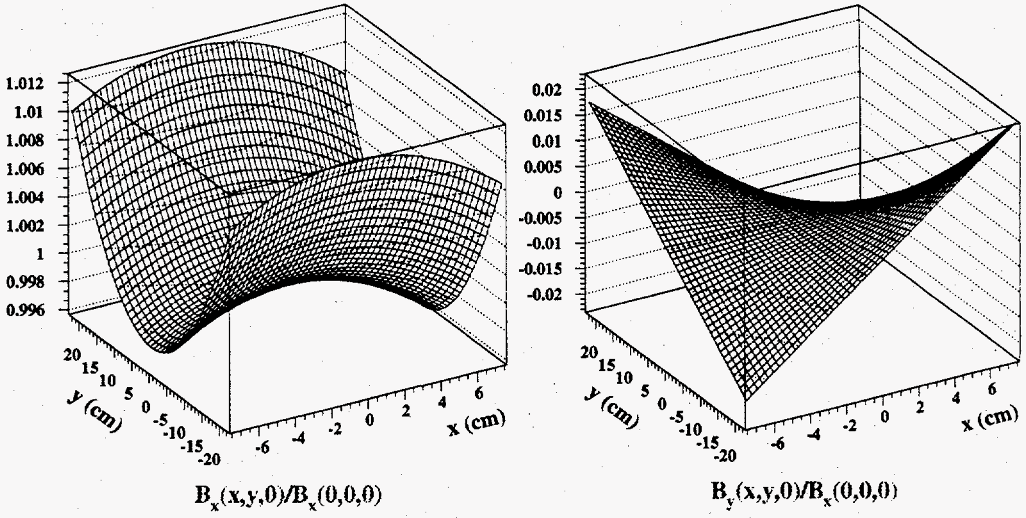

Fig. 2.17. B3 field map in the center of the magnet. B_x (left) and B_y (right) are normalized to the dipole component of the field.

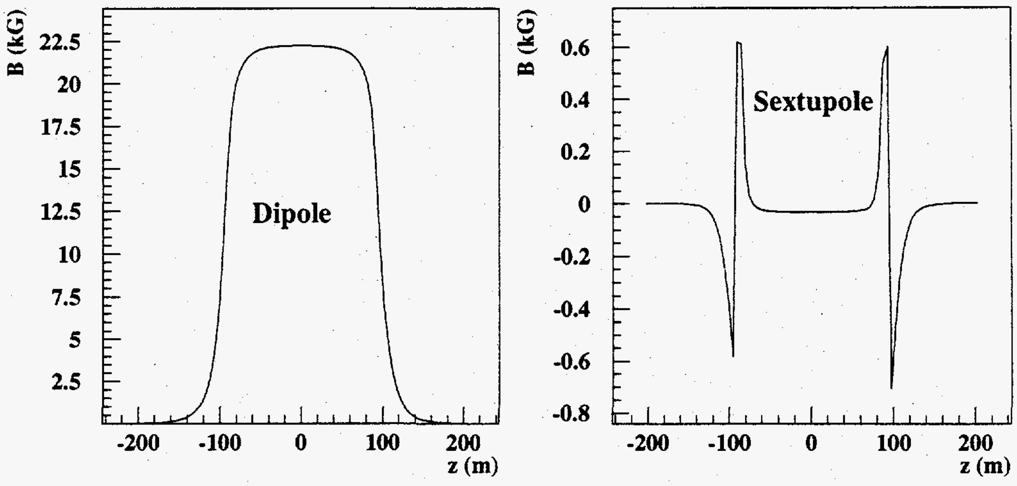

Fig. 2.18. The z dependence of the dipole (left) and sextupole (right) components of the magnetic field in B3.

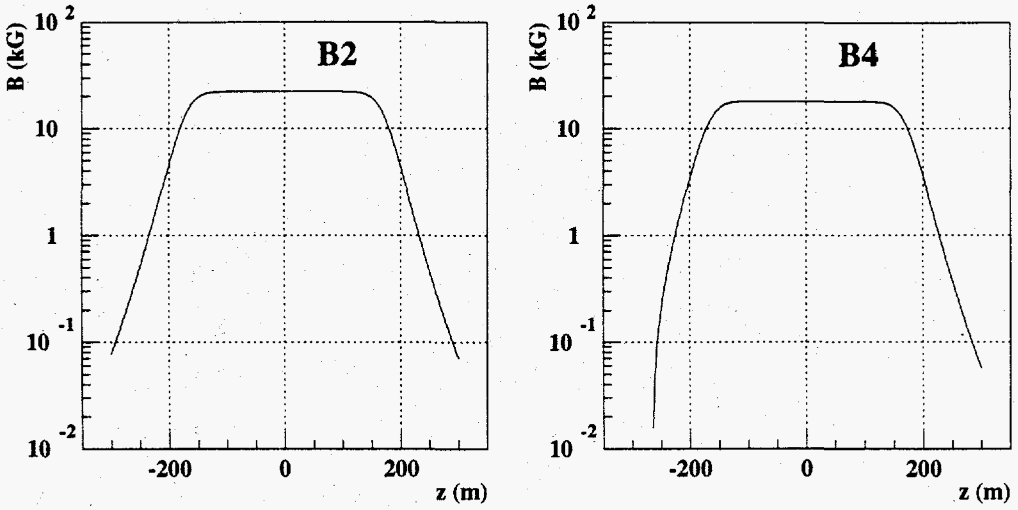

Fig. 2.19. The z dependence of the magnetic field in B2 (left) and B4 (right). Note the drop in the front fringe field of B4 due to the mirror plate of Q1.

The quadrupole Q1 (Q203) was mapped prior to E142 by the SLAC Metrology Department. The magnet is essentially a pure quadrupole with the field gradient constant up to the radius of 15.2 cm (at bigger radii the integrated gradient drops at a rate of 0.13%/cm). The magnetic center of Q1 is shifted relative to the geometrical center by 0.368 cm towards the utility (upstream) end where the mirror plate is farther from the magnet steel.

2.6.3.2 Magnetization curves

The dependence of the magnetic field on the current was also measured for all dipoles. The integrated field strength $\int Bdl$ is plotted in Fig. 2.20 as a function of current. The dependence was fitted to the polynomial function

$$I = \sum_{i=1}^{N} a_i \left(\int Bdl \right)^i , \tag{2.17}$$

where the current I is in Amperes and $\int Bdl$ is in kG-m. For Q1, the current is given by $I = 30.994 \int Gdl$, where the integrated gradient $\int Gdl$ is in kG. The coefficients a_i for the dipole magnets are given in Table 2.9.

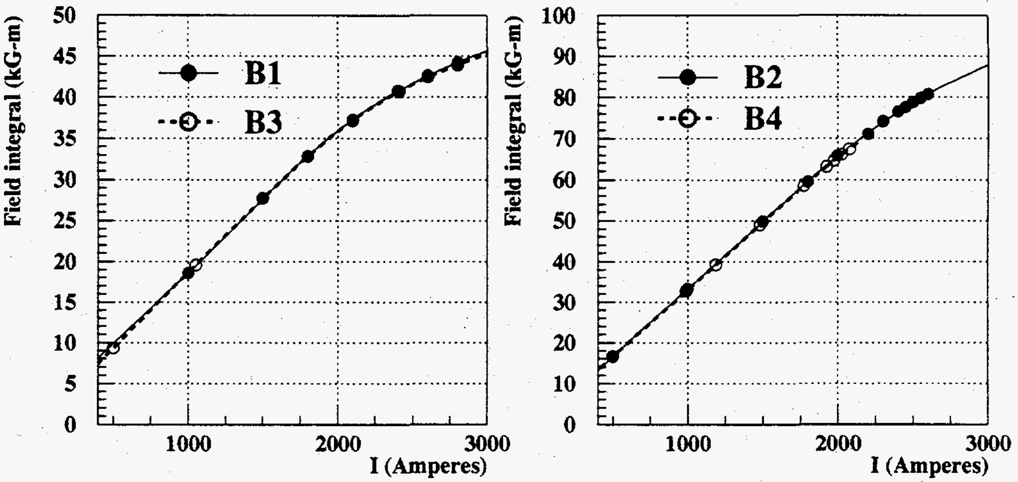

Fig. 2.20. The magnetization curves for B1 and B3 (left) and B2 and B4 (right).

Table 2.9. Coefficients a_i of the polynomial expansion of the current versus field for the E154 dipole magnets.

i	B1	B2	B3	B4
1	42.110	31.387	57.523	29.382
2	1.0830	-0.1797	-0.7300	0.05130
3	-0.01828	$0.7714 \cdot 10^{-2}$	0.04010	$-0.6346 \cdot 10^{-3}$
4	$-0.6584 \cdot 10^{-3}$	$-0.1344 \cdot 10^{-3}$	$-0.3785 \cdot 10^{-3}$	$-0.5804 \cdot 10^{-5}$
5	$0.1726 \cdot 10^{-4}$	$0.8413 \cdot 10^{-6}$	$-0.2350 \cdot 10^{-4}$	$0.2020 \cdot 10^{-7}$
6			$0.4917 \cdot 10^{-6}$	$0.1545 \cdot 10^{-8}$

2.6.3.3 Fringe field effects

Due to the small angles of the spectrometers, the magnets of the 5.5° spectrometer are close to the 2.75° line. The fringe fields of B1 and B2 can therefore affect the particle trajectories in the small angle spectrometer. The fringe fields from these two magnets measured along the 2.75° line are shown in Fig. 2.21. One can clearly see the effects of the front coil of B1 ($z \approx 520$ cm), the rear coil of B1 ($z \approx 720$ cm), and the front coil of B2 ($z \approx 1120$ cm). The fringe fields could be approximated in the optics model by introducing two additional dipole magnets into the 2.75° spectrometer: one centered at $z = 580$ cm with $\int B_x dl = -70$ G-m, and another at $z = 720$ cm with $\int B_y dl = -120$ G-m. The fringe field results in a shift of the reconstructed momentum of $\approx 0.4\%$ at low $p = 10$ GeV, and smaller at higher momenta.

2.6.4 Calibration

The optics model and the inverse matrix elements are generated solely by Monte Carlo simulation using the measured field maps and the precision alignment data for the magnets and detectors. The shower counters are calibrated with real electrons using momentum information, and no independent experimental calibration was attempted. Consequently, the reconstruction of the kinematic variables (Bjorken x and Q^2) relies heavily on the accuracy of the Monte Carlo results and alignment data.

Two tests were performed to check the integrity of the optics model. In one of them, we put a tungsten mask with small holes (dubbed a *"jailbar"*, or more appropriately, a "sieve slit") in front of the spectrometer so that the angles of the scattered electrons were well-defined. After determining these angles using tracking, we checked for biases in the angle reconstruction and compared the resolution with the model. The jailbar data do not determine how accurate the momentum

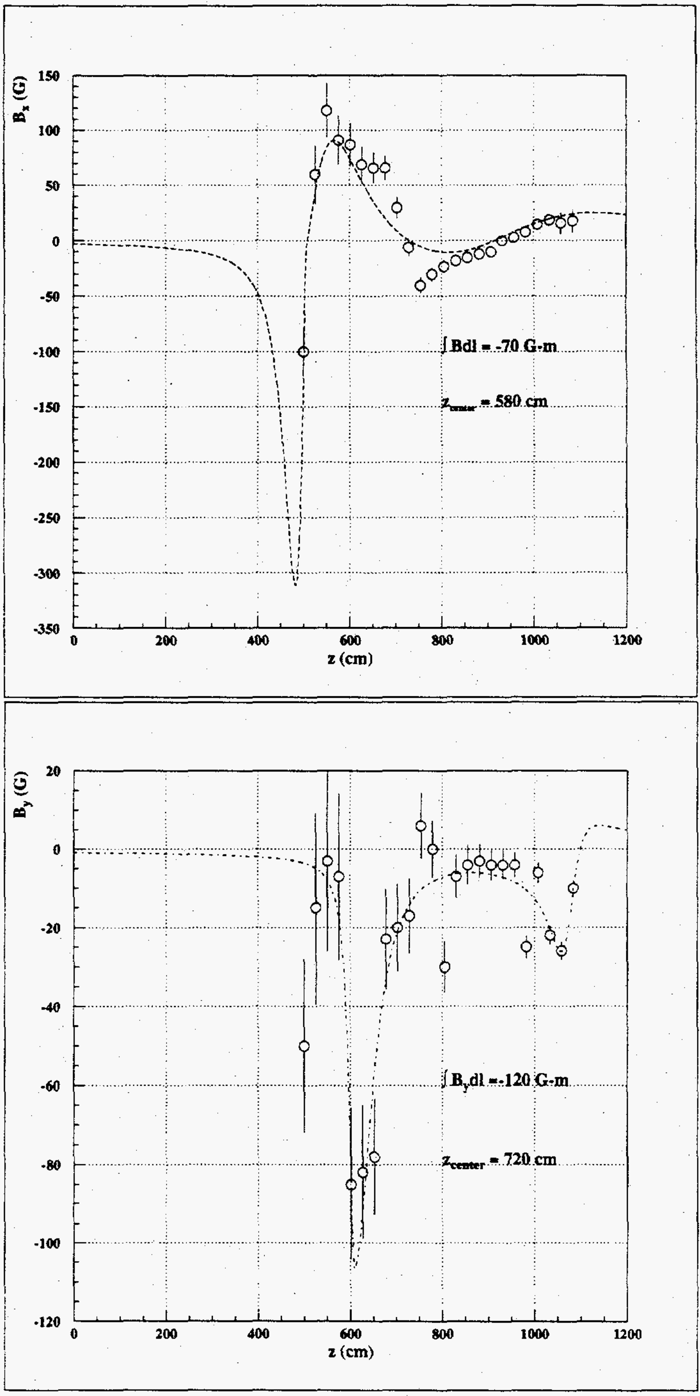

Fig. 2.21: The x (top) and y (bottom) components of the fringe field of the 5.5° magnets along the 2.75° spectrometer line.

reconstruction is. However, the reconstruction of momentum and the bend plane scattering angle are closely related, and if the angle reconstruction is correct, the momentum is also right. Secondly, we took data with the beam energy of ≈ 8 GeV and reduced the central momentum of the spectrometers, so the elastic peak could be observed. The position of the elastic peak (or the shape of the cross section near the end point if the elastic peak is not visible) directly determines the momentum scale. This method relies on the assumption that the magnetic fields simply scale with the central momentum (*i.e.* the x, y, z dependence remains the same as at $p_c = 20$ GeV). This assumption is a source of uncertainty in the interpretation of the data.

2.6.4.1 Jailbar runs

The principle the jailbar calibration is illustrated in Fig. 2.22. The mask constructed of tungsten that is sufficiently thick to stop electrons, had precisely machined holes and was located before the first dipole of the spectrometer. The positions of the holes determined the angular acceptance; only electrons with certain values of θ and ϕ reached the detectors. These reconstructed angles can be compared to the known positions of the holes. The difference between the reconstructed and real hole positions determines the bias in the reconstruction of scattering angles; the width of the distribution checks the angular resolution.

The 1 inch thick tungsten masks were positioned in front of the dipoles B1 and B3 (behind the collimator 5SC1 and in front of 2SC1). Fifteen round holes were drilled in the 2.75° mask (only twelve holes were actually visible in the spectrometer), and the 5.5° mask had 25 holes equally spaced in $\hat{x}$ and $\hat{y}$ (15 holes visible). The positions of the holes are given in Table 2.10.

The ideal case for the jailbar calibration is a point-like target. We did not have such a target at our disposal, so the empty reference cell was used. The

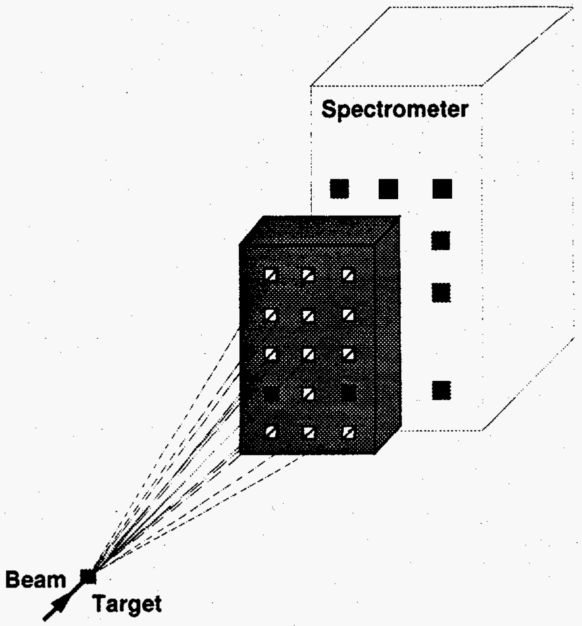

Fig. 2.22. The jailbar (sieve slit) calibration.

Table 2.10. Positions and sizes of the jailbar holes. The positions of the holes are relative to the target center $z_0 = 0$.

	2.75°	5.5°
z position (cm)	1050	515
Diameter (cm)	0.64	0.48
θ_{hole} (mr)	−2.3, 0.1, 2.6	−9.1, −4.6, −0.2, 4.3, 8.8
ϕ_{hole} (mr)	−22.2, −17.3, −11.3, −4.6	−13.6, −4.8, 4.0

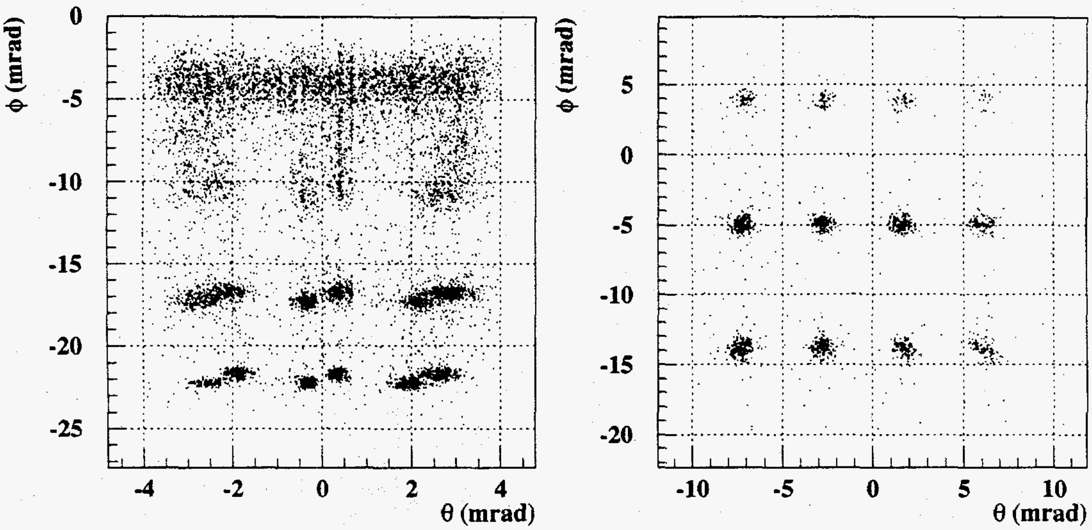

Fig. 2.23. Images of the reconstructed jailbar holes in the 2.75° (left) and 5.5° (right) spectrometers.

difference between positions of two target windows created a parallax which was most noticeable in the horizontal direction. The apparent angular position of the jailbar holes was displaced from the values given in Table 2.10, and the direction of the displacement was opposite for two windows. This can be seen in Fig. 2.23 where two images are reconstructed for every hole in the 2.75° spectrometer. The effect was so big in the 5.5° spectrometer that images of two adjacent holes merged. For example, electrons scattered from the downstream window at $\theta \approx -6.5$ mr went through the hole $\theta_{\text{hole}} = -9.1$ mr and merged with electrons scattered by $\theta \approx -7.2$ mr from the upstream window that went through the hole $\theta_{\text{hole}} = -4.6$ mr. Thus, one sees only 12 hole images in Fig. 2.23 for the 5.5° spectrometer.

The comparison of the jailbar data with Monte Carlo is shown in Fig. 2.24. We have applied a cut of $p > 14$ GeV in the 2.75° spectrometer to eliminate the contamination by pions that penetrate the tungsten mask. These pions can be seen as a continuum background at $\phi > -10$ mr (low momenta) in Fig. 2.23 (left). Due to the cut, the top row of the jailbar holes in the 2.75° spectrometer cannot be seen.

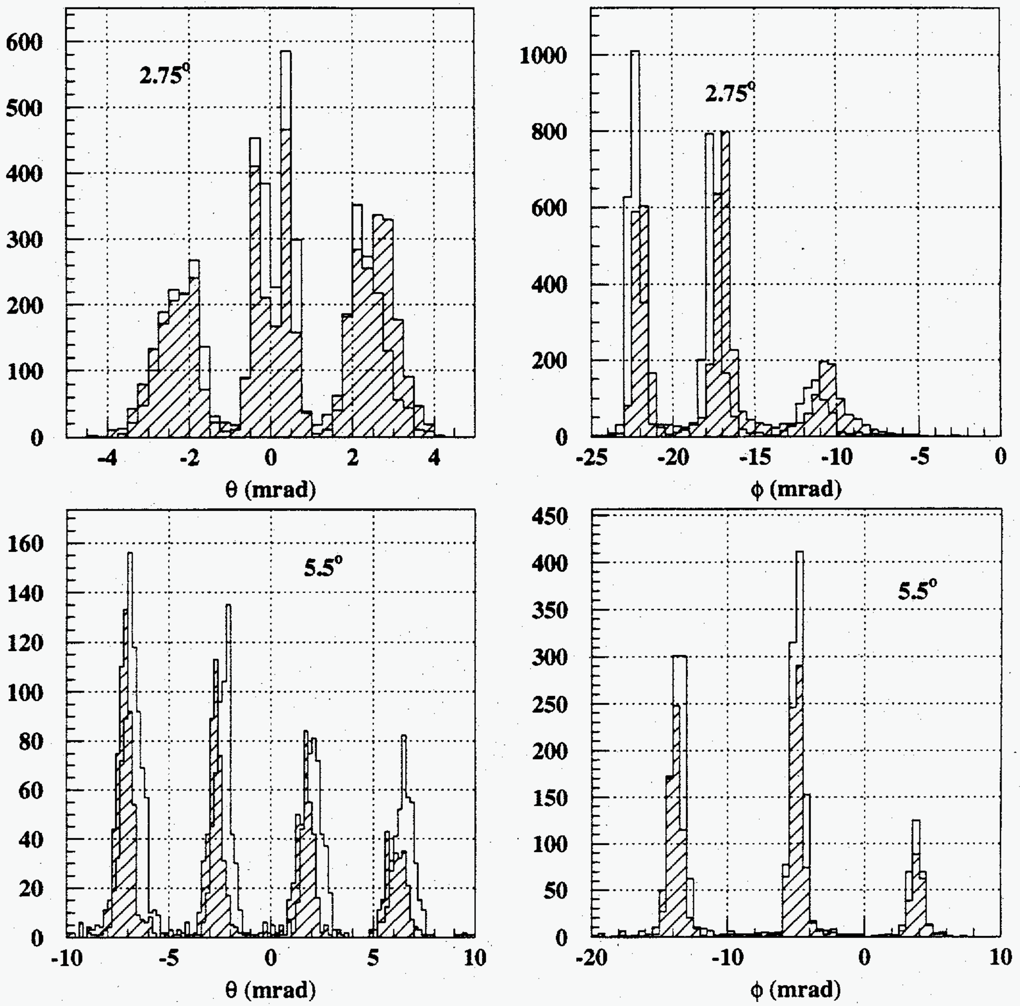

Fig. 2.24. Comparison of the Monte Carlo (open histograms) and the jailbar data (hatched histograms).

The agreement between the data and Monte Carlo results is generally quite good. The biggest disagreement is in 5.5° reconstruction of θ $(0.3-0.4$ mr) which is most likely due to a misalignment (the displacement is in the same direction for all the holes and is independent of momentum). The deviation of the data from Monte Carlo results in ϕ for the 2.75° spectrometer is ≈ 0.3 mr. These errors are negligible compared to the required resolution in Bjorken x.

2.6.4.2 8 GeV runs

The 8 GeV data were taken with the reference cell filled with 10 atm of hydrogen. The energy of the beam was set to 8.095 GeV[90] (where the error quoted by Ref. [90] is < 0.04 GeV). The data in the 2.75°spectrometer were taken with the jailbar mask in front of the 2SP1 collimator (the positions of the holes were reproduced in the data to ≈ 0.2 mr). The central momenta of two spectrometers were set at 5, 7, 9, and 11 GeV. The distribution of events near the end-point of the cross section is shown in Fig. 2.25 (for the 7 GeV spectrometer central momentum). The average Q^2 in the 5.5° spectrometer was too high and the elastic peak could not be clearly separated from the DIS background. In the 2.75° spectrometer the elastic peak is clearly seen, however, the data are statistics-limited. Also shown in Fig. 2.25 is the calculated cross section at $E = 8.095$ GeV convoluted with the spectrometer resolution. A fit to the end-point behavior yields the beam energy of 7.91 GeV (2.75°) and 7.94 (5.5°). Corrections to the shape of the magnetic field (increase in the effective length of the magnets at lower currents) and to the $\int Bdl$ of B1 and B3 change the fitted beam energy by +0.23 GeV and +0.04 GeV in the 2.75° and 5.5° spectrometers, respectively. The final results for the beam energy are $E = 8.16 \pm 0.16$ GeV (2.75°) and $E = 7.95 \pm 0.16$ GeV (5.5°) where the errors are dominated by systematics. These values are in agreement with the beam energy of 8.095 GeV. As a result, we will include a 2% error on the energy of the scattered electrons into the systematic error on g_1^n.

2.7 Detectors

2.7.1 Cherenkov counters

Each spectrometer was equipped with a pair of gas threshold Cherenkov counters that provided electron identification. The existing E142/E143 counters were modified (extended) for E154, and many parts (mirrors, mounts, exit and entrance

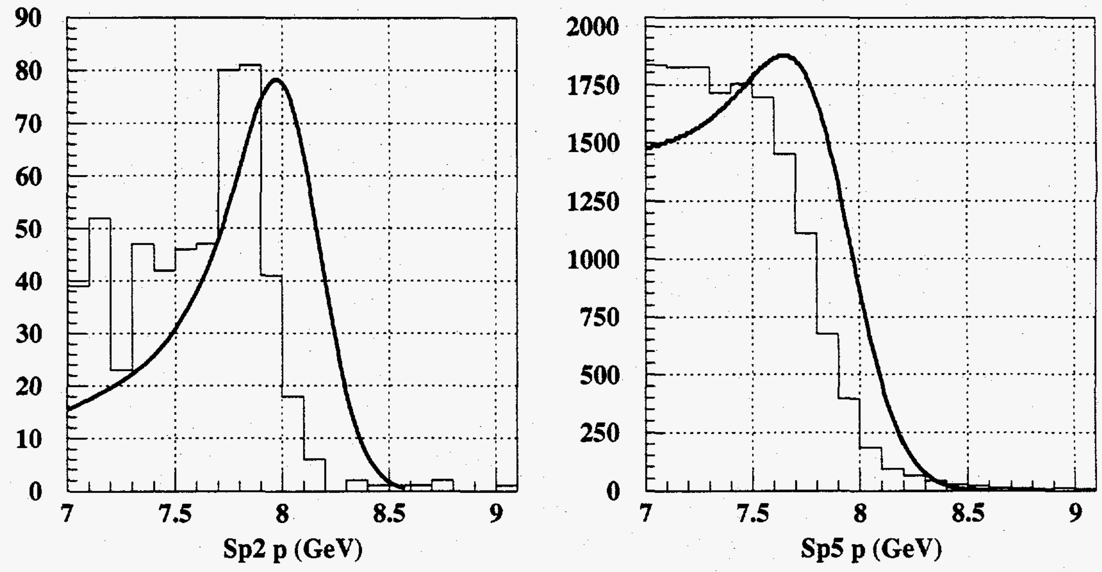

Fig. 2.25. Electron rate in the 2.75° (left) and 5.5° (right) spectrometers near the end-point of the cross section for a beam energy of 8.095 GeV and a central momentum of 7 GeV. Data (histogram) are compared to the calculated cross section (curve) convoluted with the spectrometer resolution.

Table 2.11. Parameters of the E154 Cherenkov counters.

Tank	Pion Threshold (GeV)	Physical Length (m)	Radiator Length (m)	Mirror Curvature (m)	Pressure (psi)	N_{pe} (scaled E143)
2C1	19	5.6	5.3	1.2	1.4	4.3
2C2	19	6.5	6.1	1.6	1.4	5.0
5C1	16	5.8	5.6	1.2	2.0	6.4
5C2	16	4.3	4.0	1.6	2.0	4.6

windows, vacuum system, phototubes, etc.) were reused. The counters were filled with N_2 at sub-atmospheric pressures. Higher beam energy and higher pion production rate (compared to the electron cross section) required raising the Cherenkov threshold for pions to 19 (16) GeV in the 2.75° (5.5°) spectrometer, and therefore lower pressures compared to E142/3. The relevant Cherenkov parameters are summarized in Table 2.11.

The pion threshold for the Cherenkov radiation is given by the requirement

$$\frac{1}{\beta_\pi n} < 1 \tag{2.18}$$

where $\beta_\pi = p_\pi / E_\pi = 1/\sqrt{1 + (m_\pi / p_\pi)^2}$ and n is the index of refraction of the radiator. The number of Cherenkov photons emitted by a charged particle above the threshold is proportional to $L_{\rm rad} \sin^2 \theta_{\rm ch}$, where the Cherenkov cone angle is given by

$$\cos \theta_{\rm ch} = \frac{1}{\beta n} \, , \tag{2.19}$$

and $L_{\rm rad}$ is the radiator length. Since the phototube signal (number of photoelectrons emitted from the cathode N_{pe}) is proportional to the number of Cherenkov photons, the expected average pulse height for electrons is given by

$$N_{pe}^{e} = C \; L_{\rm rad} \frac{(m_\pi / p_{\rm th})^2}{1 + (m_\pi / p_{\rm th})^2} \, , \tag{2.20}$$

where $p_{\rm th}$ is the pion threshold, m_π is the pion mass, and C is a proportionality constant. The E143 data suggests this constant is $C \approx 1.6 \times 10^4$ pe/m for our counters. Since the average number of photoelectrons drops rapidly with increasing pion threshold, large counter lengths were necessary in order to keep electron efficiency at acceptable level. The expected number of photoelectrons for our counters (obtained by scaling the E143 data) is given in Table 2.11. The actually observed numbers were somewhat higher (*cf.* Table 3.1).

The pion pulse height above the threshold is given by

$$N_{pe}^{\pi}(p) = C \; L_{\rm rad} \frac{m_\pi^2 \, (1/p_{\rm th}^2 - 1/p^2)}{1 + (m_\pi / p_{\rm th})^2} \tag{2.21}$$

where $p > p_{\rm th}$ is the pion momentum. The pion signal increases very slowly with momentum and reach 75% of the electron signal only at $p \approx 2 p_{\rm th} \approx 40$ GeV, where the pion production rate is zero.

The Cherenkov counters consisted of an aluminum vessel with thin $(1 - 1.5$ mm$)$ aluminum entrance and exit windows. The spherical mirrors mounted inside near the exit window focused the Cherenkov photons on a single 5 inch Hamamatsu R1584 phototube. To prevent arcing at low pressures, the phototube base was placed in a sealed can and kept under atmospheric pressure. The phototube was coated with a wavelength shifter to increase the sensitivity to the UV Cherenkov photons.

The phototube anode signals were digitized by a Struck DL515 VME Flash ADCs and read out by the Data Acquisition System. Four channels of the 250 MHz Flash ADC were interleaved to produce an effective resolution of 1 ns. The digitization of the pulses allowed a clear particle identification even at high rates and short ≈ 250 ns beam pulses (see Section 3.3). The signals from the last dynode were fanned out and went to the coincidence scalers in the Counting House and the multi-hit TDCs (4 discriminator/TDC channels per phototube). A combination of LeCroy 623B discriminators and LeCroy 2277 TDCs was used. The TDC signals were used to synchronize the FADCs (see Section 3.3).

2.7.2 Scintillator hodoscopes

Two sets of scintillator hodoscopes, placed in front of and behind the rear Cherenkov counter, provided the tracking capabilities. The hodoscopes were finely segmented to keep high efficiencies at high instantaneous rates. The hodoscope fingers were grouped in planes with 6(4) planes in the front and 4(4) planes in the back hodoscopes in the 2.75° (5.5°) spectrometer. The E142/E143 hodoscopes were used in the 5.5° spectrometer (where the rates were sufficiently low) without major modifications. Six new planes were built for the 2.75° spectrometer. Four of them (2H3X and 2H4Y in the front and 2H7X and 2H8Y in the rear package) were split in the middle (with a piece of black plastic placed in between to prevent cross-talk) and had the phototubes attached at both ends to further reduce the rate per element. Two other new planes (2H1U and 2H2V) were tilted by 15° relative to the horizontal direction. In addition to the new planes, four E142/E143 hodoscope planes were used (2H5Y, 2H6X, 2H9Y, and 2H10X)[7]. Fingers in most of the planes overlapped by 1/3 of the width to create a finer effective segmentation. The parameters of the E154 hodoscopes are given in Table 2.12. The hodoscope planes in the 2.75° spectrometer were tilted by 30 mrad towards the target and were almost perpendicular to the central trajectory of the spectrometer. The planes were vertical in the 5.5° spectrometer.

The fingers were made of Bicron BC404 plastic scintillator that has a fast rise time and short pulse length. The fingers were wrapped with aluminum foil and black electrical tape (2H1U and 2H2V fingers were taped and enclosed in a light-tight box). Most of the planes used the 1/2 inch Hamamatsu R4014 phototubes. The signals in the 2.75° (5.5°) spectrometer went through LeCroy 3412 (4413) discriminators and were read out by LeCroy 3377 (2277) multi-hit TDCs.

2.7.3 Shower counters

The energy of the electrons was measured by a total absorption calorimeter (shower counter) in fly's eye configuration located in the rear of the spectrometer. The counters in both spectrometers consisted of 200 $6.2 \times 6.2 \times 75$ cm^3 F2 lead glass blocks (from the ASP experiment at PEP[111]) stacked in an array of 20 rows by 10 columns. Each block was wrapped in aluminum foil and two layers of black tape ($\approx$ 1 mm total thickness). The F2 lead glass is a Cherenkov radiator with the refractive index of $n = 1.62$. The radiation length is $X_0 = 3.17$ cm, so the blocks are approximately 24 radiation lengths thick. The Moliére radius $R_m \approx 5$ cm, and the electron shower occupies on average 9 blocks (*cf.* Section 3.4). The 2 inch Amperex XP2212PC photomultipliers were attached to the blocks on the downstream end.

The signal from the phototube anode was split by a passive splitter and went to the LeCroy 2282 12-bin ADC and to discriminators and TDCs. Most of the

---

[7] The active area of these planes was bigger than the particle envelope in the 2.75° spectrometer, and some fingers were not used

Table 2.12. Parameters of the E154 hodoscopes.

Name	Angle (°)	Width (mm)	Height (mm)	Channels	Scint. width (mm)	Overlap (mm)	Scint. thickness (mm)	Location
2H1U	+15	360	370	44	15	5	6	2.75° front
2H2V	−15	360	370	44	15	5	6	2.75° front
2H3X	90	363	412	64	13	1	13	2.75° front
2H4Y	0	362	413	72	13	1	13	2.75° front
2H5Y	0	430	589	31	30	10	6	2.75° front
2H6X	90	430	589	34	20	7	6	2.75° front
2H7X	90	513	992	90	13	1	13	2.75° back
2H8Y	0	512	993	90	13	1	13	2.75° back
2H9Y	0	510	1070	55	30	10	6	2.75° back
2H10X	90	510	1070	27	30	10	6	2.75° back
Total				551				
5H1U	−45	430	690	25	45	15	6	5.5° front
5H2X	90	430	690	23	30	10	6	5.5° front
5H3Y	0	430	690	36	30	10	6	5.5° front
5H4V	+45	430	690	25	45	15	6	5.5° front
5H5U	−45	527	1064	21	75	25	10	5.5° back
5H6X	90	510	1070	27	30	10	6	5.5° back
5H7Y	0	510	1070	55	30	10	6	5.5° back
5H5U	+45	527	1064	21	75	25	10	5.5° back
Total				233				

blocks had one discriminator/TDC channel while 64 blocks in the 2.75° spectrometer had three channels with increasing discriminator thresholds. We used LeCroy 4413 discriminators and 2277 multihit TDCs in the region of 1 channel/block, and LeCroy 3412 discriminators with 3377 TDCs in the region of 3 channels/block. The TDCs were operated in the "burst-guard" mode so both leading and trailing edges of the discriminator output were detected. This allowed the use of timing information in the reconstruction of the overlapped events (see Section 3.4).

2.8 Electronics and DAQ

Most of the detector electronics was CAMAC-based, so we kept the modules used in E142/E143. Unlike those experiments, all spectrometer electronics modules were placed inside the 2.75° spectrometer hut, so long cables and associated signal deterioration were avoided. The main elements of the detector electronics have been described above. The discriminators for the hodoscopes were located near the detectors, and all other modules were placed in the general electronics racks in the south-east end of the 2.75° hut. The signals were brought by coaxial cables to the discriminators and by twisted-pair cables to the TDCs.

The short SLED beam pulses made it impractical to set up a trigger. The only trigger for the detector electronics was the A2N accelerator timing signal generated at the source at 120 Hz. It was used to generate the TDC and FADC starts and stops and the ADC gates. The gates were set $\approx$ 400 ns wide so the full phototube signals could be integrated.

Experiment E154 was the first ESA experiment to use the VME-based Data Acquisition system (DAQ). The previous system, based on the "Qbus" CAMAC interface run on a DEC MicroVAX 4000-200 and was limited to a data transfer rate of about 300 kBytes/s, which was not adequate for the 50 GeV experiments. The diagram of the VME-based DAQ system developed for E154 and E155 is shown in Fig. 2.26.[112] The front end of the system was implemented in three VME crates.

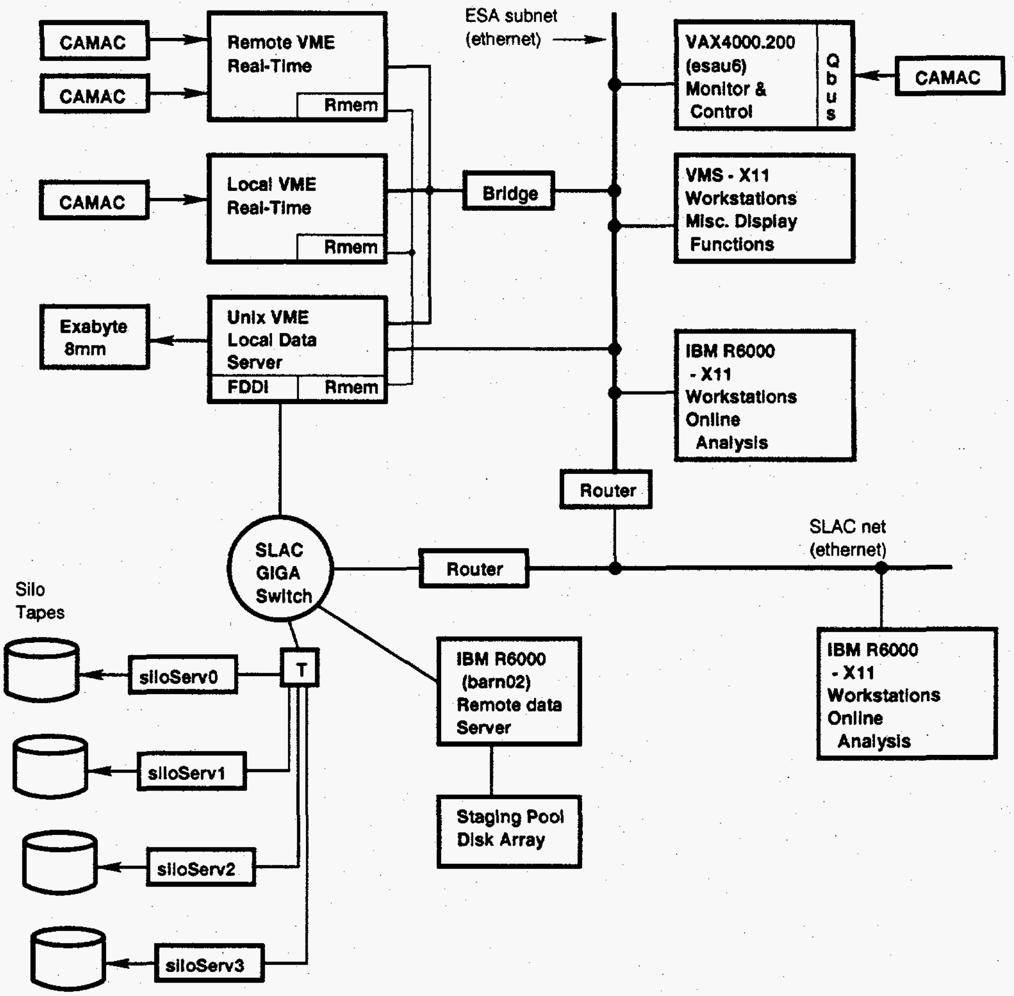

Fig. 2.26. The block diagram of the VME-based DAQ system for ESA.

Two of the VME crates contained the real-time components of the DAQ system and were located in the Counting House (the *local* VME crate) and in the 2.75° detector hut (the *remote* crate). The third, *UNIX* VME crate, was located in the Counting House and contained the Unix processors and interfaces to the data logging systems. The crates were linked by a *reflective memory* subsystem that allowed the data to be shared and processed by all three crates.

The local and remote VME crates contained interfaces to three CAMAC branches, the beam branch, that was read out by the local crate, and two spectrometer branches that ware handled by the remote crate. The Flash ADCs were VME-based and were read out by the remote VME crate. Each real-time crate contained a Motorola MVME166 processor that controlled the raw data readout and writing to the reflective memory. The Unix crate had two Motorola MVME197 processors one used for logging the data, and the other used for application software development and downloading into the real-time processors. The maximum data transfer rates achieved by the DAQ system during E154 were on the order of $0.7-0.8$ MBytes/sec, somewhat below the design goal of 1 MBytes/s, and were limited by the CAMAC readout. However, the actual data rates were sufficiently low that truncations of the data due to the DAQ system were negligible. The detailed description of the DAQ system is given in Ref. [112].

During the course of the experiment, the Unix crate logged the data remotely in the SLAC Computer Center (SCS) staging system. The connection was via the FDDI network that provided the data transfer rates on the order of 2 MBytes/sec. A separate process running on an IBM RS6000 workstation in the SCS wrote data onto a temporary disk storage, and then after the run completion issued the command to write the data to tape in the robotized silo. An alternative system was available that could allow writing the data locally onto an 8 mm tapes in case of a FDDI link failure or other difficulties with the remote logging. This system was never used in E154. In addition, the process running in the Unix crate could serve the data over the network (using the TCP/IP protocol) to any number of on-line analysis jobs running on separate workstations.

The data were stored in the SCS silo on 1 GByte tapes and was available for the off-line analysis through the automated staging system. The full data set was also copied onto 5 GByte 8 mm tapes and was used in the off-site data analysis based at Caltech.

The on-line control and monitoring processes were running on a MicroVAX 4000-200 workstation that was connected to the DAQ Unix crate via the TCP/IP-based network. These processes were used to start/stop the runs, issue data logging commands, set and monitor high voltages, magnet currents, set run types, etc. Two IBM RS6000 workstations were dedicated to the on-line analysis; they received data from the DAQ Unix crate over the network. The off-line analysis will be discussed in the following Chapter.

CHAPTER 3

DATA ANALYSIS

3.1 Overview

Data were taken in experiment E154 in October and November of 1995. The deep inelastic data were taken at the beam energy of 48.3 GeV and at three nominal beam currents: $3 \cdot 10^{10}$, $5 \cdot 10^{10}$, and $9 \cdot 10^{10}$ electrons per pulse. Nine polarized target cells and four reference cells were used through the course of the experiment. The typical electron rate was 0.5 electrons per pulse in the 2.75° spectrometer and varied from 0.07 to 0.2 electrons per pulse in the 5.5° spectrometer. The data were collected in runs which were each typically 200,000 spills long (or approximately half an hour). The data set consisted of more than 1800 runs that included asymmetry data (in parallel and perpendicular target polarization configurations), reference cell runs to determine the dilution factor, runs with the magnet polarity reversed to measure the charge symmetric backgrounds, and miscellaneous calibration and test runs. About 1.4 TBytes of data were stored on magnetic tapes. After all cuts, about 100 million deep inelastic events were used in the analysis.

The analysis was done in two steps. First, the raw data tapes were analyzed and the Data Summary Tapes (DSTs) were produced. The DST tapes contained the information about the Cherenkov hits, shower clusters, and tracks found in each spectrometer, as well as beam information. The DST production took seven weeks on four DEC Alpha 600 5/266 computers. A separate program was used to process the DST tapes and place electron events in x and Q^2 bins for each beam helicity. The summary files produced in this process were used to calculate the physics asymmetries and structure functions.

The analysis was done independently by two groups based at SLAC and Caltech[1]. The results of both groups agree to a very high degree, and for the publications we have chosen to average the results of two groups. We will primarily present the analysis and results obtained at Caltech, and describe the main differences with the SLAC analysis. After first describing the analysis of the raw data, our attention will be turned to the DST analysis and physics results.

3.2 Coordinate system

In the following discussion, we will use the "analysis" coordinate system that is related to the central trajectory in the spectrometer. This is a natural system since trajectories of all particles in the detector hut are roughly symmetric around the central ray. The $\hat{z}$ axis of the analysis frame coincides with the central ray in the detector hut which is pitched up by $\phi_{\rm cr} = 0.81°$ $(2.65°)$ and offset down by $\Delta y_{\rm cr} = 104.9$ cm (114.3 cm) in the 2.75° (5.5°) spectrometer relative to the regular "spectrometer" system (*cf.* Section 2.6.2). The rotation is around the $\hat{x}$ axis, so it is the same in both frames. The origin of the is chosen in such a way that the target is at $z = 0$ in the new frame. Hence, the transformation from the spectrometer to the analysis frame is given by

$$\begin{pmatrix} x \\ y \\ z \end{pmatrix}_{\text{analysis}} = \begin{pmatrix} 1 & 0 & 0 \\ 0 & \cos\phi_{\rm cr} & -\sin\phi_{\rm cr} \\ 0 & \sin\phi_{\rm cr} & \cos\phi_{\rm cr} \end{pmatrix} \begin{pmatrix} x \\ y \\ z \end{pmatrix}_{\text{spec}} + \begin{pmatrix} 0 \\ \Delta y_{\rm cr} \\ 0 \end{pmatrix} . \qquad (3.1)$$

Two coordinate systems are illustrated in Fig. 3.1.

3.3 Cherenkov analysis

In E154, each of the four Cherenkov counters was equipped with a Flash ADC (FADC) to digitize the phototube pulses. The four channels of the FADC, running

---

[1] The "off-site" analysis based at Caltech was a collaborative effort of physicists from Caltech, UMass, Princeton, Syracuse University, and Temple University.

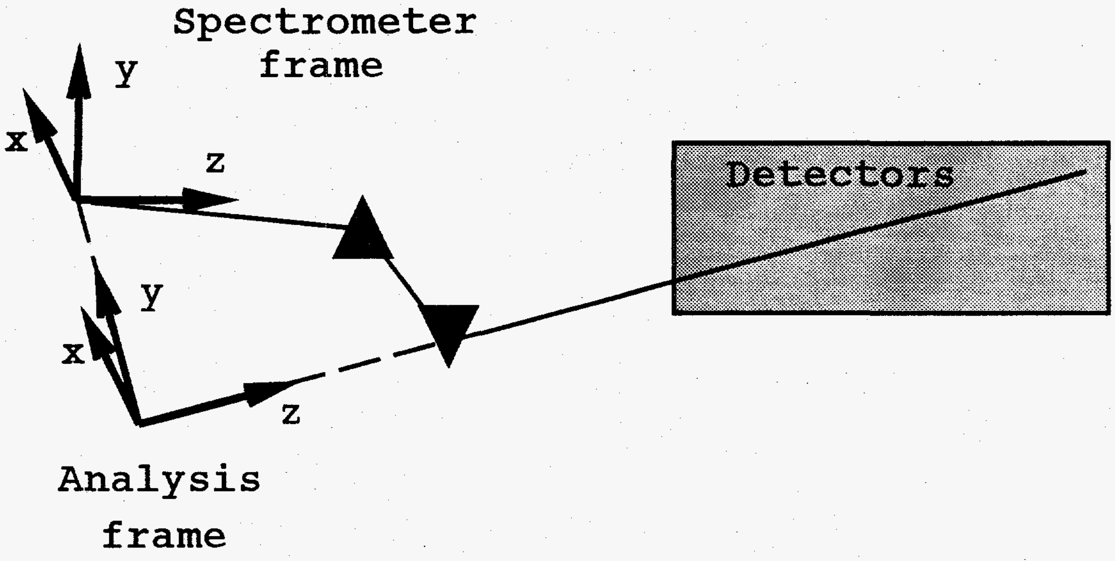

Fig. 3.1. The "spectrometer" and "analysis" coordinate systems. The prisms denote the dipole magnets.

with internal clock frequency of 250 MHz, were interleaved to produce effective time bins of 1 nsec. An example of the waveform recorded by a Flash ADC is shown in Fig. 3.2. The primary purpose of the Cherenkov code was to single out separate phototube pulses and determine their time and amplitude (or total charge) which is proportional to the total number of photoelectrons emitted from the cathode of the phototube.

A brief outline of the algorithm follows. First, we calculate the time derivative of the waveform and find all local maxima. Then, we determine the flat background for the waveform in the regions sufficiently far from all pulses and subtract it from the waveform. For each pulse found, we determine the pulse height (later to be related to the number of photoelectrons) and integrate the pulse to find the total charge. Corrections are made, if necessary, to account for saturated pulses (pulses higher than FADC range of 255 bits (about 2 V) are truncated to 255 bits), truncated pulses (that are late in the spill so the full charge is not recorded), and overlaps. The time

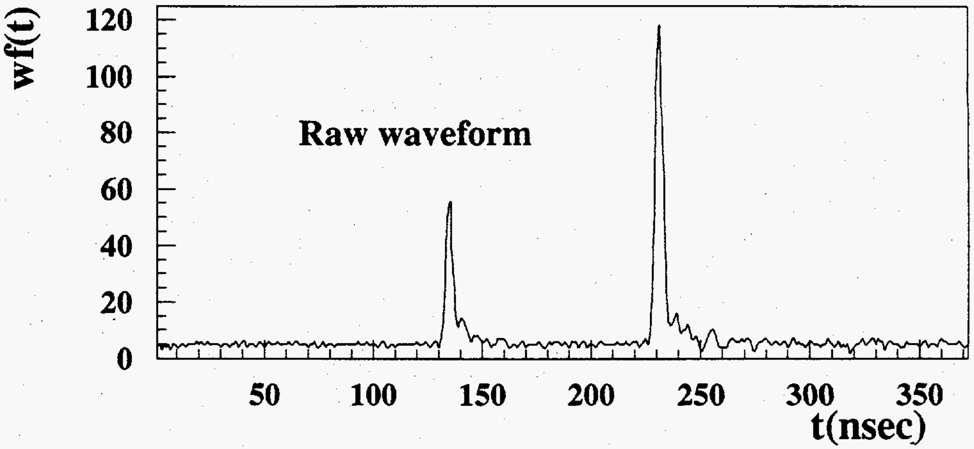

Fig. 3.2. A typical event (spill) in the Cherenkov detector recorded by a Flash ADC.

of the pulse is determined by the time at the half height. The average signal shape, scaled by the height of the processed pulse, is used to separate overlapping pulses.

The time resolution of the Cherenkov FADCs was found to be ≈ 1.3 ns (see Fig. 3.3, left). This is quite below par for the Hamamatsu R1584-01 phototubes, and is explained by the time jitter of the FADC clock. The clocks of each FADC, running at 250 MHz, were not synchronized. This produced a random jitter of 4 nsec and contributed $\approx 4/\sqrt{12} = 1.2$ nsec[2] to the time resolution. The solution,[113] implemented in the Caltech analysis[3], was to use TDCs clocked at 1 GHz to synchronize the FADCs. The resolution improved to ≈ 0.8 nsec (Fig. 3.3, right), reducing the accidental background in tracking and thus helping to reduce the pion contamination.

The algorithm was found to be reasonably robust with an intrinsic dead time of less than 5 nsec. A typical response of a Cherenkov counter to electrons and pions is shown in Fig. 3.4. The response to electrons (the average number of photoelectrons)

---

[2] We here loosely use the RMS of the uniform distribution that is given by $4/\sqrt{12}$ for a fixed width of 4.

[3] The problem was solved too late to be implemented in the SLAC DST production.

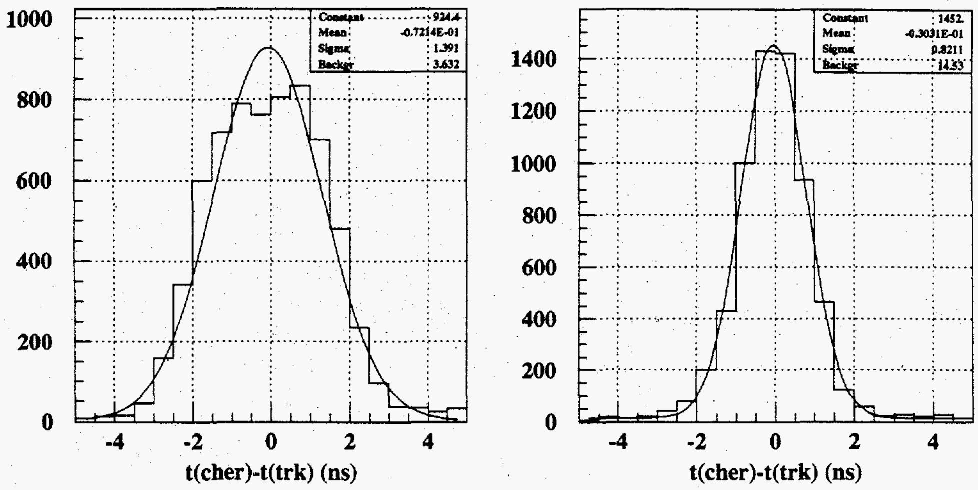

Fig. 3.3. Time resolution for a FADC alone (left), and for a FADC with TDC synchronization (right).

Table 3.1. Average Cherenkov response to electrons.

Tank	2C1	2C2	5C1	5C2
# of photoelectrons	5.7	5.1	6.2	5.0
C_{v2pe}	16.8	14.1	12.1	13.6

of all counters is summarized in Table 3.1.[114] The relation between the Cherenkov peak voltage and number of photoelectrons is given by

$$V_{\mathrm{peak}} = C_{\mathrm{v2pe}}(\mathrm{tank})PE \ , \tag{3.2}$$

where coefficients C_{v2pe} are also given in Table 3.1.

The Cherenkov efficiency for electrons was found to be $\approx$ 95%[115] and was limited by the intrinsic pulse height cutoff of the algorithm (4–6 FADC units) and Cherenkov dead time. Efficiency for a typical Cherenkov cut used in the analysis (see Section 3.7.3.2) is about 90%.

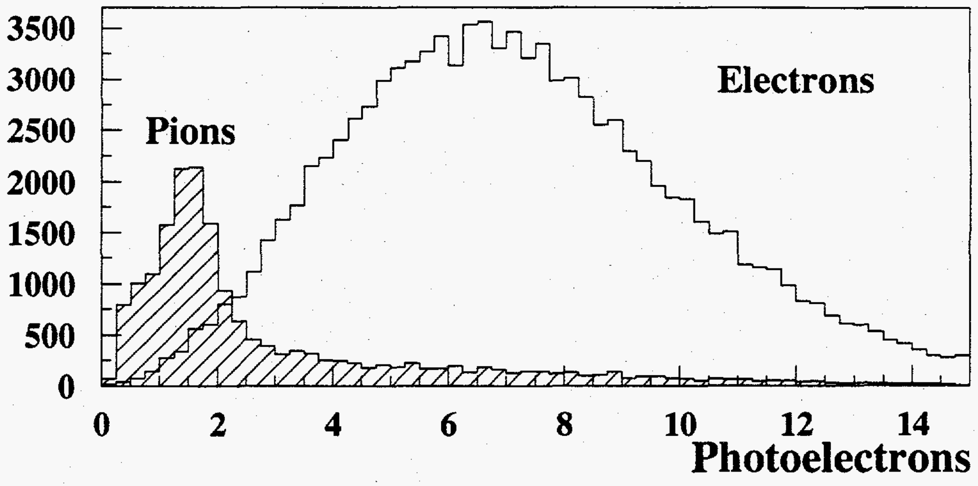

Fig. 3.4. Typical Cherenkov response to electrons (open) and pions (hatched).

3.4 Shower analysis

3.4.1 Introduction

The shower code is one of the major parts of the raw analysis that was different from the one used in the SLAC DST production. The shower counters provide electron identification via energy, E/p, and shower profile (shape, neural net) cuts. The cluster information is the basis for the tracking algorithm (see Section 3.5); in addition, the shower position resolution directly affects momentum and angular resolution. The shower analysis meets certain challenges in the high rate environment of E154 due to the overlaps of the electron and pion clusters (Fig. 3.5). Such overlaps create rate-dependent biases in energy and position reconstruction and calorimeter-based electron identification, and thus have a potential to alter experimental asymmetries. It is important to have an analysis algorithm that is robust in the high rate environment; it is also necessary to study and correct for any possible rate dependence.

The code benefited greatly from the experience with the existing SLAC code.[116] At the same time, it was an entirely new code, and therefore provided an important

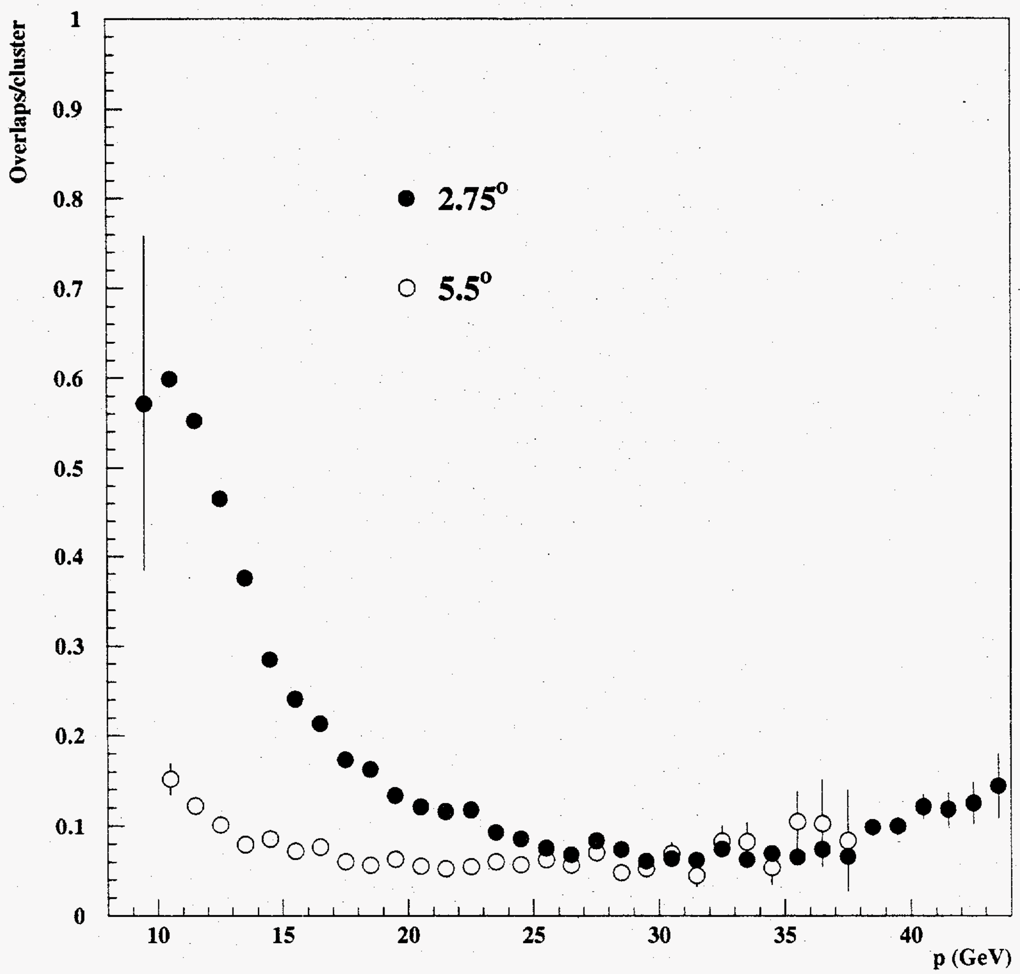

Fig. 3.5. Number of overlaps per electron cluster versus momentum of the electron in 2.75° (closed circles) and 5.5° (open circles) spectrometers for the typical running conditions (run 3366, beam current of $5 \cdot 10^{10}$ electrons/spill). A sharp rise at low momenta corresponds to increasing pion production rate.

cross-check of the existing algorithm. In addition, the spatial and timing resolutions were improved, and biases in the cluster position and energy reconstruction were eliminated. Also, as an alternative to the neural network used in the SLAC analysis, a particle identification (ID) method based on the information about the lateral shower profile was developed (the "shape cut"). The clustering algorithm and the shape analysis will be discussed in the following pages.

In this Section, we follow the definitions adopted in the SLAC shower code.[116,117] An elementary *cell* is a signal induced by one particle in one block. Each cell is characterized by its *time* and *energy*. We record times of both leading (LE) and trailing edges (TE) of the photomultiplier pulses. Cell time is determined by its LE time. Cell energy is determined by the difference between TE and LE times as will be discussed below. Energies of all cells in one block always add up to the total energy deposited in that block in one spill. If a block does not have any TDC hits within one spill, we create one cell which carries full energy deposited in the block; the time of such a cell is undefined. A cell with a definite time is required to have a LE, but it does not always have a TE (misses of TE happen less than 1% of the time). A *cluster* is a collection of cells with common time that are grouped according to the set of rules to be discussed below.

3.4.2 Clustering algorithm

3.4.2.1 5 × 5 clusters

Contrary to the standard SLAC analysis which employs the *cellular automaton*[118] technique, we have chosen a simpler and faster method sometimes referred to as "vector approach".[118] As a first step, after the data from the TDCs and ADCs are copied into the local common blocks, we search the 10 × 20 shower array for the local energy maxima ("central blocks") that pass the following criteria:

1. There is at least 1 TDC hit in the central block;

2. The sum over 9 blocks around the central block

$$\sum_{3\times3} E_i > E_{cut} = C_{\mathrm{cut}} p_{\mathrm{min}}(\mathrm{row}).$$

The first requirement ensures that the cluster candidate has timing information. Electron energy deposition in the central block is always higher than the TDC threshold; the lack of a timing hit signals either a DAQ failure or an event affected by an overlap. Such clusters cannot be used in the further analysis. The second requirement provides a simple and effective pion rejection at the very early stage of the analysis. The value $p_{\mathrm{min}}(\mathrm{row})$ is determined by the lowest momentum of electrons that hit the particular block after passing through the spectrometer. This value is in principle different for every row (and is increasing from top to bottom of the calorimeter). In practice the value of 9 GeV was used for every block. The constant C_{cut} was chosen to be 0.7, safely below any reasonable E/p cut value[4]. Thus, most pions that deposit energy of less than 6.3 GeV are cut before the main clustering and tracking started, significantly reducing the precessing time.

Having found the central block, we share its energy among its cells. The cluster is started with the highest energy cell of the central block. We add to the cluster cells from the surrounding 5×5 matrix that

- among 8 blocks closest to the center and
    1. Are in time with the central block, or
    2. Have no TDC hits
- among the outer 16 blocks and
    1. Are in time with the central block, or
    2. Have no TDC hits and no other cluster nearby

---

[4] For the dedicated pion DST production, this value was lowered to 0.05.

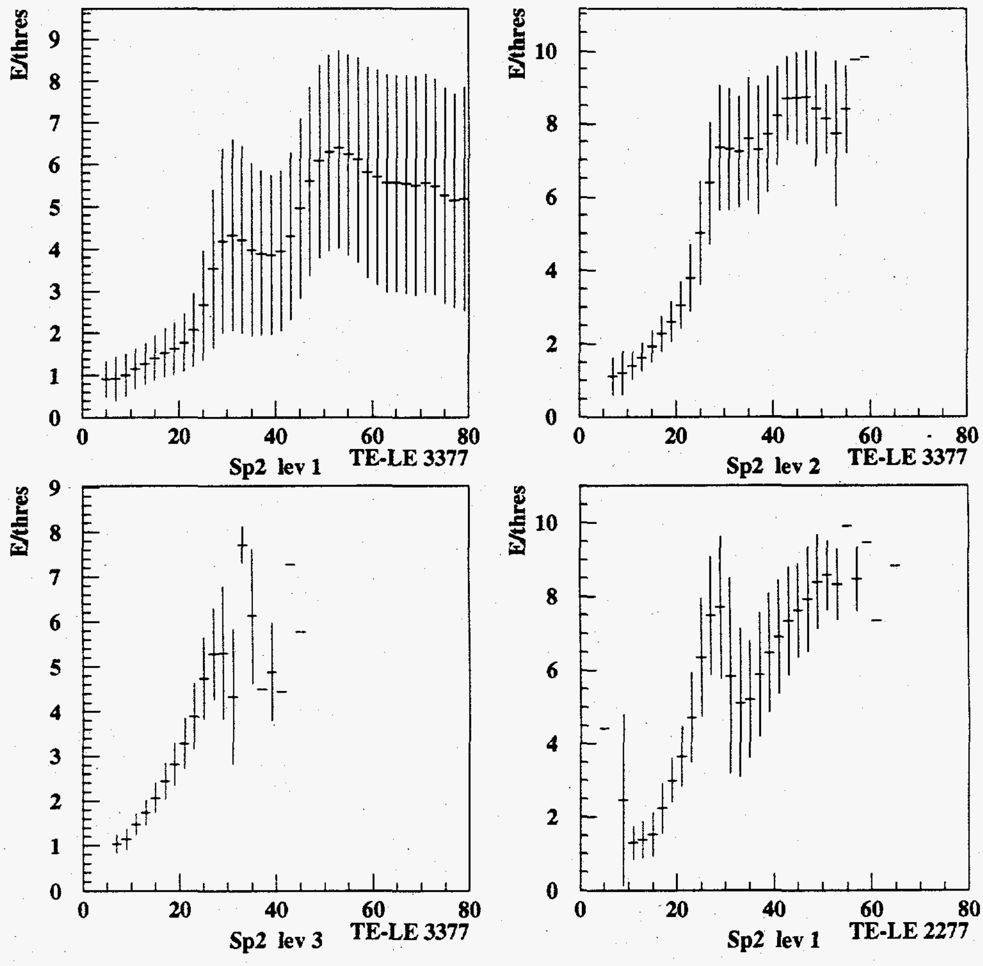

Fig. 3.6. The pulse height as a function of the difference between the leading and trailing edge times for different discriminator levels. The error bars represent the RMS of the distribution.

The time window is set to be $|\Delta t| \leq 5$ nsec.

3.4.2.2 Energy sharing

When two or more particles hit one block, energies are added in the ADC. To separate them, we use the correlation between the pulse height and the time difference between the leading (LE) and trailing edges (TE) of the pulse (Fig. 3.6). For all pairs of leading and trailing edges (*cells*), we calculate the expected energy

$e_i = f(t_i^{TE} - t_i^{LE})$ and error σ_i. We then minimize

$$\chi^2 = \sum_i \left(\frac{E_i - e_i}{\sigma_i}\right)^2 \tag{3.3}$$

with a constraint

$$\sum_i E_i = E_{tot} , \tag{3.4}$$

where E_{tot} is the full energy deposit in the block, and solve for cell energies E_i. The benefit of such an approach is obvious. For any TDC level, the dynamical range for the energy sharing is limited; from Fig. 3.6 one can see that the meaningful information can only be extracted if the ratio of the pulse height to threshold $E/E_{thres} \leq 4$. Electron pulses are often much higher than that, especially for the low thresholds [5]. Pion pulses, on the contrary, are predominantly small. Thus, combining the pion and electron information reduces the error in electron energy determination. This is important to minimize the rate dependence associated with the E/p cut.

3.4.2.3 Cluster time and position

An energy-weighted average used by SLAC analysis

$$x = \frac{\sum_{blocks} x_i E_i}{\sum_{blocks} E_i} \tag{3.5}$$

is known[119] to give a biased estimate of the cluster position due to the relatively coarse transverse segmentation of the calorimeter. It results in a bias towards the coordinate of the central block, as could be clearly seen in Fig. 3.7 which shows the difference between the cluster position and the position of an associated track for the SLAC code. The position offset is as large as 1 cm, and maximizes when electrons hit the boundary of the block ($x_{\mathrm{tr}} - x_{\mathrm{sh}} = \pm 32$ mm). Alternatively, we

---

[5] The values of the discriminator thresholds are summarized in Table 3.2. Note the thresholds were set in mV, and the spread of thresholds in GeV corresponds to the spread of calibration constants.

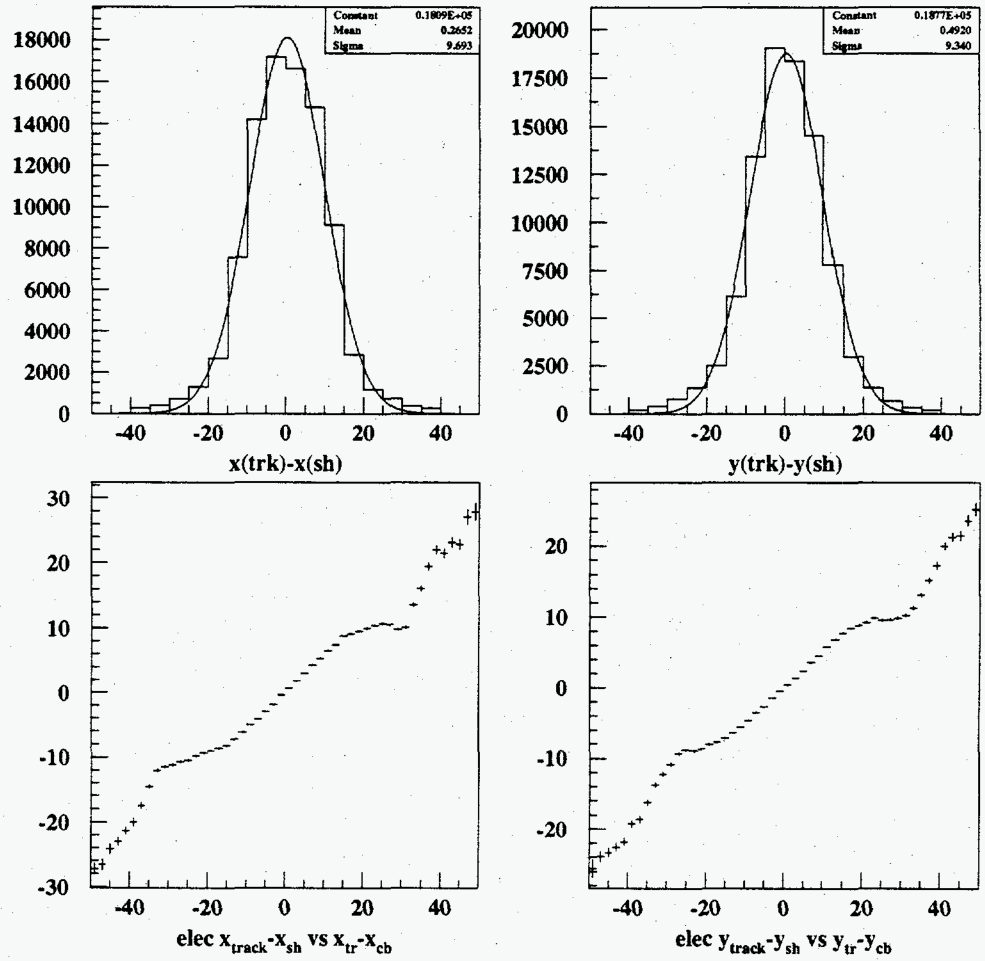

Fig. 3.7. Performance of the SLAC shower code. (top) Shower position resolution. (bottom) Cluster spatial offset versus the position of the track relative to the center of the central block. All numbers are in mm.

Table 3.2. Range of discriminator thresholds.

Runs	Spec	mV	GeV		
			min	max	average
1304–2058	2.75°	20	0.08	0.6	0.3
		125	0.4	2.8	1.6
		800	2.7	20.0	9.9
		50	0.16	1.2	0.3
2059–2543	2.75°	20	0.08	0.4	0.2
	2.75°	125	0.4	1.9	1.12
	2.75°	800	2.7	15.4	6.7
	2.75°	50	0.15	1.16	0.4
2544–2902	2.75°	20	0.09	0.23	0.15
	2.75°	125	0.5	1.4	0.8
	2.75°	800	2.8	8.0	4.7
	2.75°	50	0.16	1.2	0.5
2902–3788	2.75°	20	0.09	0.23	0.15
	2.75°	125	0.5	1.4	0.8
	2.75°	500	1.8	5.5	3.1
	2.75°	50	0.16	1.2	0.5
1304–3788	5.5°	50	0.0	0.8	0.4

Table 3.3. Parameters of Eq. (3.6).

A_x	b_x	c_x	d_x
17.1	0.031	3.	31.

calculate the cluster position using a phenomenological fit to the data (see Fig. 3.8)

$$x = A_x\left[2 - \exp(-c_x(r - b_x)) - \exp(-d_x(r - b_x))\right] \tag{3.6}$$

where $r = E_{side}/E_{c.b.}$ is the ratio of the energies in the side and central blocks. Coordinates determined by the blocks on either side of the central block are weighted by the uncertainties to calculate the cluster position. The parameters of the "double-spinup" function in Eq. (3.6), determined from the data (Fig. 3.8), are listed in Table 3.3. The spatial resolution of the 2.75° and 5.5° shower counters is shown in Fig. 3.9. The resolution in x was determined to be 5.9 mm (2.75°) and 7.9 mm

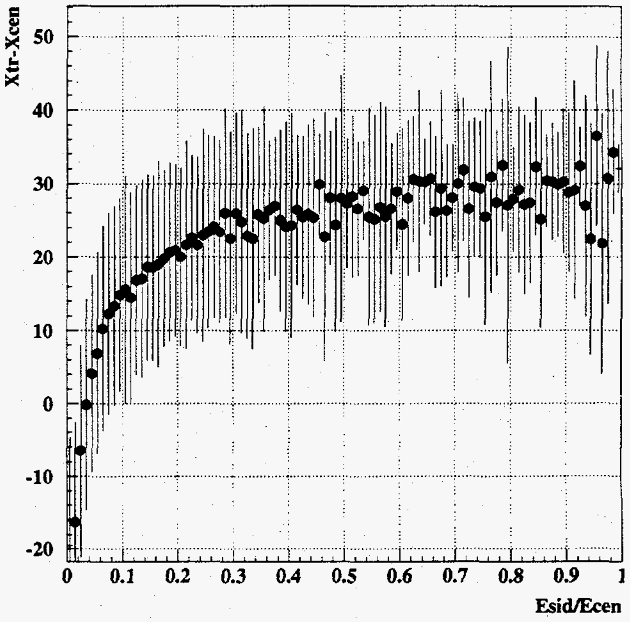

Fig. 3.8. Cluster position versus the ratio of energies in the side and central blocks. Error bars represent the RMS of the distribution.

(5.5°), and in y direction the resolution is 7.5 mm (2.75°) and 7.9 mm (5.5°). This is to be compared to $\sigma_x = 9.7$ mm and $\sigma_y = 9.3$ mm for the SLAC code (see Fig. 3.7, top). The improvement in the position resolution results in a better angular and momentum resolution (see Section 3.5). Note that the resolution was determined by comparing the coordinate of the shower cluster with the coordinate of the electron track at the z position of the shower counter. The tracking spatial resolution without cluster constraints (*i.e.* for class 3 tracks used to determine the resolution) is expected to be $4-5$ mm at the shower counter, so the actual position resolution of the clustering might be even better than the numbers quoted above. The wings of the distribution are due to effects of accidental and correlated (delta rays) backgrounds in tracking. Figure 3.10 shows the distribution of the electron clusters in the calorimeter and the difference between the track position and the cluster position plotted versus the position of the track. Notice that there are no significant biases in either x or y direction (*cf.* Fig. 3.7, bottom).

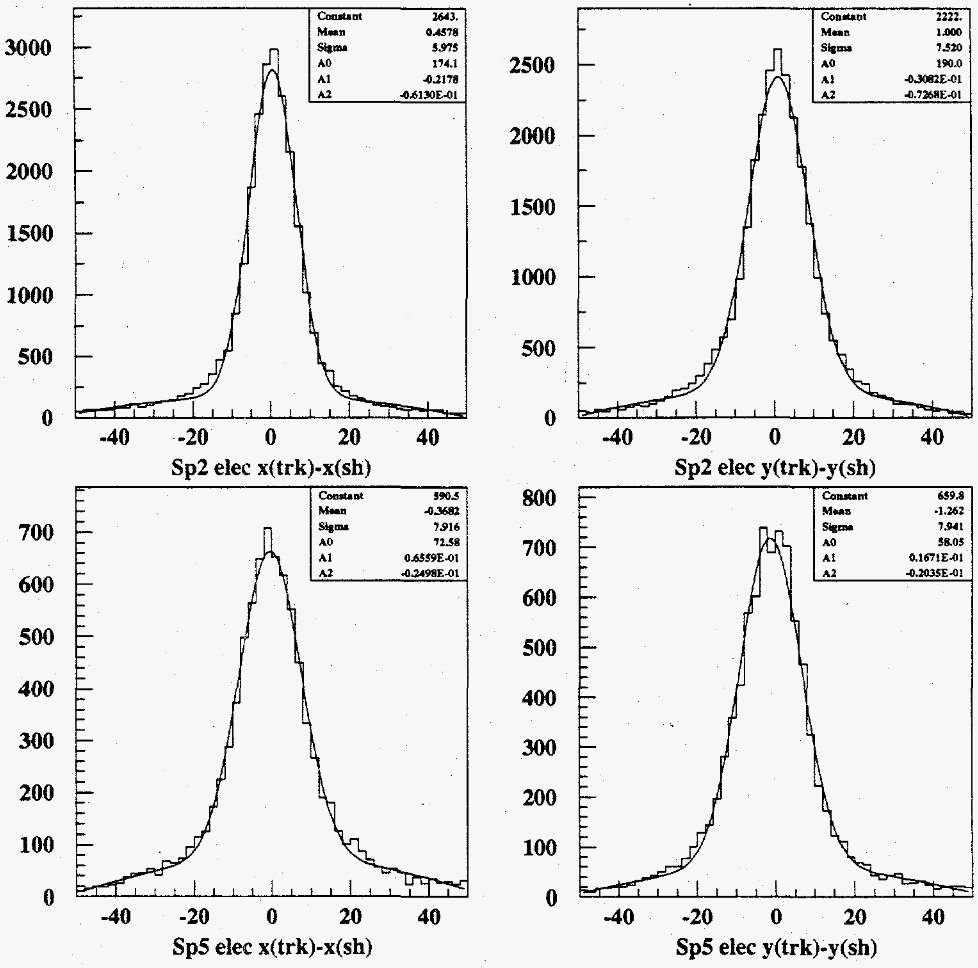

Fig. 3.9. The position resolution for electrons in 2.75° (top) and 5.5° (bottom) calorimeters. The fit is Gaussian with quadratic background. All numbers are in mm.

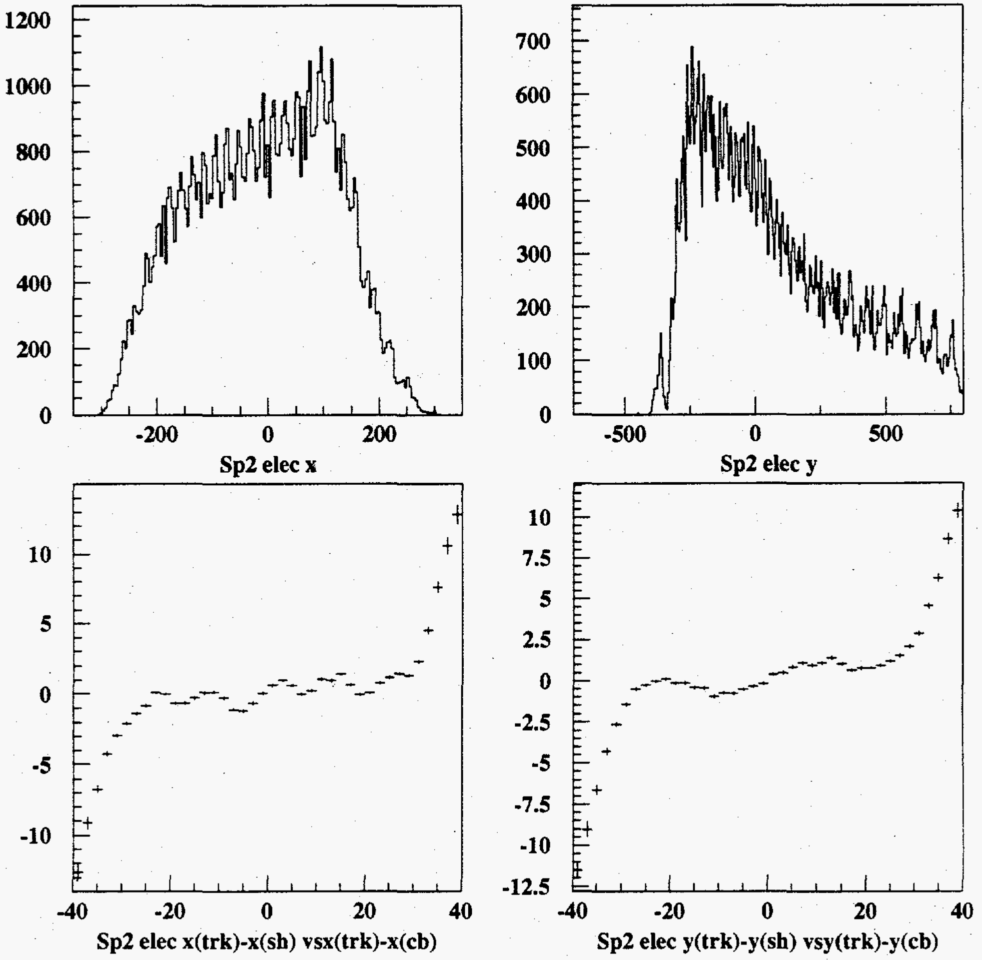

Fig. 3.10. (top) Cluster position distribution in the 2.75° shower counter for Caltech analysis. (bottom) The cluster spatial offset versus the position of the track relative to the center of the central block. The error bars are statistical.

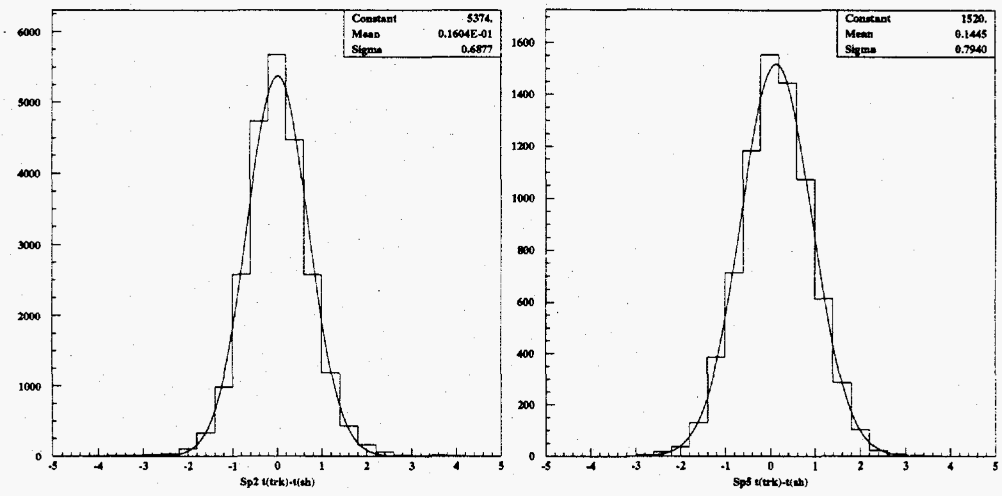

Fig. 3.11. Time resolution (in ns) for electrons in 2.75° (left) and 5.5° (right) calorimeters. The fit is gaussian.

The time of the cluster was determined by averaging TDC times of all blocks for which the energy deposited was at least 10% of the central block energy:

$$t = \frac{\sum_i t_i/\sigma^2(t_i)}{\sum_i 1/\sigma^2(t_i)}\,, \tag{3.7}$$

where $\sigma(t_i)$ is the time uncertainty for each block. The energy cut minimized the effect of timing jitter for the small pulses. Another potential problem with using blocks with small energy deposit is that they are usually on the tails of the shower and the effective z position of the particles in the shower tail is significantly deeper than the core of the shower. The light from the shower tails reaches the phototube earlier than the light from the core (since the shower develops with the speed of light in the vacuum c whereas the light propagation speed is c/n with the index of refraction $n = 1.62$. The energy cut minimizes this effect so no correction is necessary.

The time resolution of both calorimeters is shown in Fig. 3.11. With the technique described above we achieved the resolution of $\approx$ 0.7 nsec (for electrons), compared to $\approx$ 0.9 nsec for the SLAC code.

3.4.2.4 *Shower shape*

The differences in the transverse profiles of the showers produced by electrons and pions (to which we will loosely refer as electron or pion "shapes") are frequently used to separate the particles in the electromagnetic calorimeter. While the electrons develop electromagnetic showers, the pions undergo the strong interactions that lead to the hadronic showers, wider and less symmetric than electromagnetic ones. Charged pions may also convert to the neutral pions via the charge exchange $\pi^- p \rightarrow \pi^0 n$, where the π^0 decays instantly into two photons. In that case the shower is electromagnetic and its profile is almost indistinguishable from the electron shower. However, even in this case (and in case of the hadronic showers), pions rarely deposit their full energy in the electromagnetic form, and a simple E/p cut can be used to separate them from electrons.

The standard measure of the electromagnetic shower cross section is the scaling variable referred to as the Moliére radius R_m[119]; for ASP(F2) lead glass used in our calorimeters $R_m \approx 5$ cm. For electromagnetic showers, 90% and 95% of the shower energy are contained in the cylinders with radii R_m and $2R_m$ respectively. A simple approximation of the lateral shower profile is a single-exponential form[119]

$$A(R) = A(0)\exp(-R/R_0)\ , \tag{3.8}$$

where R is the transverse shower dimension and $R_0 = 0.25R_m$ is the damping constant. A more realistic model is a double-exponential shape[120]

$$A(R) = A_1\exp(-R/R_1) + A_2\exp(-R/R_2)\ , \tag{3.9}$$

where the first exponent describes the narrow shower core, and the second corresponds to a longer tail of soft electrons and photons. For a finite calorimeter block of size $2s$, one can calculate the energy deposited from the shower centered at (x_0, y_0):

$$E = E_0 \int_{-s}^{s}\int_{-s}^{s} dxdy\, a\left(\sqrt{(x-x_0)^2 + (y-y_0)^2}\right)\ , \tag{3.10}$$

Table 3.4. Parameters of the shower shape in Eq. (3.11).

s (mm)	h	r	R_1 (mm)	R_2 (mm)	p
34.0	0.872	0.3	4.0	19.0	2.9

where $a(R)$ is a normalized shower profile of Equations (3.8) or (3.9) and E_0 is the total cluster energy. The resulting distribution is fitted to the following functional form:

$$\frac{E}{E_0} = \mathcal{S}(x - x_0, y - y_0) = \begin{cases} h\,\{\,[1 - \exp(-s/R_1)\cosh(d/R_1)]+ & \\ \quad r[1 - \exp(-s/R_2)\cosh(d/R_2)]\,\} & |d| \le s \\ h\,\{\,\sinh(s/R_1)\exp(-d/R_1)+ & \\ \quad r\sinh(s/R_2)\exp(-d/R_2)\,\} & |d| > s\,, \end{cases} \tag{3.11}$$

where

$$d = (|x - x_0|^p + |y - y_0|^p)^{1/p}\ , \tag{3.12}$$

(x, y) is the center of a given block, and (x_0, y_0) is the shower position. The electron shower profile is shown in Fig. 3.12. The parameters of Eq. (3.11) are given in Table 3.4. The pion hadronic showers are wider on average (Fig. 3.12), and the individual pion clusters are much less symmetric than the electron ones.

3.4.2.5 Iterating the cluster shape

The energy sharing using the LE and TE information is not always perfect. First of all, it has a limited dynamic range. Pions with energy deposit below threshold are not detected by TDCs. Secondly, if electron energy deposit in one block is much bigger than the threshold, the time information is not reliable and leads to large errors in energy sharing. The latter effect is potentially more important: if the energy of the cluster is underestimated due to energy sharing, the event may not pass the E/p cut (typically, $E/p > 0.8$ cut is a part of electron definition). Another important factor is the cluster position bias due to overlaps that translates into the error in

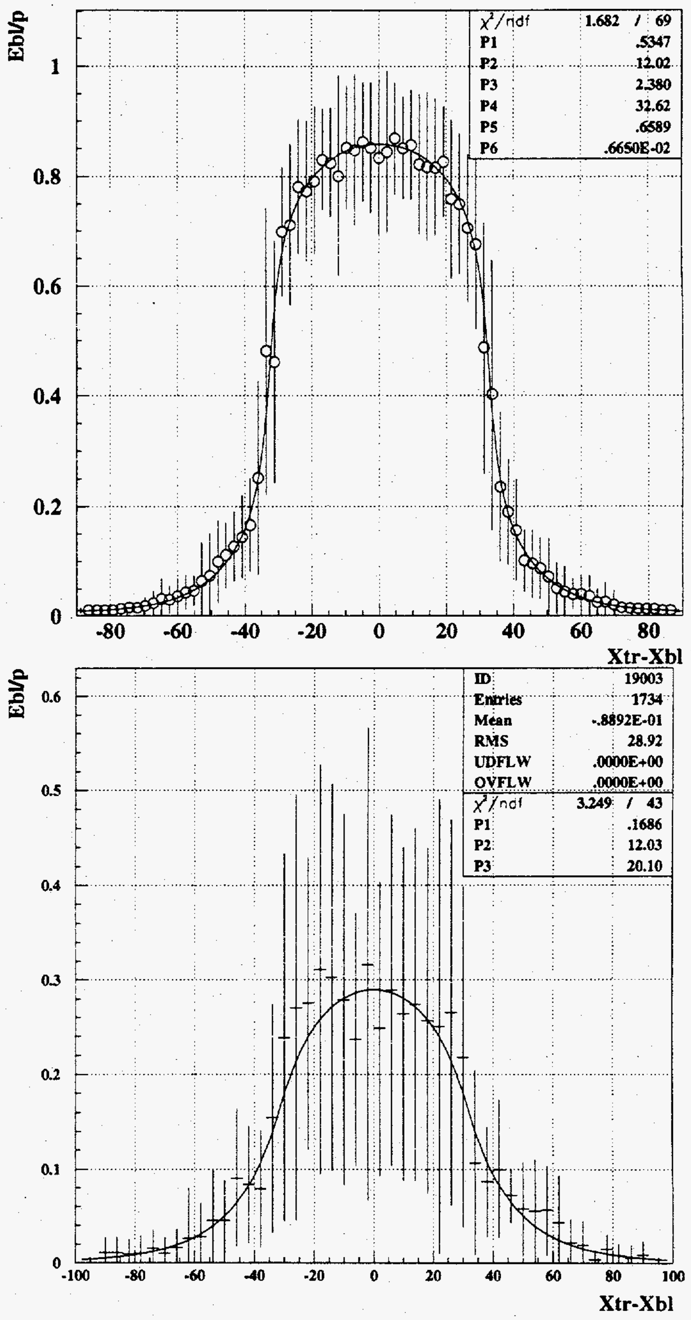

Fig. 3.12. Average shapes of the showers for electrons (top) and pions (bottom). Error bars represent the spread of the distributions.

momentum reconstruction. All these effects are rate-dependent and thus can bias the measured asymmetry.

In order to further reduce the rate-dependent effects in the cluster energy and position reconstruction, we developed an iterative procedure using the typical electron shape of Eq. (3.11)[6]. It works in two steps. First, we calculate the cluster position (x_0, y_0) using Eq. (3.6) and the initial estimate of the cluster energy

$$E^{(0)} = \frac{E_c}{\mathcal{S}(x_c - x_0, y_c - y_0)} , \tag{3.13}$$

where E_c and (x_c, y_c) are the energy and position of the central cell. We then calculate

$$\chi^2 = \sum_i \left(\frac{E_i^{(0)} - E^{(0)} \mathcal{S}(x_i - x_0, y_i - y_0) - E_{\text{back}}}{\sigma_i} \right)^2 \tag{3.14}$$

where the sum is over all cell in the cluster. Here $E_i^{(0)}$ is the initial energy of each cell determined as described in Section 3.4.2.2. $E_{\text{back}} = 50$ MeV is the average background noise, and σ_i is the uncertainty of the block energy given by

$$\sigma_i^2 = a^2 + \left(bE_i + c\sqrt{E_i} \right)^2 + \sigma_{\text{share}}^2 , \tag{3.15}$$

where σ_{share} is the uncertainty in energy sharing. A fit to the data yields $a = 0.15$ GeV, $b = 0$, and $c = 0.2$.

Minimizing χ^2, we find a new estimate of energy $E = E^{(1)}$ and position $(x_0, y_0)^{(1)}$ (we linearize the problem by treating $\Delta x = x_0^{(1)} - x_0^{(0)}$ as a perturbation). The energies of each cell E_i are allowed to vary within their uncertainties. The cell is "frozen" (*i.e.* its energy is fixed) if change in its energy exceeds the uncertainty. The χ^2 minimization is repeated with new cell energies $E_i^{(1)}$. The iterations converge if one of the following conditions is met:

- Cluster position does not change

---

[6] It is not used for special pion DST production.

- All cells are frozen
- Number of iterations exceeds 10

The convergence is typically achieved in 1–2 iterations. Cluster position $(x_0^{(n)}, y_0^{(n)})$ and its uncertainty are copied to the output common block and used in tracking.

After a track has been associated with the cluster, the electron coordinates at the shower counter are determined quite accurately. We can now fix the cluster position (x_0, y_0) in Eq. (3.14) to be the track position at the shower counter, and minimize shape residuals varying only the cluster energy E.

3.4.2.6 Energy measurement

Three energy variables and corresponding uncertainties are reported by the shower code and are written to DSTs:

- $\mathbf{E_9}$: Sum of cells in 3 × 3 matrix around the central block.
- $\mathbf{E_4}$: Sum of four most energetic blocks in the cluster (the central block, the most energetic blocks in x and y directions, and 1 diagonal block). The sum is scaled by a factor of 1.05 to normalize it to E_9.
- $\mathbf{E_1}$: energy determined in iterative process (after tracking).

The ratios E_1/E_9 and E_4/E_9 and their momentum dependence are shown in Fig. 3.13. E_9 is a basic energy definition and is used for shower calibration. The advantage of E_4 and E_1 over E_9 is reduced sensitivity to overlaps. E_4 samples a smaller number of blocks than E_9 and therefore the pileup probability for E_4 is lower. The drawback is that E_4 is an approximation that is reasonably good up to energies of ≈ 30 GeV. At higher energies, the shower broadens and energy deposit into other blocks of the 3×3 matrix becomes increasingly important. This is evident from Fig. 3.13:

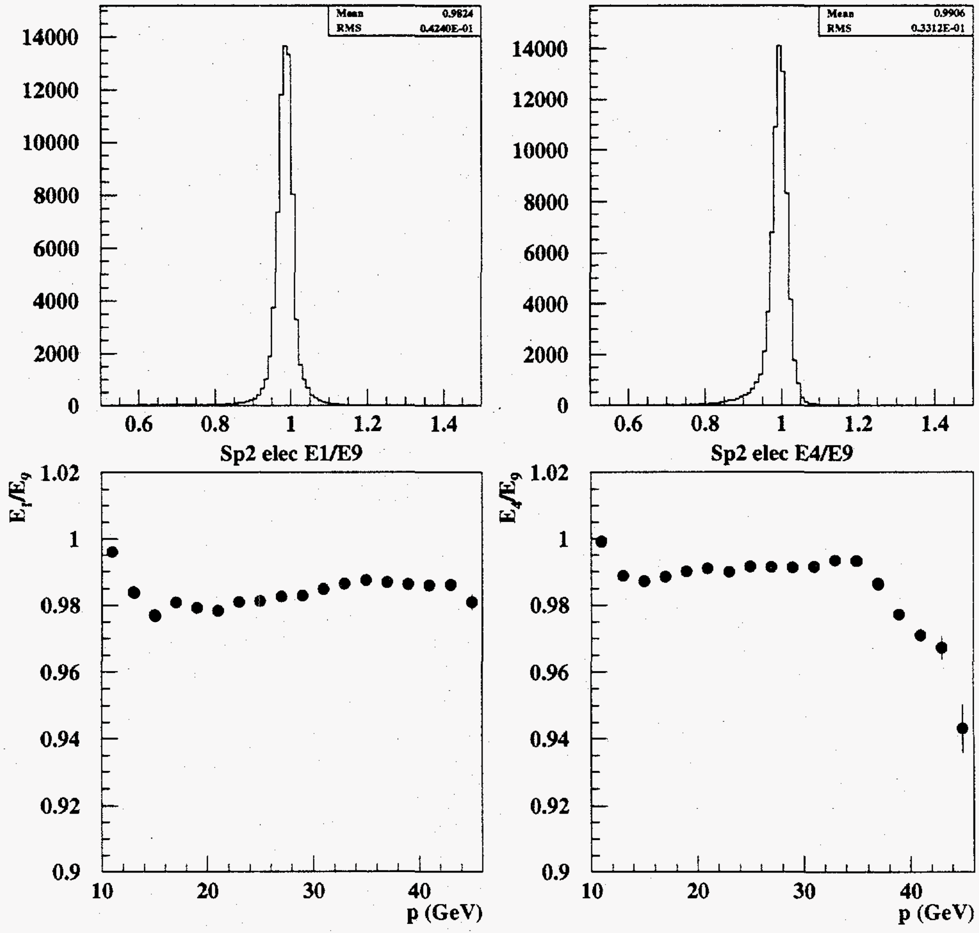

Fig. 3.13. Ratios of energies E_1/E_9 (top, left) and E_4/E_9 (top, right) and their momentum dependence (bottom).

the ratio E_4/E_9 deviates significantly from 1 starting at $p \approx 30$ GeV. The iterated energy E_1 does not exhibit such a behavior (Fig. 3.13).

The shower counter blocks were calibrated using a sample of electrons identified by a high threshold cut in the Cherenkovs. Low rate runs (empty reference cell runs at $\approx 1 \cdot 10^{10}$ electrons/pulse beam current) were used to minimize the rate-dependent effects. The calibration constants were adjusted interatively until the mean of the Gaussian fitted to the distribution of the ratios E_9/p reached unity for every block. This method could not be directly applied to the the blocks on the edges of the calorimeter and blocks with low phototube gain. For the edge blocks, we used the ratio E_4/p which is less sensitive to the leakage of the shower outside the detector. We also used a clean sample of muons and pions that do not produce a shower in the calorimeter. Such particles leave a single Cherenkov track in one shower block, and are seen as a monochromatic line with $E = 0.92 \pm 0.15$ GeV in our calorimeter.

Figure 3.14 shows the ratio E/p for electrons in both spectrometers. Left plots correspond to E_9 energy, and right plots are for E_1 energy. The energy resolution is comparable to that of the SLAC code. In Fig. 3.15 we show the ratio E_1/p in the 2.75° calorimeter for four special cases: clusters with no overlaps (top left), clusters with an overlap in any of the blocks (top right), clusters in overlaps in the central block (bottom left), and clusters with the central block on the edge of the calorimeter. No significant degradation of energy resolution and no significant bias is observed for either case. Fig. 3.16 shows the same plots for the low x (2.75° spectrometer, $9 < p < 12$ GeV). Again, energy determination is reasonably stable.

3.4.3 Shape cut

The difference between pion and electron shapes (Fig. 3.12) can be used to separate electrons from pions using only shower counter information. The SLAC analysis uses the algorithm based on a multi-layered neural network.[118,121] A set of input parameters (discriminating variables), e. g. energy deposited in each cluster

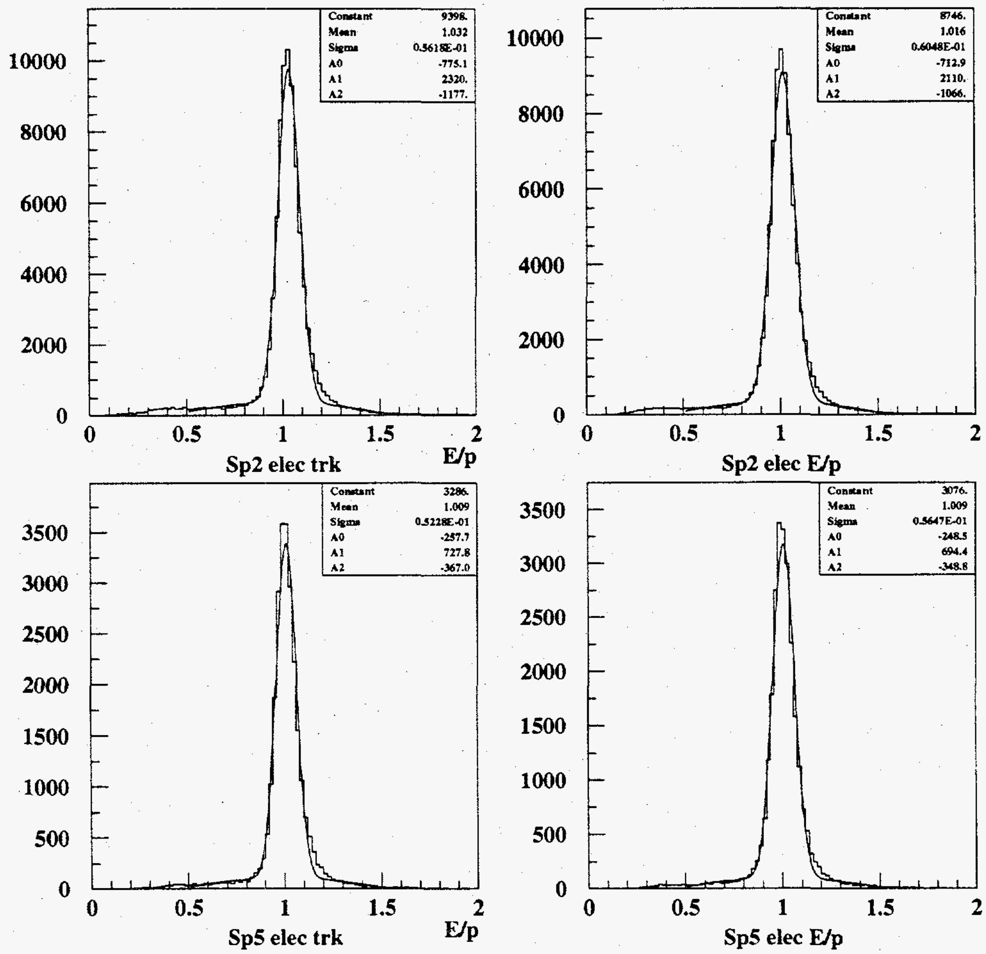

Fig. 3.14. Ratios E_9/p (left) and E_1/p (right) for electrons in 2.75° (top) and 5.5° (bottom) spectrometers. The fit is gaussian with quadratic background.

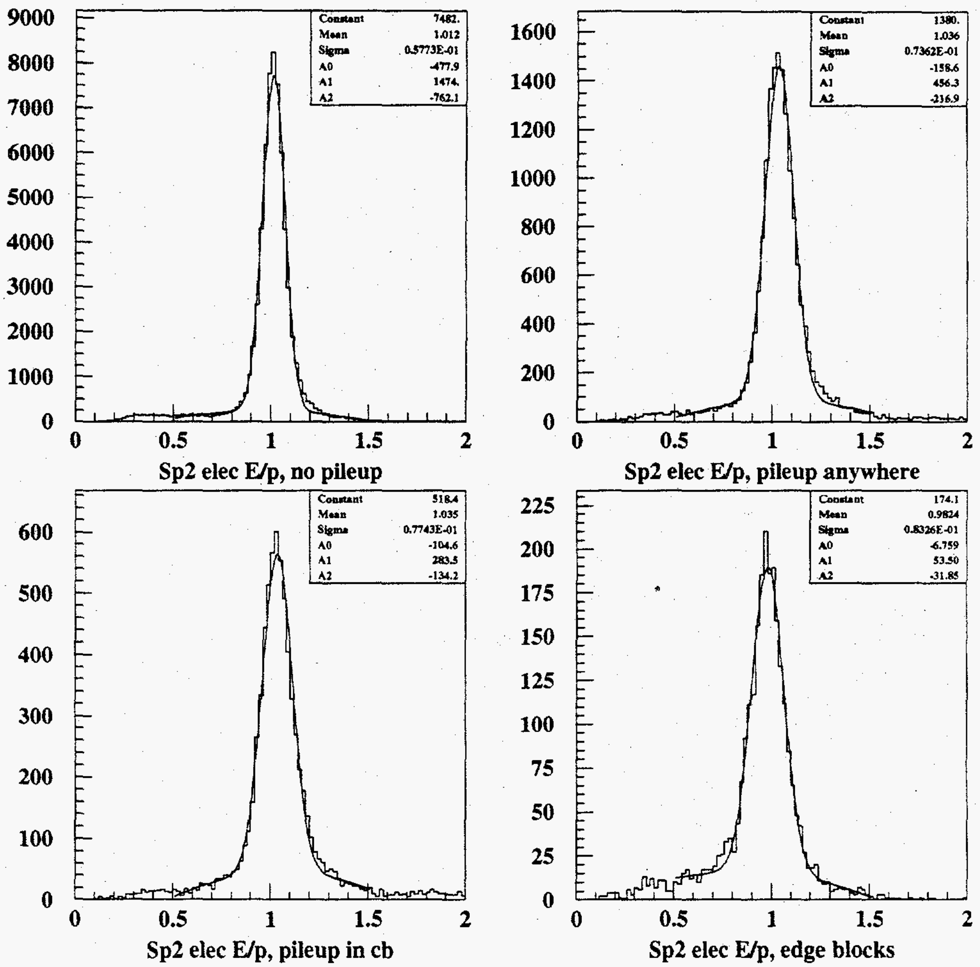

Fig. 3.15. Ratios E_1/p for electron clusters in 2.75° counter with (top left) no overlaps, (top right) overlaps in any of the cluster blocks, (bottom left) overlaps in central block, (bottom right) clusters with the central block on the edge of the calorimeter.

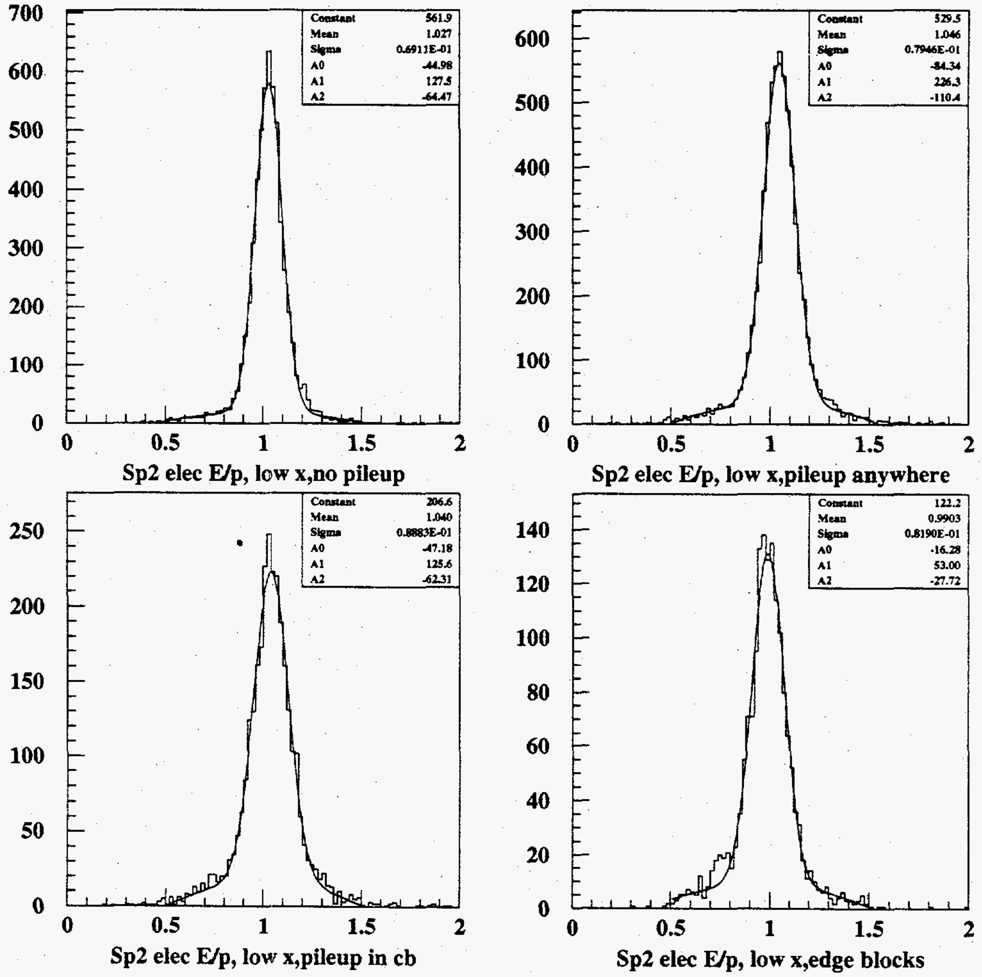

Fig. 3.16. Same as Fig. 3.15 for electrons with $9 < p < 12$ GeV.

block, cluster position, etc., combined in a non-linear fashion, identifies the event. Due to its non-linear nature, the properties of the network highly depend on the environment (rate, pion to electron ratio, etc.) and the event sample on which the network is "trained" (*i.e.* the way the relative weights of the input parameters are determined). Thus, the neural network efficiency is potentially rate dependent,[121,122] especially at low momentum where the rate of pion-electron overlaps is high. The overall efficiency is about 90% at low x,[121] and increases with momentum.

We discriminate between electron and pion showers by calculating the deviation from the electron shower shape χ

$$\chi = \frac{1}{E_4}\sqrt{\sum_i \left(E_i - E_4\mathcal{S}(x_i - x_0, y_i - y_0) - E_{\text{back}}\right)^2} \tag{3.16}$$

where the summation is over all cluster blocks, except for four most energetic ones used in the definition of E_4. The electrons are identified by the requirement $\chi \leq 0.045$. The distribution of the variable χ for electrons and pions is shown in Fig. 3.17. The efficiency was defined as a ratio of events that passed the cut to the total number of events. The electron and pion efficiencies are shown in Fig. 3.18. The electrons were selected by requiring a track with Cherenkov pulses in both tanks higher than 4.5 photoelectrons and a good match with the shower cluster. The pions were defined as class 2 (no Cherenkov signals and a good match with a shower cluster) tracks. Open circles in Fig. 3.18 show the efficiencies for the electron and pion samples that included the additional cut $E/p > 0.8$.

Several observations can be made. First, the pion rejection power of the χ cut is about 10:1. However, for the pions that have $E/p > 0.8$, it is at best 2:1, comparable to the SLAC neural network performance under the same conditions.[121] The reason is that pions usually deposit large amount of energy if they undergo a charge exchange $\pi^- p \rightarrow \pi^0 n$. The π^0 decays instantly into two photons and develops an electromagnetic shower; such a cluster is almost indistinguishable from an electron

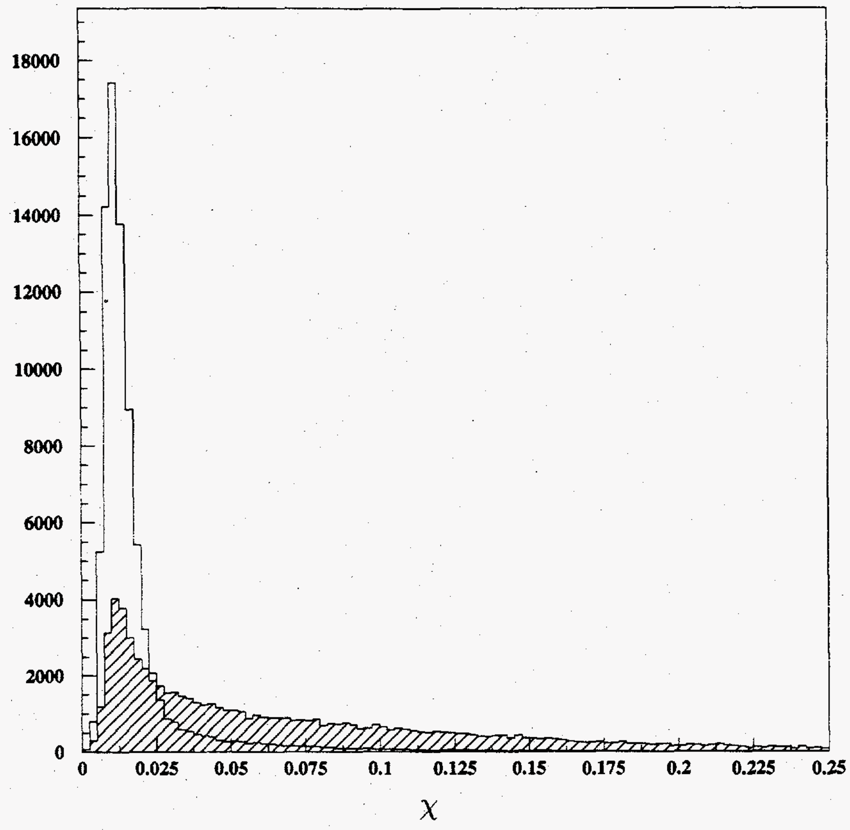

Fig. 3.17. Distribution of the shower shape variable χ for electrons (open) and pions (hatched).

cluster. Since the shape or neural net cut is optional and is usually applied *in addition* to the E/p cut, it is the latter rejection power that is relevant for the background analysis.

Electron efficiency ranges from 92% to 95% at low x (depending on the run), and slowly increases with momentum. It is comparable, if not slightly higher, than the neural network efficiency.[121] The variations with the run conditions are smaller than quoted for the SLAC code[121] that implies smaller rate dependence[7]. The reason for a sharp drop at about 30 GeV is use of the variable E_4 in Eq. (3.16). As was shown above (Fig. 3.13), it deviates significantly from the true cluster energy

---

[7] The rate dependence of the overall shower efficiency, including the shape cut, was studied by Piotr Zyla[123] and was found to be small (see Section 3.6).

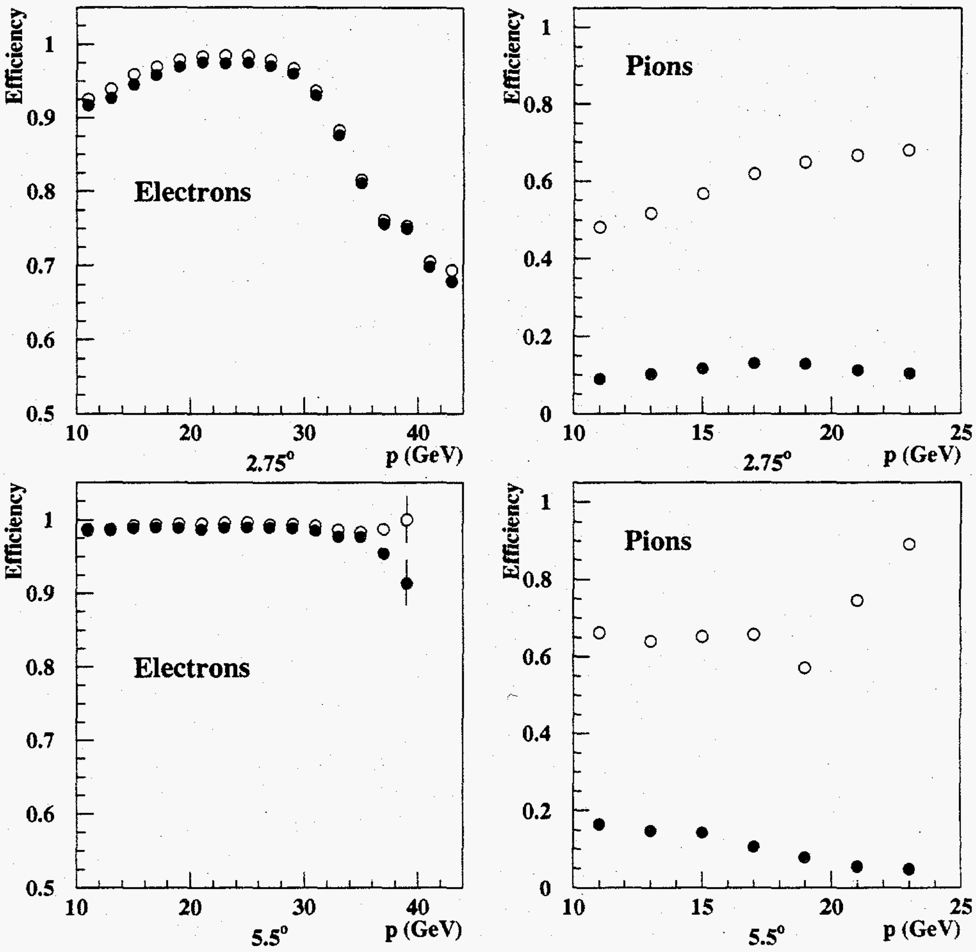

Fig. 3.18. Efficiencies of the shape cut for electrons (left) and pions (right) for 2.75° (top) and 5.5° (bottom) shower counters. A sample of electrons and pions is formed using the tracking and Cherenkov information as described in the text (closed circles). Open circles show efficiencies for the samples that included $E/p > 0.8$ cut.

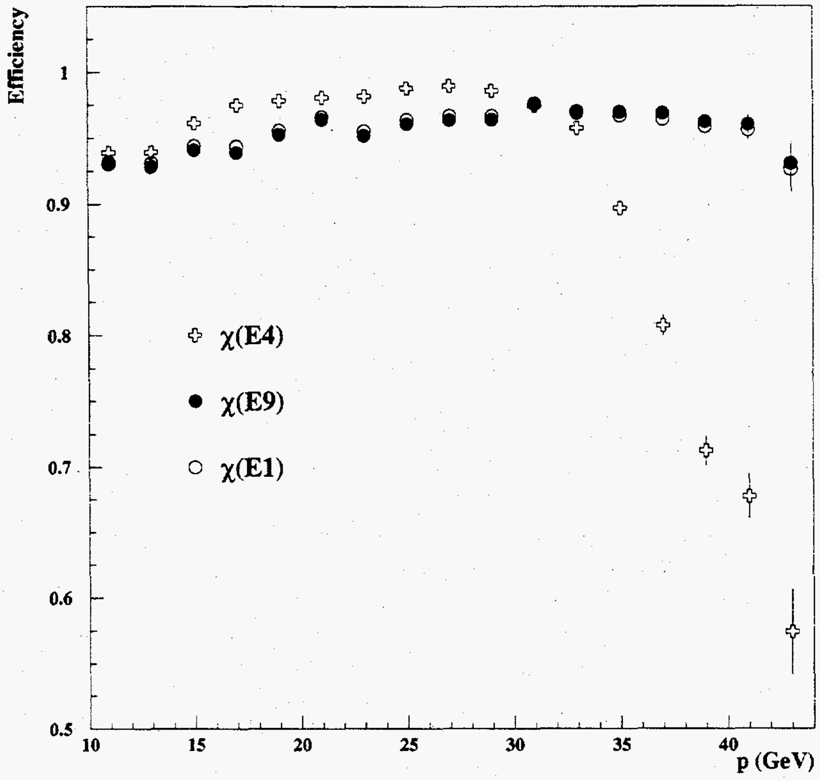

Fig. 3.19. Efficiency of the shape cut with different energy variables. Energy used in Eq. (3.16) is E_4 (crosses), E_1 (open circles), E_9 (closed circles). Note that the drop in efficiency disappears for E_1 and E_9.

starting at about 30 GeV, and the shape function $E_4\mathcal{S}(x_i-x_0, y_i-y_0)$ systematically underestimates true cell energy. The situation is improved, indeed, if other energy variables, E_1 or E_9 are used in Eq. (3.16) (Fig. 3.19). This effect was discovered too late to be applied to the DST production code. Instead, we turn off the shape cut for $p > 30$ GeV where pion contamination is negligible (see Section 3.7.3.2).

3.5 Tracking code

3.5.1 Introduction

The tracking code combines information from the hodoscopes, Cherenkov counters, and the shower counter to reconstruct charged particle tracks in the spectrometer. The standard electron definitions for the asymmetry analysis rely on the tracking information. The momentum of an electron track is used to calculate the kinematics (x and Q^2) of the event. Thus, tracking is an important component of the physics analysis. In this note, we will describe the algorithm and its implementation, and discuss the efficiency and rate dependence.

3.5.2 Tracking algorithm

3.5.2.1 Track classes

In the following, we will often refer to the track *class* , *i.e.* a particular combination of detector systems used to fit a track. We recognize 4 track classes:

1. A shower cluster, at least one Cherenkov hit, and at least a minimum number (see below) of hodoscope hits.
2. A shower cluster and hodoscope hits; no Cherenkov hit is found within the time window.
3. At least one Cherenkov hit and hodoscope hits. No shower cluster is found within time and space limits.
4. Hodoscope hits only.

The track classes are exclusive, *i.e.* one track cannot be a member of two classes. Tracks of class 1 are electron candidates, and class 2 tracks are most probably pions. Tracks of class 3 are used primarily for the calibration of the shower counter (when cluster information is deliberately removed from tracking to eliminate biases), they are never used in the asymmetry analysis[8]. Class 4 tracks are used for diagnostic purposes.

---

[8] Class 3 tracks could be identified as real particles, for example, muons or pions with momentum above the Cherenkov threshold (12 GeV for muons and 19 GeV for pions in 2.75° spectrometer) that deposit a small amount of energy into the calorimeter and are therefore undetected. In the high rate environment of E154, however, most of such tracks are random coincidences.

3.5.2.2 Initialization

The tracking subroutines are called every spill for each spectrometer. As a first step, we copy information from the Cherenkov, hodoscope, and shower counter common blocks into the local data banks. For every detector hit, we calculate the target time

$$\tau_i = t_i - z_i/c \,, \tag{3.17}$$

where z_i is the z position of each detector and t_i is the actual time of the hit. By convention, the z position for the Cherenkov hits is taken in the center of the mirror, the z position of a hodoscope finger is in its geometrical center, and the z position of the shower cluster is associated with the center of gravity of the electron shower which is located approximately 5 radiation length deep.[124]

Each hit is characterized by its time τ, and the time resolution $\sigma(\tau)$. Hodoscope and shower hits also have the coordinate information. For the shower hit, we keep (x, y) positions of the cluster and the position uncertainties (σ_x, σ_y). For the hodoscope hits, we calculate the coordinate

$$u = x\cos\theta_u + y\sin\theta_u \,, \tag{3.18}$$

where $0 \leq \theta_u \leq \pi$ is the angle between the longest side of the finger and the $\hat{y}$ axis (counting counterclockwise)[9]. The direction $\hat{u}$ is perpendicular to the finger direction; thus, u is the coordinate *measured* by the finger. The finger resolution $\sigma(u) = w/\sqrt{12}$, where w is the finger width. The hodoscope planes are grouped in "packages" – the front hodoscope package (H1U, H2V, H3X, H4Y, H5Y, and H6X in the 2.75° spectrometer and H1U, H2X, H3Y, and H4V in the 5.5° spectrometer) and the back hodoscope package (H7X, H8Y, H9Y, and H10X in the 2.75° spectrometer and H5U, H6X, H7Y, H8V in the 5.5° spectrometer).

---

[9] The finger tilt in $(\hat{y}, \hat{z})$ plane is not important numerically and is ignored.

3.5.2.3 Optics cuts

One of the main strengths of the E154 tracking code is the use of optics cuts to reduce the combinatorial background in the hodoscopes, important in the high background rate environment. We employ the following strategy. The search for track candidates starts with the shower cluster. For charged particles originating from the target, the direction of the momentum is strongly correlated with the impact point at the shower counter. This can be clearly seen in Fig. 3.20. The correlation is strongest in $\hat{x}$ direction, where the effect of the magnetic field is small. In fact, the main reason for a non-zero width of the $\hat{x}$ distribution in the 5.5° spectrometer is the finite target length since there is almost no vertical component to the magnetic field. Even in the 2.75° spectrometer the correlation is strong. The correlation is not so strong in the $\hat{y}$ direction in both spectrometers; the peculiar shape of the $\hat{y}$ distributions is due to the reverse-bend optics of the spectrometers. Clearly, the optics cuts are strongest at the top of the spectrometer, *i.e.* at low momentum. The random background, that is thought to be caused by low-energy photons and neutrons, is roughly (within a factor of two) uniform across the face of the hodoscopes. Thus, the optics information enhances the signal/noise ratio in the search region of the hodoscopes.

The cut is implemented in the following way. The maps $\Theta_{\mathsf{min}}(x_{\mathsf{sh}})$, $\Theta_{\mathsf{max}}(x_{\mathsf{sh}})$, $\Phi_{\mathsf{min}}(y_{\mathsf{sh}})$, and $\Phi_{\mathsf{max}}(y_{\mathsf{sh}})$ are generated using a Monte Carlo program. Here $\left(\frac{dx}{dz}\right) \equiv \Theta$ and $\left(\frac{dy}{dz}\right) \equiv \Phi$ are track slopes, and min and max denote the minimum and maximum slopes for a particle scattered at the target and with a coordinate at the shower counter $(x_{\mathrm{sh}}, y_{\mathrm{sh}})$. We take into account the spatial resolution of the shower counter by increasing the slope range:

$$\begin{aligned}\Theta_{\mathsf{min}} &= \min\left(\Theta_{\mathsf{min}}(x_{\mathsf{sh}} \pm C_L\sigma(x_{\mathsf{sh}}))\right)\\ \Theta_{\mathsf{max}} &= \max\left(\Theta_{\mathsf{max}}(x_{\mathsf{sh}} \pm C_L\sigma(x_{\mathsf{sh}}))\right)\end{aligned} \tag{3.19}$$

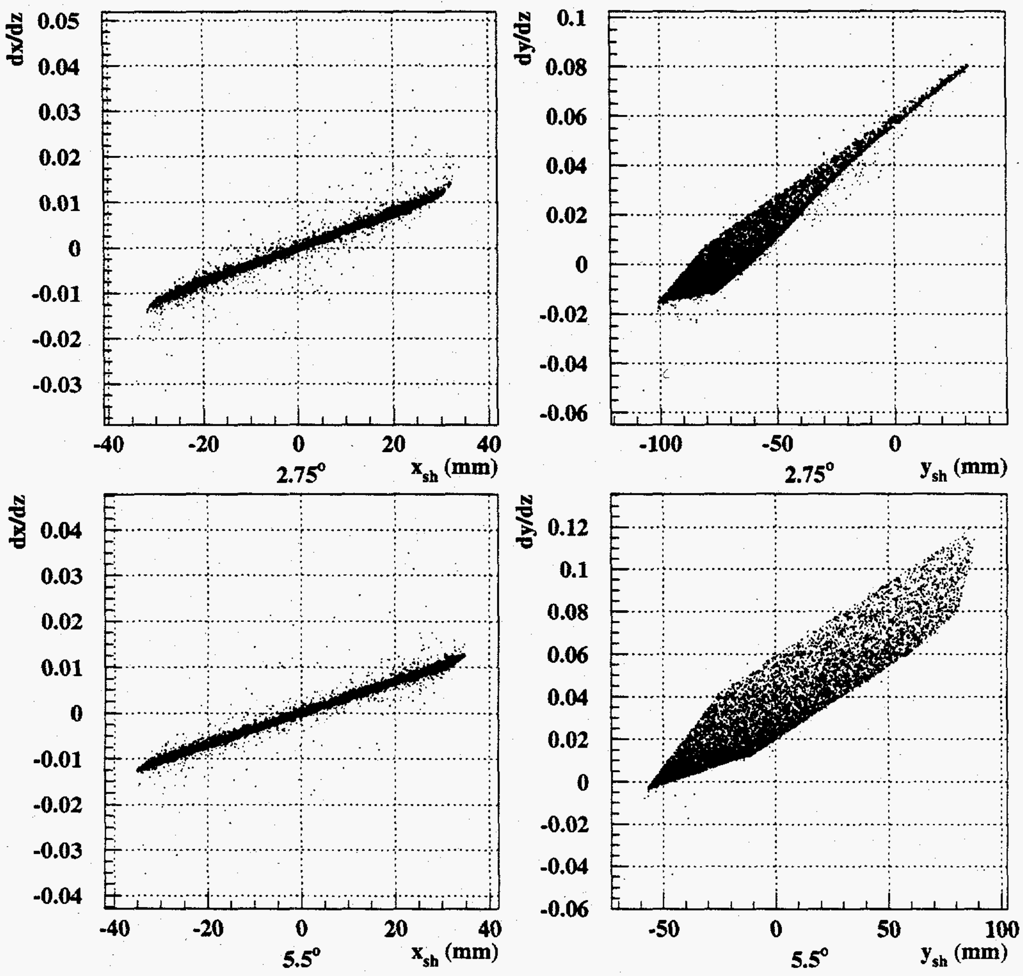

Fig. 3.20. Distribution of slopes of charged particle tracks (in $\hat{x}$, left, and $\hat{y}$, right) versus track position at the shower counter for 2.75° (top) and 5.5° (bottom) spectrometers.

and analogously in $\hat{y}$ direction. The "confidence level" factor C_L was chosen to be 5 to optimize efficiency[10]. Now for every hodoscope plane we determine the range of allowed coordinates:

$$\begin{aligned} u_{\text{min}} &= \min(u_1, u_2, u_3, u_4) - C_X \cdot w \\ u_{\text{max}} &= \max(u_1, u_2, u_3, u_4) + C_X \cdot w \;, \end{aligned} \tag{3.20}$$

where $C_X = 3$ is a factor that allows for the finite hodoscope resolution and w is the hodoscope width (the combination of these two factors makes the search area bigger by one finger in each direction). Finally, the combinations u_1, u_2, u_3, and u_4 are

$$\begin{aligned} u_1 &= x_{\text{min}} \cos\theta_u + y_{\text{min}} \sin\theta_u \\ u_2 &= x_{\text{min}} \cos\theta_u + y_{\text{max}} \sin\theta_u \\ u_3 &= x_{\text{max}} \cos\theta_u + y_{\text{min}} \sin\theta_u \\ u_4 &= x_{\text{max}} \cos\theta_u + y_{\text{max}} \sin\theta_u \;, \end{aligned} \tag{3.21}$$

where θ_u is defined in Eq. (3.18). Corners of the region allowed by optics are

$$\begin{aligned} x_{\text{min}} &= [x_{\text{sh}} - C_L\sigma(x_{\text{sh}})] + \Delta z\Theta_{\text{min}} \\ x_{\text{max}} &= [x_{\text{sh}} + C_L\sigma(x_{\text{sh}})] + \Delta z\Theta_{\text{max}} \\ y_{\text{min}} &= [y_{\text{sh}} - C_L\sigma(y_{\text{sh}})] + \Delta z\Phi_{\text{min}} \\ y_{\text{max}} &= [y_{\text{sh}} + C_L\sigma(y_{\text{sh}})] + \Delta z\Phi_{\text{max}} \;, \end{aligned} \tag{3.22}$$

where $\Delta z = (z_{\text{hod}} - z_{\text{sh}})$.

---

[10] This factor also reflects a non-gaussian shape of the calorimeter resolution due to multiple scattering and bremsstrahlung in the spectrometer.

3.5.2.4 Track candidates

We will discuss the algorithm for the first two track classes. Algorithm for classes 3 and 4, that do not include clusters, is a simple extension of the main algorithm and will be discussed later.

We loop first over the shower clusters that are identified as electrons by the shower particle ID algorithm (neural net for SLAC analysis and shape cut for Caltech), and then over all remaining clusters. For every cluster, we look for time coincidence with a Cherenkov signals. We first select Cherenkov hits that are within a time window

$$\Delta\tau = \tau_{\rm sh} - \tau_{\rm ch} = C_T \cdot \sqrt{\sigma^2(\tau_{\rm sh}) + \sigma^2(\tau_{\rm ch})} \tag{3.23}$$

from the shower cluster. Here τ is the "target" time (see Eq. (3.17)), and $\sigma(\tau_{\rm sh})$ and $\sigma(\tau_{\rm ch})$ are shower time and Cherenkov resolutions. Factor C_T is typically set to 3. Among all selected hits, we pick two (or one, if hits from only one tank are found) that minimize χ^2

$$\chi^2 = \sum_i \frac{(\tau_i - \langle\tau\rangle)^2}{\sigma^2(\tau_i)} \,, \tag{3.24}$$

where the summation includes the shower cluster and Cherenkov hits from each tank. The average time $\langle\tau\rangle$ is given as usual by

$$\langle\tau\rangle = \frac{\sum_i \tau_i/\sigma^2(\tau_i)}{\sum_i 1/\sigma^2(\tau_i)} \,. \tag{3.25}$$

This average time and its uncertainty

$$\sigma^2(\langle\tau\rangle) = \frac{1}{\sum_i 1/\sigma^2(\tau_i)} \tag{3.26}$$

are used to define the time window for the hodoscope hits. If no Cherenkov hits are found to match the cluster, the track is a class 2 candidate; time $\langle\tau\rangle$ and its uncertainty are then taken from the shower cluster.

3.5.2.5 Hodoscope mini-clusters

After the Cherenkov and shower cluster match is found, we select the hodoscope hits that pass the optics cuts and are sufficiently close in time to the average time $\langle\tau\rangle$ to be with the window $\langle\tau\rangle \pm \Delta\tau$, where

$$\Delta\tau = C_T \cdot \sqrt{\sigma^2(\langle\tau\rangle) + \sigma^2(\tau_{\text{hod}})}\ . \tag{3.27}$$

The next step is to arrange the hits within a hodoscope package (front and rear) into local clusters. The idea is to eliminate combinations of fingers that cannot geometrically belong to one track. To reduce the pattern recognition problem to two dimensions, we first project all fingers onto a common plane (taken at the z position of the last plane of the package). We use a stereographic projection along the line connecting the center of a given finger and the shower cluster:

$$\begin{aligned} x_c &\rightarrow x_c' = x_c + (x_{\text{sh}} - x_c)\frac{z' - z}{z_{\text{sh}} - z} \\ y_c &\rightarrow y_c' = y_c + (y_{\text{sh}} - y_c)\frac{z' - z}{z_{\text{sh}} - z} \\ w &\rightarrow w' = w + (w_{\text{sh}} - w)\frac{z' - z}{z_{\text{sh}} - z}\ . \end{aligned} \tag{3.28}$$

Here (x_c, y_c) is the position of the finger center, z is the finger z position, and z' is the position of the plane of projection. Note that the finger width w is also modified; the shower width w_{sh} is given by

$$w_{\text{sh}} = 3\,(\sigma(x_{\text{sh}})|\cos\theta_u| + \sigma(y_{\text{sh}})|\sin\theta_u|)\ . \tag{3.29}$$

Now the problem is reduced to selecting sets of overlapping rectangles (fingers). This is done iteratively. We first find all crossings among all hit fingers in the first two planes of the package. Crossed fingers are replaced by a rectangle that represents the area common to both fingers. This is shown in Fig. 3.21. For simplicity, we make the resulting box parallel to the $\hat{x} - \hat{y}$ axes. Every such finger overlap makes a new

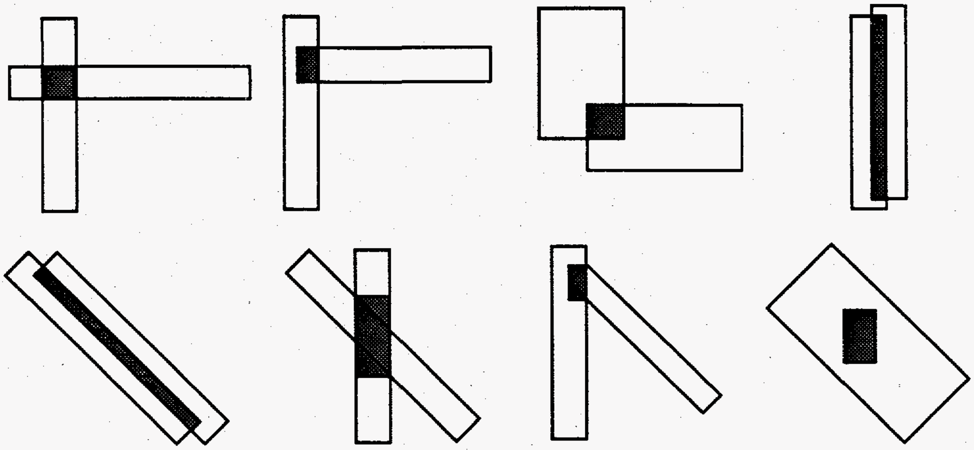

Fig. 3.21. Possible two-finger mini-clusters.

hodoscope mini-cluster. We then loop over fingers in the next plane of the package and look for fingers that cross either an existing cluster, or a finger in the first two planes. In the former case, the finger is added to the existing mini-cluster, in the latter, a new mini-cluster is created. The procedure is repeated until all possible mini-clusters are found. Examples of hodoscope mini-clusters are shown in Fig. 3.22.

3.5.2.6 Fitting

The track candidates are formed from the shower clusters, Cherenkov hits, and all combinations of hodoscope mini-clusters. All tracks are straight in the detector hut, so for every track we calculate 5 parameters: line intercepts and slopes (x_0, Θ, y_0, Φ), and track time at the target τ_0. This is done by minimizing

$$\chi^2 = \sum_i \left(\frac{(x_0 + z_i\Theta)\cos\theta_u + (y_0 + z_i\Phi)\sin\theta_u - u_i}{\sigma(u_i)} \right)^2 + \sum_j \left(\frac{\tau_0 - \tau_i}{\sigma(\tau_i)} \right)^2 . \quad (3.30)$$

The first sum in Eq. (3.30) includes the hodoscope hits and the shower cluster (for the latter we have two entries: $u \equiv x$ and $u \equiv y$). The second sum also includes Cherenkov hits. The resulting system of linear equations can be factorized into the

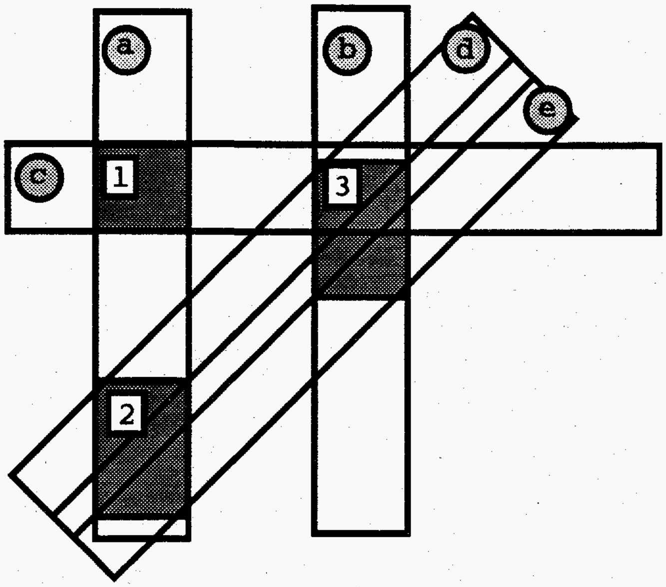

Fig. 3.22. Three mini-clusters are formed from five hit fingers. Cluster (1) consists of fingers (a) and (c), (2) of (a), (d), and (e), and (3) of (b), (c), (d), and (e).

space and time parts. The time of the track τ_0 is then readily found as an average of all hits, weighted by the uncertainty $\sigma(\tau_i)$. In order to increase performance, we in fact first do the fitting in the time domain only, remove all hits with times τ_i outside the $\chi^2_{\max}$ cut (see next section), and then repeat the fit in both space and time.

The detector time τ_i needs to be corrected for the time of the light propagation from the point where the track crosses the detector (hodoscope finger or Cherenkov mirror) to the phototube. For the hodoscopes, it is the time of light propagation inside the finger. By convention, the time offsets for the hodoscope fingers are calculated for a track that passes through the geometrical center of the finger, so such tracks need no propagation time correction. Therefore, the correction is proportional to the distance from the finger center to the track:

$$\Delta\tau_{\text{hod}} = \frac{1}{v}\left[-(x_0 + z_c\Theta - x_c)\sin\theta_u + (y_0 + z_c\Phi - y_c)\cos\theta_u\right] , \tag{3.31}$$

where (x_c, y_c, x_c) is the geometrical center of the finger. The correction is positive (the track passed later than τ_i) if the track position is closer to the phototube than the finger center. The constant v is the effective light propagation speed along the finger. It is a phenomenological constant that reflects the geometry of the fingers and peculiarities of the light collection, and is unique to every plane. It ranges from 135 mm/ns to 213 mm/ns[11].

For the Cherenkov detectors, we correct for the light propagation from the mirror to the phototube. The time offsets for the Cherenkov counters correspond to the geometrical center of the mirror. Thus, the correction is related to the *difference* between the distance from the track position at the mirror to the phototube and the distance from the mirror center to the phototube:

$$\begin{aligned}\Delta\tau_{\text{hod}} &= \frac{1}{c}\Bigg[\sqrt{(x_0 + z_m\Theta - x_p)^2 + (y_0 + z_m\Phi - y_p)^2 + (z_m - z_p)^2} - \\ &\qquad \sqrt{(x_m - x_p)^2 + (y_m - y_p)^2 + (z_m - z_p)^2}\,\Bigg] , \end{aligned} \tag{3.32}$$

where (x_m, y_m, z_m) is the center of the mirror, (x_p, y_p, z_p) are the phototube positions, and c is the speed of light. We neglect mirror curvature and yaw.

3.5.2.7 Selecting the best track candidate

After the track parameters are found, we calculate the time and spatial residuals for every hodoscope and Cherenkov hit, and find the hit with the worst

$$\chi_i^2 = \left(\frac{(x_0 + z_i\Theta)\cos\theta_u + (y_0 + z_i\Phi)\sin\theta_u - u_i}{\sigma(u_i)}\right)^2 + \left(\frac{\tau_0 - \tau_i}{\sigma(\tau_i)}\right)^2 . \tag{3.33}$$

For the Cherenkovs, there is indeed no spatial residual. We set the limit $\chi^2_{\text{max}} = 8$ for the fit in the time domain and $\chi^2_{\text{max}} = 16$ for the combined space-time fit. If $\chi^2_{\text{worst}} > \chi^2_{\text{max}}$, the worst hit is removed from the track candidate unless

- The number of hits in the hodoscope package drops below the threshold. The minimum number of hits was set to 4 for the front hodoscope package in 2.75°

---

[11] Note that the physical light propagation speed for Bicron BC404 is 190 mm/ns that corresponds to the refractive index of 1.58.

spectrometer and to 3 for the back package in 2.75° and for both packages in 5.5° spectrometer. This number is half the expected average number of hits per package if the hodoscopes are 100% efficient (except the back hodoscope package of 2.75° spectrometer where the expected average number of hits is 5).

- One of the sums

  $$\sum_{\text{planes}} |\cos\theta_u|\,, \quad \sum_{\text{planes}} |\sin\theta_u|$$

  drops below the threshold of 0.5 for one of the hodoscope packages. This requirement assures that both $\hat{x}$ and $\hat{y}$ projections are determined.

If one of the conditions above is met, the entire track candidate is dropped. Otherwise, the worst hit is removed and the fit is repeated. The fitting converges if either all hits are within χ^2_{max} limit, or the candidate is dropped. Out of all successful track candidates (combinations of hodoscope mini-clusters), we pick one with the best total χ^2 per degree of freedom.

If the track is fitted successfully, the hits are marked to prevent them from being used on another track[12].

3.5.2.8 Class 3 and 4 tracks

The algorithm for class 3 and 4 tracks (that do not include a shower cluster) is an extension of the general algorithm discussed above. First, the spill is divided into 6 nsec time intervals. Let τ_0 denote the center of an interval. We find the time slice with the most Cherenkov and hodoscope hits within ± 9 nsec around τ_0 (preference is always given to the intervals with most Cherenkov hits). Then, a "fake" shower cluster is created with time τ_0, time uncertainty $9/C_T$ nsec (C_T is the time "confidence level factor" of Eq. (3.27)), and infinite position resolution. From

---

[12] For Caltech DST production, we disabled marking of Cherenkov hits and reduced rate dependence by about 0.5%.

this point, the algorithm proceeds exactly as described above for classes 1 and 2 with the following trivial modifications:

- The minimum and maximum track slopes are used to define the stereographic projection in Eq. (3.29).
- The "fake" shower cluster is not used in fitting.

The search for class 3 and 4 tracks stops when track candidates in all time slices are exhausted.

3.5.3 Performance

Typically, an electron track in the 2.75° spectrometer is constructed of 16-17 hits (including all detectors, Fig. 3.23). The average number of hits per hodoscope package is found to be close to the expectation (8 for the front package and 5 for the rear package) that implies that the hodoscope inefficiency is not big. We estimate the tracking efficiency by comparing the number of shower clusters with the number of associated tracks. The inefficiency, defined as the ratio $(N_{\text{clusters}} - N_{\text{tracks}})/N_{\text{clusters}}$, is shown in Fig. 3.24 for all clusters (top left), and for electron clusters. The low energy clusters are mostly pions, and the tracking efficiency for them is low. This is mostly due to the fact that the resolution (both spatial and time) of the shower counter is worse for pions than it is for electrons, and hence the initial cuts (optics and time) are not as efficient as for electrons. The electron efficiency is better than 90%, even after the E/p cuts. To identify the electron clusters in Fig. 3.24, we require a time coincidence among the cluster and two Cherenkov hits with the peak voltage greater than 50. This sample is still somewhat contaminated by random coincidences of pion clusters with Cherenkov hits, so the values of inefficiencies in Fig. 3.24 are upper limits of true electron inefficiencies.

An independent determination of the tracking efficiencies was based on a Monte Carlo technique. Electron tracks, generated using the optics model of the spectrom-

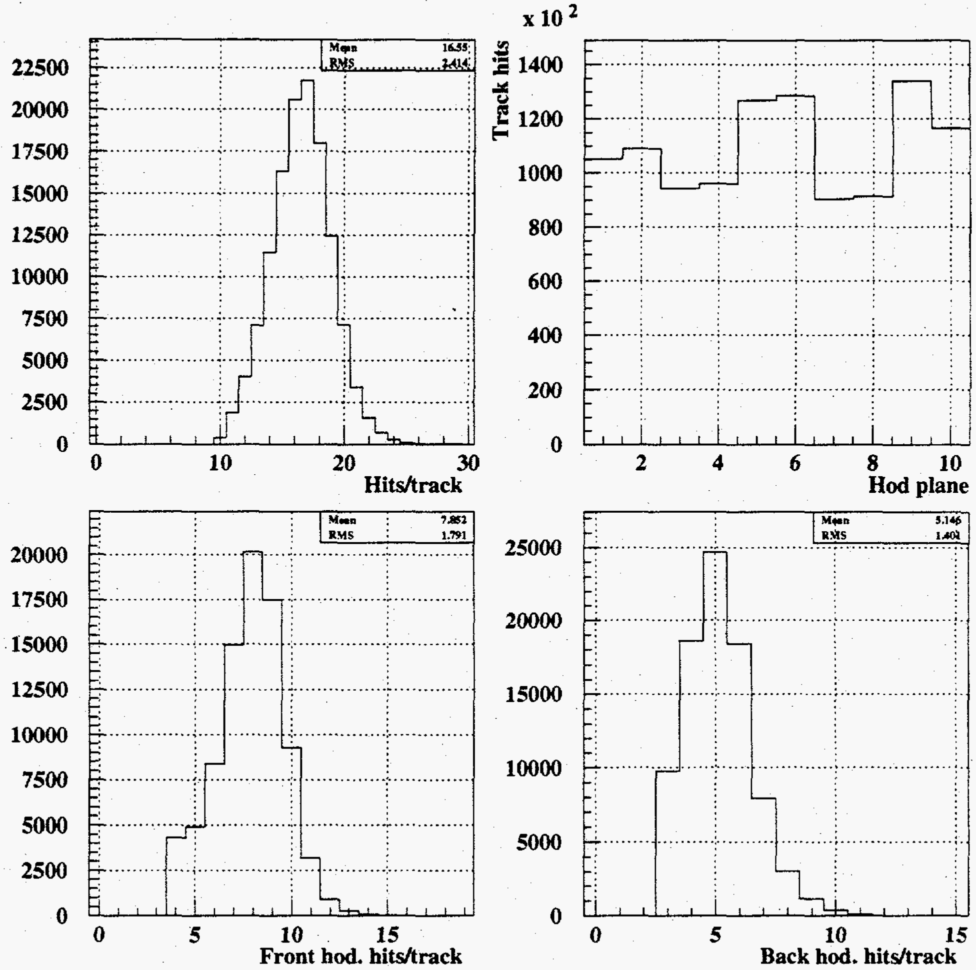

Fig. 3.23. Distribution of hits per track (top left), hits per hodoscope plane (top right), and distributions of track hits in the front (bottom left) and back (bottom right) hodoscope packages. All plots are for electrons in the 2.75° spectrometer.

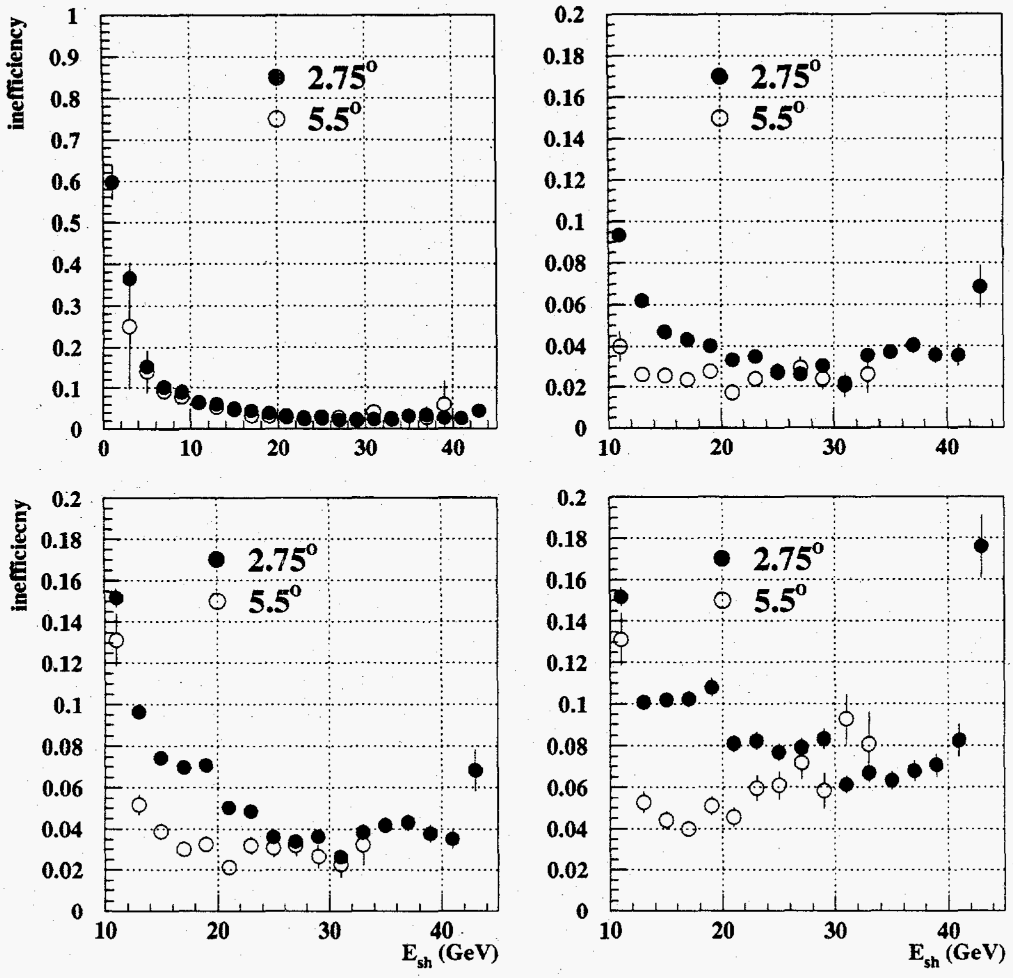

Fig. 3.24. Tracking inefficiency determined by the data (see text) for all clusters (top left) and for electron clusters (top right). Additional cuts are applied to electron tracks: $0.8 < E/p$ (bottom left) and $0.8 < E/p < 1.25$ (bottom right). Data are for ruin 3366 (beam current of $5 \cdot 10^{10}$ electrons/spill).

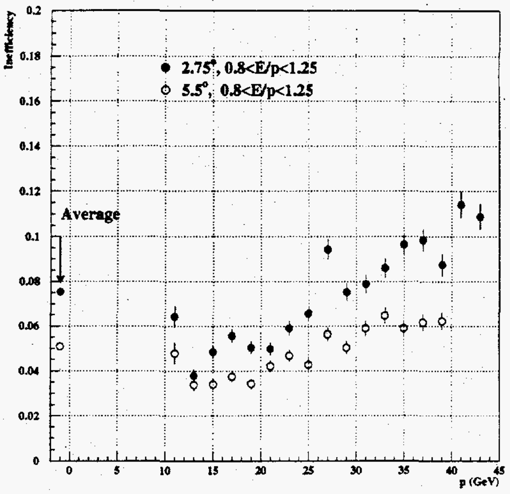

Fig. 3.25. Tracking inefficiencies for two spectrometers determined by the Monte Carlo method.

eter, were "seeded" among the real data and then reconstructed by the standard analysis code. The resolution and dead-time effects were taken into account. The efficiency was determined as the ratio of the number of reconstructed tracks with $0.8 \leq E/p \leq 1.25$ to the number of seeded tracks (see Fig. 3.25). It is consistent with the efficiencies determined by the data. The effect of the optics cuts described in Section 3.5.2.3 is demonstrated in Fig. 3.26. The tracking efficiency significantly decreases (by up to 5% in 2.75° spectrometer) when the optics cuts are turned off. Roughly the same decrease in efficiency was found when the local hodoscope clustering was turned off. Both effects is due to random coincidences in hodoscopes and are strongly rate dependent.

The largest contributions to inefficiency for 2.75° spectrometer are (on average):

- Momentum and energy resolution (in E/p cut): $\approx 2.5\%$;
- Hodoscope dead time: $\approx 2\%$
- Algorithm (cuts): $\approx 2\%$
- Hodoscope random coincidences: $\approx 1\%$

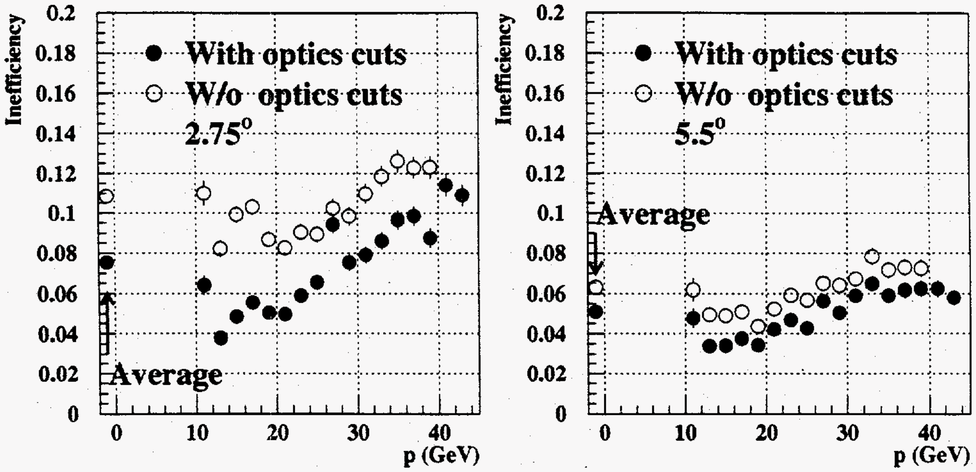

Fig. 3.26. Monte Carlo tracking inefficiencies for codes with and without optics cuts.

Contributions from the rate dependent sources (hodoscope dead time and random coincidences) are not large. The largest momentum dependence of inefficiency is due to E/p cuts; inefficiency increases with momentum as the resolution is degraded.

The rate dependence of tracking was studied by Piotr Zyla.[123] The contributions to the rate-dependent inefficiency from the hodoscope noise was found to be within 2% for every target (consistent with the estimates above). It was also found that the momentum determination is robust against the rate changes, much more than the energy determined by the shower counter (see Fig. 3.27).

3.5.4 Resolution

The tracking resolutions were determined by Monte Carlo (see above). Tracking timing resolution is $\approx 0.25 - 0.3$ nsec in both spectrometers (Fig. 3.28). Fig. 3.29 shows the spatial resolution in both spectrometers at the z position of the shower counter for electrons[13]. The spatial resolution for class 3 tracks (that do not use shower clusters) is shown in Fig. 3.30. It is significantly worse than that of class 1 and 2 tracks, and is in fact comparable to the position resolution of the shower counter

---

[13] All plots in this section are for Caltech analysis.

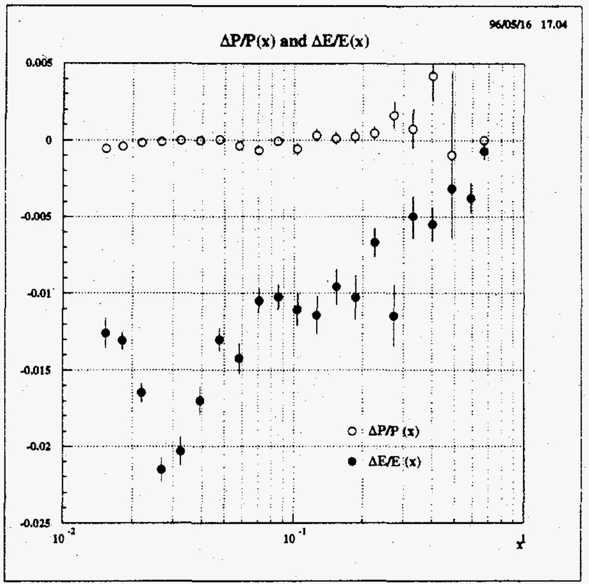

Fig. 3.27. Rate dependence of momentum and energy reconstruction. Plotted are the relative changes in momentum (open circles) and energy (closed circles) versus Bjorken x in 2.75° spectrometer when the detector rate is doubled. Courtesy of Piotr Zyla.[123]

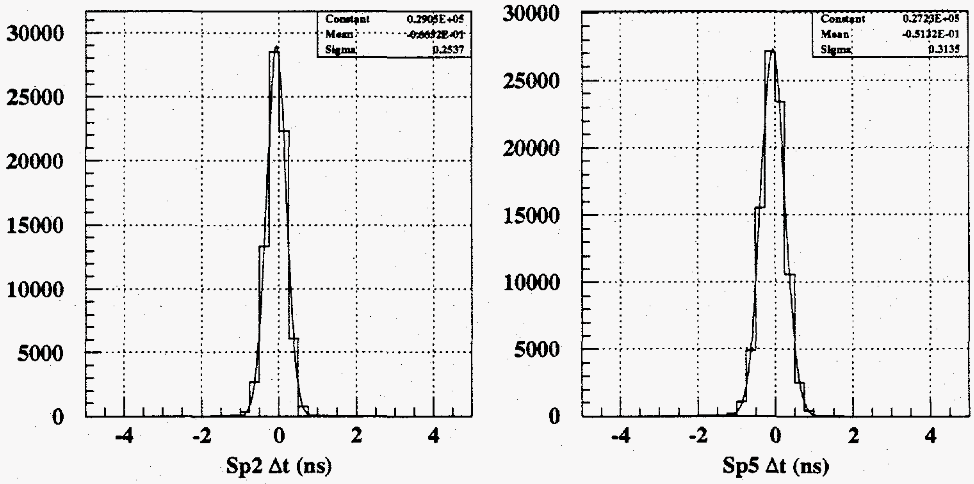

Fig. 3.28. Tracking time resolution in 2.75° (left) and 5.5° (right) spectrometers.

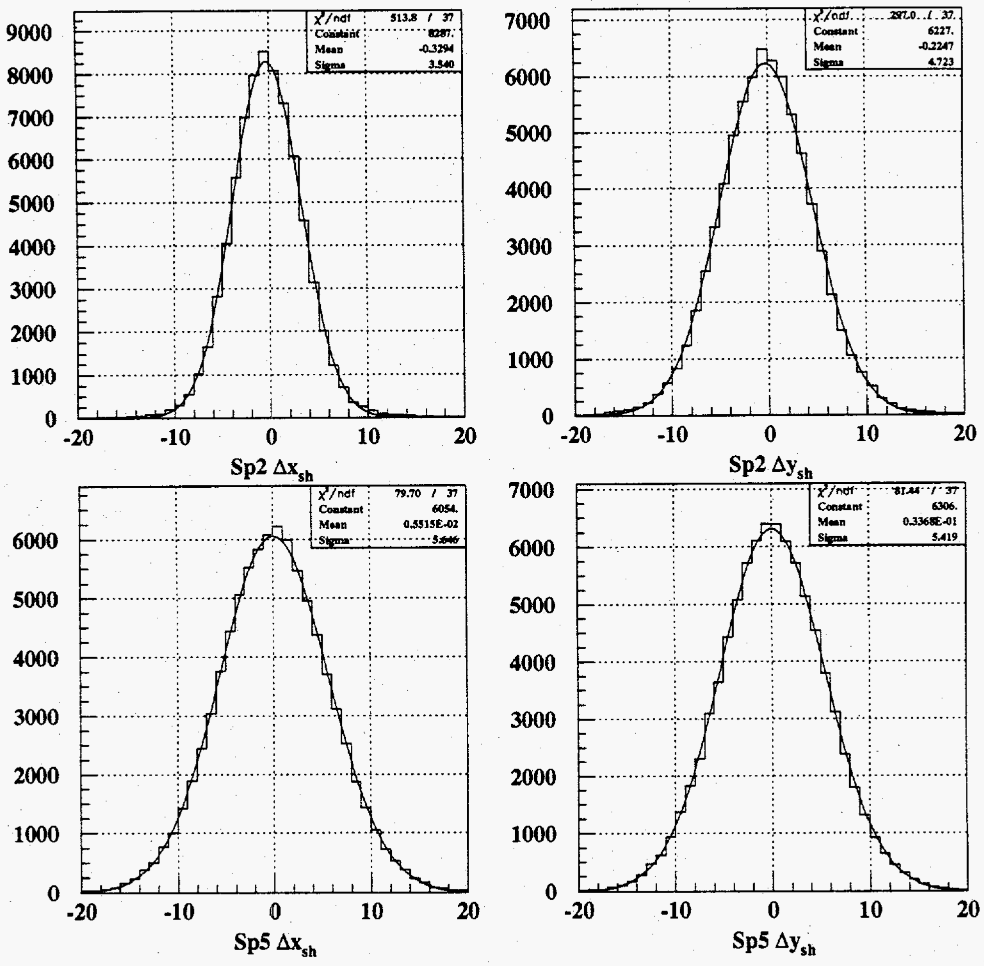

Fig. 3.29. Tracking resolution in x (left) and y at the z position of the shower counter for class 1 electrons. 2.75° (top) and 5.5° (bottom) spectrometers. All numbers are in mm.

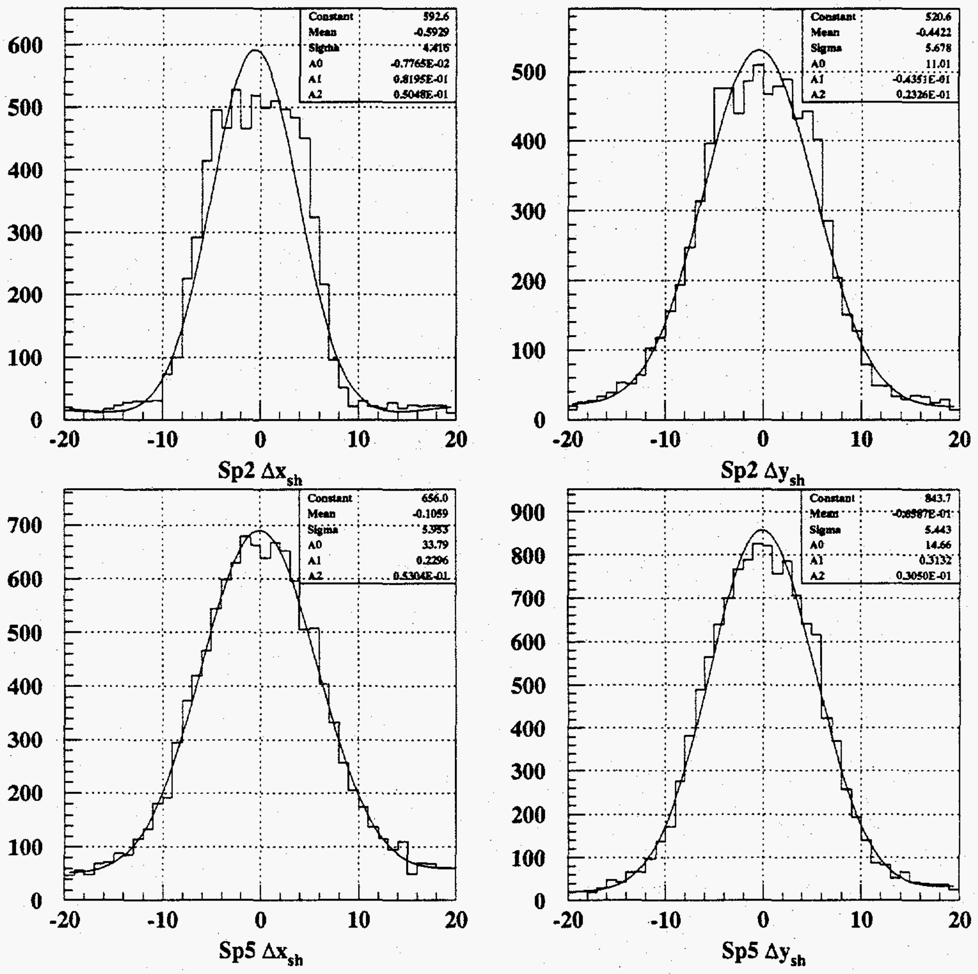

Fig. 3.30. Tracking resolution in x (left) and y (right) at the z position of the shower counter for class 3 tracks. 2.75° (top) and 5.5° (bottom) spectrometers. Overlaid is a Gaussian fit with quadratic background. All numbers are in mm.

alone (see Section 3.4). The shape of the distribution is clearly not Gaussian. Its core reflects the finite size of the hodoscope fingers, and the tails are due to random background in the hodoscopes.

The resolutions of the reconstructed momenta and scattering angles are shown in Fig. 3.31 (for original, *i.e.* before cell the Picard setting of Q1). The average momentum resolution is 2.4% in the 2.75° spectrometer and 2.7% in the 5.5° spectrometer (weighted by acceptance). The average angular resolution is ≈ 0.4 mrad in both spectrometers. The momentum dependence of the momentum resolution is shown in Fig. 3.32. For the original quadrupole setting (pre-Picard runs), the resolution degrades rapidly at low momentum in the 2.75° spectrometer. This is due to strong quadrupole focusing that results in almost ambiguous optics in the upper part of the spectrometer. The angular resolution in the bend plane ($\sigma(\phi)$) also shows very strong momentum dependence. On the contrary, the angular resolution in the non-bend plane ($\sigma(\theta)$) is almost constant with momentum.

The parameterizations for the momentum and angular resolution are given by

$$\begin{aligned}
\frac{\sigma(p)}{p} &= \sqrt{\frac{0.013}{(\tilde{p}-7.58)^2}+(0.93\cdot 10^{-3}\tilde{p})^2}\,, \quad \text{Caltech, 2.75°, pre-Picard} \\
\frac{\sigma(p)}{p} &= \sqrt{0.011^2+(0.81\cdot 10^{-3}\tilde{p})^2}\,, \quad \text{Caltech, 2.75°, Picard} \qquad (3.34) \\
\frac{\sigma(p)}{p} &= \sqrt{0.015^2+(1.01\cdot 10^{-3}\tilde{p})^2}\,, \quad \text{Caltech, 5.5°}
\end{aligned}$$

$$\begin{aligned}
\frac{\sigma(p)}{p} &= \sqrt{\frac{0.013}{(\tilde{p}-7.54)^2}+(0.98\cdot 10^{-3}\tilde{p})^2}\,, \quad \text{SLAC, 2.75°, pre-Picard} \\
\frac{\sigma(p)}{p} &= \sqrt{0.011^2+(0.89\cdot 10^{-3}\tilde{p})^2}\,, \quad \text{SLAC, 2.75°, Picard} \qquad (3.35) \\
\frac{\sigma(p)}{p} &= \sqrt{0.015^2+(1.14\cdot 10^{-3}\tilde{p})^2}\,, \quad \text{SLAC, 5.5°}
\end{aligned}$$

where $\tilde{p} = \frac{20}{p_c}p$, and p_c is the central momentum of the spectrometer (all momenta are in GeV).

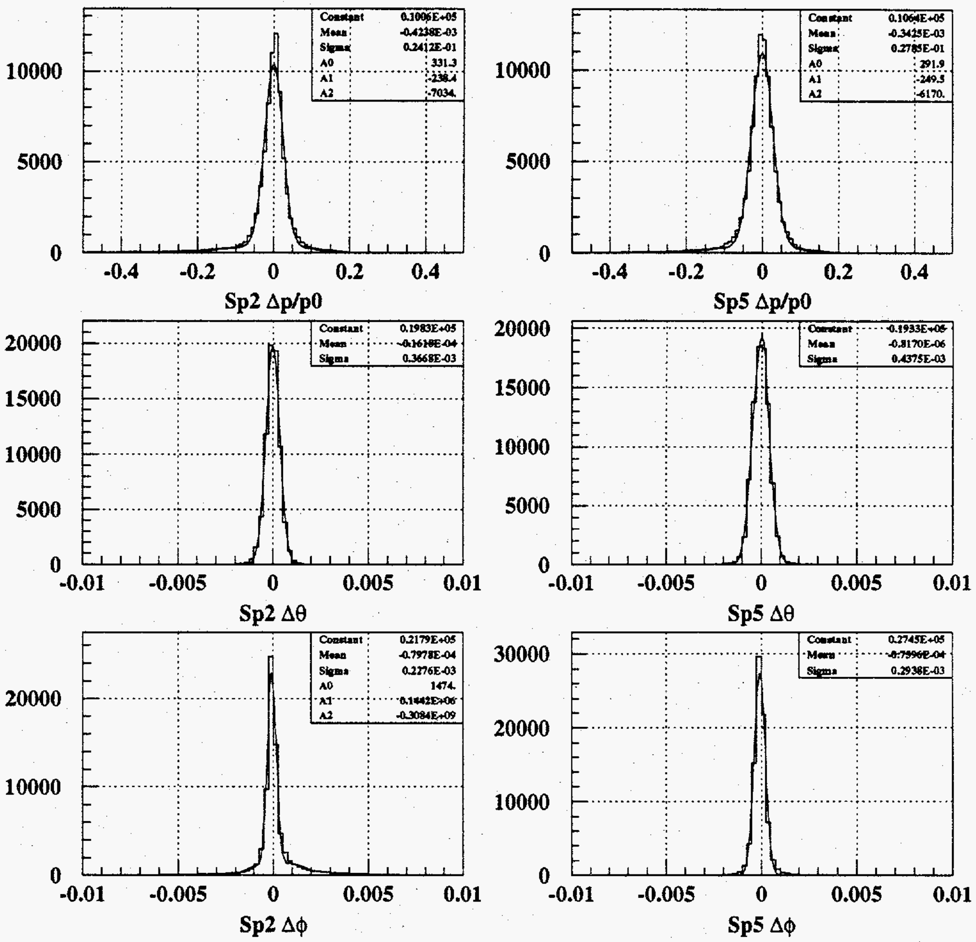

Fig. 3.31. Average momentum (top) and angular resolution in the bend (middle) and non-bend (bottom) planes. 2.75° (left) and 5.5° spectrometers (right)

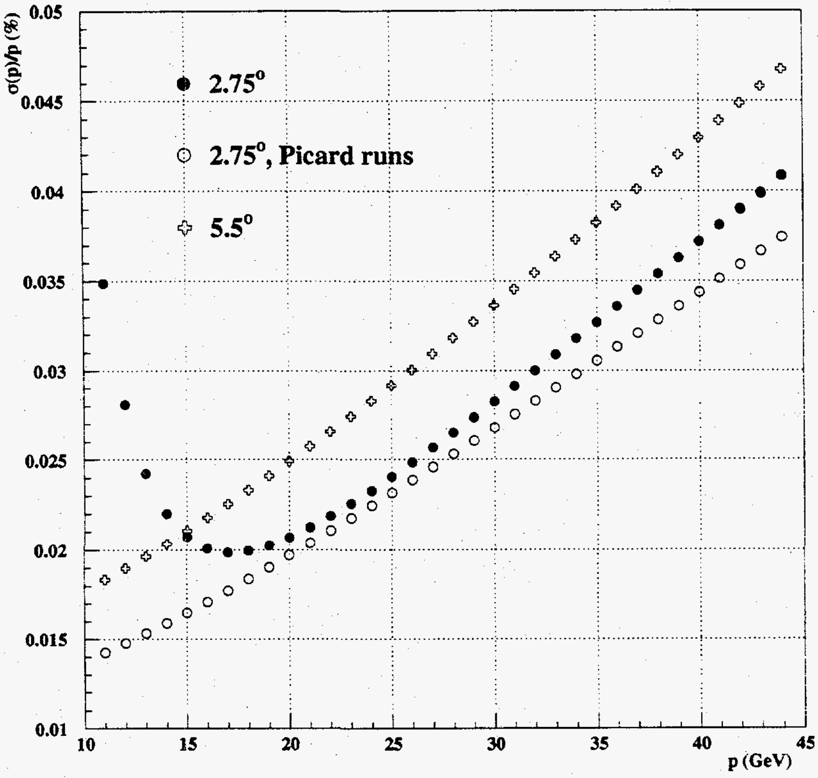

Fig. 3.32. Momentum dependence of the tracking momentum resolution. Standard optics configuration of 2.75° spectrometer is shown by solid circles, Picard optics is by open circles, and 5.5° spectrometer is shown by crosses.

The angular resolution in the bend plane is given by

$$\begin{aligned}\sigma(\phi) &= \frac{0.037}{(\tilde{p}-7.58)^2} + 0.194 \cdot 10^{-3}\ , \quad 2.75°\text{, pre-Picard} \\ \sigma(\phi) &= \frac{0.002}{(\tilde{p}-7.58)^{0.71}}\ , \quad 2.75°\text{, Picard}\ . \end{aligned} \tag{3.36}$$

The angular resolution in 5.5° spectrometer is independent of momentum. The difference between SLAC and Caltech values is negligible.

3.6 Efficiency and rate dependence

In E154, we measure asymmetry between cross sections in two different helicity states (see Section 1.2.1). The polarization direction of the target was reversed six times during the experiment. On another hand, the beam helicity was flipped every pulse according to a pseudo-random pattern. Due to such rapid helicity changes, spectrometer acceptance and slow changes in efficiency average out between two polarization states and can be ignored. The average efficiency factorizes in Equations (1.10) and (1.11), and is cancelled. Thus, unlike experiments which measure absolute cross sections, the overall efficiency is not particularly important for E154 as long as it does not significantly impact statistics of the experiment.

The efficiency of each detector system, relative to other detectors in the spectrometer, was estimated by using the tracking code. For instance, when the efficiency of the Cherenkovs for electrons was studied, class 2 tracks with shower energy $E > 9$ GeV and $E/p > 0.8$ were selected. Efficiency was defined as the ratio of number of time coincidences between such tracks and Cherenkov signals to the total number of selected tracks. For a typical Cherenkov cut used in the analysis that required hits in both tanks in coincidence with one of them higher than 2.5 photoelectrons (see Section 3.7.3.2), the efficiency was about 90%. The intrinsic efficiency of the total absorption shower counter should in principle be very close to 100% (excluding dead blocks and similar hardware problems) at small rates (see below for the discussion of the rate dependence). The efficiency of the shower electron ID cut, such as χ cut (see Section 3.4) or neural network cut used in SLAC analysis[121] is typically $\approx 90-95\%$. Tracking efficiency, determined as described in Section 3.5, was also on the order $90-95\%$. Overall, the electron reconstruction efficiency is estimated to be $70-80\%$. Unfortunately, there is insufficient redundancy in the detector system to determine this number more precisely.

The rate dependence of the efficiency is potentially a much more important effect. Suppose, the reconstruction efficiency depends (linearly) on the electron rate:

$$\epsilon = \epsilon_0 (1 - \beta N) \ , \tag{3.37}$$

where ϵ is electron efficiency, β is a small linearity coefficient, and N is rate (in arbitrary units). The measured rate for each helicity is then

$$N^{L(R)} = N_0^{L(R)} \epsilon_0 \left(1 - \beta N_0^{L(R)}\right) \ , \tag{3.38}$$

where indices $L(R)$ denote the helicity state. It is easy to show that in this case the measured asymmetry will be biased:

$$A^{\text{meas}} \equiv \frac{N^L - N^R}{N^L + N^R} \approx A_0 - \beta \langle N \rangle A_0 \ . \tag{3.39}$$

Here $A_0 = \frac{N_0^L - N_0^R}{N_0^L + N_0^R}$ is the true asymmetry, the average electron rate is $\langle N \rangle = 1/2(N_0^L + N_0^R)$, and all higher order terms (in β and A_0) have been dropped. Thus, the measured asymmetry will be biased by an amount proportional to the rate dependence of the efficiency.

The rate dependence of the reconstruction efficiency was studied[123] using a Monte Carlo technique dubbed "*pulse fiction*"[14]. The idea is to analyze two consecutive spills in one spectrometer, and then merge them on the level of raw data taking into account dead time, etc. Thus, the merged pulse will appear as taken at "double rate". The ratio of the number of electrons in merged pulses to the sum of the number of electrons in the original pulses determined the product $\alpha \equiv \beta\langle N \rangle$. Since electron efficiency depends primarily on the environmental rate (*i.e.* the total rate in the detectors and not only the electron rate), the individual coefficients α_{cher}, α_{hodo}, and α_{shw} were determined for Cherenkovs, hodoscope, and the shower counter by merging raw data from individual detectors. The rate dependence correction to the measured asymmetry is given similarly to Eq. (3.39) by

$$\Delta A^{\text{rate}} \equiv A_0 - A^{\text{meas}} = \alpha_{\text{cher}} A_{\text{cher}} + \alpha_{\text{hodo}} A_{\text{hodo}} + \alpha_{\text{shw}} A_{\text{shw}} \ , \tag{3.40}$$

where A_{cher}, A_{hodo}, and A_{shw} are asymmetries in rates for individual detectors. The coefficients $\alpha_i \equiv \beta_i \langle N_i \rangle$ for every detector and the coefficient α_{tot} (determined by merging all detectors at the same time) are shown in Fig. 3.33 for all polarized

---

[14] The name was inspired by a popular, as of time of analysis, motion picture.

^{3}He cells.[123] There is an obvious correlation of the rate dependence to the overall rate in the spectrometers. The runs taken at the high beam current of $\approx 9 \cdot 10^{10}$ electrons/spill (target cells Dave, Riker, Bob, SMC, and Generals) show a stronger rate dependence than the runs at the intermediate current of $\approx 5 \cdot 10^{10}$ electrons/spill (target cells Hermes, Prelims, and Chance), or the low current of $3 \cdot 10^{10}$ electrons/spill (target cell Picard). The rate dependence was also sensitive to the beam quality that was improving over the course of the experiment, and to the target window thickness. There is an apparent jump in the rate dependence in the 5.5° spectrometer for target Chance. This target had the thickest windows, and unlike the 2.75° spectrometer, the acceptance of the 5.5° spectrometer was fixed. Note also that α_{tot} is usually somewhat higher than the sum of rate dependences for individual detectors. This is due to subtle correlations that exist in tracking. If we assume that the rate asymmetries in the individual detectors are uncorrelated (which is a good approximation since the detectors are sensitive to different types of the background), these correlations should be ignored in Eq. (3.40).

The rate dependence was typically $6-8\%$ in the 2.75° spectrometer and $3-5\%$ in the 5.5° spectrometer, and showed mild dependence on electron momentum.[123]

3.7 DST analysis

The Data Summary Tapes contained pre-processed information about the Cherenkov hits, shower clusters, and tracks in the spectrometers, as well as information about the beam charge, position, helicity etc. A typical size of a DST file for one run was about 130 Mbytes – more than factor of six reduction in size compared to the raw data tapes. The main advantage of using DST tapes was the processing speed. Contrary to the raw data analysis, the DST analysis code was not CPU-intensive, and the speed was limited only by the I/O throughput. Thus, the entire data set of E154 could be analyzed in less than three days. The analysis speed

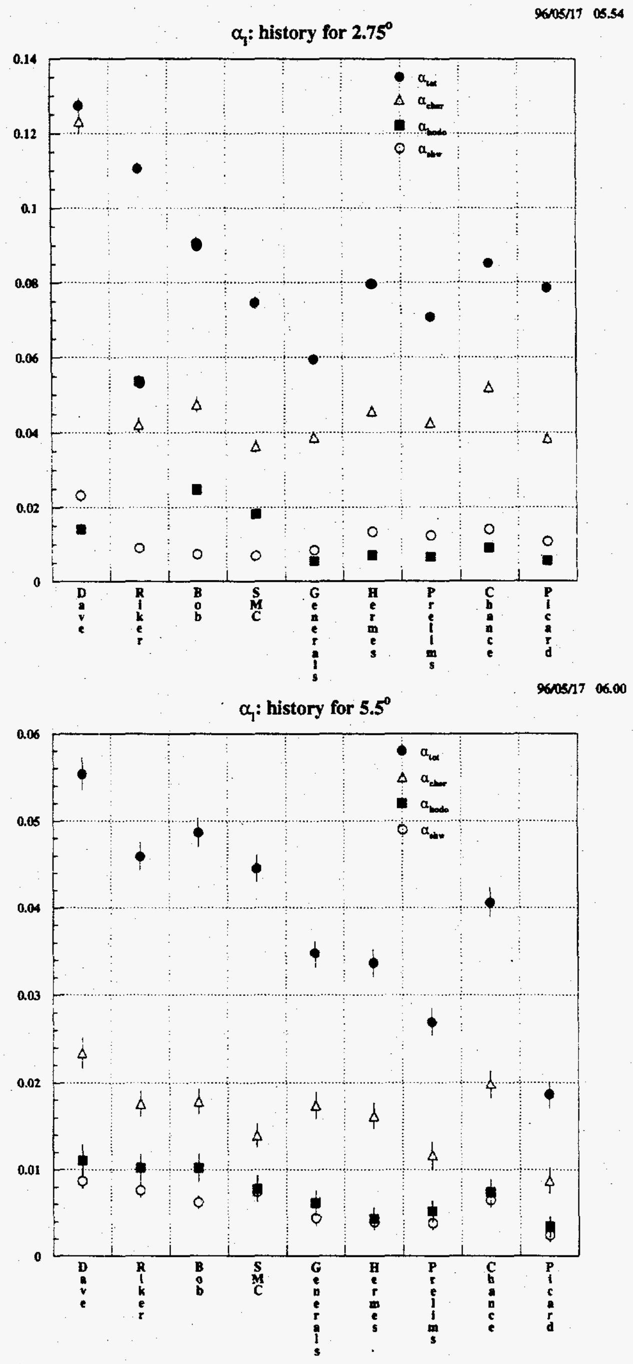

Fig. 3.33. Rate dependence coefficients α (see text) for the 2.75° (top) and 5.5° (bottom) spectrometers.

offered great flexibility in studying detector performance, effects of electron cuts, pion contamination, and other systematic effects.

For each run, the DST analysis code counted events satisfying certain electron (or pion) definitions, and placed them in appropriate x and Q^2 bins for each beam helicity. The summary files produces for each run were then used by a separate program to calculate physics asymmetries.

3.7.1 Kinematics

The kinematics of each event is determined by tracking. The scattering angle of an electron is given by

$$\vartheta = \sqrt{(\theta_0 + \theta)^2 + \phi^2} \tag{3.41}$$

where $\theta_0 = -2.75°(+5.5°)$, and θ and ϕ are scattering angles in non-bend and bend planes respectively. Track momentum p determines the scattered electron energy E'. The kinematic variables are calculated as follows:

$$\begin{aligned} Q^2 &= 4EE' \sin^2 \vartheta/2 \\ x &= \frac{Q^2}{2M(E - E')} \\ W^2 &= M^2 + Q^2 \frac{1-x}{x} \, . \end{aligned} \tag{3.42}$$

The beam energy is E and M is the proton mass.

3.7.2 Run selection

The polarized data taking started with run 1329 on October 9, 1995 (target Dave) and ended with run 3785 on November 20, 1995. The total of 1467 polarized ^{3}He runs were written to tape. Only 956 of them were used for the asymmetry analysis. Below, we describe runs that did not satisfy the selection criteria. Some of the cuts apply to the reference cell runs as well (cuts not related to polarization or beam asymmetries).

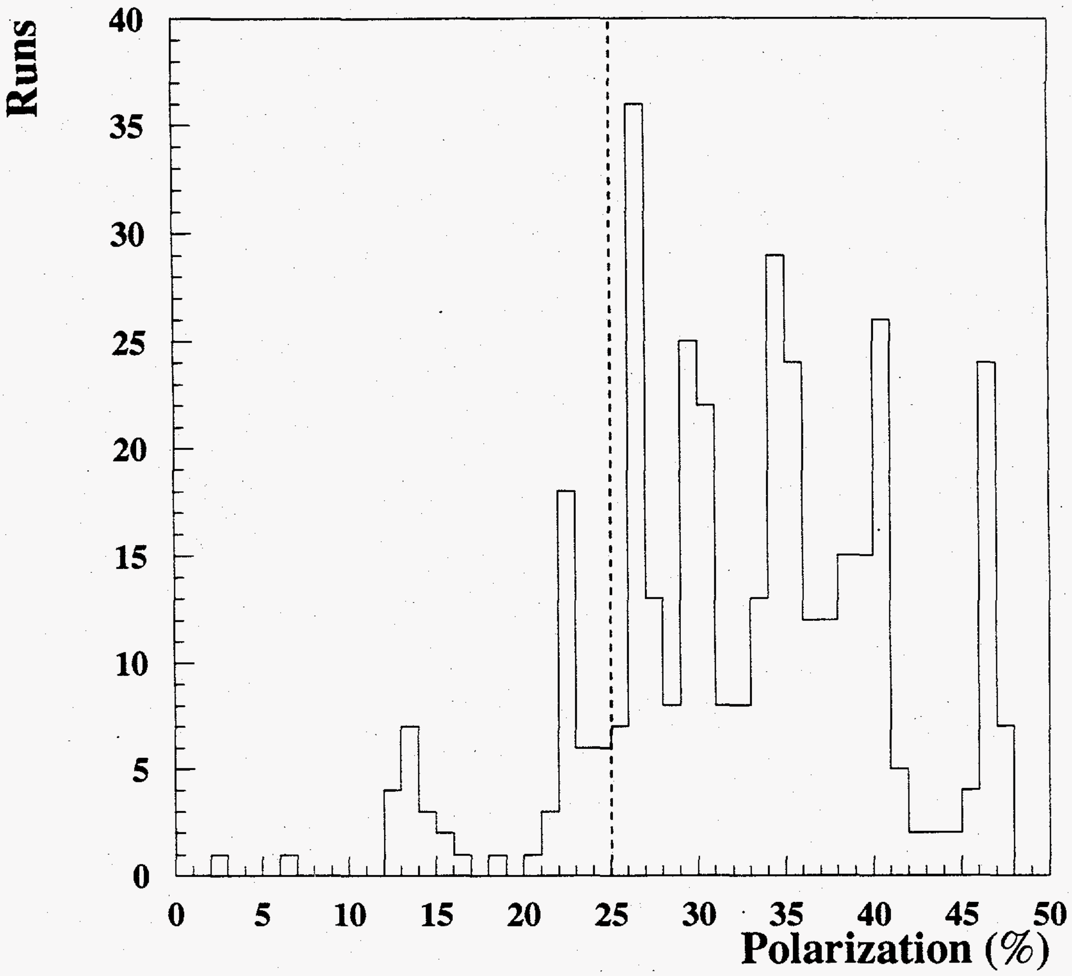

Fig. 3.34. Distribution of target polarization measurements. Only runs with polarization above 25% (dashed line) are included in the asymmetry analysis.

3.7.2.1 Target polarization

Only runs with the target polarization higher than 25% were used in the asymmetry analysis. Most of the runs that failed the cut were taken either during the spin-up of the target or in in special target tests, and polarization was not very stable. The distribution of the target polarization measurements is shown in Fig. 3.34. The target polarization cut eliminated 190 runs. If included, these runs, however, would have a negligible impact on overall statistics of E154.

3.7.2.2 Beam and hardware problems

Certain runs, identified as "bad" by a shift crew and marked in the log book, were actually written to tape. Such runs were removed from the data sample. The beam problems listed in log books included test runs (when the beam or spectrometer configuration was not normal), runs with frequent beam trips and/or poor beam quality, runs affected by hardware failures or hardware changes, and runs affected DAQ or control software problems. We also removed runs that were shorter than 30,000 spills (a typical run size was 200,000 spills). 270 runs have been eliminated.

3.7.2.3 Charge and beam position asymmetry

The raw asymmetries measured in our experiments are small, typically, on the order of $10^{-4} - 10^{-3}$. In order to minimize systematic effects, it is important to keep beam-related asymmetries to the minimum. The rate dependence of electron efficiency was typically on the order of 10% (see Section 3.6), so the beam charge asymmetry has to be below 10^{-3} in order to keep asymmetry bias below 10^{-4} for every run. The distribution and history of beam charge asymmetry is shown in Fig. 3.35. We have cut runs with charge asymmetry $|A_{\text{charge}}| = |(Q_L - Q_R)/(Q_L + Q_R)| > 5 \cdot 10^{-4}$. A total of 34 runs have been eliminated.

Another potential source of systematic biases in measured raw asymmetry is asymmetry in beam position. Due to the variation of the target cell window thickness, spectrometer rate depends on the relative positions of the beam and the target cell,[114] as was determined by moving an empty reference cell vertically through the beam. This dependence is illustrated in Fig. 3.36. The distribution of beam position asymmetries is shown in Fig. 3.37.[125]

For asymmetry analysis, we select runs with position asymmetries $|\langle x_L\rangle - \langle x_R\rangle| \leq 0.004$ mm, and $|\langle y_L\rangle - \langle y_R\rangle| \leq 0.005$ mm. Here $\langle x_{L(R)}\rangle$ is the average beam position

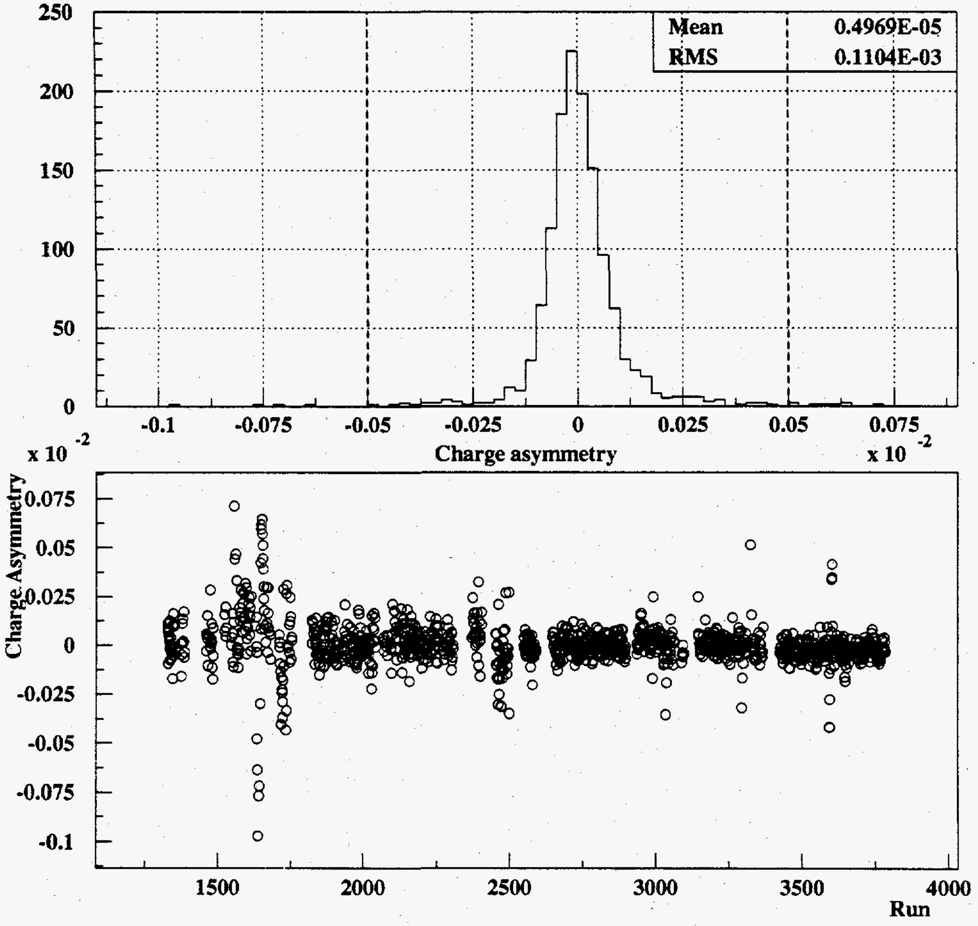

Fig. 3.35. Distribution (top) and history (bottom) of beam charge asymmetry versus E154 run number. The applied cut is shown as a dashed line.

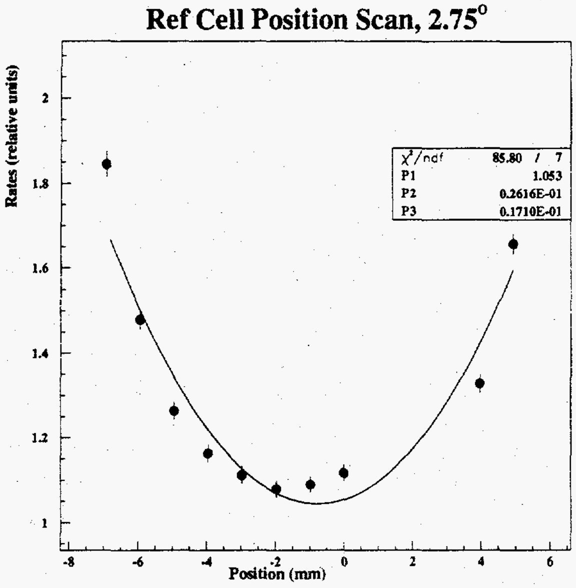

Fig. 3.36. Dependence of the electron rate in the 2.75° spectrometer on the relative beam position. Overlaid is a quadratic fit. Courtesy of Piotr Zyla.

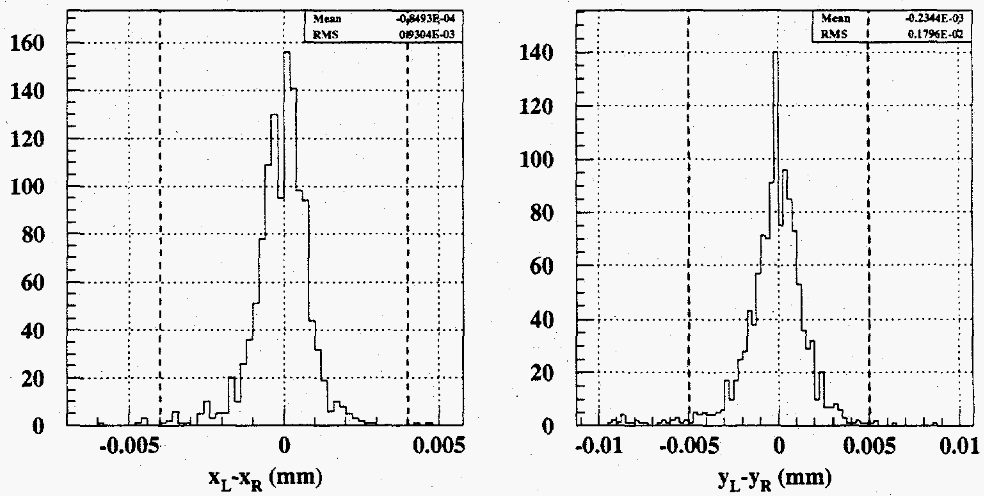

Fig. 3.37. Difference between average over run beam positions for left and right helicities. Cut values are shown by dashed lines.

for "left" ("right") electrons in x. The cut eliminates 33 polarized runs. It ensures that the position-dependent bias to the raw asymmetry does not exceed $0.5 \cdot 10^{-4}$.

3.7.2.4 Polarization bit

The polarization state of the beam was sent to the Data Acquisition System via four physically distinct pathways: the PMON line, Mach line, Pockels Cell High Voltage Line and the Veto Bits. Each measurement delivered a two-bit combination, where the combination '01' referred to positive helicity photons and '10' meant that the photons incident on the photocathode were of negative helicity. Combination '00' in the PMON meant that the beam is unpolarized, and '11' marked an error condition. During E142, reading of the Veto module was found to fail at high rates[126] that caused a bias in the asymmetry analysis. The problem was solved prior to E154.

The electron helicity was governed by a pseudo-random bit generator at the electron source. The seed of the generator can be determined by measuring the polarization state of 33 consecutive spills.[92] After the seed is determined, the polarization state of any subsequent spill can be predicted if the sequence number of the spill is known. Such a sequence number was provided by the PMON module. The predictor code thus provided a fifth determination of the spill helicity state.

All methods typically agreed to $\approx 10^{-5}$ level[92] (the failure rate can only be tested to $\approx 5 \cdot 10^{-6}$ level for a given run since the typical run size is 200,000 spills). However, 18 runs were found to have a failure rate of more than $10 \cdot 10^{-4}$,[92] *i.e.* comparable to the raw asymmetry. These runs have been excluded from the asymmetry analysis. In addition, for 35 runs in the range 2454 through 2494, the Veto signal was in error.[92] Those runs are included in the asymmetry analysis and the polarization state is determined by other four measurements.

3.7.3 Event selection

3.7.3.1 Beam cut

The purpose of the beam cut was to get rid of spills with beam properties very different from the average, for these may potentially bias the measured electron asymmetry. Such a cut should be reasonably mild, on another hand, as tight cuts have lower efficiency and may adversely affect the electron asymmetry if a particular beam parameter has large left-right asymmetry. We applied a cut of 4σ to the following beam quantities:

1. Beam charge.
2. Good spill ADC.
3. Bad spill ADC.
4. Beam width at the wire array in x.
5. Beam width at the wire array in y.
6. Beam position at the wire array in x.
7. Beam position at the wire array in y.
8. Beam position at the TWBPM in x.
9. Beam position at the TWBPM in y.

The distributions of bad spill ADCs and beam position in y before and after the cut are shown in Fig. 3.38. The number of spills rejected by each cut is given in Fig. 3.39.

Cuts (1), (3), and (7) are most important. We believe this is justified. Big fluctuations in the incident charge could introduce fluctuation in electron rate due

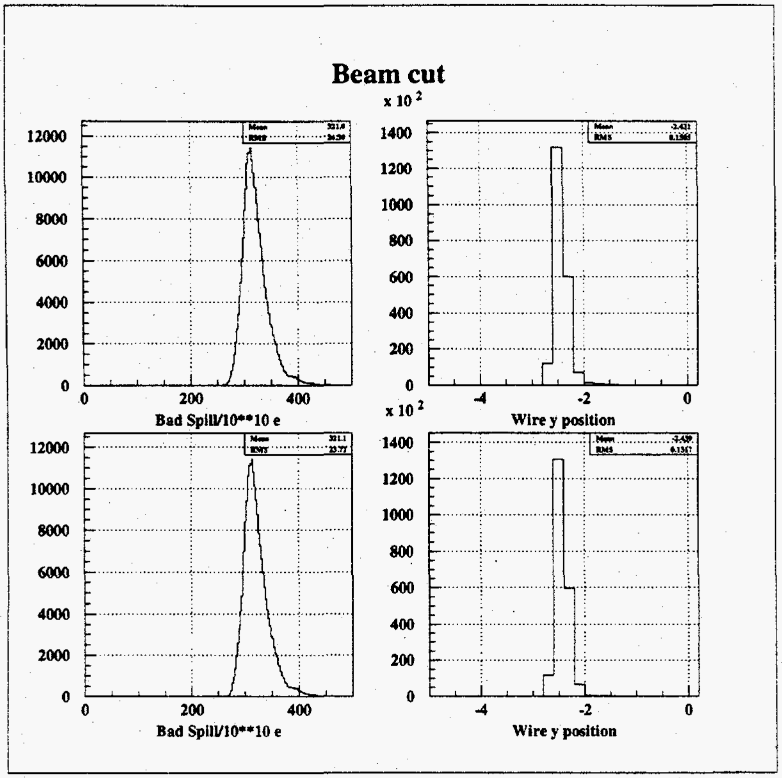

Fig. 3.38. Distribution of two quantities used in the beam cut before (top) and after (bottom) the cut. Bad spill ADC is shown on the left and the beam position at the wire array in y is on the right. The tails of both distributions are smaller after the cut.

to rate dependence. The dependence of electron rate on the beam position has been observed (see Fig. 3.36) and is not insignificant. The bad spill ADC, positioned in the alcove, has historically been an indicator of overall beam quality.

In addition to the 4σ cut, we selected only spills with $0.5 \leq Q \leq 12$ (in units of 10^{10} electrons: cut # 0 in Fig. 3.39). This mainly gets rid of the "witness" pulses used for accelerator tuning. We also require the match of all four hardware polarization signals (PMON, Mach Line, Scaler, and Veto: cut # -1 in Fig. 3.39)[15].

We calculated the mean and RMS of every value used in the cut every 1056 spills (32 cycles of the random number generator for the polarization bits). These values

---

[15] For runs between 2440 and 2495, the Veto module is believed to have been malfunctioning[92], so we are using a three-fold coincidence.

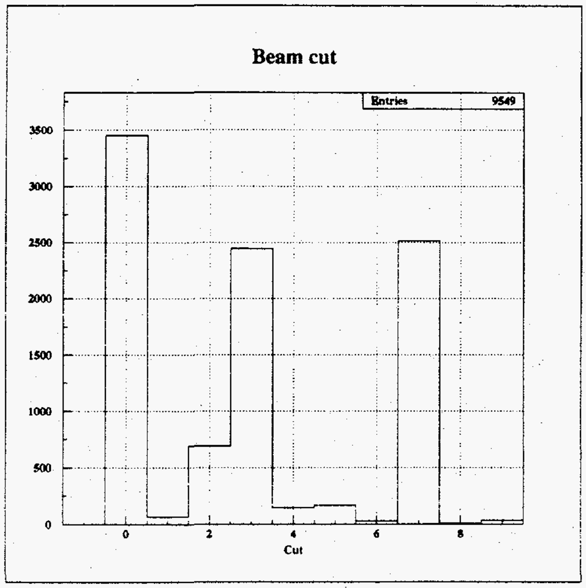

Fig. 3.39. Number of spills rejected by each beam cut. See text for explanation of cut numbers.

are then applied to the next 1056 spills. Thus, the cut is "sliding", it follows slow changes in the beam quantities. On another hand, short beam trips and random "flyers" that last less than ≈ 9 sec are rejected.

3.7.3.2 Electron selection

For systematic studies, we implemented 52 electron definitions and 14 pion definitions. The main definition for the asymmetry analysis was chosen to maximize efficiency (statistics), minimize pion contamination, and minimize rate dependence. The electron definition, found as a best compromise among the criteria above and denoted as "definition 33", is defined by the following set of cuts:

1. Class 1 track with both Cherenkov in coincidence;
2. Acceptance cut passed;
3. $8\ \mathrm{GeV} < p < 48.3\ \mathrm{GeV}$;

4. $Q^2 \geq 1$ GeV^2, $W^2 \geq 8$ GeV^2;
5. One of the Cherenkov signals greater than 2.5 photoelectrons ("AND-OR" cut)
6. $E > 7.5$ GeV;
7. $E/p \geq 0.8$;
8. Shower shape $\chi \leq 0.045$ for $p < 30$ GeV (see Eq. (3.16));
9. No DAQ failures for the spill in the given spectrometer.

The acceptance cut (2) is defined by

$$-\theta_{\max} \leq \theta \leq \theta_{\max}, \quad \phi_{\min} \leq \phi \leq \phi_{\max}, \tag{3.43}$$

where θ and ϕ are the horizontal and vertical scattering angles at the target limited by $\theta_{\max} = 0.006(0.013)$, $\phi_{\min} = -0.031(-0.028)$, and $\phi_{\max} = 0.005(0.01)$ for 2.75°(5.5°) spectrometer (all angles are relative to the central spectrometer angle and are in rad). The relation between the Cherenkov peak voltage and number of photoelectrons in cut (5) is given in Section 3.3.

The main differences with the SLAC analysis are in cuts (5), (7) and (8). The differences between the shower shape χ cut and neural network cut used at SLAC (cut (8)) are discussed in Section 3.4. The "AND-OR" cut (5) was found to have a smaller rate dependence by about 1%[114] compared to the "AND" cut used at SLAC (which required both Cherenkov hits to be higher than 25 FADC units). It also had a slightly higher efficiency (by about 2.5%) than the "AND" cut with a comparable pion rejection power. In addition to the $E/p \geq 0.8$ cut (7), SLAC analysis required a cut on high side of the peak $E/p \leq 1.2$. This cut was found to have a significant rate dependence[114] (about 2%, or more than a factor of two higher than low E/p cut) without compensating gain in the pion rejection.

3.8 Asymmetry analysis

Summary files produced for each run in the DST analysis were used to extract the raw experimental asymmetries $A_{\parallel}^{\mathrm{raw}}$ and $A_{\perp}^{\mathrm{raw}}$:

$$A_{\parallel}^{\mathrm{raw}}(x) = \frac{(N(x)/Q)^{\downarrow\Uparrow} - (N(x)/Q)^{\uparrow\Uparrow}}{(N(x)/Q)^{\downarrow\Uparrow} + (N(x)/Q)^{\uparrow\Uparrow}}\,, \tag{3.44}$$

where $N(x)/Q$ is the number of events in each helicity state passing the analysis cuts normalized to the incident charge. The expression for $A_{\perp}^{\mathrm{raw}}$ is analogous to Eq. (3.44). The Bjorken x and four momentum transfer squared Q^2 of an event were determined from the momentum and scattering angle of reconstructed electrons. The statistical error, in the limit of small $A_{\parallel}^{\mathrm{raw}}$ (the raw electron asymmetries are on the order of 10^{-3}) is given by

$$\sigma(A_{\parallel}^{\mathrm{raw}}) = \frac{\sqrt{(N(x)/Q^2)^{\downarrow\Uparrow} + (N(x)/Q^2)^{\uparrow\Uparrow}}}{(N(x)/Q)^{\downarrow\Uparrow} + (N(x)/Q)^{\uparrow\Uparrow}}\,. \tag{3.45}$$

The raw experimental asymmetries in Eq. (3.44) must be corrected before they can be used in Eq. (1.23) and Eq. (1.24) to calculate the spin-dependent structure functions. First, we account for the fact that the target and beam were not completely polarized, and that the detected electrons can be scattered from the unpolarized materials in the target such as glass cell end windows. The correction is applied by multiplying the raw asymmetries by a factor $1/(fP_bP_t)$ (*cf.* Eq. (1.10) and Eq. (1.11)). Second, some events that passed our cuts are not the true DIS events whose asymmetry we are interested in. Furthermore, the data sample is contaminated to a small degree by pions misidentified as electrons. In addition, a certain portion of electrons came from the charge symmetric processes (such as $\pi^0 \rightarrow e^+e^-\gamma$, $\gamma \rightarrow e^+e^-$ etc.). Such events should be subtracted from the data sample. The raw asymmetries are also corrected for rate dependence of asymmetries as discussed in Section 3.6 and radiative effects. Finally, a small correction is applied to account for a parity-violating asymmetry coming from the interference of the γ

and Z^0 exchange amplitudes. Combining all corrections, the physics asymmetry that can be used to calculate the polarized structure functions takes the form:

$$A^{\text{phys}} = \frac{A^{\text{raw}}_{e^-} + \Delta A^{\text{rate}} - P_b A^{\text{EW}}}{f P_b P_t} + \Delta A^{\text{RC}} \,, \tag{3.46}$$

where $A^{\text{raw}}_{e^-}$ is the raw asymmetry (with backgrounds subtracted), ΔA^{rate} is the rate dependence correction of Eq. (3.40), A^{EW} is the electro-weak parity-violating asymmetry, ΔA^{RC} is the additive radiative correction, f, P_b, and P_t are the ^{3}He dilution factor, beam, and target polarizations, respectively.

We will discuss the corrections mentioned above in the following Sections.

3.9 Background subtraction

The sample of events that passed our electron cuts is not purely electrons coming from the DIS events. First, charged hadrons (pions, and to a much lesser degree kaons) and muons could be misidentified as electrons. Moreover, a certain portion of electrons we detected came from the charge symmetric processes (such as charge symmetric decays and pair production). These events dilute the DIS sample, and could even distort the asymmetry if the production processes have significant spin dependence. Let π/e and A_π denote the fraction of misidentified hadrons (relative to the number of all electrons) and pion asymmetry, respectively. Similarly, let e^+/e^- and A_{e^+} denote the fraction of electrons from the charge symmetric processes and their asymmetry. The asymmetry of purely DIS events is then given by (x dependence omitted)

$$A^{\text{raw}}_{e^-} = \frac{1}{1 - e^+/e^-} \left[\frac{A^{\text{raw}} - (\pi/e) A_\pi}{1 - \pi/e} - (e^+/e^-) A_{e^+} \right] . \tag{3.47}$$

We will discuss each background separately.

3.9.1 Pion background

3.9.1.1 Pion contamination

The number of negatively charged hadrons (referred to as π^- hereafter) in the electron data sample was estimated by comparing the E/p spectrum of well-identified pions and the E/p distribution of the events passing our cuts. As an example, we will take the electron "definition 2", that requires 2 Cherenkov signals in coincidence higher than 1.5 photoelectrons, $E/p \geq 0.8$, and does not use the shower shape cut. Pions can be identified requiring a veto in both Cherenkovs with a negligible electron contamination. The E/p spectrum of events satisfying definition 2 at low E/p is dominated by pions. Matching two spectra at low E/p (where both spectra have a peak due to pions that do not shower), we can estimate the size of a pion tail leaking under the electron E/p peak (see Fig. 3.40). The pion contamination π/e is given by the ratio of the number of pions to the number of electrons with $E/p \geq 0.8$. The same procedure was applied to the electron definitions that do use the shower shape χ cut, but the statistical uncertainty was bigger in those cases.

The pion contamination for the worst case, target Dave (data were taken at "high" current of $9 \cdot 10^{10}$ electrons per spill) , is plotted in Fig. 3.41 for definition 33. Even for this target, it does not exceed 10%. The average pion contamination at low x in the 2.75° spectrometer was 2.8% and smaller at higher values of x. Two independent methods were employed to check the estimates of the pion contaminaiton[127] and were found to yield similar results. The error on π/e is dominated by systematics (estimated as a discrepancy between different methods used to determine the contamination) and is taken to be 50% of the value of π/e.

3.9.1.2 Pion asymmetry

Pion asymmetry was measured using the DST tapes produced in the dedicated production (in which we included class 2 tracks and lifted the energy cut-off in

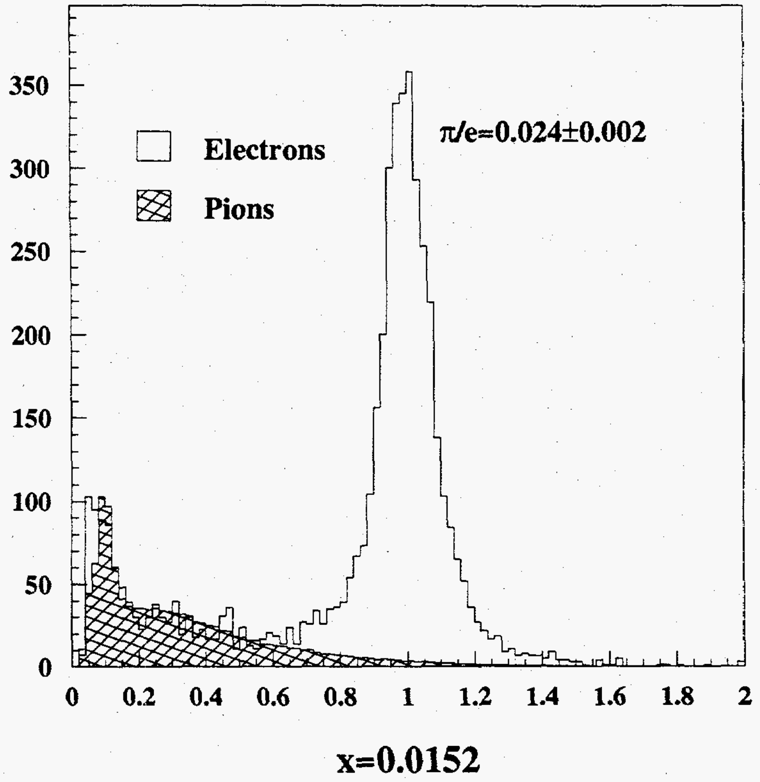

Fig. 3.40. Pion contamination in the 2.75° spectrometer at $x = 0.0152$. Error is statistical. See text for discussion.

clustering (see Section 3.4.2). The pion asymmetry $A_{\parallel}^{\pi}$ (divided by the dilution factor and beam and target polarizations) for both negatively and positively charged pions is shown in Fig. 3.42. This is perhaps the largest data sample on asymmetry in the inclusive hadron photo-production. The asymmetry is approximately three times smaller than the electron asymmetry and is *not* consistent with zero. It is interesting to note that the π^+ asymmetry is almost a factor of two bigger (in absolute value) than the π^- asymmetry.

3.9.2 Charge symmetric background

The event rate of electrons originating in the charge symmetric processes was measured by reversing the polarity of the spectrometer magnets. The positron

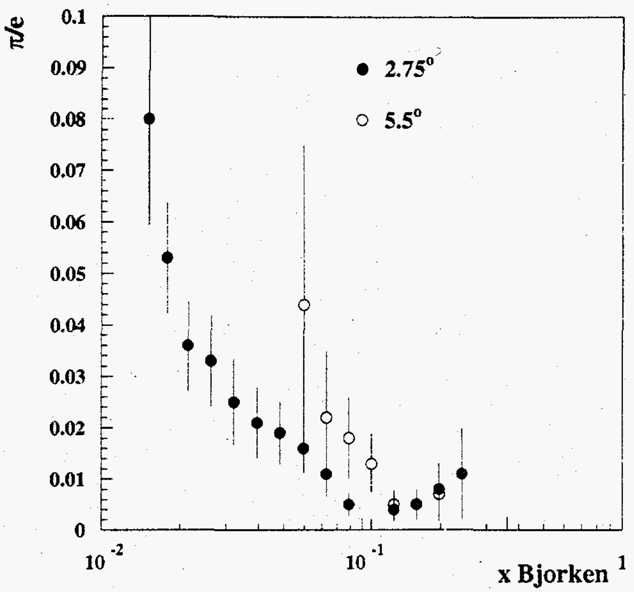

Fig. 3.41. Pion contamination in the 2.75° (solid circles) and 5.5° (open circles) spectrometers versus Bjorken x for electron definition 33, target Dave. Error is statistical.

component of the background was measured and assumed equal to the electron component of the charge symmetric background.

A total of 81 positron runs (with the longitudinally polarized target) with target cell Picard was used to determine the ratio e^+/e^- and the asymmetry A_{e^+}. The extracted "positron contamination" e^+/e^- is shown in Fig. 3.43 and the positron asymmetry (divided by the dilution factor and beam and target polarizations) is shown in Fig. 3.44.

The positron rate was also measured with the empty and full reference cells. It is believed that the main source of the charge symmetric background is photoproduction (or electro-production with $Q^2 \approx 0$) via processes $\gamma p \to \pi^0 p$, $\pi^0 \to e^+e^-\gamma$ and $\gamma \to e^+e^-$ etc. The rate of real (or almost real) photons depends on the radiation length (thickness) of the target and the rate of the photon conversion is approximately linear with it, hence the positron rate increases as a second (or even higher) power of the target thickness. Since the electron rate is to the zeroth order

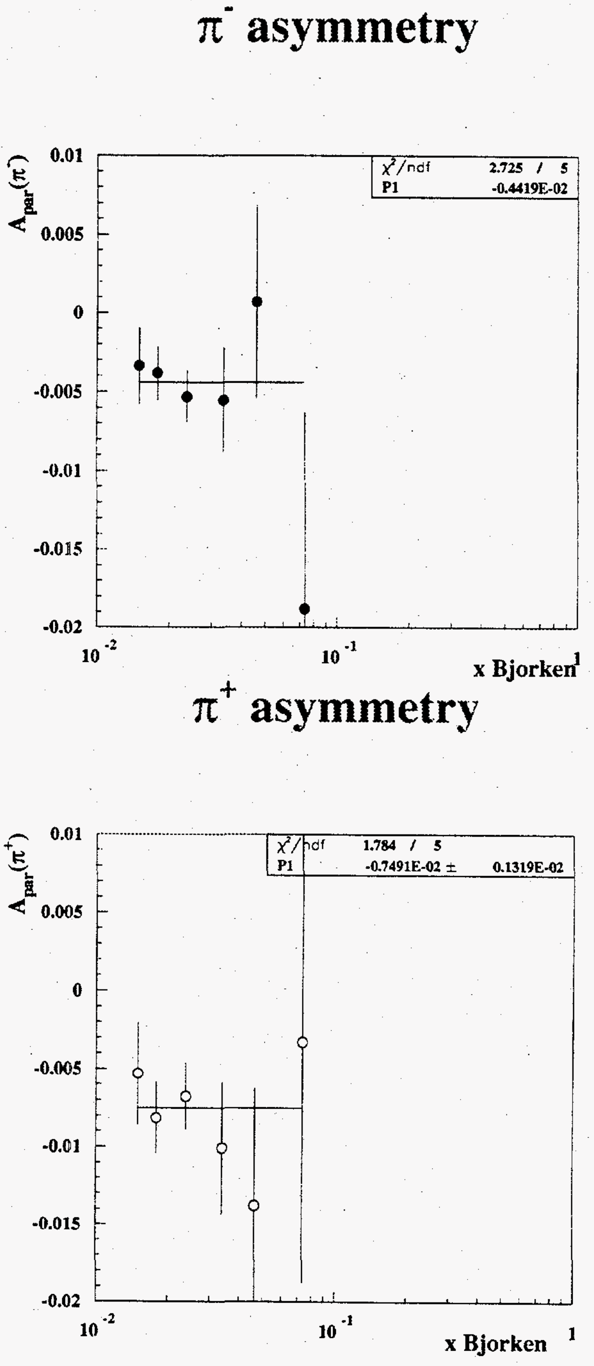

Fig. 3.42. Asymmetries for production of negative (top) and positive (bottom) pions as a function of x.

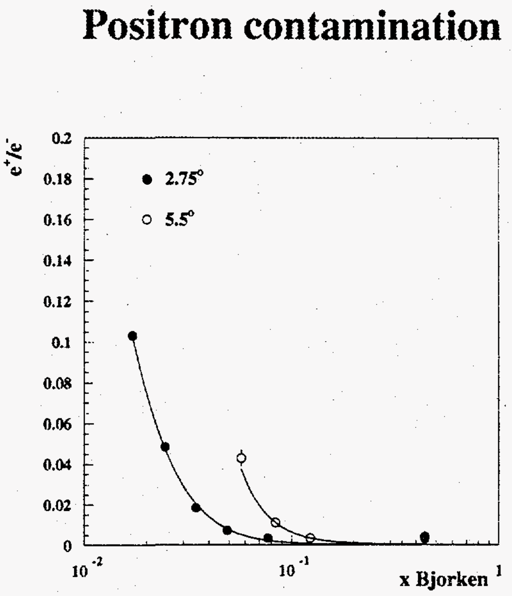

Fig. 3.43. Ratio e^+/e^- in 2.75° (solid circles) and 5.5° (open circles) spectrometers as a function of x. Error bars are statistical only.

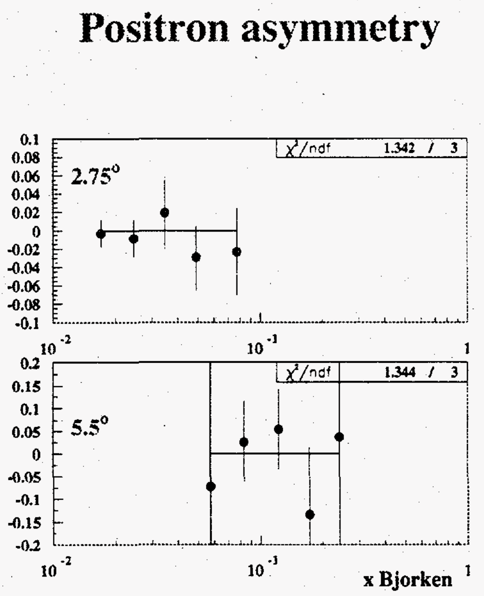

Fig. 3.44. Positron asymmetry measured in 2.75° (top) and 5.5° (bottom) spectrometers as a function of x. The χ^2 for the asymmetry being consistent with zero is given for reference.

proportional to the target thickness, the ratio e^+/e^- is expected to be different for different target pressures and geometries. The variation of about 20% was observed with different empty reference cells, and about 10% with full reference cells. Since the positron runs were not taken with every polarized cell, we assign a 20% systematic error to the ratio e^+/e^-.

The positron asymmetry is found to be consistent with zero, albeit with large uncertainty. It is also consistent within errors with both π^- and π^+ asymmetries. For the electron asymmetry correction, we assume the positron asymmetry $A_{e^+} = 0$ and use the statistical errors on the measurement to estimate the systematic uncertainty on g_1^n due to the charge symmetric backgrounds. This uncertainty dominates the systematic error on g_1^n in the lowest x ($x = 0.017$) where the e^+/e^- ratio is the biggest (see Section 4.2). This error could be significantly decreased if a theoretical guidance regarding the physics of the charge-symmetric backgrounds was available. For instance, if the dominant mechanism for the creation of the e^+e^- pairs is the photo-production (either direct or via the π^0 decay), the same process that dominates the pion production, it seems feasible (on the basis of isospin symmetry) that the positron asymmetry is bound by π^- and π^+ asymmetries. If we used such a bound, the systematic uncertainty in the lowest x would have decreased by $\approx 40\%$. On another hand, if we averaged the positron data over all x (relying on an assumption that the kinematic dependence of the asymmetry is not very strong), the systematic error at $x = 0.017$ would have decreased by $\approx 30\%$. Lacking the theoretical guidance, we have taken a conservative approach and subtracted the charge-symmetric background bin-by-bin.

3.10 Dilution Factor

In order to extract the physics asymmetries $A_{\parallel}^{\mathrm{phys}}$ and $A_{\perp}^{\mathrm{phys}}$ for ^{3}He, we should correct for events that have originated from scattering off the unpolarized material in the target. The ratio

$$f = \frac{\text{number of electrons scattered off } ^3\text{He}}{\text{total of number of events}} \tag{3.48}$$

is called a dilution factor. This factor is roughly 1/2 where the rest of the events come from the glass end windows and a small amount of nitrogen in the target. The dilution factor can be calculated using measured unpolarized cross sections, and knowing the composition of the target.[128] The dilution factor can also be measured with the reference cells by varying ^{3}He pressure. Both methods are discussed below.

3.10.1 Theoretical dilution factor

The theoretical expression for the dilution factor is given by

$$f(x, Q^2) = \frac{R_{\rm He}(x, Q^2)}{R_{\rm He}(x, Q^2) + R_{\rm N}(x, Q^2) + R_{\rm gl}(x, Q^2)} \tag{3.49}$$

where $R_{\rm He,N,gl}$ are the rates of scattering off ^{3}He, N_2, and glass. These are given by

$$R_i(x, Q^2) = (Z_i\, F_2^p(x, Q^2) + (A_i - Z_i)\, F_2^n(x, Q^2))\, f_{\rm RC}\, f_{\rm EMC}(A_i, x)\, n_i\, L_i\ , \tag{3.50}$$

where A_i and Z_i are the atomic weight and number of each target component, F_2 is the unpolarized structure function,[129] $f_{\rm RC}$ is the unpolarized multiplicative radiative correction, and $f_{\rm EMC}$ is the EMC factor[74] that takes into account effects of nuclear binding and motion. The atomic density and the length of the material i are n_i and L_i.

For the calculation, we use F_2 parameterization from Ref. [129], and parameterizations of the EMC effect from Ref. [130,131]. The parameters of the target model are given in Ref. [132] (see also Section 2.5). On average, 53% of all events are coming from scattering off ^{3}He, 43% off glass, and the remaining 4% off N_2. The biggest systematic error is due to the uncertainty in radiative corrections, that corresponds to uncertainty and variations of the target model, and ranges from 5% at low x to 0.7 at mid-x. Uncertainties in window thickness and F_2 each contribute $\approx$ 1% to the error on dilution factor.

3.10.2 Experimental dilution factor

An important feature of our experiment is the ability to measure the dilution factor experimentally using the reference cells. Reference cells are targets with geometry similar to that of the polarized ^{3}He targets, but that could have a variable ^{3}He pressure. To the extent that the geometries of the reference and polarized target cells are exactly the same, the dilution factor can be measured as

$$f(x,Q^2) = \frac{R_{\text{full}}(x,Q^2) - R_{\text{empty}}(x,Q^2)}{R_{\text{polarized}}} , \tag{3.51}$$

where $R_{\text{full,empty,polarized}}$ are scattering rates from the full and empty reference cells and polarized ^{3}He target, respectively. In reality, we extract the dilution factor by measuring the slope of event rate versus ^{3}He pressure and comparing it to the scattering rate from the polarized cell:

$$f = \frac{\partial R_{\text{ref}}}{\partial P_{\text{ref}}} \frac{P_{\text{polarized}}}{R_{\text{polarized}}} \frac{L_{\text{polarized}}}{L_{\text{ref}}} , \tag{3.52}$$

where P_{ref} and $P_{\text{polarized}}$ are the reference and polarized cell pressure, and L_{ref} and $L_{\text{polarized}}$ are the lengths of the reference and polarized cells. The scattering rates are corrected for rate dependence, and for charge symmetric and hadronic backgrounds.

3.10.3 Dilution factor results

The comparison of the theoretical and experimental dilution factor from target cell Picard is shown in Fig. 3.45. The agreement is generally very good. The experimental results are limited by statistics, especially at high x in the 5.5° spectrometer. For the asymmetry analysis, we use the theoretical values. For each target cell, we add in quadrature the average disagreement between two methods (on average, less than 1%) to the error on the theoretically calculated dilution factor. The average error on dilution factor, weighted by statistical error on $A_{\parallel}$ is 5.1%.[128]

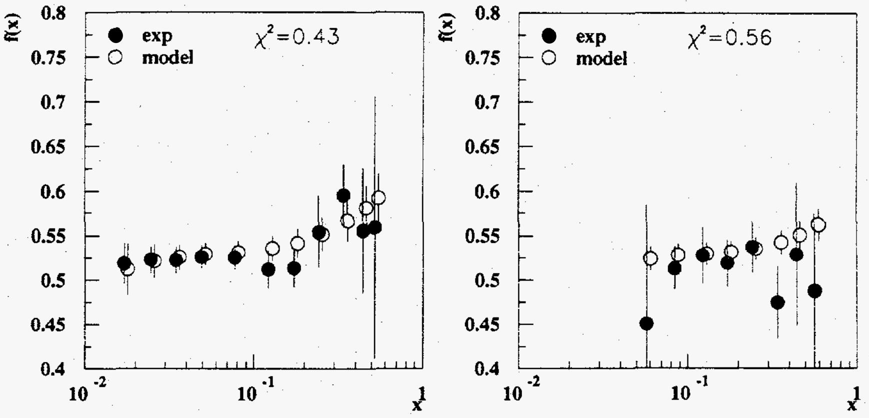

Fig. 3.45. Comparison of the theoretically calculated (open circles) and experimentally determined (closed circles) dilution factor for the 2.75° (left) and 5.5° (right) spectrometers.

3.11 Radiative corrections

The structure functions $g_1^n(x, Q^2)$ and $g_2^n(x, Q^2)$ are defined in the Born limit, *i.e.*, for a single virtual photon exchange in the deep inelastic regime. However, experimentally observed lepton-nucleon scattering includes contributions from higher order processes as well as from elastic, quasielastic, and inelastic tails. In addition, electrons may lose energy before or after scattering due to bremsstrahlung or ionization in external material (target cell entrance and exit windows and side walls). These processes modify the measured asymmetry in Eq. (1.10), so corrections have to be applied in order to extract Born asymmetries.

The radiative corrections are traditionally divided into "*internal*" and "*external*". The internal effects are those occurring at the ^{3}He nucleus where the inelastic scattering occurs. The electrons are off-shell between the emission of the photon and the nuclear scattering. The external effects are those which modify the electron energy before or after the DIS event, hence, the electrons are on-shell.

3.11.1 Internal radiative correction

In addition to the single-photon exchange, the experimentally observed lepton-nucleon scattering cross sections include contributions from higher order processes. At any $(x_{\rm DIS}, Q^2_{\rm DIS})$, there is radiative leakage from other kinematic points ($x \geq x_{\rm DIS}$, $Q^2 \leq Q^2_{\rm DIS}$ for radiation before, and $Q^2 \geq Q^2_{\rm DIS}$ for radiation after scattering), referred to as elastic, quasielastic, and inelastic tails. Since the asymmetries of the tails are not *a priori* identical to the deep-inelastic Born asymmetries, the measured asymmetry must be corrected. The formalism for calculating the radiative corrections (RC) to spin-dependent DIS has been developed by Kukhto, Shumeiko, and Akushevich[133] and implemented in their Fortran code POLRAD 1.5.[134] An independent code was developed by Linda Stuart[135] based on the formalism of Ref. [133] and produced identical results.

At any kinematic point (x, Q^2), the measured asymmetries are given by

$$A^{\rm meas} = \frac{\Delta\sigma^{\rm Born} V + \Delta\sigma^{\rm tails}}{\sigma^{\rm Born} V + \sigma^{\rm tails}} \,, \tag{3.53}$$

where

$$\sigma^{\rm tails} = \sigma^{\rm el} + \sigma^{\rm qel} + \sigma^{\rm res} + \int_{\tilde{x} \geq x} d\tilde{x} \int d\tilde{Q}^2 \, \sigma^{\rm DIS}(\tilde{x}, \tilde{Q}^2) \tag{3.54}$$

are the contributions from the elastic, quasielastic, resonance, and DIS radiative tails, respectively. The correction due to higher-order processes V is given by

$$V = \delta_R^{IR} + \delta_{\rm vert} + \delta^l_{\rm vac} + \delta^h_{\rm vac} \,. \tag{3.55}$$

Here σ_R^{IR} is the correction due to soft photon emission (where the infra-red divergence is cancelled by a similar contribution to DIS tail[136]), $\sigma_{\rm vert}$ is the lepton vertex correction, $\sigma^l_{\rm vac}$ is the lepton vacuum polarization, and $\sigma^h_{\rm vac}$ is the hadronic vacuum polarization. The soft photon and virtual corrections to the cross section are insensitive to the helicity state; these contributions factorize in Eq. (3.53). Thus, the radiative corrections come entirely from the difference between the Born asymmetry

Table 3.5. Contributions to the measured polarized and unpolarized cross sections at $x = 0.017$ from radiative tails, virtual and external corrections (relative to the Born cross section).

	Elastic	Quasielastic	DIS	Resonance	Virtual	External
Unpolarized	0.12	0.20	0.30	0.06	0.11	−0.02
Polarized	0.11	−0.01	0.02	0.04	0.11	−0.02

and asymmetries of the radiative tails. We will now discuss the contributions from each of the tails.

With the emission of a hard photon by the incident electron before scattering, the energy and Q^2 of the event are lowered. Since the form factors of the nucleons in ^{3}He are roughly proportional to $1/Q^4$ at high Q^2, the probability of scattering quasielastically is enhanced. The asymmetry of the quasielastic scattering, expressible in terms of products of form factors $G_E G_M$ and G_M^2,[137] is different from the DIS asymmetry. Radiative effects thus mix in this asymmetry with the DIS asymmetry in which we are interested. The magnitude of this contribution increases as we move to lower x and Q^2. Details of the nuclear structure of ^{3}He are important in the evaluation of this contribution. Predictions for the S, S', and D percentages of the ^{3}He wave function (see Section 1.6) are used to determine the relative contributions from the quasielastic asymmetries of the protons and neutrons in ^{3}He. The correction due to the elastic scattering off the ^{3}He nucleus is small for the E154 kinematics. The relative contributions of elastic and quasielastic tails to the unpolarized and polarized cross sections are summarized in Table 3.5.

The inelastic tail contribution arises similarly to the processes discussed above. Electrons detected in the spectrometers that undergo hard photon emission before the scattering have their energy E' overestimated. Similarly, bremsstrahlung after the scattering results in underestimation of the scattered electron energy E'. In both cases, the event is assigned a lower value of Bjorken x (and higher value of

Q^2). Therefore, DIS asymmetries from higher x, as well as asymmetries from the resonance region $W^2 < 4$ GeV^2 are mixed into the asymmetry measured at lower x.

3.11.2 External radiative correction

Before and after the DIS event, electrons may lose energy by bremsstrahlung and, to much smaller extent, by ionization in interactions with other target nuclei. Similar to internal effects, these interactions mix the asymmetry at a given kinematic point $x_{\mathrm{DIS}}, Q^2_{\mathrm{DIS}}$) with asymmetries from a broad region $x \geq x_{\mathrm{DIS}}$. Thus, the measured (uncorrected) asymmetries are given in terms of convolutions of polarized and unpolarized cross sections and electron straggling probabilities over this kinematic range. The external radiative corrections are calculated using the formalism of Mo and Tsai.[138]

The external radiative effects depend on the thickness of the material traversed by the electrons before and after the DIS interaction. The dominant source of external radiative corrections are the side walls of the target through which the electrons pass at very shallow angles. The target NMR pickup coils were modified prior to E154, and one of the major contributions to the external radiative corrections, important for E142,[122] was eliminated. Overall, the effect of external radiative corrections to the measured asymmetries is very small.

3.11.3 Calculating the correction

Equation (3.53) can be re-written in terms of the convolution of the Born DIS cross section and the internal (external) bremsstrahlung probabilities (with the helicity indices suppressed):

$$\begin{aligned}\sigma^{\mathrm{meas}}(E_0, E') &= \sigma^{\mathrm{Born}}(E_0, E') + \int d\epsilon_0 \psi_{\mathrm{in}}(\epsilon_0/E_0, E')\sigma^{\mathrm{Born}}(\epsilon_0, E') + \\ &\quad \int d\epsilon \psi_{\mathrm{out}}(E_0, E'/\epsilon)\sigma^{\mathrm{Born}}(E_0, \epsilon) , \qquad (3.56)\end{aligned}$$

where E_0 and E' are the initial and final electron energies, and ψ_{in} and ψ_{out} are the straggling probabilities before and after the scattering, respectively. Evaluation of the integrals in Eq. (3.56) requires knowledge of the unpolarized and polarized cross sections over the large phase space, including the DIS region, which is precisely what we are trying to extract. Thus, we cannot solve it analytically; instead, an iterative technique is employed. We define the radiative correction to the measured asymmetry by

$$\Delta A^{\mathrm{RC}} \equiv A^{\mathrm{Born}} - A^{\mathrm{meas}} . \tag{3.57}$$

A smooth parameterization to the measured $g_1^{\mathrm{He}}(x)/F_1^{\mathrm{He}}$ is used to calculate the initial estimate of A^{Born}, then at every i-th iteration we take $A_i^{\mathrm{Born}} = A_{i-1}^{\mathrm{Born}} + \Delta A_{i-1}^{\mathrm{RC}}$. The process typically converges after 3-4 iterations.

3.11.4 Radiative correction and experimental Errors

It is obvious from the discussions above, that the experimental uncertainties on ΔA^{RC} are correlated to those on A^{meas}. Not only is this true at every experimental point, but the convolutions in Eq. (3.56) also introduce point-to-point correlations. This makes the propagation of errors through the radiative corrections a rather complicated issue. We identify three types of experimental errors on A^{Born}:

- Statistical error $\sigma_{\mathrm{stat}}(A^{\mathrm{Born}})$: propagated statistical error on A^{meas};
- Systematic error $\sigma_{\mathrm{syst}}(A^{\mathrm{Born}})$: propagated systematic error on A^{meas} due to sources other than RC; and
- Errors on A^{tail} and unpolarized cross sections – true RC systematic error $\sigma_{\mathrm{RC}}(A^{\mathrm{Born}})$ – to be added in quadrature to other systematic errors.

The statistical errors on A^{meas} are uncorrelated from point to point, and we assume systematic errors to be 100% correlated from point to point. Then, for a given experimental point i, the propagated errors are given by

$$\sigma^2_{\mathrm{stat}}(A_i^{\mathrm{Born}}) \;=\; \sigma^2_{\mathrm{stat}}(A_i^{\mathrm{meas}}) \left(1 + \frac{\partial \Delta A_i^{\mathrm{RC}}}{\partial A_i^{\mathrm{meas}}}\right)^2 + \sum_{j \neq i} \sigma^2_{\mathrm{stat}}(A_j^{\mathrm{meas}}) \left(\frac{\partial \Delta A_i^{\mathrm{RC}}}{\partial A_j^{\mathrm{meas}}}\right)^2 \tag{3.58}$$

$$\sigma_{\text{syst}}(A_i^{\text{Born}}) = \sigma_{\text{syst}}(A_i^{\text{meas}})\left(1+\frac{\partial \Delta A_i^{\text{RC}}}{\partial A_i^{\text{meas}}}\right) + \sum_{j\neq i}\sigma_{\text{stat}}(A_j^{\text{meas}})\left(\frac{\partial \Delta A_i^{\text{RC}}}{\partial A_j^{\text{meas}}}\right). \tag{3.59}$$

In practice, the partial derivatives are evaluated numerically by varying the value of A_i^{meas} for every point independently within its statistical and systematic uncertainties. In order to include point-to-point correlations into the error on the integrals of g_1^n and g_2^n, the full correlation matrix is constructed. The off-diagonal elements of the correlation matrix are typically small.

In the absence of the off-diagonal elements, the uncertainty on the Born asymmetry is bigger than the error on the measured asymmetry by a factor

$$\frac{1}{f} = 1 + \frac{\partial \Delta A_i^{\text{RC}}}{\partial A_i^{\text{meas}}}\,. \tag{3.60}$$

The factor f can be viewed as a "dilution factor" that accounts for the fact that the radiative tails are really backgrounds to our measurement. This dilution factor is given by the ratio of the unpolarized cross sections

$$f = \frac{\sigma^{\text{meas}} - \sigma^{\text{tails}}}{\sigma^{\text{meas}}}\,, \tag{3.61}$$

where the "tails" include contributions from the elastic, quasi-elastic, resonance, and parts of the DIS tails. Due to the infra-red divergence,[136] the definition of the DIS tail is ambiguous.[139] We only include those points in x that are more than two bins away from the x of the measurement, beyond the range of a typical variation of g_1.[139] The "dilution factor" method of calculating the error on the Born asymmetry agrees with the method of Equations (3.58) and (3.59), and for practical purposes was adopted for the published results.

The systematic uncertainty on the radiative corrections is estimated by varying the input models of unpolarized and polarized cross sections (form factors for elastic and quasielastic scattering, nuclear corrections in ^{3}He unpolarized structure functions, models of the resonance region, contributions from g_2, and possible Q^2

Table 3.6. Systematic errors of the radiative corrections for the 2.75° and 5.5° spectrometers (× 100).

x bin	F_2	g_1 reson.	Q^2 dep.	g_2	$G^{p,n}_{e,m}$	Pauli	Elast
2.75° spectrometer							
0.017	0.018	0.025	0.031	0.019	0.017	0.006	0.004
0.025	0.049	0.022	0.011	0.015	0.007	0.004	0.003
0.035	0.030	0.020	0.003	0.010	0.003	0.002	0.002
0.049	0.010	0.018	0.000	0.007	0.001	0.001	0.001
0.078	0.006	0.015	0.000	0.004	0.000	0.000	0.000
0.123	0.013	0.014	0.000	0.002	0.000	0.000	0.000
0.173	0.001	0.015	0.000	0.003	0.000	0.000	0.000
0.241	0.000	0.018	0.000	0.003	0.000	0.000	0.000
0.340	0.001	0.026	0.000	0.005	0.000	0.000	0.000
0.423	0.000	0.045	0.000	0.007	0.000	0.000	0.000
5.5° spectrometer							
0.057	0.039	0.045	0.000	0.034	0.012	0.003	0.006
0.084	0.023	0.041	0.000	0.024	0.007	0.002	0.004
0.123	0.005	0.031	0.000	0.019	0.005	0.001	0.002
0.173	0.021	0.023	0.000	0.016	0.002	0.000	0.002
0.242	0.001	0.017	0.000	0.014	0.001	0.000	0.001
0.342	0.000	0.009	0.000	0.018	0.000	0.000	0.000
0.442	0.000	0.007	0.000	0.029	0.000	0.000	0.000
0.564	0.000	0.008	0.000	0.062	0.000	0.000	0.000

dependence[77] of the ratio g_1/F_1 below $Q^2 = 1$ GeV^2) and the target model (for external corrections). The contributions from the various sources for two spectrometers are given in Table 3.6.[139] The radiative corrections for $A_{\|}$[140] and their errors[139] are given in Table 3.7.

Note that traditionally the "radiative dilution factor" was calculated assuming that only the elastic and quasi-elastic tails are backgrounds to the DIS measurement.[135] The uncertainty in the DIS asymmetries was included into the overall systematic error by varying the *shape* of the function used to parameterize the measured asymmetries.[140] This approach is inconsistent, subjective, and generally leads to incorrect results. First, the resonance and DIS tails have to be treated as

Table 3.7. Radiative corrections (× 100), the effect on the propagated errors, and the systematic errors of the radiative corrections.

x bin	ΔA^{RC}	$\sigma\left(A^{\mathrm{Born}}\right)/\sigma\left(A^{\mathrm{meas}}\right)$	Syst.
2.75° spectrometer			
0.017	-0.341	1.686	0.051
0.025	-0.285	1.500	0.057
0.035	-0.233	1.334	0.038
0.049	-0.192	1.216	0.022
0.078	-0.151	1.154	0.017
0.123	-0.122	1.113	0.019
0.173	-0.099	1.068	0.015
0.241	-0.081	1.049	0.018
0.340	-0.061	1.048	0.026
0.423	-0.051	1.102	0.046
5.5° spectrometer			
0.0573	-0.290	1.319	0.070
0.0837	-0.251	1.202	0.053
0.1231	-0.227	1.123	0.037
0.1725	-0.210	1.066	0.035
0.2420	-0.185	1.039	0.022
0.3424	-0.152	1.022	0.020
0.4423	-0.124	1.009	0.030
0.5643	-0.102	1.028	0.063

backgrounds and such events have to be subtracted from the data sample. Second, the variations of the functional form used to fit the measured data, deemed to test any possible "model dependence" of the radiative corrections, only change the relative weights of the data points. Many functional forms with acceptable χ^2 differ from one another by an amount comparable to the statistical errors of the data. This amount depends on the choice of the functional forms, and is very subjective. Varying the form of the fit is equivalent to varying the input values of the measured asymmetries by some fraction of their statistical errors. Thus, the variation of the Born asymmetries due to different fits used in the radiative corrections is already included into the statistical error $\sigma_{\text{stat}}(A^{\text{Born}})$. Including this variation into the systematic error $\sigma_{\text{RC}}(A^{\text{Born}})$ introduces unphysical correlations of the statistical and systematic errors, and in case of E154 increases the uncertainty $\sigma_{\text{RC}}(A^{\text{Born}})$ by about factor of two. The model dependence may appear, however, when the data are *extrapolated* outside the kinematic range of the measurement. Thus, the uncertainty due to extrapolation of the data into the low Q^2 region is included in the systematic error.

3.12 Rate dependence and electroweak corrections

The rate dependence to $A_{\|}$ is calculated as described in Section 3.6. The detector asymmetries (electron asymmetry diluted by the pion and noise hits) were typically $(3-5)\cdot 10^{-4}$ in the Cherenkov detectors, $(1-4)\cdot 10^{-4}$ in the hodoscopes, and $(1-4)\cdot 10^{-3}$ in the shower counter. The rate dependence coefficients α_i determined by pulse fiction actually place the upper limit on the true rate dependence. The "true" rate dependence is proportional to the derivative of the efficiency with respect to rate. Pulse fiction measures the finite difference of efficiencies at normal and double rate. Since the second derivative of efficiency versus rate is normally negative (*i.e.* has the same sign as the first derivative), the coefficients α_i found by pulse fiction are somewhat overestimated. So we treat the pulse fiction results as upper limits and apply only half of $\Delta A^{\rm rate}$ as a correction to the raw asymmetries, and use the full value of $\Delta A^{\rm rate}$ as a systematic error. This error ranges from 4% of $A_{||}$ at low x to 8% at high x.

The electroweak parity-violating asymmetry arises from the interference of the γ and Z^0 exchange amplitudes. It is given by[20]

$$A^{\rm EW} \equiv \frac{\sigma_R - \sigma_L}{\sigma_R + \sigma_L} = Q^2 \left(a_1 + a_2 \frac{1-(1-y)^2}{1+(1-y)^2} \right) , \tag{3.62}$$

where σ_L and σ_R are cross sections for left and right electrons, and y is the fractional energy transfer from the electron to hadrons. For an isoscalar target, neglecting strange sea, one has

$$\begin{aligned} a_1 &\approx \frac{3G_F}{5\sqrt{2}\pi\alpha} \left(-\frac{3}{4} + \frac{5}{3}\sin^2\theta_W \right) \quad \text{and} \\ a_2 &\approx \frac{9G_F}{5\sqrt{2}\pi\alpha} \left(\sin^2\theta_W - \frac{1}{4} \right) . \end{aligned} \tag{3.63}$$

The factors in the equation are the Fermi constant G_F, the fine structure constant α, and the Weinberg angle θ_W. The electroweak asymmetry is not sensitive to the polarization of the target, and it is suppressed by the reversals of the target spin. The correction is the biggest at high Q^2 (and high x) and reaches 10% of $A_{||}$ (it is however much smaller than the statistical error on $A_{||}$). We use 20% of the correction as the associated systematic uncertainty.

3.13 Final asymmetry results

The corrected physics asymmetries $A^{\rm phys}$, calculated for every run according to Eq. (3.46), were weighted by the statistical error and averaged. The results for two spectrometers are given in Table 3.8.

Table 3.8. Final results on ^{3}He asymmetries $A_\parallel$ and $A_\perp$.

x bin	$\langle x \rangle$	$\langle Q^2 \rangle$ (GeV^2)	$A_\parallel$ ± stat. ± syst.	$A_\perp$ ± stat. ± syst.
2.75° spectrometer				
0.014 − 0.02	0.017	1.21	−0.0140 ± 0.0041 ± 0.0036	0.0052 ± 0.0125 ± 0.0017
0.02 − 0.03	0.025	1.59	−0.0174 ± 0.0030 ± 0.0025	−0.0021 ± 0.0094 ± 0.0013
0.03 − 0.04	0.035	2.05	−0.0164 ± 0.0031 ± 0.0018	−0.0187 ± 0.0100 ± 0.0019
0.04 − 0.06	0.049	2.57	−0.0136 ± 0.0025 ± 0.0011	0.0142 ± 0.0080 ± 0.0015
0.06 − 0.10	0.078	3.32	−0.0107 ± 0.0023 ± 0.0009	0.0083 ± 0.0075 ± 0.0013
0.10 − 0.15	0.122	4.09	−0.0080 ± 0.0027 ± 0.0007	0.0101 ± 0.0095 ± 0.0022
0.15 − 0.20	0.173	4.63	−0.0102 ± 0.0034 ± 0.0008	0.0013 ± 0.0123 ± 0.0022
0.20 − 0.30	0.241	5.09	−0.0085 ± 0.0034 ± 0.0007	−0.0097 ± 0.0121 ± 0.0020
0.30 − 0.40	0.340	5.51	−0.0030 ± 0.0058 ± 0.0005	0.0357 ± 0.0200 ± 0.0038
0.40 − 0.50	0.423	5.82	0.0035 ± 0.0137 ± 0.0007	0.0043 ± 0.0443 ± 0.0008
5.5° spectrometer				
0.04 − 0.06	0.057	4.03	0.0126 ± 0.0256 ± 0.0027	0.1669 ± 0.1219 ± 0.0151
0.06 − 0.10	0.084	5.47	−0.0222 ± 0.0035 ± 0.0022	0.0294 ± 0.0163 ± 0.0026
0.10 − 0.15	0.123	7.23	−0.0219 ± 0.0026 ± 0.0017	0.0052 ± 0.0124 ± 0.0025
0.15 − 0.20	0.172	8.94	−0.0153 ± 0.0033 ± 0.0012	0.0043 ± 0.0154 ± 0.0033
0.20 − 0.30	0.242	10.71	−0.0161 ± 0.0033 ± 0.0013	0.0137 ± 0.0153 ± 0.0034
0.30 − 0.40	0.342	12.55	−0.0089 ± 0.0051 ± 0.0018	−0.0106 ± 0.0237 ± 0.0022
0.40 − 0.50	0.442	13.83	−0.0132 ± 0.0079 ± 0.0013	−0.0092 ± 0.0365 ± 0.0015
0.50 − 0.70	0.564	15.00	−0.0010 ± 0.0113 ± 0.0008	−0.0036 ± 0.0519 ± 0.0035

CHAPTER 4

NEUTRON SPIN STRUCTURE FUNCTIONS

4.1 From asymmetries to the structure functions

4.1.1 Structure functions and photon-nucleon asymmetries

The fully-corrected asymmetries in Table 3.8 are ready to be used to calculate the quantities of interest: the spin dependent structure functions and the virtual photon-nucleon asymmetries. At this time it is also logical to compare the results of two independent analyses. While the raw asymmetries could have been somewhat different in the SLAC and Caltech analyses (due to different contamination and corrections), the final asymmetries $A_{||}$ and $A_{\perp}$ must be identical within allowed statistical fluctuations, if both analyses are correct. For completeness, we will here list the main differences between two analyses:

- *Raw analysis*

  The DST production had started earlier at SLAC, and certain ideas were not implemented. The most important one was the FADC synchronization using the TDC information (see Section 3.3). The shower code described in Section 3.4 was used only in the Caltech analysis; the SLAC code is described in Ref. [116]. The tracking used by both analyses is described in Section 3.5 with very minor improvements not implemented in the SLAC version. The Caltech analysis stored only class 1 tracks on the DST tapes while at SLAC tracks of classes 1, 2, and 3 were kept (only class 1 tracks were used as electron candidates).

- *Run selection*

  Both analyses used the same set of runs, as described in Section 3.7.2.

- *DST analysis*

  Both codes were very similar at the level of the DST analysis. The main difference was in the beam cut, which was very generous for the SLAC analysis[141] and somewhat more restrictive at Caltech (see Section 3.7.3.1).

- *Electron selection*

  The two analyses differed in the definition of electrons (*cf.* Section 3.7.3.2). For completeness, we list below the definition adopted by the SLAC group:[141]

  1. Class 1 track with both Cherenkovs in coincidence;
  2. Acceptance cut passed;
  3. $8 \text{ GeV} < p < 48.3 \text{ GeV}$;
  4. $1 \text{ GeV}^2 \leq Q^2 \leq 25 \text{ GeV}^2$, $W^2 \geq 8 \text{ GeV}^2$;
  5. Peak voltage in both Cherenkov tanks ≥ 25 (in FADC units);
  6. $0.8 \leq E/p \leq 1.2$;
  7. Neural Network ≥ -0.98.[121]

- *Background subtraction and corrections to the raw asymmetries*

  The estimates of the pion contamination were quite different in the two analyses (*cf.* Section 3.9.1.1). The SLAC group estimated a less than 1% pion contamination using an indirect technique of scaling the π^+/e^+ ratio by the ratio of the π^-/π^+ production cross sections and the measured e^+/e^- rates[142] (a more sophisticated method, similar to the one described in Section 3.9.1.1, has been applied to the SLAC analysis data[143] and gives bigger estimates of the pion contamination, consistent with our analysis). The pion contamination was only measured for runs with the target cell Picard (the only time interval when the polarized "positron" runs were taken), and the SLAC group assumed that the contamination was constant with time. Fortunately, the pion contamination was at most 5 – 10% for the highest rate runs (see Section 3.9.1.1), so the error associated with such an assumption is not big. The background from the charge-symmetric processes was independent of the analysis cuts, and estimates of the background rates by both groups agree. The rate dependence correction was only applied to the Caltech data and was neglected by the SLAC group.

The comparison between the two sets of asymmetries is shown in Fig. 4.1. The agreement is as good as it could be, since the majority of the selected events is common. The differences between the two results are consistent with statistical fluctuations if $\approx 10 - 15\%$ of the events in the two samples are different. For the publications, we have chosen to average two results (straight average), and we have taken the larger statistical error. The averaged asymmetries are given in Table 4.1.

The averaged asymmetries $A_{||}$ and $A_{\perp}$ were used to calculate the spin dependent structure functions g_1^n and g_2^n and the photon-nucleon asymmetries A_1^n and A_2^n. Since the experimental asymmetries are given for ^{3}He, we first calculate $A_{||}$ and $A_{\perp}$ for the neutron (*cf.* Eq. (1.89)):

$$A_{||}^n = \frac{1}{p_n F_2^n}\left(A_{||}^{^3\mathrm{He}}(2F_2^p + F_2^n)f_{\mathrm{EMC}} - 2A_{||}^p p_p F_2^p\right) , \tag{4.1}$$

where $p_{n(p)}$ is the neutron (proton) polarization in ^{3}He (see Section 1.6), f_{EMC} is the EMC effect factor,[74] and $F_2^{n(p)}$ is the unpolarized structure function of the neutron (proton) (we assume that the ratio of the longitudinal to transverse cross sections $R(x, Q^2)$ is the same for proton and neutron[79]). We use the fit to the world data on g_1^p[10,12] to calculate the proton asymmetry $A_{||}^p$. The contribution of g_2^p is calculated using the Wandzura-Wilczek[36] twist-2 expression (see Eq. (1.47)) and the fit to g_1^p mentioned above. The expression for $A_{\perp}^n$ is similar to Eq. (4.1).

We use Equations (1.23) and (1.24) to calculate the spin dependent structure functions g_1^n and g_2^n of the neutron. The neutron virtual asymmetries A_1^n and A_2^n are given by Equations (1.25) and (1.26). The structure functions and the photon-

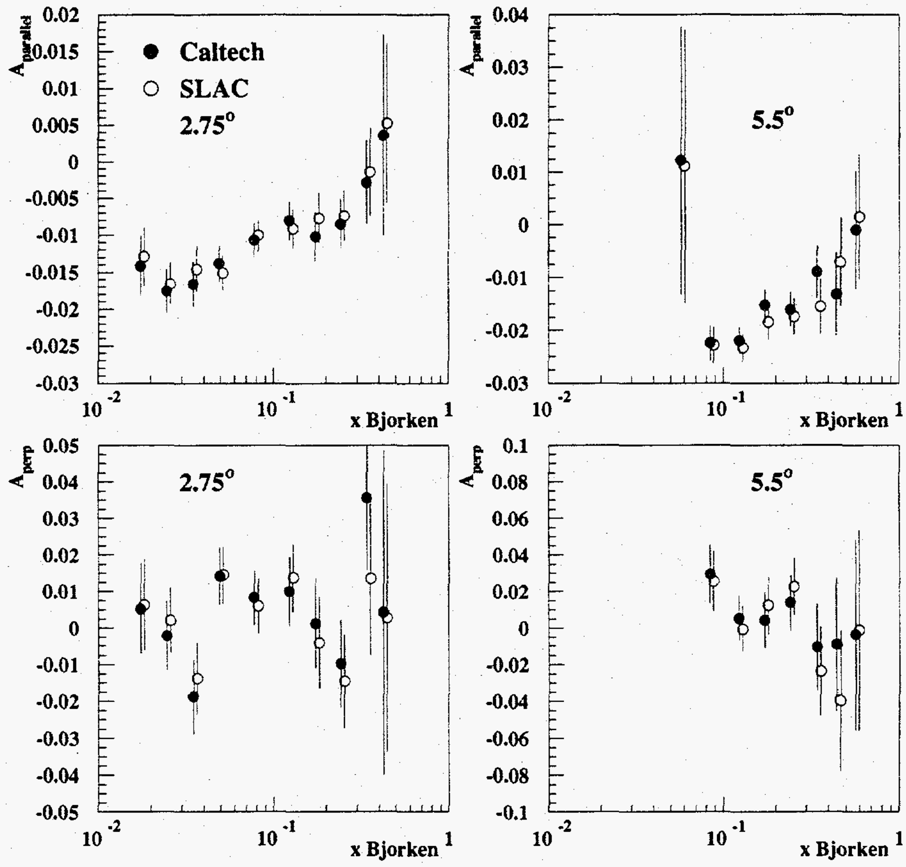

Fig. 4.1. The comparison between asymmetries $A_{||}$ (top) and $A_{\perp}$ (bottom) given by the SLAC (open circles) and Caltech (closed circles) analyses.

Table 4.1. Averaged results of the two analyses on ^{3}He asymmetries $A_{\parallel}$ and $A_{\perp}$.

x bin	$\langle x \rangle$	$\langle Q^2 \rangle$ (GeV^2)	$A_{\parallel} \pm$ stat. $\pm$ syst.	$A_{\perp} \pm$ stat. $\pm$ syst.
2.75° spectrometer				
0.014 – 0.02	0.017	1.21	$-0.0133 \pm 0.0041 \pm 0.0036$	$0.0058 \pm 0.0126 \pm 0.0018$
0.02 – 0.03	0.025	1.59	$-0.0169 \pm 0.0030 \pm 0.0025$	$0.0000 \pm 0.0094 \pm 0.0013$
0.03 – 0.04	0.035	2.05	$-0.0154 \pm 0.0031 \pm 0.0018$	$-0.0163 \pm 0.0100 \pm 0.0018$
0.04 – 0.06	0.049	2.57	$-0.0143 \pm 0.0025 \pm 0.0012$	$0.0144 \pm 0.0080 \pm 0.0015$
0.06 – 0.10	0.078	3.32	$-0.0103 \pm 0.0023 \pm 0.0009$	$0.0072 \pm 0.0075 \pm 0.0013$
0.10 – 0.15	0.122	4.09	$-0.0085 \pm 0.0027 \pm 0.0007$	$0.0120 \pm 0.0095 \pm 0.0022$
0.15 – 0.20	0.173	4.63	$-0.0089 \pm 0.0034 \pm 0.0008$	$-0.0014 \pm 0.0125 \pm 0.0022$
0.20 – 0.30	0.241	5.09	$-0.0080 \pm 0.0034 \pm 0.0007$	$-0.0121 \pm 0.0127 \pm 0.0021$
0.30 – 0.40	0.340	5.51	$-0.0022 \pm 0.0060 \pm 0.0005$	$0.0247 \pm 0.0210 \pm 0.0035$
0.40 – 0.50	0.423	5.82	$0.0044 \pm 0.0137 \pm 0.0007$	$0.0036 \pm 0.0443 \pm 0.0007$
5.5° spectrometer				
0.04 – 0.06	0.057	4.03	$0.0120 \pm 0.0260 \pm 0.0027$	$0.1582 \pm 0.1219 \pm 0.0146$
0.06 – 0.10	0.084	5.47	$-0.0224 \pm 0.0035 \pm 0.0022$	$0.0274 \pm 0.0165 \pm 0.0025$
0.10 – 0.15	0.123	7.23	$-0.0226 \pm 0.0027 \pm 0.0018$	$0.0023 \pm 0.0126 \pm 0.0025$
0.15 – 0.20	0.172	8.94	$-0.0168 \pm 0.0034 \pm 0.0013$	$0.0082 \pm 0.0157 \pm 0.0033$
0.20 – 0.30	0.242	10.71	$-0.0168 \pm 0.0034 \pm 0.0013$	$0.0182 \pm 0.0158 \pm 0.0035$
0.30 – 0.40	0.342	12.55	$-0.0123 \pm 0.0053 \pm 0.0019$	$-0.0171 \pm 0.0246 \pm 0.0024$
0.40 – 0.50	0.442	13.83	$-0.0102 \pm 0.0084 \pm 0.0012$	$-0.0245 \pm 0.0383 \pm 0.0020$
0.50 – 0.70	0.564	15.00	$0.0003 \pm 0.0119 \pm 0.0008$	$-0.0024 \pm 0.0548 \pm 0.0034$

Table 4.2. The spin dependent structure function g_1^n and the photon-nucleon asymmetry A_1^n.

$\langle x \rangle$	$\langle Q^2 \rangle$ (GeV^2)	$g_1^n \pm$ stat. $\pm$ syst.	$A_1^n \pm$ stat. $\pm$ syst.
		2.75° spectrometer	
0.017	1.21	$-0.351 \pm 0.115 \pm 0.104$	$-0.058 \pm 0.019 \pm 0.017$
0.024	1.59	$-0.374 \pm 0.071 \pm 0.062$	$-0.080 \pm 0.015 \pm 0.014$
0.035	2.05	$-0.290 \pm 0.061 \pm 0.037$	$-0.078 \pm 0.018 \pm 0.011$
0.049	2.57	$-0.212 \pm 0.041 \pm 0.021$	$-0.089 \pm 0.016 \pm 0.010$
0.078	3.32	$-0.119 \pm 0.031 \pm 0.013$	$-0.078 \pm 0.019 \pm 0.009$
0.123	4.09	$-0.075 \pm 0.030 \pm 0.009$	$-0.089 \pm 0.031 \pm 0.011$
0.173	4.63	$-0.070 \pm 0.033 \pm 0.009$	$-0.100 \pm 0.053 \pm 0.014$
0.241	5.09	$-0.053 \pm 0.028 \pm 0.007$	$-0.078 \pm 0.077 \pm 0.018$
0.340	5.51	$0.001 \pm 0.036 \pm 0.004$	$-0.166 \pm 0.206 \pm 0.051$
0.423	5.82	$0.027 \pm 0.059 \pm 0.007$	$0.166 \pm 0.606 \pm 0.038$
		5.5° spectrometer	
0.057	4.03	$0.224 \pm 0.285 \pm 0.035$	$0.045 \pm 0.120 \pm 0.012$
0.084	5.47	$-0.152 \pm 0.029 \pm 0.019$	$-0.104 \pm 0.018 \pm 0.013$
0.123	7.23	$-0.117 \pm 0.017 \pm 0.012$	$-0.110 \pm 0.015 \pm 0.012$
0.172	8.94	$-0.059 \pm 0.016 \pm 0.007$	$-0.090 \pm 0.023 \pm 0.011$
0.242	10.71	$-0.040 \pm 0.012 \pm 0.005$	$-0.118 \pm 0.030 \pm 0.016$
0.342	12.55	$-0.019 \pm 0.012 \pm 0.005$	$-0.057 \pm 0.068 \pm 0.022$
0.442	13.83	$-0.009 \pm 0.012 \pm 0.002$	$-0.013 \pm 0.146 \pm 0.018$
0.564	15.00	$0.003 \pm 0.008 \pm 0.001$	$0.100 \pm 0.294 \pm 0.032$

nucleon asymmetries are given for the two spectrometers in Table 4.2 and Table 4.3. The structure function xg_1^n is plotted in Fig. 4.2, and xg_2^n is shown in Fig. 4.3.

4.1.2 Traditional Q^2 evolution

Since the QCD sum rules are defined at a fixed four-momentum transfer, one needs to evolve the data from the Q^2 of the measurement (which is given along the line $Q^2 = Q^2(x)$, see Fig. 2.10) to a constant value, usually taken to be the average Q^2. The average Q^2 for E154 (weighted by statistics of $A_{\|}$) is ≈ 5 GeV^2. Traditionally, experiments have been using the fact that the data, albeit of the limited precision to be conclusive, are consistent with the assumption that for $Q^2 > 1$ GeV^2 the ratio of the polarized to the unpolarized structure functions g_1/F_1, or

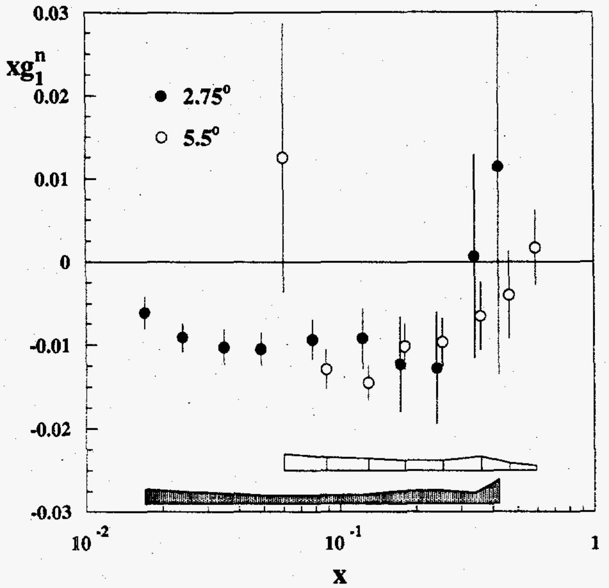

Fig. 4.2. The structure function xg_1^n measured in the 2.75° (closed circles) and 5.5° (open circles) spectrometers. The 5.5° data points are slightly offset in x for clarity. The shaded area represents one standard deviation systematic errors.

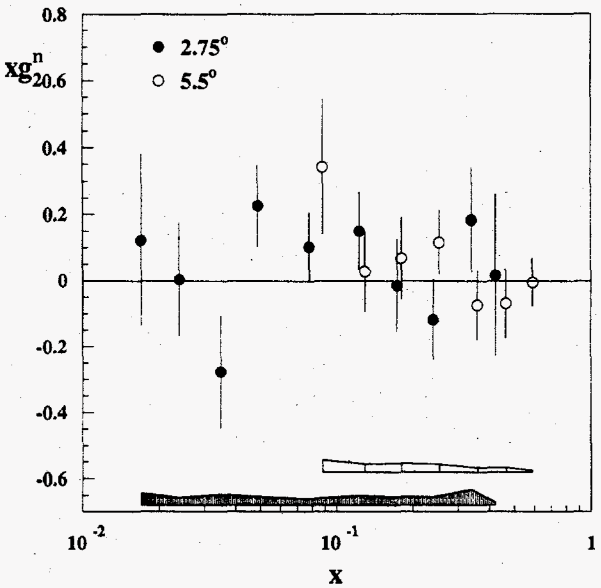

Fig. 4.3. The structure function xg_2^n measured in the 2.75° and 5.5° spectrometers. The shaded area represents one standard deviation systematic errors.

Table 4.3. The spin dependent structure function g_2^n and the photon-nucleon asymmetry A_2^n.

$\langle x\rangle$	$\langle Q^2\rangle$ (GeV^2)	$g_2^n \pm$ stat. $\pm$ syst.	$A_2^n \pm$ stat. $\pm$ syst.
		2.75° spectrometer	
0.017	1.21	$7.167 \pm 15.312 \pm 2.169$	$0.033 \pm 0.074 \pm 0.010$
0.024	1.59	$0.154 \pm 7.232 \pm 0.980$	$-0.002 \pm 0.056 \pm 0.007$
0.035	2.05	$-7.870 \pm 4.890 \pm 0.958$	$-0.106 \pm 0.064 \pm 0.013$
0.049	2.57	$4.605 \pm 2.504 \pm 0.543$	$0.099 \pm 0.056 \pm 0.012$
0.078	3.32	$1.318 \pm 1.331 \pm 0.245$	$0.058 \pm 0.065 \pm 0.012$
0.123	4.09	$1.223 \pm 0.953 \pm 0.237$	$0.127 \pm 0.106 \pm 0.026$
0.173	4.63	$-0.080 \pm 0.810 \pm 0.145$	$-0.033 \pm 0.179 \pm 0.033$
0.241	5.09	$-0.486 \pm 0.515 \pm 0.105$	$-0.251 \pm 0.241 \pm 0.049$
0.340	5.51	$0.541 \pm 0.466 \pm 0.145$	$0.635 \pm 0.550 \pm 0.126$
0.423	5.82	$0.040 \pm 0.580 \pm 0.018$	$0.162 \pm 1.414 \pm 0.040$
		5.5° spectrometer	
0.057	4.03	$41.007 \pm 31.640 \pm 4.458$	$0.945 \pm 0.727 \pm 0.103$
0.084	5.47	$4.077 \pm 2.403 \pm 0.434$	$0.161 \pm 0.099 \pm 0.018$
0.123	7.23	$0.231 \pm 1.003 \pm 0.196$	$0.009 \pm 0.080 \pm 0.016$
0.172	8.94	$0.398 \pm 0.723 \pm 0.153$	$0.052 \pm 0.112 \pm 0.024$
0.242	10.71	$0.477 \pm 0.407 \pm 0.098$	$0.145 \pm 0.136 \pm 0.031$
0.342	12.55	$-0.216 \pm 0.311 \pm 0.039$	$-0.205 \pm 0.273 \pm 0.032$
0.442	13.83	$-0.155 \pm 0.239 \pm 0.030$	$-0.360 \pm 0.532 \pm 0.047$
0.564	15.00	$-0.008 \pm 0.132 \pm 0.009$	$-0.036 \pm 0.953 \pm 0.058$

the virtual photon-nucleon asymmetry A_1 are independent of Q^2 *for any given value of* x.[77] Although the assumption contradicts a perturbative QCD analysis (as will be discussed in Chapter 5), it could be a reasonable approximation if the range of Q^2 is not very big and/or if the error due to the approximation is significantly smaller than the uncertainty on the data. We will follow the traditional approach and evolve the data to $Q^2 = 5$ GeV^2 assuming the scaling (Q^2-independence) of g_1^n/F_1^n. We will carry out the Next-to-Leading order perturbative QCD analysis of the polarized DIS data in the next chapter and return to the question of Q^2 evolution.

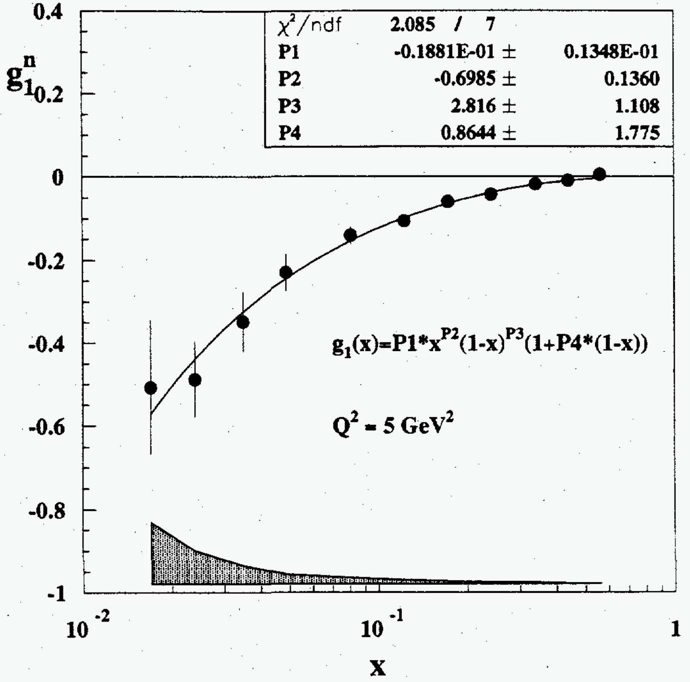

Fig. 4.4. The structure function g_1^n evaluated at $Q^2 = 5$ GeV^2. Overlaid is a fit to the data. The shaded area represents one standard deviation systematic errors.

4.1.3 Combining data from two spectrometers

The structure function g_1^n was evolved to the average $Q^2 = 5$ GeV^2 assuming the scaling of g_1^n/F_1^n, and the values of g_1 from the two spectrometers were averaged at $Q^2 = 5$ GeV^2 in the common x bins (weighted by the statistical error of g_1^n at 5 GeV^2). The average Bjorken $\langle x \rangle$ and $\langle Q^2 \rangle$ for each bin were also weighted by the statistical error of g_1^n. The average values for the structure function g_1^n and the asymmetry A_1^n are given in Table 4.4. The structure function g_1^n, evaluated at 5 GeV^2, is shown in Fig. 4.4.

4.2 Systematic errors

Many of the systematic uncertainties that affected the determination of the structure functions were mentioned in the previous sections. The contributions from

Table 4.4. Results on A_1^n and g_1^n at the measured Q^2, along with g_1^n evaluated at $Q^2 = 5$ (GeV)^2 assuming that the ratio g_1^n/F_1^n scales with Q^2. The data of two spectrometers have been averaged.

x bin	$\langle x \rangle$	$\langle Q^2 \rangle$ GeV^2	$g_1^n \pm$ stat. $\pm$ syst.	$A_1^n \pm$ stat. $\pm$ syst.	$g_1^n \pm$ stat. $\pm$ syst. ($Q^2 = 5$ GeV^2)
0.014 – 0.02	0.017	1.2	$-0.351 \pm 0.115 \pm 0.104$	$-0.058 \pm 0.019 \pm 0.017$	$-0.497 \pm 0.163 \pm 0.148$
0.02 – 0.03	0.024	1.6	$-0.374 \pm 0.071 \pm 0.063$	$-0.080 \pm 0.015 \pm 0.014$	$-0.481 \pm 0.092 \pm 0.081$
0.03 – 0.04	0.035	2.0	$-0.290 \pm 0.061 \pm 0.039$	$-0.078 \pm 0.018 \pm 0.011$	$-0.345 \pm 0.073 \pm 0.046$
0.04 – 0.06	0.049	2.6	$-0.204 \pm 0.040 \pm 0.022$	$-0.086 \pm 0.016 \pm 0.010$	$-0.228 \pm 0.045 \pm 0.024$
0.06 – 0.10	0.081	4.4	$-0.137 \pm 0.021 \pm 0.016$	$-0.092 \pm 0.013 \pm 0.011$	$-0.139 \pm 0.022 \pm 0.016$
0.10 – 0.15	0.123	6.6	$-0.108 \pm 0.015 \pm 0.011$	$-0.106 \pm 0.014 \pm 0.012$	$-0.105 \pm 0.014 \pm 0.011$
0.15 – 0.20	0.173	8.2	$-0.061 \pm 0.014 \pm 0.007$	$-0.092 \pm 0.021 \pm 0.011$	$-0.060 \pm 0.014 \pm 0.007$
0.20 – 0.30	0.242	9.8	$-0.042 \pm 0.011 \pm 0.005$	$-0.112 \pm 0.028 \pm 0.016$	$-0.043 \pm 0.011 \pm 0.005$
0.30 – 0.40	0.342	11.7	$-0.017 \pm 0.011 \pm 0.004$	$-0.068 \pm 0.065 \pm 0.021$	$-0.018 \pm 0.013 \pm 0.005$
0.40 – 0.50	0.441	13.3	$-0.007 \pm 0.011 \pm 0.002$	$-0.003 \pm 0.142 \pm 0.017$	$-0.009 \pm 0.014 \pm 0.002$
0.50 – 0.70	0.564	15.0	$0.003 \pm 0.008 \pm 0.001$	$0.100 \pm 0.294 \pm 0.032$	$0.005 \pm 0.012 \pm 0.001$

the various sources to the systematic error on $g_1^n(x)$ and on the integral in the measured range are summarized in Table 4.5.

The biggest contributions to the error on the integral in the measured range come from the scale uncertainties: dilution factor (relative error is approximately independent of x) and the target polarization. The biggest uncertainty at the lowest $x = 0.017$ is due to the asymmetry in the charge-symmetric processes. This error could potentially be reduced if some theoretical guidance (regarding the kinematic dependence of the asymmetry or its relation to the well measured pion asymmetry) was available (see Section 3.9.2).

4.3 Discussion of the results

The E154 data on g_1^n give the most precise determination of the spin-dependent structure function of the neutron to date. Our results are compared with the data from the previous SLAC experiments E142[9] and E143[10,11] in Fig. 4.5. The agreement among the data sets is very good. The E154 data extends the measurement of g_1^n to lower values of x and improves the precision by about factor of 2. Our results are compared to the data of the SMC experiment at CERN[12,13] in Fig. 4.6. The two data sets are complementary at low x since the SMC data extends to $x \approx 0.003$, albeit with large uncertainties.

The most striking feature of the E154 data is the behavior of the structure function at low x. Not only does it not converge to zero as x becomes smaller, but the behavior is very divergent (see Fig. 4.4). This is even more evident if the data are plotted on a log-log scale (Fig. 4.7). The data below $x = 0.1$ can be accurately fitted with a $g_1^n \sim x^{-0.8}$ power law. The low x power of the global fit (see Fig. 4.4) is -0.7 ± 0.1, or several standard deviations away from the naive Regge expectation[1]

---

[1] To actually estimate the statistical significance of the results one needs to take into account the correlations between the parameters of the fit. We will return to this question in Section 4.4.3.

Table 4.5. Contributions to the systematic error on g_1^n for every x bin and on the integral over the measured range.

Contribution	$\langle x \rangle$											Integral
	0.017	0.024	0.035	0.049	0.081	0.123	0.173	0.242	0.342	0.441	0.564	
P_b	0.0177	0.0171	0.0113	0.0070	0.0044	0.0033	0.0019	0.0014	0.0007	0.0004	0.0000	0.0012
P_t	0.0328	0.0316	0.0209	0.0130	0.0081	0.0061	0.0036	0.0026	0.0013	0.0007	0.0001	0.0023
f	0.0436	0.0291	0.0173	0.0094	0.0077	0.0054	0.0037	0.0029	0.0011	0.0017	0.0004	0.0024
F_2	0.0088	0.0074	0.0051	0.0039	0.0022	0.0018	0.0010	0.0008	0.0004	0.0003	0.0002	0.0007
R	0.0196	0.0182	0.0131	0.0070	0.0030	0.0017	0.0006	0.0002	0.0000	0.0000	0.0001	0.0008
E'	0.0105	0.0100	0.0071	0.0047	0.0032	0.0026	0.0019	0.0019	0.0009	0.0005	0.0009	0.0008
p_n	0.0116	0.0112	0.0080	0.0053	0.0032	0.0024	0.0014	0.0010	0.0004	0.0002	0.0001	0.0008
p_p	0.0041	0.0038	0.0035	0.0032	0.0028	0.0026	0.0024	0.0021	0.0016	0.0012	0.0007	0.0011
g_1^p	0.0282	0.0221	0.0078	0.0047	0.0027	0.0015	0.0015	0.0010	0.0005	0.0004	0.0004	0.0004
RC	0.0189	0.0163	0.0083	0.0046	0.0034	0.0028	0.0022	0.0004	0.0004	0.0006	0.0005	0.0011
Rate	0.0376	0.0261	0.0153	0.0084	0.0032	0.0015	0.0011	0.0007	0.0006	0.0002	0.0001	0.0012
A_π	0.0049	0.0031	0.0014	0.0008	0.0004	0.0002	0.0001	0.0000	0.0000	0.0000	0.0000	0.0001
π/e	0.0056	0.0067	0.0031	0.0011	0.0008	0.0004	0.0001	0.0000	0.0000	0.0000	0.0000	0.0002
A_{e^+}	0.1208	0.0469	0.0231	0.0063	0.0066	0.0021	0.0008	0.0007	0.0037	0.0000	0.0000	0.0011
e^+/e^-	0.0238	0.0098	0.0024	0.0005	0.0004	0.0001	0.0000	0.0000	0.0000	0.0000	0.0000	0.0003
EW	0.0010	0.0008	0.0006	0.0006	0.0006	0.0005	0.0005	0.0004	0.0003	0.0003	0.0002	0.0002
Total	0.1476	0.0809	0.0459	0.0242	0.0162	0.0110	0.0072	0.0054	0.0047	0.0025	0.0014	0.0045

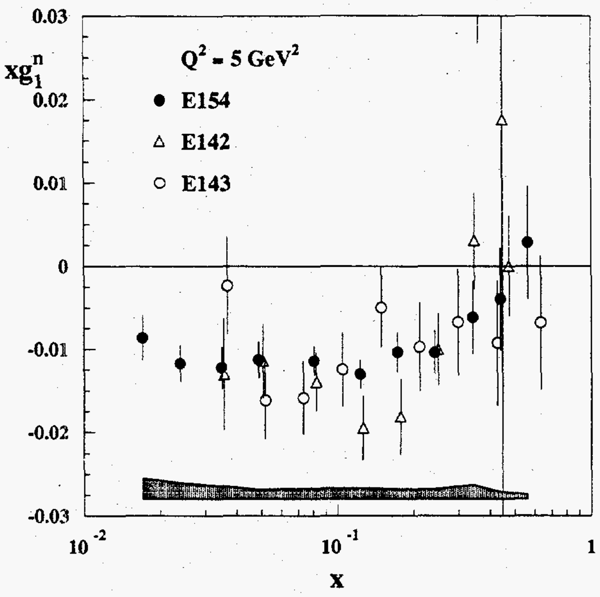

Fig. 4.5. The E154 results on the structure function xg_1^n (closed circles) compared to the E142 (open triangles) and E143 (open circles) data. The E142 and E143 data points are slightly offset in x for clarity. The shaded area represents one sigma systematic errors of E154.

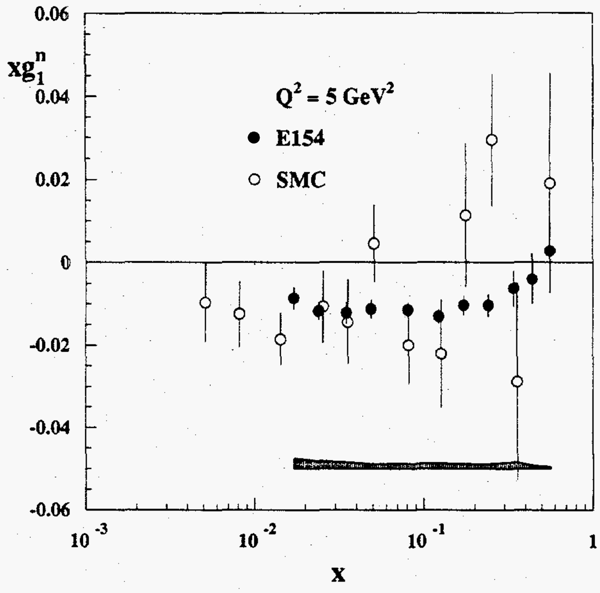

Fig. 4.6. A comparison of the E154 (closed circles) and SMC (open circles) data. The shaded are represents one standard deviation systematic errors.

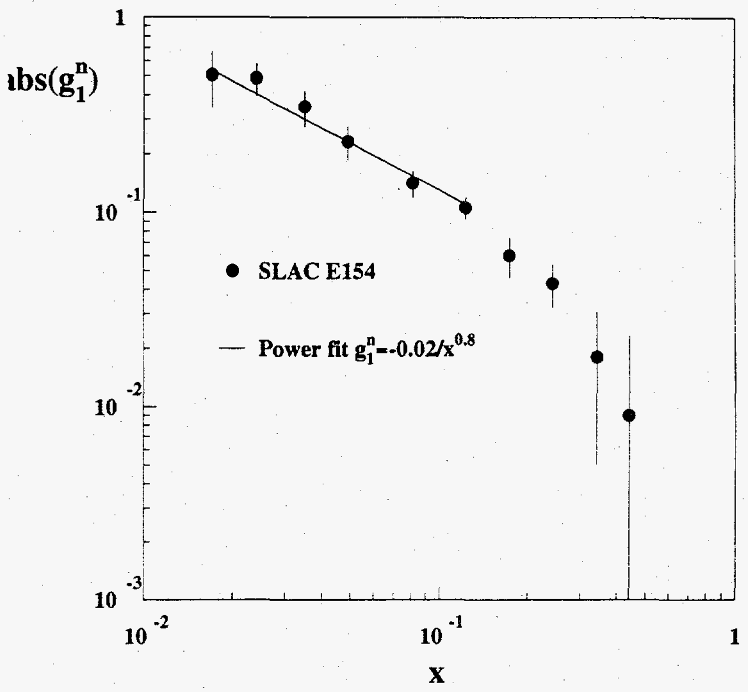

Fig. 4.7. The absolute value of structure function g_1^n is plotted on a log-log scale. The low x data points of E154 are fitted with a power-law function $g_1 \sim x^{-0.8}$.

$\alpha = 0$. Such a divergent behavior makes the extrapolation to $x = 0$ problematic, as will be discussed in the following Section.

4.4 Integrals

4.4.1 Data range

The integral of g_1^n in the data range was obtained by summing the values of the structure function in every bin multiplied by the width of the bin. The statistical errors are uncorrelated from bin to bin, and are added in quadrature. Most of the systematic errors are largely correlated bin-to-bin and therefore are added linearly. The uncorrelated errors (errors on positron asymmetry, pion asymmetry, and g_1^p) are added in quadrature. The final result for the integral in the data range is

$$\int_{0.0135}^{0.7} dx\ g_1^n(x) = -0.0360 \pm 0.0039 \pm 0.0045\ , \tag{4.2}$$

where the first uncertainty is statistical, and the second is systematic.

4.4.2 High x extrapolation

The kinematic range of any experiment is limited, and the data need to be extrapolated to $x = 0$ and $x = 1$ in order to compute the full integral of g_1 and test the sum rules. The extrapolation to $x = 1$ is straightforward. The quark-counting rules predict (see Section 1.4.1) the leading twist contribution of the structure function to fall off as $g_1 \sim (1-x)^3$ (or even faster due to the Q^2 evolution) as $x \to 1$. The higher-twist contributions may have a slower dependence (see Section 1.3.2.2), but it is the leading twist contribution that we are interested in. We assume the $(1-x)^3$ dependence of g_1^n at high x and use the value of g_1^n in the last bin to set the scale. The contribution to the integral from the unmeasured high x region is then

$$\int_{0.7}^{1} dx \ g_1^n(x) = (0.15 \pm 0.42 \pm 0.04) \cdot 10^{-3} \ , \tag{4.3}$$

where the first uncertainty is statistical, and the second is systematic.

4.4.3 Low x extrapolation

A much more important contribution comes from the unmeasured low-x region. While the high-x extrapolation is well justified theoretically and the contribution to the integral is negligible, the extrapolation to $x = 0$ is much less certain. As was discussed in Section 1.5, the theoretical models vary widely in this region. The traditional approach, taken by all spin structure experiments prior to E154, was to assume the convergent Regge behavior $g_1 \sim x^{-\alpha}$ where the Regge intercept α is associated with the trajectory of the a_1 meson and is bound between -0.5 and 0.[65,66] This assumption was consistent with the E142 neutron data,[9] and the E143 proton[10] and deuteron[11] data (which was limited to $x > 0.03$), but just barely agreed with the high energy SMC proton data.[12] The Regge theory does not explicitly specify the kinematic domain in which the prediction of the asymptotic behavior is applicable (see Section 1.5). The approach adopted by the experimental collaborations[9-11] was to fit the data with the Regge-type function $g_1 \sim x^{-\alpha}$, $\alpha < 0$ below $x = 0.1$ (that corresponds to $\sqrt{s} > 6$ GeV cutoff at $Q^2 \approx 5$ GeV^2, and the total γp cross sections are successfully described in that kinematic range by Regge theory[64]). This function does not apparently fit the E154 neutron data. Fitting the g_1^n data with a $g_1^n = const$ form (*i.e.* saturating the upper limit on the a_1 intercept) results in a $\chi^2 = 24$ for 4 degrees of freedom (where only uncorrelated errors are taken into account). This χ^2 corresponds to the confidence level of $0.8 \cdot 10^{-4}$; inclusion of the point-to-point correlated errors increases the confidence level to $0.4 \cdot 10^{-3}$. However, one may still fit the three lowest x points ($x < 0.04$) to a constant with a reasonable $\chi^2 = 1.7$ for 2 degrees of freedom. Since the Regge prediction is not very specific, we may not *a priori* discard the possibility that the convergent behavior sets in at this, or even lower value of x.

Lacking a satisfactory description of the low x data by a conventional theory, we shall resort to other phenomenological fits to the data. Several possible functional forms have been discussed in Section 1.5. To illustrate the possible spread among models divergent at low x, we fit the data to the Pomeron-Pomeron cut form[67,68] $g_1^n \sim 1/(x \ln^2 x)$, and to the generic power law $g_1^n \sim x^{-\alpha}$ with α being a free parameter. The Pomeron-Pomeron form fits reasonably well the four lowest x points ($x \leq 0.06$). To fit the power-law form we use the five lowest x points ($x \leq 0.1$). In addition, a "global" parameterization of the form

$$g_1^n = C x^{-\alpha} (1-x)^{\beta} \tag{4.4}$$

that does not require a low-x cutoff, could be used to extrapolate the data to $x = 0$. All eleven data points are used to obtain the parameters of the "global" fit (Fig. 4.4). The results of the fits are listed in Table 4.6 together with the integral from the unmeasured low x region and the resulting integral over the full x range[2]. Three

---

[2] For the multi-parameter fits, the parameter correlation matrix was used to calculate the error on the integrals.

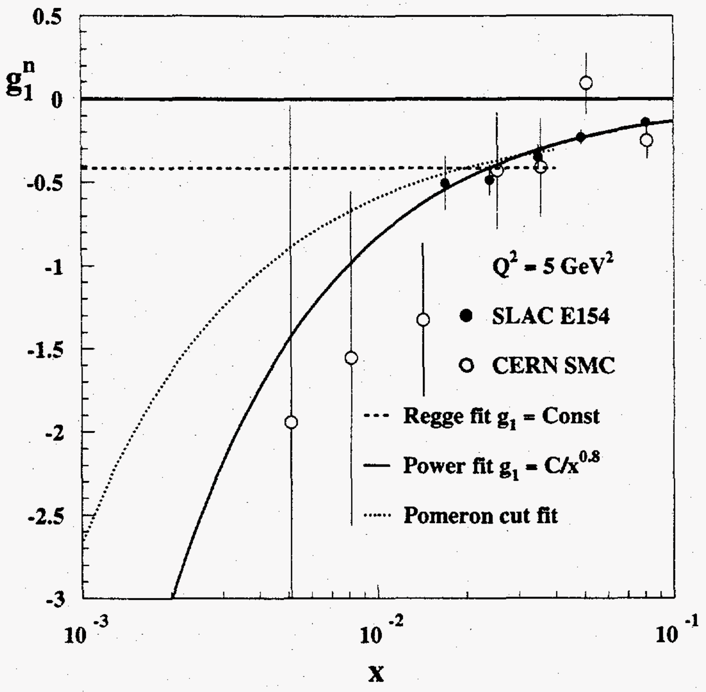

Fig. 4.8. Three representative fits to the low x data of E154. Also included are the low-x data of SMC (open circles).

representative fits are shown in Fig. 4.8 for which the low-x power was fixed at 0.8, the average of the "global" and free power fit.

The spread of the possible contributions from the low x region is very big even for moderately convergent models. Note that the free-power fit gives a value of the exponent α that is very close to unity, in fact, $\alpha > 1$ is consistent with the data within statistical or systematic errors. Since the integral diverges if $\alpha > 1$, we do not quote any uncertainty; the integral is simply *less than 1 standard deviation from infinity.* This is not very satisfactory; clearly, precise high energy data are needed to determine the behavior of the structure functions at low x.

4.5 Sum rules

Given the spread of the models at low x, we feel that the evaluation of the Ellis-Jaffe sum rule is not possible at present. Relatively large values of the neutron

Table 4.6. Results of the fits to the low x data of E154. The first uncertainty is statistical and the second is systematic.

Fit	points	Parameters	$\int_0^{0.0135} dx\ g_1^n$	$\int_0^1 dx\ g_1^n$
$g_1^n = C$	3	$C = -0.41 \pm 0.05 \pm 0.06$	$-0.0055 \pm 0.0007 \pm 0.0008$	$-0.0414 \pm 0.0044 \pm 0.0057$
$g_1^n = C/(x \ln^2 x)$	4	$C = -0.125 \pm 0.014 \pm 0.016$	$-0.0291 \pm 0.0032 \pm 0.0036$	$-0.0649 \pm 0.0062 \pm 0.0085$
$g_1^n = Cx^{-\alpha}$	5	$C = -0.014 \pm 0.007 \pm 0.004$ $\alpha = 0.92 \pm 0.16 \pm 0.09$	$-0.14 \pm \infty \pm \infty$	-0.17
$g_1^n = Cx^{-\alpha}(1-x)^{\beta}$	11	$C = -0.034 \pm 0.021 \pm 0.011$ $\alpha = 0.70 \pm 0.18 \pm 0.10$ $\beta = 3.2 \pm 1.6 \pm 0.7$	$-0.031 \pm 0.022 \pm 0.013$	$-0.067 \pm 0.024 \pm 0.017$

spin structure function g_1^n at low x question the validity of a naive application of the Regge theory to the present-day spin structure experiments. It would seem unnatural if the situation was any better with the proton and deuteron structure functions: most likely, the experiments have not yet reached the kinematic range and precision required to see the true asymptotic behavior at low x. A possible interpretation of our data is that the neutron structure function (or at least its derivative with respect to x) is dominated by the sea quark and gluon contributions, which in fact could produce very divergent behavior at low x[71] (we will return to this question in Chapter 5). Consequently, we do not quote a number for the quark helicity contribution $\Delta\Sigma = \Delta u + \Delta d + \Delta s$.

Figures 4.9 and 4.10 show the values of the Ellis-Jaffe and Bjorken integrals integrated from a given x_{min} value to 1. The integral over the data range of the neutron structure function exceeds the Ellis-Jaffe prediction by about factor of two, and the Bjorken sum rule is almost saturated by the integral over the measured range.

Even if the neutron and proton integrals diverge, the Bjorken sum rule could still be evaluated from the present data. The difference $(g_1^p - g_1^n)(x)$ is a purely non-singlet, valence quark distribution (if one assumed $\Delta\bar{u} = \Delta\bar{d}$) and is expected to behave much softer at low x than its singlet counterpart.[71] The difference $(g_1^p - g_1^n)(x)$ is plotted versus x in Fig. 4.11. We take E143[10] and SMC[12] data to evaluate the contribution from the proton structure function. The difference of two structure functions indeed shows a more convergent behavior; fitting a free power-law function $(g_1^p - g_1^n) = Cx^{-\alpha}$ to the first five points ($x \leq 0.1$), we get

$$\begin{aligned} C &= 0.120 \pm 0.036 \text{ (stat.)} \pm 0.005 \text{ (syst.)} \\ \alpha &= 0.52 \pm 0.10 \text{ (stat.)} \pm 0.04 \text{ (syst.)}\,. \end{aligned} \tag{4.5}$$

The contributions to the integral are

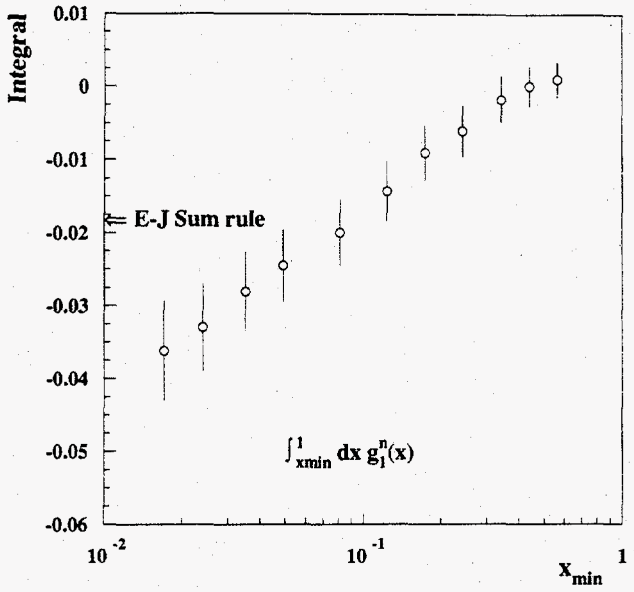

Fig. 4.9. The spin dependent structure function $g_1^n(x)$ of the neutron integrated from $x_{\rm min}$ to 1 and plotted versus $x_{\rm min}$. The statistical and systematic errors have been added in quadrature. The errors in the plot are strongly correlated from point to point.

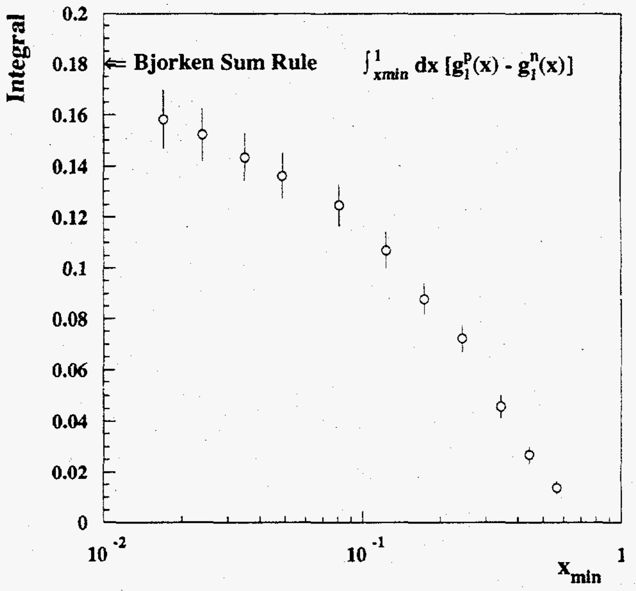

Fig. 4.10. The difference between the spin dependent structure functions g_1 of the proton and neutron integrated from $x_{\rm min}$ to 1 and plotted versus $x_{\rm min}$. E154 data was used to evaluate g_1^n, and a fit to the E143 and SMC data was used for g_1^p. The statistical and systematic errors have been added in quadrature. The errors in the plot are strongly correlated from point to point.

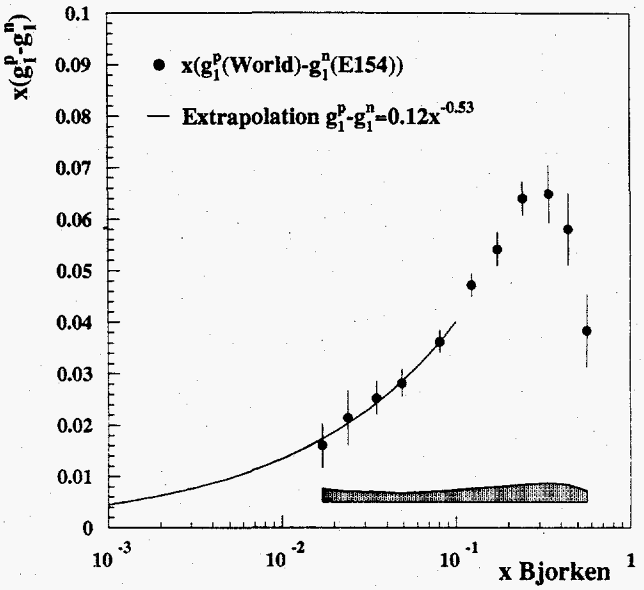

Fig. 4.11. The difference between the spin dependent structure functions xg_1 of the proton and neutron. E154 data was used to evaluate g_1^n, and a fit to the E143 and SMC data was used for g_1^p.

$$\begin{aligned} \int_{0.0135}^{0.7} dx\ (g_1^p - g_1^n) &= 0.1583 \pm 0.0052\ (\text{stat.}) \pm 0.0103\ (\text{syst.}) \\ \int_{0}^{0.0135} dx\ (g_1^p - g_1^n) &= 0.0321 \pm 0.0130\ (\text{stat.}) \pm 0.0071\ (\text{syst.}) \qquad (4.6) \\ \int_{0.7}^{1} dx\ (g_1^p - g_1^n) &= 0.0017 \pm 0.0003\ (\text{stat.}) \pm 0.0001\ (\text{syst.})\ , \end{aligned}$$

and the full integral is

$$\int_{0}^{1} dx\ (g_1^p - g_1^n) = 0.192 \pm 0.016\ (\text{stat.}) \pm 0.018\ (\text{syst.}) \qquad (4.7)$$

in a reasonable agreement with the prediction $\Gamma^{p-n} = 0.181 \pm 0.003$ evaluated at $Q^2 = 5$ GeV^2 to $O(\alpha_S^3)$ with $\alpha_S(M_Z) = 0.118 \pm 0.003$.[20] This result is quite robust against possible variations in the low x behavior: even if we assumed "Regge" behavior $(g_1^p - g_1^n) \sim const$ at low x, the full integral would be $\Gamma^{p-n} = 0.170 \pm 0.006 \pm 0.011$, consistent within uncertainties with the value in Eq. (4.7).

CHAPTER 5

NEXT-TO-LEADING ORDER QCD ANALYSIS OF THE POLARIZED DEEP INELASTIC SCATTERING DATA

5.1 Introduction

For more than two decades since the pioneering experiments in the late 1970's at SLAC,[6,7] deep inelastic scattering (DIS) of polarized leptons off polarized targets has provided information about the internal spin structure of the proton and neutron. Recent progress in both experiment and theory has made polarized DIS into a powerful tool for QCD phenomenology. On the theoretical side, a full calculation of the Next-to-Leading Order (NLO) spin-dependent anomalous dimensions has been recently completed.[37] This provides for a perturbative QCD (pQCD) analysis of polarized DIS analogous to the treatment of the unpolarized data.[144–146] At the same time, improvement in the precision of the experimental data and increased kinematic coverage has made such an analysis increasingly more meaningful.

The data reported in this dissertation is the newest addition to the world data on the spin-dependent structure functions. They are the most precise up to date determination of the neutron structure function g_1^n. The kinematic range of the measurement was extended compared to the previous SLAC experiments[9–11] to $0.014 \leq x \leq 0.7$ in the Bjorken variable and $1 \text{ GeV}^2 \leq Q^2 \leq 17 \text{ GeV}^2$ in the four-momentum transfer. Two independent spectrometers used in E154 also provided for a possibility to study the Q^2 dependence of the structure function g_1^n. The kinematic coverage of the polarized DIS experiments is illustrated in Fig. 5.1. Although, as we mentioned in Section 4.1.2, the present data are consistent with the assumption that the asymmetry A_1 (or the ratio g_1/F_1) is independent of Q^2, information on

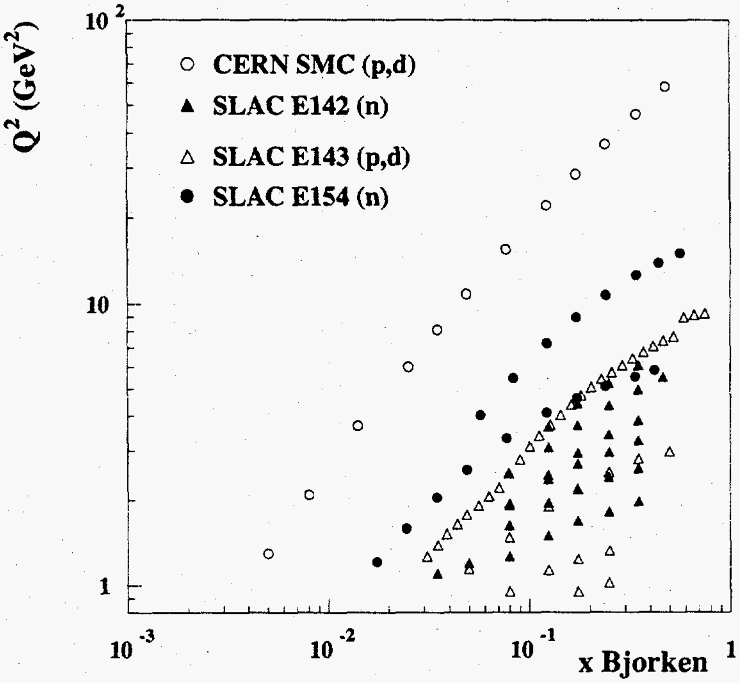

Fig. 5.1. Kinematic coverage of the present polarized DIS experiments.

the evolution of asymmetries can be extracted from the data in the framework of a consistent pQCD analysis.

As was discussed in Section 4.4.3, the relatively large values of g_1^n at low x show an apparent disagreement with a traditional Regge behavior that could be attributed to a large contribution to g_1^n from the singlet quark distribution. This implies the importance of the dynamics of polarized quark and gluon distributions, and in particular, a possibly sizable Q^2 dependence of the experimental asymmetries. It is therefore important to perform a consistent NLO analysis of the available data that would take into account theoretical and experimental uncertainties, both statistical and systematic. Among the analyses performed so far,[63,86,147] only Ref. [63] gives a detailed treatment of errors involved in extraction of the first moments of polarized parton distributions; however, the effect of experimental systematic uncertainties was underestimated. The analyses of Ref. [63,86,147] had been done before the E154 results became available, and it is interesting to see what additional information can be extracted from the new data.

In this Chapter, while paying a careful attention to the theoretical and experimental errors involved in the analysis, we will:

1. Discuss the results on the Next-to-Leading Order perturbative QCD analysis of the world data on polarized deep inelastic scattering;
2. Estimate the Q^2 dependence of the experimental asymmetries;
3. Discuss additional constraints that can be placed on the low x extrapolation of the experimental data;
4. Extract the first moments of the polarized parton distributions and structure functions.

5.2 Formalism

In the following, we will follow the notation introduced in Section 1.3. The helicity-dependent distribution functions of the quarks and antiquarks will be denoted as $\delta q(x)$ and $\delta\bar{q}(x)$, respectively. The total polarized distribution of the quarks of flavor q will be denoted as $\Delta q(x) \equiv \delta q(x) + \delta\bar{q}(x)$. The polarized gluon distribution is $\Delta G(x)$. Whenever the explicit x dependence is not specified, we will imply the *first moment* of a polarized distribution, *i.e.* $\Delta q \equiv \int_0^1 dx\, \Delta q(x)$ and $\Delta G \equiv \int_0^1 dx\, \Delta G(x)$.

In the QCD-improved parton model, the polarized structure function $g_1(x)$ of the nucleon is related to the polarized quark, antiquark, and gluon distributions $\delta q(x)$, $\delta\bar{q}(x)$, and $\Delta G(x)$ via the factorization theorem[148]

$$g_1(x, Q^2) = \frac{1}{2}\sum_q^{N_f} e_q^2 \left[C_q \otimes (\delta q + \delta\bar{q}) + \frac{1}{N_f} C_G \otimes \Delta G\right] \tag{5.1}$$

with the convolution $\otimes$ defined as

$$(C \otimes q)(x, Q^2) = \int_x^1 \frac{dz}{z} C\left(\frac{x}{z}, \alpha_S\right) q(z, Q^2). \tag{5.2}$$

The sum is over all active quark flavors N_f.

The first moments of the structure functions of the proton and neutron g_1^p and g_1^n allow one to test the fundamental Bjorken sum rule[26] and determine the helicity contents of the proton. The information on the x and Q^2 dependence gives insight into the perturbative and non-perturbative dynamics of quarks and gluons inside the nucleon. Coefficient functions $C_{q,G}(x, \alpha_S)$ correspond to the hard scattering photon-quark(gluon) cross sections and are also referred to as Wilson coefficients. They are calculated in perturbative QCD as an expansion in powers of the strong coupling constant α_S:

$$C(x, \alpha_S) = C^{(0)}(x) + \frac{\alpha_S(Q^2)}{2\pi} C^{(1)}(x) + \cdots . \tag{5.3}$$

In the leading order, $C_q^{(0)} = \delta(1-x)$ and $C_G^{(0)} = 0$ according to the simple partonic picture (*i.e.* gluons carry no net electric charge and do not couple directly to the photons, so the structure functions depend only on quark contributions, *cf.* Eq. (1.48)). The polarized NLO coefficient functions $C_q^{(1)}$ and $C_G^{(1)}$ in the modified minimal subtraction ($\overline{\mathrm{MS}}$) renormalization and factorization schemes are given in Ref. [37]. In the following, we will follow the conventional approach[86,145] and use the fixed-flavor scheme and set $N_f = 3$ in Eq. (5.1). This is justified since the Q^2 of the experiments is relatively low and even above the pair-creation threshold the heavy quarks (charm and bottom) contribute very little to the structure function g_1. The heavy quark contributions will be included in the two-loop running of α_S[20]

$$\frac{\alpha_S(Q^2)}{4\pi} = \frac{1}{\beta_0 \ln(Q^2/\Lambda_{(f)}^2)} - \frac{\beta_1}{\beta_0^3} \frac{\ln\left(\ln(Q^2/\Lambda_{(f)}^2)\right)}{\left(\ln(Q^2/\Lambda_{(f)}^2)\right)^2} \tag{5.4}$$

where the coefficients of the QCD beta function are $\beta_0 = 11 - 2f/3$ and $\beta_1 = 102 - 38f/3$. The number of active flavors f in $\alpha_S(Q^2)$ is determined by the number of quarks with $m_q^2 \leq Q^2$, $\Lambda_{(f)}$ are determined by the matching condition at the quark threshold $\alpha_S(m_q^2, f) = \alpha_S(m_q^2, f+1)$. For consistency with the evolution of the unpolarized distributions, we take[145]

$$\Lambda_{(3,4,5)}^{\overline{\mathrm{MS}}} = 248,\ 200,\ 131 \quad \mathrm{MeV} \tag{5.5}$$

with $m_c = 1.5$ GeV and $m_b = 4.5$ GeV that corresponds to $\alpha_S(M_Z^2) = 0.109$ or $\alpha_S(5\ \mathrm{GeV}^2) = 0.237$. We include the uncertainty associated with the value of α_S as will be discussed below. The parton distributions in Eq. (5.1) are those of the proton. The neutron structure function is obtained by the isospin interchange $u \Leftrightarrow d$, and the deuteron structure function is defined as

$$g_1^d = (1/2)(g_1^p + g_1^n)(1 - 1.5\omega_D)\,, \tag{5.6}$$

where the D-state probability $\omega_D = 0.05 \pm 0.01$.[149]

The Q^2 evolution of the parton densities is governed by the DGLAP equations[41–43]

$$\begin{aligned} Q^2 \frac{d}{dQ^2} \Delta q_{\mathrm{NS}}^{\eta}(x) &= \frac{\alpha_S(Q^2)}{2\pi} P_{\mathrm{NS}}^{\eta} \otimes \Delta q_{\mathrm{NS}}^{\eta}, \quad \eta = \pm 1 \\ \text{and} \quad Q^2 \frac{d}{dQ^2} \begin{pmatrix} \Delta\Sigma(x) \\ \Delta G(x) \end{pmatrix} &= \frac{\alpha_S(Q^2)}{2\pi} \begin{pmatrix} P_{qq} & P_{qG} \\ P_{Gq} & P_{GG} \end{pmatrix} \otimes \begin{pmatrix} \Delta\Sigma \\ \Delta G \end{pmatrix}, \end{aligned} \tag{5.7}$$

where the index NS stands for the the non-singlet quark distributions: valence ($\eta = 1$) $\Delta u_V(x,Q^2) = \delta u - \delta\bar{u}$, $\Delta d_V(x,Q^2) = \delta d - \delta\bar{d}$, and the $SU(3)_{\text{flavor}}$ non-singlet combinations ($\eta = -1$) $\Delta q_3(x,Q^2) = \Delta u(x,Q^2) - \Delta d(x,Q^2)$ and $\Delta q_8(x,Q^2) = \Delta u(x,Q^2) + \Delta d(x,Q^2) - 2\Delta s(x,Q^2)$. The $SU(3)_{\text{flavor}}$ singlet distribution is $\Delta\Sigma = \Delta u(x,Q^2) + \Delta d(x,Q^2) + \Delta s(x,Q^2)$. The splitting functions P_{NS}^{η} and P_{ij} are calculated perturbatively

$$P(x, \alpha_S) = P^{(0)}(x) + \frac{\alpha_S(Q^2)}{2\pi} P^{(1)}(x) + \cdots \tag{5.8}$$

with the leading order functions given in Eq. (1.58), and the next-to-leading order expressions recently obtained in Ref. [37]. Note that in the leading order, the evolution of both types of non-singlet distributions is the same: $P_{\mathrm{NS}}^{(0)\eta=-1} = P_{\mathrm{NS}}^{(0)\eta=+1} = P_{qq}^{(0)}$ and the differences only appear in the next-to-leading order. Starting with a parameterization of the parton densities at some initial scale Q_0^2, the distributions at any value of $Q^2 > Q_0^2$ are obtained using the solutions of the NLO DGLAP equations in the Mellin n-moment space[39,150] with the n-th moment defined by

$$f(n) = \int_0^1 dx\, x^{n-1} f(x). \tag{5.9}$$

In Mellin space, the DGLAP evolution is controlled by the matrix of anomalous dimensions that are related to the n-th moments of the splitting functions. We use the convention of Ref. [150] for the anomalous dimensions

$$\gamma_{ij}(n) = \left(\frac{\alpha_S(Q^2)}{4\pi}\right)\gamma_{ij}^{(0)}(n) + \left(\frac{\alpha_S(Q^2)}{4\pi}\right)^2 \gamma_{ij}^{(1)}(n) + \cdots \tag{5.10}$$

with $\gamma_{ij}^{(0)}(n) = -4\int_0^1 dx\, x^{n-1} P_{ij}^{(0)}(x)$ and $\gamma_{ij}^{(1)}(n) = -8\int_0^1 dx\, x^{n-1} P_{ij}^{(1)}(x)$. The complete set of the LO and NLO anomalous dimensions can be found in Appendix B. The parton densities evolved in Mellin space are inverted back to Bjorken x space using the prescription of Ref. [150] (see Appendix B).

One of the primary uncertainties in the interpretation of the deep inelastic scattering data at the next-to-leading order is the relative freedom in defining the hard scattering cross sections $C_{q,G}^{(1)}$ and the singlet quark density $\Delta\Sigma$ in Eq. (5.1), known as the factorization scheme dependence.[39,61,62] The factorization theorem states that at some scale Q^2, the DIS cross section can be separated into the hard part that can be calculated in perturbation theory, and soft non-perturbative quantities sensitive to the nucleon wavefunction, the parton distribution functions. Such separation is *a priori* arbitrary; since the hard-scattering cross sections $C_{q,G}$ are calculated perturbatively and need to be renormalized, one defines them by specifying an explicit renormalization procedure (*factorization scheme*)[39,62][1]. In the polarized case, the situation is further complicated by the freedom of a definition

---

[1] In DIS, the dependence on the renormalization procedure comes in two places. The *factorization scheme* applies to renormalization of the hard-scattering cross sections in Eq. (5.1). There is also a genuine *renormalization scheme* that defines the way the strong coupling is renormalized in Eq. (5.7). The two renormalization procedures do not have to be the same. However, one most often chooses the same schemes, such as $\overline{\text{MS}}$ in both cases.

of the γ_5 matrix and the Levi-Civita tensor in $n \neq 4$ dimensions[61] in dimensional regularization.[151] The choice of scale at which the factorization theorem is applied (a *factorization scale*) is also *a priori* arbitrary[152]; so in a complete calculation one always specifies a particular factorization scheme, and chooses a scale (in DIS one typically uses Q^2 as a factorization scale, as we did in Eq. (5.1)). Additional uncertainty comes from the lack of knowledge of the higher order corrections, and is conventionally referred to as a *renormalization scale* dependence (*i.e.* dependence of the results on a choice of the scale for the coupling constant in Eq. (5.3)). Several prescriptions for setting the renormalization scale exist.[153] Typically, one chooses Q^2 to be the renormalization scale and the uncertainty is estimated by varying the scale.

Given the anomalous dimensions and Wilson coefficients in one factorization scheme, any other factorization scheme can be constructed by a transformation[39]

$$\begin{aligned} \gamma_{\rm NS}^{\eta}(n) &\rightarrow \gamma_{\rm NS}^{\eta}(n) + 4\beta_0 Z_{qq}(n) \\ \gamma_{ij}^{(1)}(n) &\rightarrow \gamma_{ij}^{(1)}(n) + 2\left[Z(n), \gamma^{(0)}(n)\right]_{ij} + 4\beta_0 Z_{ij}(n) \end{aligned} \qquad (5.11)$$

$$\text{and} \quad \begin{aligned} C_q^{(1)}(n) &\rightarrow C_q^{(1)}(n) - Z_{qq}(n) \\ C_G^{(1)}(n) &\rightarrow C_G^{(1)}(n) - Z_{qG}(n)\,, \end{aligned} \qquad (5.12)$$

where $Z(n)$ is an arbitrary 2×2 scheme transformation matrix. The NLO anomalous dimensions and coefficient functions are given in Ref. [37] in the $\overline{\rm MS}$ scheme with the definition of the γ_5 matrix following Ref. [151]. The specific feature of this scheme is that the first moment of the gluon coefficient function vanishes $C_G^{(1)}(n=1) = 0$, and the gluon density does not contribute to the integral of g_1. This has been a matter of debate[56–58,61] with several authors advocating the scheme change by which the axial anomaly contribution $-(\alpha_S(Q^2)/4\pi)\sum_q e_q^2 \Delta G$ is included into the integral of g_1. This implies that for the first moment of the gluon coefficient function

$$C_G^{(1)}(n=1) = -N_f\,. \qquad (5.13)$$

An attractive feature of such a scheme is that the total quark helicity in this case is redefined as

$$\Delta\Sigma \to \Delta\Sigma(Q^2) + \frac{N_f \alpha_S(Q^2)}{2\pi}\Delta G(Q^2) \tag{5.14}$$

and is independent of Q^2 even beyond the leading order. It could also resurrect the intuitive Quark-Parton model expectation $\Delta\Sigma \approx 0.6 - 0.7$ and explain the violation of the Ellis-Jaffe sum rule if the product $\alpha_S(Q^2)\Delta G(Q^2)$ turned out to be large.[56–58]

The product $\alpha_S(Q^2)\Delta G(Q^2)$ is independent of Q^2 in the leading order since its anomalous dimension expansion starts at order α_S^2.[154] This implies that as α_S decreases logarithmically with Q^2, ΔG grows as $1/\alpha_S(Q^2)$. This growth is compensated by the increasing (with opposite sign) orbital angular momentum contribution $\langle L_z \rangle$[66,155] in order to satisfy the proton angular momentum sum rule

$$\frac{1}{2}\Delta\Sigma + \Delta G + \langle L_z \rangle = \frac{1}{2}. \tag{5.15}$$

Another consequence is that the ambiguity in the definition of the total quark helicity in Eq. (5.14) does not vanish at infinite Q^2, or in other words, the quark helicity can only be defined up to a Q^2-independent (in the leading order) constant. However, one does not lose the predictive power of perturbative QCD: as long as the factorization and renormalization schemes are used consistently, NLO predictions can be made for the spin dependent structure functions and other hadronic processes involving spin degrees of freedom (once the parton distributions are determined in one scheme and at one scale).

A transformation from the $\overline{\text{MS}}$ scheme of t'Hooft and Veltman[151] to the so-called Adler-Bardeen (AB hereafter) scheme that satisfies Eq. (5.13) was constructed in Ref. [63]. The inverse Mellin transform $Z(x)$ of matrix $Z(n)$ in Equations (5.11) and (5.12) was taken to be independent of x, the first moments of the matrix elements were fixed by the conservation of the non-singlet axial current ($Z_{qq}(n = 1) = 0$) and

Table 5.1. NLO initial unpolarized parton distributions at $Q_0^2 = 0.34$ GeV^2.[145]

$$\begin{aligned}
u_V(x, Q_0^2) &= 0.988x^{-0.457}(1-x)^{3.380}(1 + 1.58x^{1/2} + 2.58x + 18.1x^{3/2}) \\
d_V(x, Q_0^2) &= 0.182x^{-0.684}(1-x)^{4.113}(1 + 2.51x^{1/2} + 25.0x + 11.4x^{3/2}) \\
\bar{Q}(x, Q_0^2) &= 0.545x^{-0.70}(1-x)^{8.33}(1 + 2.65x) \\
G(x, Q_0^2) &= 26.2x^{0.9}(1-x)^{4.0}
\end{aligned}$$

by Eq. (5.13), and the lower entries of the matrix were taken to be zero. Hence, the transformation matrix is

$$Z(n)_{\overline{\mathrm{MS}}\to\mathrm{AB}} = \frac{1}{n}\begin{pmatrix} 0 & N_f \\ 0 & 0 \end{pmatrix} . \tag{5.16}$$

This scheme is the minimal modification of $\overline{\mathrm{MS}}$ since it preserves the low and high x behavior of the coefficient functions and anomalous dimensions, and thus the asymptotic behavior of parton distributions is not modified. In order to demonstrate the effects of the factorization scheme dependence, we perform our calculations in both $\overline{\mathrm{MS}}$ and AB schemes.

5.3 Fits

Following the ansatz of Ref. [86], we parameterize the polarized parton distribution at the low initial scale $Q_0^2 = 0.34$ GeV^2 as follows:

$$\Delta f(x, Q_0^2) = A_f x^{\alpha_f}(1-x)^{\beta_f} f(x, Q_0^2) \, , \tag{5.17}$$

where $\Delta f = \Delta u_V$, Δd_V, $\Delta\bar{Q}$, ΔG are the polarized valence, sea, and gluon distributions (see below for the definition of $\Delta\bar{Q}$), and $f(x, Q_0^2)$ are the unpolarized parton distributions from Ref. [145] (Table 5.1).

Since the inclusive deep inelastic scattering does not provide sufficient information about the flavor separation of the polarized sea, we assume isospin symmetry

$$\delta\bar{u} = \delta\bar{d} \equiv \frac{1}{2}\left(\delta\bar{u} + \delta\bar{d}\right) \, . \tag{5.18}$$

Under this assumption, the sea quark contribution to the polarized structure functions of the proton and neutron is the same:

$$g_1^{p\ \text{sea}} = g_1^{n\ \text{sea}} = (5/9)C_q \otimes \left[1/2(\delta\bar{u} + \delta\bar{d}) + 1/5\delta\bar{s}\right] \ . \tag{5.19}$$

Thus, the inclusive DIS does not probe the light and strange sea independently[2], and the only sensitivity to the difference between $\delta\bar{u}$, $\delta\bar{d}$, and $\delta\bar{s}$ comes from the difference in the evolution of the two types of non-singlet distributions ($\eta = \pm 1$ in Eq. (5.7)). However, if one started with the equal sea distributions ($\delta\bar{u} = \delta\bar{d} = \delta\bar{s}$) at $Q_0^2 = 0.34$ GeV^2, at $Q^2 = 100$ GeV^2 and $x = 0.001$ the difference between the light and strange sea distributions would only be $\approx 2\%$ (and smaller at higher x), beyond the reach of the present-day experiments. Hence, we will parameterize a particular combination of the sea quark distributions that appears in Eq. (5.19):

$$\Delta\bar{Q} \equiv 1/2(\delta\bar{u} + \delta\bar{d}) + 1/5\delta\bar{s} \ . \tag{5.20}$$

Furthermore, we assume the x dependence of the polarized strange and light sea to be the same and fix the normalization of the strange sea by

$$\delta s = \lambda_s \frac{\delta\bar{u} + \delta\bar{d}}{2} = \frac{\lambda_s}{1 + \lambda_s/5}\Delta\bar{Q} \ , \tag{5.21}$$

with the $SU(3)_{\text{flavor}}$ symmetry breaking parameter λ_s varying between 1 and 0 (where the latter choice corresponds to the unpolarized strange sea).

The positivity constraint,

$$|\delta f(x)| \leq f(x) \tag{5.22}$$

enforced (within uncertainties) at the initial scale Q_0^2 holds at all scales $Q^2 > Q_0^2$; it leads to constraints $\alpha_f \geq 0$ and $\beta_f \geq 0$. In addition, we assume the helicity retention properties of the parton distributions[49] (see Section 1.4.1) that constrain[3] $\beta_f = 0$.

---

[2] Information on the flavor separation of the polarized sea could be obtained from the *semi-inclusive* reactions, *i.e.* when a hadron that carries the struck quark is observed in the final state.

[3] We have checked that the data are consistent with this assumption.

Table 5.2. Fitted values of the free parameters in Eq. (5.17) in $\overline{\mathrm{MS}}$ and AB schemes. Also quoted are the statistical, systematic, and theoretical errors.

	$\overline{\mathrm{MS}}$				AB			
	Value	Stat.	Syst.	Theory	Value	Stat.	Syst.	Theory
A_u	0.99	$^{+0.08}_{-0.08}$	$^{+0.04}_{-0.05}$	$^{+0.97}_{-0.11}$	0.96	$^{+0.07}_{-0.06}$	$^{+0.03}_{-0.05}$	$^{+0.96}_{-0.09}$
A_d	-0.74	$^{+0.14}_{-0.21}$	$^{+0.05}_{-0.07}$	$^{+0.05}_{-1.28}$	-0.82	$^{+0.05}_{-0.05}$	$^{+0.07}_{-0.06}$	$^{+0.31}_{-1.21}$
A_Q	-0.01	$^{+0.02}_{-0.05}$	$^{+0.01}_{-0.02}$	$^{+0.01}_{-0.35}$	-0.03	$^{+0.01}_{-0.02}$	$^{+0.01}_{-0.01}$	$^{+0.03}_{-0.06}$
A_G	1.3	$^{+1.1}_{-0.7}$	$^{+0.7}_{-0.5}$	$^{+0.2}_{-1.3}$	0.1	$^{+2.3}_{-1.1}$	$^{+1.7}_{-1.1}$	$^{+0.1}_{-0.6}$
α_u	0.64	$^{+0.06}_{-0.07}$	$^{+0.03}_{-0.05}$	$^{+0.36}_{-0.06}$	0.54	$^{+0.08}_{-0.06}$	$^{+0.03}_{-0.04}$	$^{+0.56}_{-0.05}$
α_d	0.25	$^{+0.16}_{-0.11}$	$^{+0.07}_{-0.04}$	$^{+0.75}_{-0.03}$	0.40	$^{+0.20}_{-0.12}$	$^{+0.07}_{-0.13}$	$^{+0.53}_{-0.34}$
α_Q	0.01	$^{+0.19}_{-0.01}$	$^{+0.13}_{-0.01}$	$^{+0.55}_{-0.01}$	0.00	$^{+0.17}_{-0.00}$	$^{+0.17}_{-0.00}$	$^{+0.00}_{-0.00}$
α_G	0.7	$^{+0.4}_{-0.5}$	$^{+0.3}_{-0.3}$	$^{+0.1}_{-0.6}$	0.0	$^{+0.7}_{-0.0}$	$^{+1.0}_{-0.0}$	$^{+1.0}_{-0.0}$

The remaining eight coefficients are determined by the fit to the available data on the spin dependent structure function $g_1^{p,n,d}$ of the proton, neutron, and deuteron with $Q^2 > 0.95$ GeV^2. We determine the structure functions at the experimental values of Q^2 using the quoted results for g_1/F_1. The unpolarized structure function F_1 is obtained from the recent parameterization of $F_2(x, Q^2)$ from NMC[129] and the fit to the data on $R(x, Q^2)$, the ratio of longitudinal to transverse photoabsorption cross sections, from SLAC.[79] The weight of each point is determined by the statistical error. The multi-parameter fit is performed using MINUIT from the CERN program library.[156] The best fit coefficients are listed in Table 5.2 and the χ^2 contributions from various experiments are listed in Table 5.3.

Table 5.3. Contributions to the total χ^2 from each experiment.

Exp. Source	E142 [9]	E143-p [10,77]	E143-d [11,77]	SMC-p [12]	SMC-d [13]	E154 Chapter 4	total
Points	32	40	34	12	12	18	149
χ^2 ($\overline{\mathrm{MS}}$)	24.6	45.5	33.7	11.0	15.9	9.8	140.4
χ^2 (AB)	24.6	48.6	31.9	11.3	16.5	9.4	142.3

5.4 Error analysis

5.4.1 Experimental errors

The statistical errors on the parameters of the fit could in principle be extracted from the correlation matrix returned by the fitting program.[156] However, the estimates provided by MINUIT should be taken with some caution: the χ^2 distribution around the minimum in the parameter space is quite shallow (the precision of the data is still limited), and the correlation matrix returned by the program is not always accurate. In addition, the correlation matrix in the parameter space is not very practical if one wants to calculate the errors on the structure functions, or uncertainty in the Q^2 evolution. Moreover, it is not trivial to include the systematic errors into the χ^2 formalism.[157]

Instead of relying on MINUIT estimates, we use the standard error propagation technique. The statistical errors on the parameters of the fit as well as on the extracted parton densities δq, $\delta \bar{q}$, and ΔG can be calculated by adding in quadrature statistical contributions from experimental points. The weight of every point is obtained by varying the point within its statistical error and calculating the change in the parton density. This is equivalent to taking a derivative of the quantity in question with respect to the value of g_1 at every experimental point by finite differences[4]; thus

---

[4] *cf.* Section 3.11 where such a technique was applied to the radiative corrections

$$\sigma^2_{\text{stat}}(\Delta f) = \sum_i \left(\frac{\partial \Delta f}{\partial g_1^i}\right)^2 \sigma^2_{\text{stat}}(g_1^i) \ , \tag{5.23}$$

where f is, for instance, a parton density, and the sum is over all experimental points g_1^i.

One has to keep in mind the fact that the standard error propagation similar to Eq. (5.23) is limited to the case when the errors on each point are small compared to the ratio of the second and first derivatives $(\partial^2 \Delta f/\partial^2 g_1^i)/(\partial \Delta f/\partial g_1^i)$ (so that the Taylor expansion that leads to this formula converges fast).[20] If this is not the case, the higher order derivatives have to be taken into account. The RMS of such distribution may not be a good measure of the uncertainty and one has to define the error in terms of a probability interval. We define σ_+ and σ_- errors in such a way that the probability is 34% that the value Δf is within intervals $[f - \sigma_-(\Delta f); \langle \Delta f \rangle]$ and $[\langle \Delta f \rangle; \Delta f + \sigma_+(\Delta f)]$ (where $\langle \Delta f \rangle$ is the value of the maximum likelihood[5] of the distribution of Δf. The distributions of the quantities Δf (for instance, a parton density, or a value of g_1 at some particular x and Q^2) is obtained by randomizing every experimental point independently according to a Gaussian distribution with mean of the measured value of g_1^i and variance of $\sigma^2_{\text{stat}}(g_1^i)$ and repeating the NLO fit. A typical "statistical" sample consists of 800 fits. The distribution of first moments of the polarized parton densities is shown in Fig. 5.2.

The systematic errors for every point are usually dominated by the normalization errors (target and beam polarizations, dilution factor, etc.). Thus the systematic errors are to a large extent correlated point to point within one experiment[6]. We therefore assume 100% correlated systematic errors for any given experiment and add systematic contributions within one experiment linearly. The propagated sys-

---

[5] Note that for asymmetric distributions $\langle \Delta f \rangle$ may not coincide with the mean of the distribution.

[6] This includes both proton and deuteron data taken in a single experiment, such as E143 and SMC.

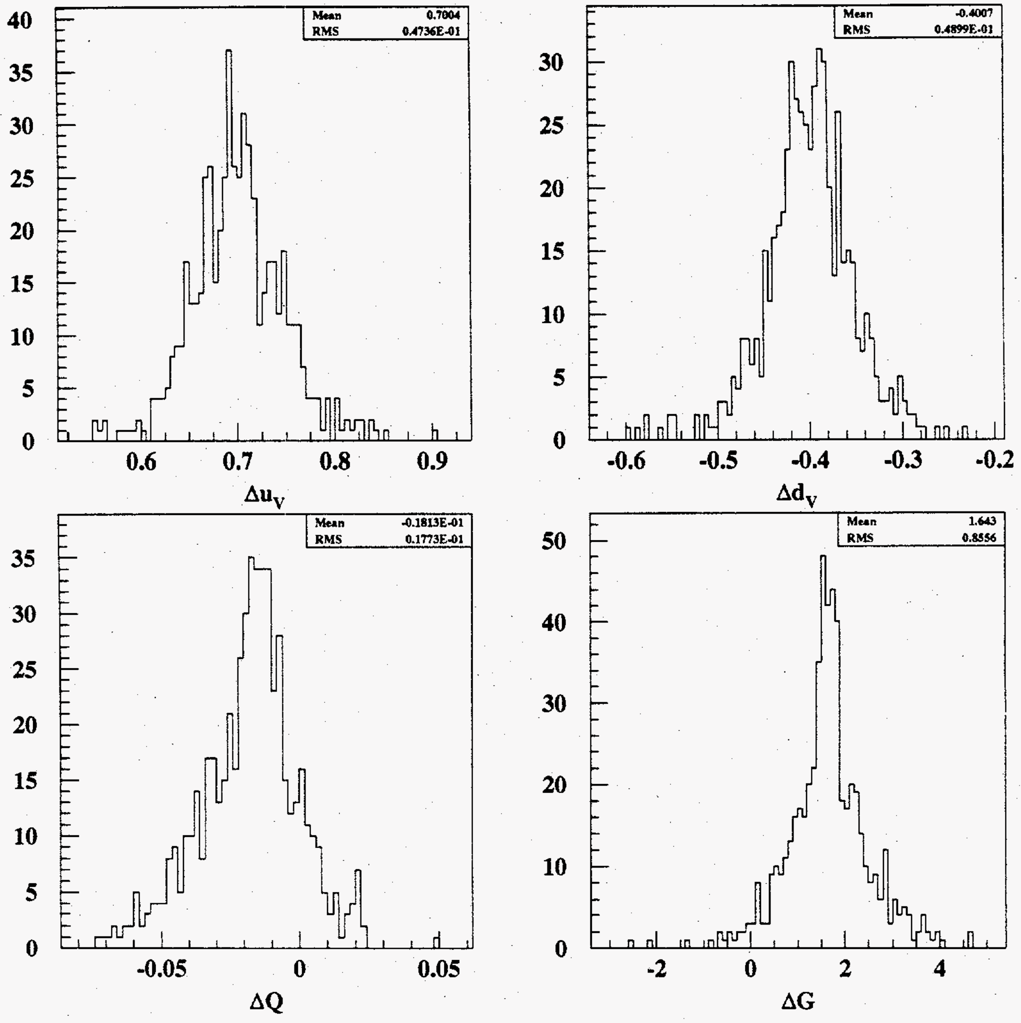

Fig. 5.2. Distributions of the first moments of the polarized parton densities obtained in the $\overline{\text{MS}}$ scheme by randomizing the input values of g_1 as described in the text.

tematic errors of each experiment are then added quadratically to obtain the systematic errors on parton densities. Within our "Monte Carlo" framework, it means that one random variable (with normal Gaussian distribution) that represents the fraction of the systematic error is generated for every experiment, and all points are shifted by that fraction.

5.4.2 Theoretical errors

The biggest source of theoretical uncertainty is the error on the value of α_S. We estimate it by repeating the fits[7] with $\alpha_S(M_Z^2)$ varied in the range allowed by the unpolarized DIS experiments[20] $\alpha_S(M_Z^2) = 0.108 - 0.116$. The scale uncertainty is included in the error on α_S. We also vary current quark masses in the range $m_c = 1 - 2$ GeV and $m_b = 4 - 5$ GeV. The sensitivity to the shape of the initial distributions and the value of the starting scale Q_0^2 is estimated by repeating the fit with initial unpolarized distributions taken from Ref. [144] at $Q_0^2 = 1$ GeV^2. The effect of the $SU(3)_{\text{flavor}}$ breaking is estimated by varying the parameter λ_s from 1 to 0. Possible higher twist effects are neglected since they are expected to drop as $1/W^2$[55] and the cut $W^2 > 4$ GeV^2 has been applied to all the data with the majority of them exceeding $W^2 > 8$ GeV^2.

5.5 Results and discussion

Results for the structure functions of the proton and neutron g_1^p and g_1^n at 5 GeV^2 are compared to the experimental data in Fig. 5.3. They are compared to the fits from Ref. [63,86] in Fig. 5.4. While the low x behavior of our parameterization is similar to that of Ref. [63,86], our fit is somewhat better constrained at high x. It is interesting to note that all analyses predict that the proton structure function crosses zero between $x = 0.001$ and $x = 0.01$ (at $Q^2 = 5$ GeV^2). This is due to the

---

[7] We also relax the positivity constraints Eq. (5.22).

sea and gluon contributions that start to dominate at sufficiently low x. Since the neutron structure function g_1^n is large and negative, the deuteron structure function g_1^d is expected to cross zero near $x = 0.01$. If this is true, the effect could potentially be observed by E155.[48]

The values of the first moments of parton distributions, as well as the first moments of structure functions at $Q^2 = 5$ GeV^2, are given in Table 5.4. We observe that the first moments of the valence quark distributions are determined fairly well and the moments of the sea quarks and gluons are only qualitatively constrained. One may note an apparent $\approx 1.9\sigma$ disagreement of Δq_3 with the value extracted from the neutron beta-decay[20] $\Delta q_3 = g_A = 1.2601 \pm 0.0025$. This is due to the fact that the calculation is done in NLO and thus the higher order corrections to the Bjorken sum rule are not taken into account. The corrections can be as big as 5%[28] at the weighted world average $Q^2 \approx 5$ GeV^2 and they would bring Δq_3 in better agreement with the beta decay data. For consistency with the NLO approximation, we do not include this correction; it has no effect on the physical observable g_1.

The contribution of the experimental systematic errors to the errors on the first moments of the parton distributions is comparable to the statistical contribution. Due to that, the full error on the first moment of the gluon distribution ΔG is bigger than quoted in Ref. [63] despite the fact that the new data from E154 were added. This illustrates the importance of the experimental systematic errors which were (incorrectly) assumed to be uncorrelated from point to point in Ref. [63]. The gluon distribution is constrained entirely by the evolution of the polarized structure functions, and no single experiment covers significantly broad kinematic range. Therefore, changes in relative normalization of the experiments (*i.e.* systematic errors) smear out evolution effects and impair the determination of the gluon polarization density. The theoretical uncertainty is also quite large; it could potentially be reduced if the simultaneous analysis of the unpolarized and polarized

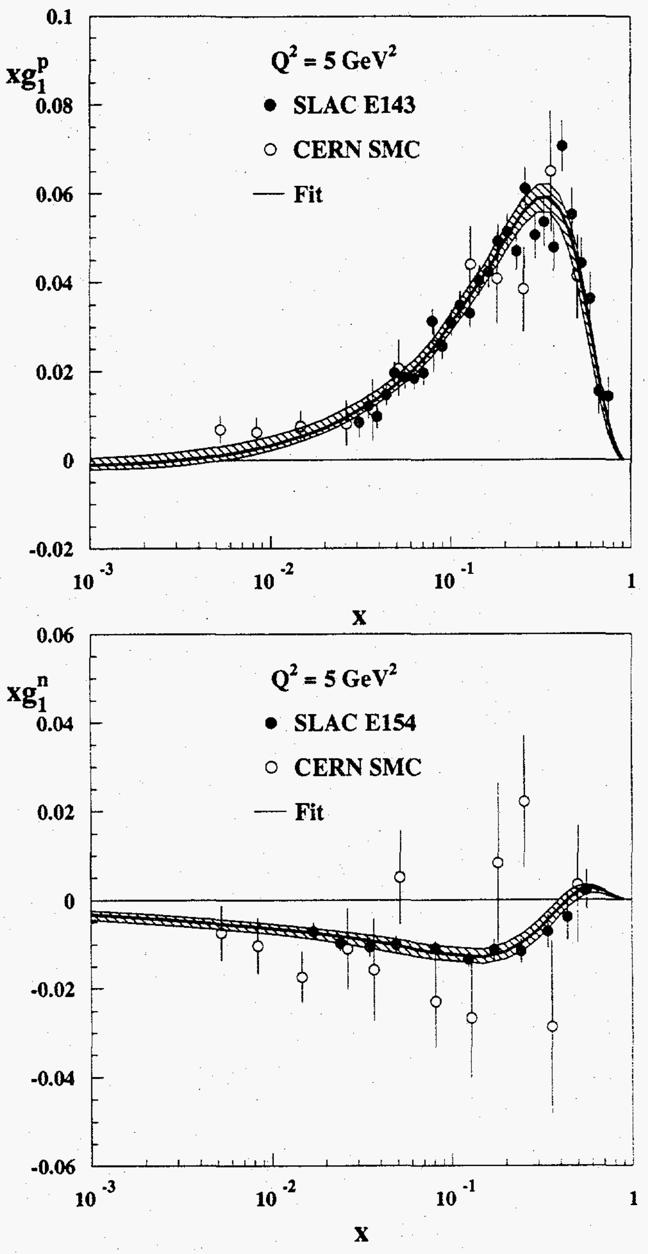

Fig. 5.3. The structure functions (top) xg_1^p and (bottom) xg_1^n at $Q^2 = 5$ GeV^2. E143, SMC, and E154 data have been evolved to $Q^2 = 5$ GeV^2 using a procedure described in the text. The result of the $\overline{\text{MS}}$ fit is shown by the solid line and the hatched area represents the total error of the fit.

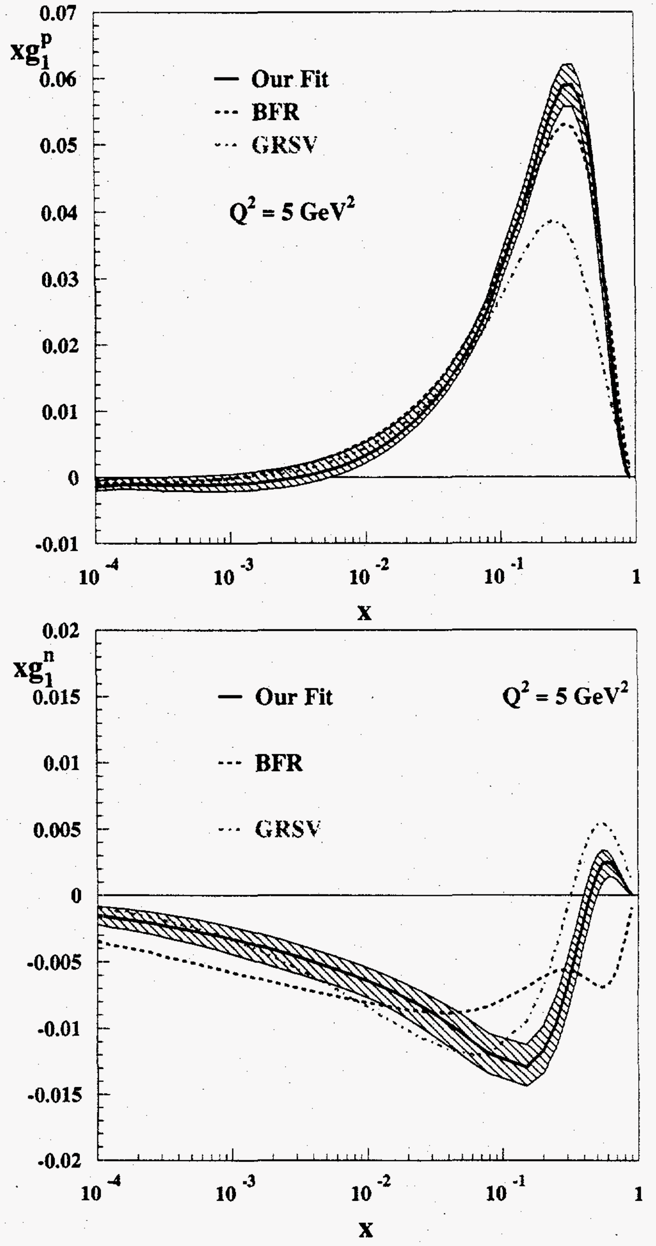

Fig. 5.4. The results of our fit for the structure functions (a) xg_1^p and (b) xg_1^n are compared to the parameterizations of Ref. [63,86] at $Q^2 = 5$ GeV^2. The AB parameterization of Ref. [63,158] is shown as dashed lines, and the "standard" NLO set of Ref. [86,159] is shown by dot-dashed lines. The result of our $\overline{\text{MS}}$ fit is shown by the solid line and the hatched area represents the total error of the fit.

Table 5.4. First moments of the polarized parton distributions and structure functions of the proton, neutron, and deuteron in $\overline{\mathrm{MS}}$ and AB schemes evaluated at $Q^2 = 5$ GeV^2. Errors are statistical, systematic, and theoretical.

	$\overline{\mathrm{MS}}$				AB			
	Value	Stat.	Syst.	Theory	Value	Stat.	Syst.	Theory
Δu_V	0.69	$^{+0.02}_{-0.02}$	$^{+0.05}_{-0.04}$	$^{+0.14}_{-0.01}$	0.74	$^{+0.02}_{-0.03}$	$^{+0.02}_{-0.03}$	$^{+0.07}_{-0.01}$
Δd_V	-0.40	$^{+0.04}_{-0.04}$	$^{+0.03}_{-0.03}$	$^{+0.07}_{-0.00}$	-0.33	$^{+0.03}_{-0.04}$	$^{+0.03}_{-0.05}$	$^{+0.01}_{-0.03}$
$\Delta\bar{Q}$	-0.02	$^{+0.01}_{-0.02}$	$^{+0.01}_{-0.01}$	$^{+0.00}_{-0.03}$	-0.03	$^{+0.02}_{-0.02}$	$^{+0.01}_{-0.01}$	$^{+0.01}_{-0.01}$
ΔG	1.6	$^{+0.7}_{-0.7}$	$^{+0.3}_{-0.6}$	$^{+0.1}_{-0.6}$	0.4	$^{+1.0}_{-0.6}$	$^{+0.9}_{-0.6}$	$^{+1.1}_{-0.1}$
Δq_3	1.09	$^{+0.03}_{-0.02}$	$^{+0.06}_{-0.05}$	$^{+0.06}_{-0.01}$	1.07	$^{+0.03}_{-0.02}$	$^{+0.05}_{-0.06}$	$^{+0.10}_{-0.01}$
Δq_8	0.30	$^{+0.06}_{-0.05}$	$^{+0.06}_{-0.04}$	$^{+0.23}_{-0.01}$	0.41	$^{+0.05}_{-0.08}$	$^{+0.02}_{-0.06}$	$^{+0.03}_{-0.01}$
$\Delta\Sigma$	0.22	$^{+0.05}_{-0.06}$	$^{+0.04}_{-0.05}$	$^{+0.01}_{-0.01}$	0.26	$^{+0.07}_{-0.07}$	$^{+0.06}_{-0.06}$	$^{+0.05}_{-0.02}$
Γ_1^p	0.115	$^{+0.006}_{-0.006}$	$^{+0.008}_{-0.008}$	$^{+0.009}_{-0.001}$	0.114	$^{+0.005}_{-0.006}$	$^{+0.008}_{-0.011}$	$^{+0.001}_{-0.003}$
Γ_1^n	-0.054	$^{+0.005}_{-0.007}$	$^{+0.005}_{-0.006}$	$^{+0.002}_{-0.001}$	-0.051	$^{+0.005}_{-0.007}$	$^{+0.006}_{-0.007}$	$^{+0.001}_{-0.012}$
Γ_1^d	0.028	$^{+0.005}_{-0.006}$	$^{+0.005}_{-0.005}$	$^{+0.005}_{-0.001}$	0.029	$^{+0.005}_{-0.006}$	$^{+0.006}_{-0.007}$	$^{+0.001}_{-0.007}$
Γ_1^{p-n}	0.169	$^{+0.005}_{-0.004}$	$^{+0.009}_{-0.008}$	$^{+0.007}_{-0.001}$	0.165	$^{+0.004}_{-0.004}$	$^{+0.007}_{-0.009}$	$^{+0.013}_{-0.001}$

data was performed (including α_S as one of the parameters). The uncertainties on the values of $\Delta\Sigma$ are larger than originally estimated[30,82] due to the uncertainty in the evolution effects and low-x extrapolation embedded in our analysis.

The results of the fits in both $\overline{\mathrm{MS}}$ and AB schemes are consistent within errors. The fits are significantly less stable in the AB scheme. Note that the values of the singlet axial charge ($a_0 = \Delta\Sigma$ in $\overline{\mathrm{MS}}$ scheme and $a_0 = \Delta\Sigma - N_f\alpha_S\Delta G/(2\pi)$ in AB scheme) are almost exactly the same in two schemes.

Using the parameterization of the parton distributions, one can obtain the polarized structure function (Eq. (5.1)) and evolve the experimental data points to a common $\langle Q^2\rangle$ using the formula:

$$g_1^{\mathrm{exp}}(x_i, \langle Q^2\rangle) = g_1^{\mathrm{exp}}(x_i, Q_i^2) - \Delta g_1^{\mathrm{fit}}(x_i, Q_i^2, \langle Q^2\rangle) \tag{5.24}$$

with

$$\Delta g_1^{\mathrm{fit}}(x_i, Q_i^2, \langle Q^2\rangle) = g_1^{\mathrm{fit}}(x_i, Q_i^2) - g_1^{\mathrm{fit}}(x_i, \langle Q^2\rangle)\ , \tag{5.25}$$

where $g_1^{\mathrm{exp}}(x_i, Q_i^2)$ is the structure function measured at the experimental kinematics, and g_1^{fit} is the fitted value. The errors on $g_1^{\mathrm{exp}}(x_i, \langle Q^2\rangle)$ have three sources:

$$\sigma^2(g_1^{\mathrm{exp}}(x_i, \langle Q^2\rangle)) = \sigma^2(g_1^{\mathrm{exp}})_{\mathrm{stat.}} + \sigma^2(g_1^{\mathrm{exp}})_{\mathrm{syst.}} + \sigma^2(g_1)_{\mathrm{evol.}}\ , \tag{5.26}$$

where statistical and systematic uncertainties should take into account the correlation between $g_1^{\mathrm{exp}}(x_i, Q_i^2)$ and g_1^{fit}, and the evolution uncertainty includes only uncorrelated experimental uncertainties as well as theoretical uncertainties added in quadrature. Table 5.5 lists the E154 data points evolved to the common $\langle Q^2\rangle =$ 5 GeV^2 using this procedure. For comparison, we have included the values of $g_1^n(5\ \mathrm{GeV}^2)$ obtained assuming that the ratio g_1/F_1 is independent of Q^2, as has been traditionally done (*cf.* Table 4.4). The difference between the NLO QCD evolution and the naive assumption is comparable to the precision of the present-day experiments and cannot be neglected.

Table 5.5. E154 results on g_1^n evolved to $\langle Q^2 \rangle = 5$ GeV^2 assuming g_1/F_1 is independent of Q^2 and according to Eq. (5.24). Errors were propagated as described in the text.

x_i	Q_i^2 GeV^2	$g_1^n(x_i, Q_i^2) \cdot \frac{F_1^n(x_i, 5\ \text{GeV}^2)}{F_1^n(x_i, Q_i^2)}$ ±stat.±syst.	$g_1^n(x_i, 5\ \text{GeV}^2)$ ±stat.±syst.±evol.
		2.75° spectrometer	
0.017	1.21	$-0.497 \pm 0.163 \pm 0.147$	$-0.419 \pm 0.115 \pm 0.104 \pm 0.014$
0.024	1.59	$-0.481 \pm 0.092 \pm 0.079$	$-0.409 \pm 0.071 \pm 0.062 \pm 0.006$
0.035	2.05	$-0.345 \pm 0.073 \pm 0.044$	$-0.304 \pm 0.061 \pm 0.037 \pm 0.005$
0.049	2.57	$-0.237 \pm 0.046 \pm 0.024$	$-0.215 \pm 0.041 \pm 0.021 \pm 0.004$
0.078	3.32	$-0.127 \pm 0.033 \pm 0.014$	$-0.117 \pm 0.031 \pm 0.013 \pm 0.002$
0.123	4.09	$-0.077 \pm 0.031 \pm 0.009$	$-0.073 \pm 0.030 \pm 0.009 \pm 0.001$
0.173	4.63	$-0.071 \pm 0.033 \pm 0.009$	$-0.069 \pm 0.033 \pm 0.009 \pm 0.001$
0.241	5.09	$-0.053 \pm 0.028 \pm 0.007$	$-0.053 \pm 0.028 \pm 0.007 \pm 0.000$
0.340	5.51	$0.002 \pm 0.037 \pm 0.004$	$0.001 \pm 0.036 \pm 0.004 \pm 0.000$
0.423	5.82	$0.028 \pm 0.061 \pm 0.008$	$0.027 \pm 0.059 \pm 0.007 \pm 0.000$
		5.5° Spectrometer	
0.057	4.03	$0.233 \pm 0.297 \pm 0.037$	$0.224 \pm 0.285 \pm 0.035 \pm 0.001$
0.084	5.47	$-0.150 \pm 0.029 \pm 0.019$	$-0.152 \pm 0.029 \pm 0.019 \pm 0.001$
0.123	7.23	$-0.113 \pm 0.016 \pm 0.012$	$-0.121 \pm 0.017 \pm 0.012 \pm 0.002$
0.172	8.94	$-0.058 \pm 0.015 \pm 0.007$	$-0.065 \pm 0.016 \pm 0.007 \pm 0.003$
0.242	10.71	$-0.041 \pm 0.012 \pm 0.005$	$-0.047 \pm 0.012 \pm 0.005 \pm 0.003$
0.342	12.55	$-0.021 \pm 0.013 \pm 0.005$	$-0.023 \pm 0.012 \pm 0.005 \pm 0.001$
0.442	13.83	$-0.011 \pm 0.014 \pm 0.003$	$-0.011 \pm 0.012 \pm 0.002 \pm 0.001$
0.564	15.00	$0.005 \pm 0.012 \pm 0.002$	$0.004 \pm 0.008 \pm 0.001 \pm 0.000$

The Q^2 dependence of the ratio g_1/F_1 for the proton and neutron is shown for several x bins in Fig. 5.5. For the neutron, the evolution if g_1^n is slower than that of F_1^n. Therefore, assuming scaling of g_1^n/F_1^n, one typically overestimates the absolute value of $g_1^n(x, \langle Q^2 \rangle)$ at low x (where $Q_i^2 < \langle Q^2 \rangle$), and underestimates it at high x (where $Q_i^2 > \langle Q^2 \rangle$). The two effects approximately cancel for the integral over the measured range in case of E154. However, the shape of the structure function at low x affects the extrapolation to $x = 0$ (the effective low x power decreases, see below). The effect of the perturbative evolution is qualitatively the same for the proton.

The data on g_1^n at $Q^2 = 5$ GeV^2 averaged between two spectrometers are given in Table 5.6. For the integral of the neutron structure function in the measured

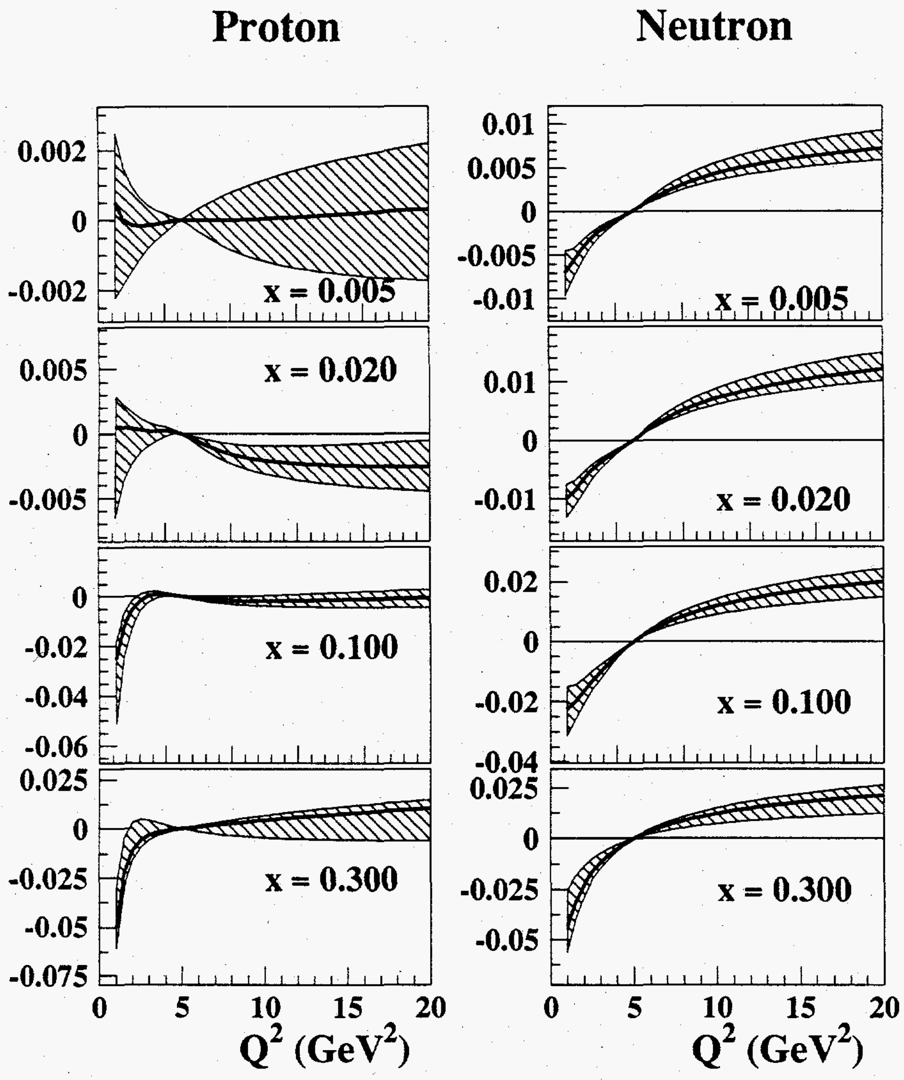

Fig. 5.5. Evolution of the ratios g_1/F_1 for proton (left) and neutron (right). Plotted is the difference $\frac{g_1}{F_1}(x, Q^2) - \frac{g_1}{F_1}(x, 5\ \mathrm{GeV}^2)$. $\overline{\mathrm{MS}}$ fit is shown in solid and the hatched area represents the total (experimental and theoretical) uncertainty.

Table 5.6. E154 results on g_1^n evolved to $Q^2 = 5$ GeV^2 according to the NLO DGLAP equations. The data of the two spectrometers have been averaged.

x	$g_1^n(x, 5\ \mathrm{GeV}^2) \pm$ stat. $\pm$ syst. $\pm$ evol.
0.017	$-0.419 \pm 0.115 \pm 0.104 \pm 0.014$
0.024	$-0.409 \pm 0.071 \pm 0.062 \pm 0.006$
0.035	$-0.304 \pm 0.061 \pm 0.037 \pm 0.005$
0.049	$-0.206 \pm 0.041 \pm 0.021 \pm 0.004$
0.081	$-0.136 \pm 0.021 \pm 0.016 \pm 0.001$
0.123	$-0.109 \pm 0.015 \pm 0.011 \pm 0.002$
0.172	$-0.066 \pm 0.014 \pm 0.007 \pm 0.003$
0.242	$-0.048 \pm 0.011 \pm 0.005 \pm 0.003$
0.342	$-0.021 \pm 0.011 \pm 0.005 \pm 0.001$
0.441	$-0.009 \pm 0.012 \pm 0.002 \pm 0.001$
0.564	$0.004 \pm 0.008 \pm 0.001 \pm 0.000$

range, we obtain

$$\int_{0.0135}^{0.7} dx\ g_1^n(x) = -0.035 \pm 0.003 \pm 0.005 \pm 0.001\ , \tag{5.27}$$

where the first error is statistical, the second is systematic, and the third is due to the uncertainty in the evolution. This value agrees well with the originally quoted number (*cf.* Eq. (4.2)).

5.6 Low x extrapolation updated

It is interesting to note that the low-x behavior of the valence distributions is reasonably convergent ($\Delta u_V(x) \sim x^{0.18^{+0.37}_{-0.10}}$ and $\Delta d_V(x) \sim x^{-0.43^{+0.77}_{-0.12}}$ as $x \to 0$), and is consistent with the Regge predictions[65] at low $Q^2 \approx Q_0^2 = 0.34$ GeV^2. In the singlet sector, the data seem to prefer small values of α_Q, and the uncertainties on α_Q and α_G are large. The reason for that is that the data are not yet sensitive enough to the true asymptotic behavior of the sea and gluon distributions at low x. The parameters α_Q and α_G should be viewed as effective powers obtained in the range $x \approx 0.005 - 0.1$ (compared to the unpolarized case where the measurements extend down to $x \approx 10^{-5}$). At higher $Q^2 = Q^2_{\mathrm{data}} > 1$ GeV$^2 > Q_0^2$, the perturbative

Table 5.7. Results of the fits to the low x data of E154, evolved to $Q^2 = 5$ GeV^2 according to Eq. (5.24). The first uncertainty is statistical, the second is systematic, and the third is due to evolution.

Fit	$g_1^n = C$	$g_1^n = Cx^{-\alpha}$
Points	3	5
C	$-0.36 \pm 0.04 \pm 0.06 \pm 0.01$	$-0.018 \pm 0.008 \pm 0.001 \pm 0.001$
α		$0.81 \pm 0.15 \pm 0.06 \pm 0.01$
$\int_0^{0.0135} dx\ g_1^n$	$-0.005 \pm 0.001 \pm 0.001 \pm 0.000$	$-0.042 \pm 0.063 \pm 0.016 \pm 0.004$
$\int_0^1 dx\ g_1^n$	$-0.040 \pm 0.004 \pm 0.006 \pm 0.001$	$-0.077 \pm 0.063 \pm 0.021 \pm 0.005$

evolution leads to a divergent behavior of the valence distributions and amplifies the divergent behavior of the sea and gluon distributions,[71] which is evident in the neutron structure function below $x = 0.1$ (see Chapter 4). The low x behavior of the singlet distributions is to a large extent decoupled from the distributions at the low initial scale; it is determined primarily by evolution. This makes the data at high Q^2 even less sensitive to the initial shape of the sea and gluon distributions.

It is interesting to compare the low x extrapolation done with the E154 data evolved according to the NLO DGLAP equations with the results presented in Section 4.4.3 (where the data have been evolved to $Q^2 = 5$ GeV^2 assuming the scaling of g_1^n/F_1^n). Results of the two fits are summarized in Table 5.7: the "Regge" fit $g_1^n = const$, and a "free power" fit. Again, although the behavior of the free-power fit is now slightly softer and it is (barely) integrable within one standard deviation, two fits give quite different values of the total integral of the neutron structure function.

One should note that the convergent behavior of the structure functions at low x and high Q^2 would be incompatible with the pQCD predictions.[160,161] In fact, at next-to-leading order, the polarized parton distributions, and therefore g_1, are expected to rise faster than any power of $\log(1/x)$ (but slower than any power of x) even if the initial distributions at low scale are convergent. At sufficiency low

x (and/or high enough Q^2), the singlet distributions start to dominate, and both proton and neutron structure functions have the same asymptotic behavior. This can be seen in Fig. 5.6 where we plotted the structure functions of proton and neutron at $Q^2 = 5$ GeV^2 and $x = 10^{-4} - 10^{-1}$. In addition to the $\overline{\mathrm{MS}}$ parameterization discussed in this Chapter, we show the behavior of the structure functions for the cases where we fix the low x power of all polarized distributions to 0 or 1 at the initial scale $Q^2 = 0.34$ GeV^2. Evidently, the asymptotic behavior for both proton and neutron is the same in all cases (Fig. 5.6, top); the structure functions are insensitive to the shape of the initial distributions below $x = 0.001$. The initial distributions, however, dictate at what values of x and Q^2 the low x behavior sets in. Thus, for the neutron, the region is between $x = 0.01$ (for soft initial distributions) and $x = 0.1$ (for our fit), but for the proton the asymptotic behavior sets in near $x = 10^{-4}$ (Fig. 5.6, bottom). Therefore, extrapolating the present proton data (limited to $x > 0.005$) at moderate Q^2 could be problematic.

To evaluate the integrals of the neutron and proton structure functions, we evolve the E154 neutron data and the E143 proton data[10] to $Q^2 = 5$ GeV^2 according to the procedure discussed above. The contributions to the integrals over the range measured by these experiments are summarized in Table 5.8. Using the $\overline{\mathrm{MS}}$ parameterization of Table 5.2, we have also evaluated the contributions to the first moments of g_1^n and g_1^p from unmeasured regions (high and low x) and obtained for the Bjorken sum

$$\Gamma_1^{p-n}(5\ \mathrm{GeV}^2) = \int_0^1 dx\ (g_1^p - g_1^n) = 0.172 \pm 0.004(\mathrm{stat.}) \pm 0.010(\mathrm{syst.}) \pm 0.007(\mathrm{evol.}) \tag{5.28}$$

in agreement with the $O(\alpha_S^3)$[28] prediction 0.186 evaluated with $\alpha_S(M_Z^2) = 0.109$. This number agrees very well with the value in Table 5.4 obtained by direct integration of the parton densities. The result is fairly insensitive to the details of the low-x extrapolation which for the difference $[g_1^p - g_1^n](x)$ is determined by the valence

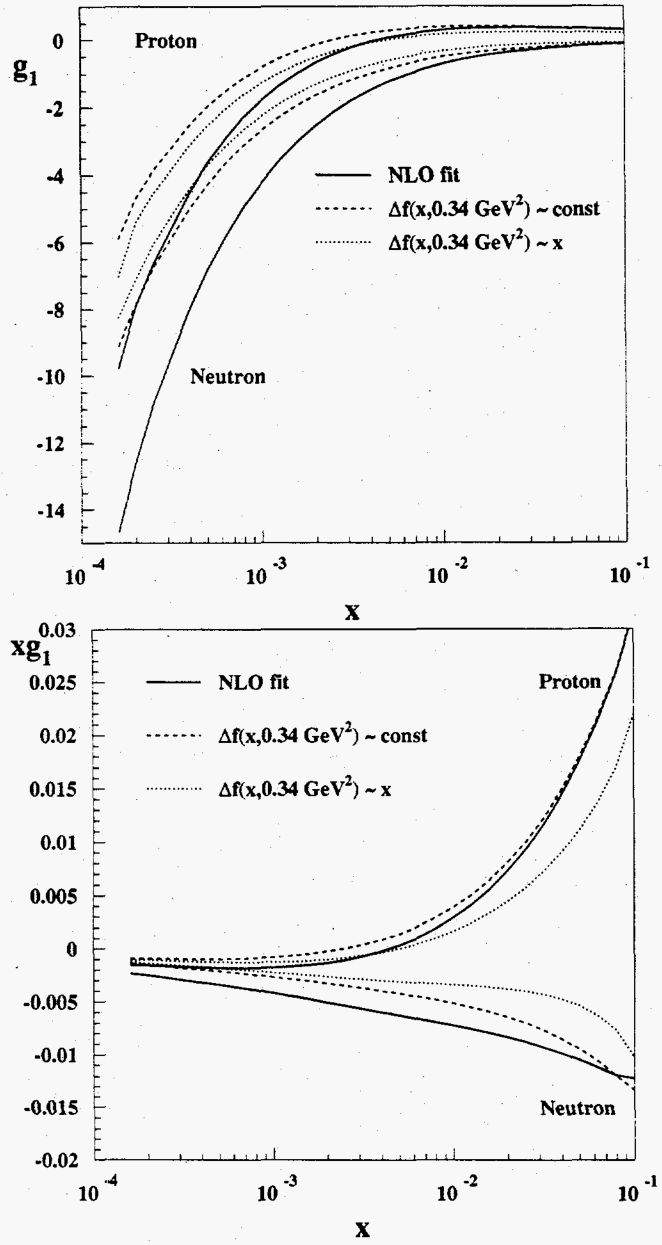

Fig. 5.6. The low x behavior of the structure functions g_1^p and g_1^n (top) and xg_1^p and xg_1^n (bottom) for different choices of the initial parton distributions. The result of the $\overline{\text{MS}}$ fit (Table 5.2) are plotted in solid, and parameterizations with constrained low x behavior $\Delta f \sim$ *const* and $\Delta f \sim x$ are shown as dashed and dotted lines, respectively.

Table 5.8. Integrals of the proton and neutron polarized structure functions evaluated at $Q^2 = 5$ GeV^2. The first error is statistical, the second is systematic, and third is due to evolution.

	E154 (g_1^n)	E143 (g_1^p)
$x_{\rm min}$	0.014	0.029
$x_{\rm max}$	0.7	0.8
$\int_{x_{\rm min}}^{x_{\rm max}}$	$-0.035 \pm 0.003 \pm 0.005 \pm 0.001$	$0.113 \pm 0.003 \pm 0.007 \pm 0.001$
$\int_0^{x_{\rm min}} + \int_{x_{\rm max}}^1$	$-0.018 \pm 0.002 \pm 0.002 \pm 0.005$	$0.005 \pm 0.003 \pm 0.002 \pm 0.009$
$\int_0^1$	$-0.053 \pm 0.004 \pm 0.007 \pm 0.006$	$0.119 \pm 0.005 \pm 0.009 \pm 0.010$

quark distributions, and is well constrained by the data. The low x behavior in the non-singlet polarized sector is also relatively insensitive to the higher-order corrections.[162] On the other hand, the low-x extrapolation of the proton and neutron integrals alone still relies on the assumption that the asymptotic behavior of sea quark and gluon distributions can be determined from the present data, and that the effects of higher-order resummations are small. These assumptions, and therefore evaluation of the total quark helicity $\Delta\Sigma$, are on potentially weaker grounds. Precise higher energy data on the polarized structure functions of both proton and neutron are required to determine this quantity.

CHAPTER 6

CONCLUSIONS AND OUTLOOK

Spin-dependent deep inelastic scattering still remains one of the most fascinating fields of particle physics. New experimental data, such as the results presented in this dissertation, increase our knowledge and understanding of the structure of the proton and neutron. At the same time, as we get a closer look into the structure and dynamics of quarks and gluons inside the nucleon, new questions arise, some of our naive expectations fall, and our uncertainty grows. The results of this experiment is one example of such *evolution* of knowledge that probably is inevitable, as was postulated seventy years ago by Heisenberg.

The results of the experiment E154 at SLAC, described in this dissertation, is the most precise determination of the spin dependent structure function g_1^n of the neutron. Compared to the previous SLAC spin structure experiments, the kinematic coverage was significantly increased. The increased beam energy allowed us to extend the measurements to lower values of Bjorken variable x and to increase the four-momentum transfer Q^2, providing for a possibility to constrain the evolution of the polarized parton distributions. Thus, not only the information about the quark contribution to the structure functions can be obtained from the present data, but also first constraints on the gluon helicity distribution are emerging.

At the same time, the data presented us with some surprises. We have observed relatively large values of g_1^n at low x, and the behavior of the structure function seems to be quite divergent. This apparently disagrees with predictions of the conventional Regge theory, and poses certain problems for extrapolating the data to $x = 0$ in order to evaluate the first moment of g_1^n and test the Ellis-Jaffe sum rule. While such a behavior is qualitatively understood in perturbative QCD, firm quantitative predictions are not yet available.

In order to reduce the ambiguity in the interpretation of the results, we have performed a Next-to-Leading Order QCD analysis of the world data on polarized deep inelastic scattering. Careful attention has been paid to the uncertainties involved, both experimental and theoretical. We find that the data constrain the first moments of the polarized valence quark distributions; the polarized gluon and sea quark distributions can only be qualitatively constrained. We determine the Q^2 dependence of the ratio g_1/F_1 for the proton and neutron and find that it is significant compared to the present experimental errors. Assuming the validity of the NLO approximation, we determine the first moments of the spin dependent structure functions of the proton and neutron, and find agreement with the Bjorken sum rule. However, for an unambiguous determination of the total quark helicity and the polarized gluon distribution, data at the higher energies are needed.

The spin structure program will continue, and is likely to bring us more exciting discoveries about the internal structure of the nucleon. At SLAC, the experiment E155[48] will utilize the 50 GeV electron beam and the same detector system as E154 (with an addition of another spectrometer arm at 10.5° relative to the beam line). Using ammonia and ^{6}LiD targets similar to the targets used in E143, the experimenters will measure the spin dependent structure functions of the proton and deuteron over the same x range as E154, and with increased (due to the new spectrometer) Q^2 coverage. This precision data, especially on the deuteron structure function, will be of great use for understanding the nucleon spin structure at low x.

In Europe, the HERMES experiment[80] at DESY is continuing to collect data. The first preliminary results from the 1995 run with the polarized ^{3}He target on the neutron spin structure function were released last summer, and are expected to be published soon. The studies of the *semi-inclusive* reactions (in which the flavor of the leading hadron is tagged) allow one to probe directly the valence and sea quark distributions inside the nucleon. The future of HERMES looks very promising, and it should continue to run into the next century. The SMC experiment[12,13] at CERN has finished taking data in 1996. The results of the 1995 deuteron run will be published soon, and the proton 1996 results are expected to be released this year.

In the 21st century, the style of the spin structure experiments will change. The HERMES experiment is likely to be the last in the generation of the "traditional" inclusive lepton-nucleon DIS experiments. A lot of attention has been devoted recently to the problem of polarizing proton beams. Such beams are planned for the RHIC collider at BNL, for the UNK at Serpukhov, Russia, and are proposed for the Fermilab Main Injector and HERA at DESY. Having polarized protons in the HERA ring would be particularly interesting since one would be able to extend the kinematic range of the polarized deep-inelastic scattering experiments to $x \approx 10^{-5}$ and $Q^2 \approx 10^4$ GeV^2, similar to the unpolarized scattering. A complementary DIS fixed target program would be possible at the Next Linear Collider (NLC). This would allow for precise determination of the behavior of the spin structure functions at low x. A perturbative QCD analysis of such data, similar to the NLO analysis described in Chapter 5, would determine the spin dependent parton distributions, including that of the gluon, with a precision comparable to the present unpolarized analyses. At the proton machines, the studies of the nuclear spin structure are planned by measuring the single- and double-spin asymmetries in the Drell-Yan muon pair production $pp \to \mu^+\mu^- X$ that at low energies (UNK and Fermilab fixed target experiments) are sensitive to the polarization of the sea quarks, and at higher energies probe the gluon helicity distributions. Another good measure of the gluon polarization is the asymmetry in the hard photon production which probes the process $g^* q \to q\gamma$. The asymmetry in the open charm lepto- or photo-production is also sensitive to the gluon polarization. Such experiments are proposed at SLAC and CERN.

There is still a lot to learn about the internal spin structure of the nucleon. Future experimental program promises to be very exciting, and the author will follow the developments in the field with great interest.

APPENDIX A

LIGHT-CONE PERTURBATION THEORY

One of the most convenient frameworks to explore the properties of hadronic structure at large momentum transfers is the time-ordered perturbation theory, or, equivalently, perturbation theory on the light cone with time variable $\tau = t + z/c$.[45,46] Let us define

$$p^{\pm} \equiv p^0 \pm p^3 \tag{A.1}$$

and

$$p^{\mu} = (p^+, p^-, \vec{p}_{\perp}). \tag{A.2}$$

The mass-shell condition is, obviously,

$$p^+ p^- - \vec{p}_{\perp}{}^2 = p^2 = m^2. \tag{A.3}$$

The light-cone energy $p^- > 0$ and then $p^+ > 0$; therefore, there are no vacuum-creation graphs (Fig. A.1). The Fock expansion constructed on the vacuum state provides a complete relativistic many-particle basis; for a hadronic wave function we can write

$$|\Psi_H\rangle = \sum_n |n\rangle \psi_n(x_i, k_{\perp i}, \lambda_i), \tag{A.4}$$

where $|n\rangle = |qqq\rangle, |qqqg\rangle \dots$ for baryons ($|n\rangle = |q\bar{q}\rangle, |q\bar{q}g\rangle \dots$ for mesons), and $\psi_n(x_i, k_{\perp i}, \lambda_i)$ is a Lorenz-frame independent wave function for a state with n on-

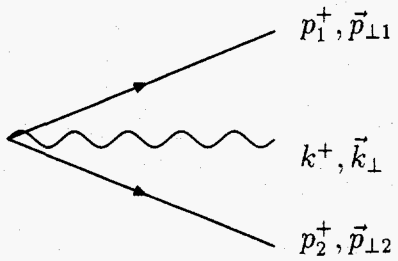

Fig. A.1. Vacuum creation graphs vanish in light-cone perturbation theory.

mass-shell constituents, and λ is the polarization index. The 4-momentum for each constituent has been parameterized as

$$k_i^\mu \equiv (k_i^+, k_i^-, \vec{k}_{\perp i}) = (x_i p^+, \frac{\vec{k}_\perp^2 + m^2}{x p^+}, \vec{k}_\perp). \tag{A.5}$$

Momentum conservation requires

$$\sum_{i=1}^{n} x_i = 1 \quad \sum_{i=1}^{n} \vec{k}_{\perp i} = 0. \tag{A.6}$$

Moreover, since $p^+ > 0$ and $k_i^+ > 0$, $x_i > 0$.

The Feynman rules for light-cone perturbation theory can be found in Ref. [46]. We will repeat some of the particularly important ones:

1. Assign a momentum k^μ to each line so that

   (a) k^+ and $\vec{k}_\perp$ are conserved at each vertex

   (b) $k^2 = m^2$, or $k^- = (\vec{k}_\perp^2 + m^2)/k^+$.

2. Include a factor $\theta(k^+)/k^+$ for each fermion, anti-fermion, or scalar. For vector bosons, assign the factor $d_{\mu\nu}\theta(k^+)/k^+$ where $d_{\mu\nu}$ is the (gauge-dependent) polarization sum. In the Feynman gauge $d_{\mu\nu} = -g_{\mu\nu}$. In the axial gauge ($\eta \cdot A = 0$ where η is an arbitrary fixed 4-vector)

$$d_{\mu\nu}(k) \;=\; \sum_{\lambda=1,2} \epsilon_\mu(k,\lambda)\epsilon_\nu(k,\lambda)$$

$$= \quad -g_{\mu\nu} + \frac{\eta_\mu k_\nu + \eta_\nu k_\mu}{\eta \cdot k} \tag{A.7}$$

where $\eta \cdot \epsilon = k \cdot \epsilon = 0$. The light-cone gauge where $\nu = (0, 2, \vec{0}_\perp)$ is particularly convenient.

3. The gluon(photon)-fermion vertices are

$$e_0 \bar{u} \gamma^\mu u, \; e_0 \bar{u} \gamma^\mu v, \; -e_0 \bar{u} \gamma^\mu v, \; -e_0 \bar{v} \gamma^\mu v \; . \tag{A.8}$$

4. For each intermediate state there is a factor

$$\frac{1}{\sum_{\text{inc}} k^- - \sum_{\text{interm}} k^- + i\epsilon} \tag{A.9}$$

where the summation is over the light-cone energies of the incoming and intermediate particles. This factor is a measure of virtuality of the intermediate state (although each particle is assumed on-shell). Thus, for a Fock state with one of the constituents having $x \sim 1$, the denominator becomes

$$\frac{1}{p^+}\left[M^2 - \sum_{i=1}^{n} \frac{\vec{k}_{\perp i}^2 + m_i^2}{x_i}\right] \sim O(\frac{\vec{k}_\perp^2 + m^2}{1-x}) \to \infty, \tag{A.10}$$

and the state is said to be far off-shell.

5. Integrate $\int dk^+ \int d^2\vec{k}_\perp / 16\pi^3$ for each independent k and sum over internal spins and polarizations.

The distribution functions $G_{q/H}(x, \lambda, Q)$ can be calculated from the overlaps of the light-cone wave functions

$$G_{q/H}(x, \lambda, Q) = \sum_n \int^{k_\perp^2 < Q^2} \pi d^2 \vec{k}_{\perp i} dx_i |\psi_n^\lambda(x_i, \vec{k}_{\perp i}, \lambda_i)|^2 \delta(x - x_q) \; , \tag{A.11}$$

where the summation is over all relevant Fock states. The asymptotic behavior of the light-cone wave functions is obtained by iterating the interaction kernel.[40] Thus, for $q\bar{q}$ mesonic states the diagram of Fig. A.2 yields:

$$\psi(x, \vec{k}_\perp) = \frac{1}{M^2 - \frac{\vec{k}_\perp^2 + m^2}{x(1-x)}} \int d^2 l_\perp V(x, \vec{k}_\perp; y, \vec{l}_\perp) \psi(y, \vec{l}_\perp) \overset{x \to 1}{\sim} (1-x), \tag{A.12}$$

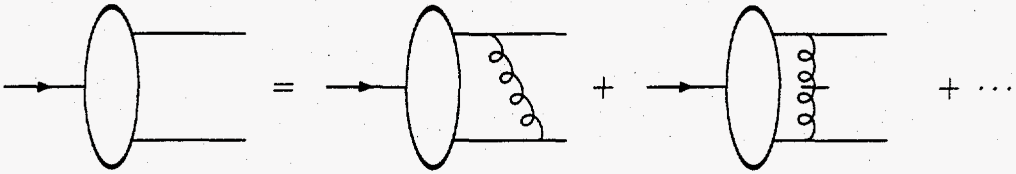

Fig. A.2. Calculation of the mesonic light-cone wave function. The second term is the instantaneous part of the gluon propagator.

where the integration represents the transition from the initial configuration with quark momentum $k_0 = (yp^+, (\vec{l}_\perp^2 + m^2)/yp^+, \vec{l}_\perp)$ and is of order α_s. The end-point $x \sim 1$ behavior of the mesonic distribution amplitude is then

$$G_{q/M}(x) \sim (1-x)^2. \tag{A.13}$$

Similarly, the leading end-point behavior of the quark distribution function $G_{q/p}(x)$ for the proton is computed from the diagram of Fig. A.3:

$$G_{q/p}(x) \sim (1-x)^3. \tag{A.14}$$

The contribution of Fig. A.4 is suppressed by two orders of $(1-x)$. It is interesting to note that the diagram of Fig. A.3 only contributes if the spectator quarks with momenta y_2 and y_3 have opposite helicities.[40] At high x it translates into the requirement that the helicity of the struck quark be aligned with the proton helicity. If it is anti-aligned, the leading behavior is

$$G_{q\downarrow/p\uparrow}(x) \sim (1-x)^5. \tag{A.15}$$

This fact illustrates the helicity retention property of the gauge interactions. Equations (A.13), (A.14), and (A.15) are the manifestation of the quark counting rules.[47]

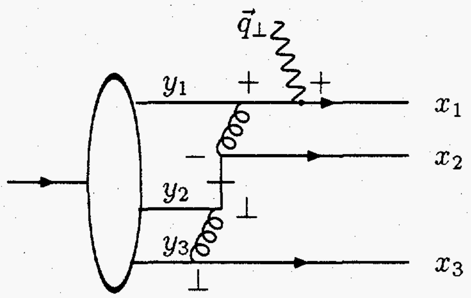

Fig. A.3. The leading contribution to the proton distribution function $G_{q/p}$ at $x \sim 1$. +, −, and ⊥ denote the current components. The quark propagator is instantaneous.

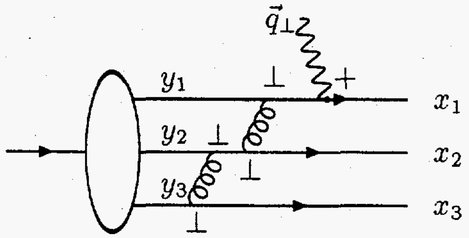

Fig. A.4. $(1-x)^5$ contribution to the proton distribution function.

APPENDIX B

NEXT-TO-LEADING ORDER EVOLUTION OF PARTON DISTRIBUTIONS

The solution of the DGLAP equations in the Mellin n-moment space is significantly simplified. A key feature of the Mellin transform is that the moment of a convolution of two functions is given simply by the product of two moments: if

$$C(x) = (f \otimes g)(x) \equiv \int_x^1 \frac{dz}{z} f\left(\frac{x}{z}\right) g(z) \,, \tag{B.1}$$

the moment is given by

$$C(n) \equiv \int_0^1 dx\; x^{n-1} C(x) = f(n) g(n) \,. \tag{B.2}$$

Thus, complicated integro-differential DGLAP equations are reduced to simple linear equations (or a system of equations in the singlet sector). One typically evolves the parton distributions and calculates the moments of the structure functions in the Mellin space, and then inverts the structure functions into the Bjorken x space. Thus, only one (numerical) integration is required. In Mellin space, the structure functions are given by (*cf.* Eq. (5.1))

$$g_1(n, Q^2) = \frac{1}{2} \sum_q^{N_f} e_q^2 \left[C_q(n) \Delta q(n, Q^2) + \frac{1}{N_f} C_G(n) \Delta G(n, Q^2) \right] \,, \tag{B.3}$$

where

$$\begin{aligned} C_q(n, \alpha_S) &= 1 + \frac{\alpha_S(Q^2)}{2\pi} C_q^{(1)}(n) + \cdots \\ C_G(n, \alpha_S) &= \frac{\alpha_S(Q^2)}{2\pi} C_G^{(1)}(n) + \cdots \end{aligned} \tag{B.4}$$

and the NLO spin dependent Wilson coefficients in $\overline{\mathrm{MS}}$ scheme are given by[37]

$$C_q^{(1)} = C_F \left[-S_2(n) + S_1(n) \left(S_1(n) + \frac{3}{2} - \frac{1}{n(n+1)} \right) + \frac{1}{n^2} + \frac{1}{2n} + \frac{1}{n+1} - \frac{9}{2} \right]$$

$$C_G = 2T_f\left[-\frac{n-1}{n(n+1)}(S_1(n)+1)-\frac{1}{n^2}+\frac{2}{n(n+1)}\right]. \tag{B.5}$$

Here $C_F = 4/3$ and $T_f = N_f/2$ are Casimir invariants for the quark representation of $SU(3)_{\text{flavor}}$ ($N_f = 3$ is the number of active flavors). The factors $S_k(n)$ will be given below.

Note that in $\overline{\text{MS}}$ scheme the first moment of the gluon coefficient function vanishes $C_G^{(1)}(n=1) = 0$, the first moment of the quark Wilson coefficient is $C_q^{(1)}(n=1) = 3C_F/2$, and the first moments of the spin-dependent structure functions are simply given by

$$\Gamma_1(Q^2) = \frac{1}{2}\sum_q e_q^2\left(1-\frac{\alpha_S(Q^2)}{\pi}\right)\Delta q(Q^2). \tag{B.6}$$

The total gluon density does not couple to the first moment of the structure function g_1 in $\overline{\text{MS}}$ scheme. A transformation to other schemes, in which the gluon contributes to the first moment of g_1 (such as Adler-Bardeen scheme), are given in Chapter 5.

The Q^2 evolution of the parton densities is governed by the the anomalous dimensions[150] which in NLO are defined as

$$\gamma_{NS} = \frac{\alpha_S}{4\pi}\gamma_{qq}^{(0)} + \left(\frac{\alpha_S}{4\pi}\right)^2\gamma_{NS}^{(1)\eta}, \quad \eta = \pm 1 \tag{B.7}$$

$$\gamma_{ij} = \frac{\alpha_S}{4\pi}\gamma_{ij}^{(0)} + \left(\frac{\alpha_S}{4\pi}\right)^2\gamma_{ij}^{(1)}, \quad i,j = q,g \tag{B.8}$$

where we suppressed the n-dependence. The non-singlet (NS) densities evolve according to[39,150]

$$\begin{aligned}\Delta q_{NS}^{\eta}(Q^2) &= \left[1+\frac{\alpha_S(Q^2)-\alpha_S(Q_0^2)}{4\pi}\left(\frac{\gamma_{NS}^{(1)\eta}}{2\beta_0}-\frac{\beta_1\,\gamma_{qq}^{(0)}}{2\beta_0^2}\right)\right] \\ &\quad \cdot\left(\frac{\alpha_S(Q^2)}{\alpha_S(Q_0^2)}\right)^{\gamma_{qq}^{(0)}/(2\beta_0)}\Delta q_{NS}^{\eta}(Q_0^2),\end{aligned} \tag{B.9}$$

where Q_0^2 is the input scale ($Q_0^2 = 0.34$ GeV^2 in our case). The distribution $\Delta q_{NS}^{\eta=+1}$ corresponds to the polarized valence quark distributions $\Delta u_V(x,Q^2) = \delta u - \delta\bar{u}$ and $\Delta d_V(x,Q^2) = \delta d - \delta\bar{d}$, and $\Delta q_{NS}^{\eta=+1}$ corresponds to the $SU(3)_{\text{flavor}}$ non-singlet combinations $\Delta q_3(x,Q^2) = \Delta u(x,Q^2) - \Delta d(x,Q^2)$ and $\Delta q_8(x,Q^2) = \Delta u(x,Q^2) + \Delta d(x,Q^2) - 2\Delta s(x,Q^2)$ (that is opposite to the situation with the unpolarized parton distributions[150]).

The NLO evolution in the flavor singlet sector

$$\Gamma(Q^2) \equiv \begin{pmatrix} \Delta\Sigma(Q^2) \\ \Delta G(Q^2) \end{pmatrix} \tag{B.10}$$

where $\Delta\Sigma = \Delta u + \Delta d + \Delta s$, is given by[39,150]

$$\begin{aligned} \Gamma(Q^2) &= \Bigg\{ \left(\frac{\alpha_S(Q^2)}{\alpha_S(Q_0^2)}\right)^{\lambda_-/(2\beta_0)} \Bigg[P_- - \frac{1}{2\beta_0}\frac{\alpha_S(Q_0^2)-\alpha_S(Q^2)}{4\pi} P_-\gamma P_- \\ &\quad - \left(\frac{\alpha_S(Q_0^2)}{4\pi} - \frac{\alpha_S(Q^2)}{4\pi} \left(\frac{\alpha_S(Q^2)}{\alpha_S(Q_0^2)}\right)^{(\lambda_+-\lambda_-)/(2\beta_0)} \right) \frac{P_-\gamma P_+}{2\beta_0 + \lambda_+ - \lambda_-} \Bigg] \\ &\quad + (+ \Leftrightarrow -) \Bigg\} . \end{aligned} \tag{B.11}$$

The miscellaneous quantities are

$$\gamma = \gamma^{(1)} - \frac{\beta_1}{\beta_0}\gamma^{(0)} \tag{B.12}$$

$$P_\pm = \pm\frac{1}{\lambda_+ - \lambda_-}\left(\gamma^{(0)} - \lambda_\mp \mathbb{I}\right) \tag{B.13}$$

$$\lambda_\pm = \frac{1}{2}\left(\gamma_{qq}^{(0)} + \gamma_{GG}^{(0)} \pm \sqrt{(\gamma_{GG}^{(0)} - \gamma_{qq}^{(0)})^2 + 4\gamma_{qG}^{(0)}\gamma_{Gq}^{(0)}}\right) , \tag{B.14}$$

where $\lambda_\pm$ are the eigenvalues of the leading order anomalous dimension matrix $\gamma_{ij}^{(0)}$, and $\mathbb{I}$ is the identity matrix.

In all equations above, the strong coupling constant is defined by the two-loop expression[20]

$$\frac{\alpha_S(Q^2)}{4\pi} = \frac{1}{\beta_0 \ln(Q^2/\Lambda_{(f)}^2)} - \frac{\beta_1}{\beta_0^3}\frac{\ln\left(\ln(Q^2/\Lambda_{(f)}^2)\right)}{\left(\ln(Q^2/\Lambda_{(f)}^2)\right)^2} \tag{B.15}$$

where the coefficients of the QCD beta function are $\beta_0 = 11 - 2f/3$ and $\beta_1 = 102 - 38f/3$. The number of active flavors f in $\alpha_S(Q^2)$ is determined by the number of quarks with $m_q^2 \leq Q^2$. The QCD parameters $\Lambda_{(f)}$ are determined by the matching condition at the quark threshold

$$\alpha_S(m_q^2, f) = \alpha_S(m_q^2, f+1) \ . \tag{B.16}$$

Thus, the derivative of α_S is discontinuous across the quark threshold in this approach. Since the coefficients β depend on the number of active flavors f, the evolution is done in steps: for $m_c^2 < Q^2 < m_b^2$ we first evolve the parton densities with $f = 3$ to the charm threshold, and then from the charm threshold to Q^2 (we would go first to m_b^2 if $Q^2 > m_b^2$).

In all equations above, the leading order (LO) results could be obtained by dropping higher order terms $(\beta_1, \gamma^{(1)}, C_{q,G}^{(1)})$.

Given the moments of the structure function $g_1(n)$, the structure function in the Bjorken x space is obtained by the inverse Mellin transform

$$g_1(x) = \frac{1}{2\pi i} \int_{c-i\infty}^{c+i\infty} dn \ x^{-n} g_1(n) \ , \tag{B.17}$$

where c is the real number that has to be chosen in such a way that $\int_0^1 dx \ x^{c-1} g_1(x)$.[163] Thus, c has to lie to the right of the rightmost singularity $n_{\max}$ of $g_1(n)$ in the complex n space. The contour of integration $\mathbf{C}_0$ in Eq. (B.17) is shown in Fig. B.1. Also shown is a deformed contour $\mathbf{C}_1$ that yields the same result since all singularities for the structure functions (denoted by crosses in Fig. B.1) are on the real axis. Converting to the integration over a real variable, we get

$$g_1(x, Q^2) = \frac{1}{\pi} \int_0^{\infty} dz \ Im \left(e^{i\phi} x^{-c-ze^{i\phi}} g_1(n = c + ze^{i\phi}, Q^2) \right) \ . \tag{B.18}$$

We take $c = 2.1$ and $\phi = 1.9$, and the limit of integration in Eq. (B.18) is 10. These parameters have been found to give stable results for $x > 10^{-4}$. We approximate the integral in Eq. (B.18) by the 24-point Gauss-Legendre quadrature formula using a CERN program library routine RGQUAD.[164]

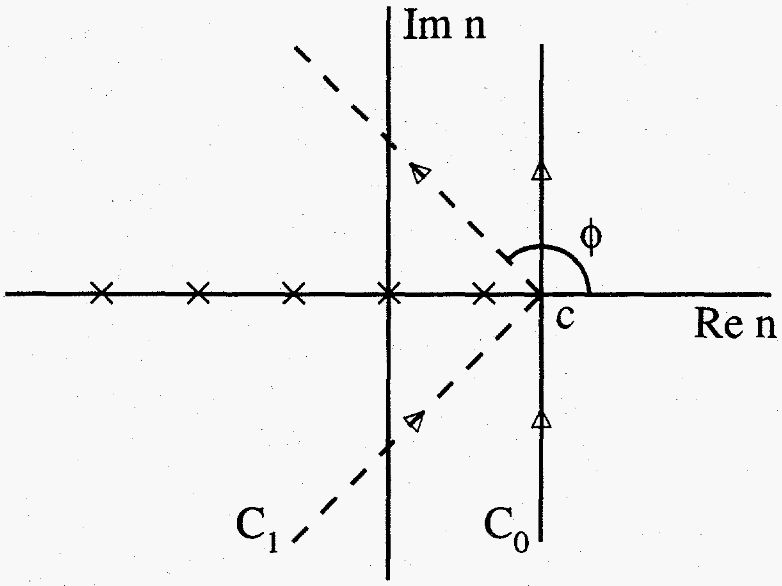

Fig. B.1. The integration contours used for the inverse Mellin transform in Equations (B.17) and (B.18). The singularities of the structure function g_1 are denoted by crosses on the real axis.

The LO spin-dependent anomalous dimensions are given by[43]

$$\begin{aligned}
\gamma_{qq}^{(0)}(n) &= 4C_F\left[2S_1(n)-\frac{1}{n(n+1)}-\frac{3}{2}\right]\\
\gamma_{qG}^{(0)}(n) &= -8T_f\,\frac{n-1}{n(n+1)}\\
\gamma_{Gq}^{(0)}(n) &= -4C_F\,\frac{n+2}{n(n+1)}\\
\gamma_{GG}^{(0)}(n) &= 4C_A\left[2S_1(n)-\frac{4}{n(n+1)}-\frac{11}{6}\right]+\frac{8}{3}T_f\,,
\end{aligned}\tag{B.19}$$

where we take $N_f = 3$ for the number of active flavors. The Casimir invariant for the adjoint representation of $SU(3)_{\text{flavor}}$ $C_A = 3$. Note that $\gamma_{NS}^{(0)}(n) = \gamma_{qq}^{(0)}(n) = \tilde{\gamma}_{qq}^{(0)}(n)$, where the $\tilde{\gamma}_{qq}^{(0)}(n)$ is the spin-averaged anomalous dimension. Thus, in the leading order, the moments of the polarized and unpolarized non-singlet distributions evolve identically, and the ratio g_1/F_1 is almost independent of Q^2 at high x where the non-singlet densities dominate. For the first $n = 1$ moment we have $\gamma_{qq}^{(0)}(1) = \gamma_{qG}^{(0)}(1) = 0$ as a consequence of helicity conservation at the quark-gluon vertex, so the first moments of the quark distributions are conserved in the leading order.

The spin-dependent NLO anomalous dimensions in the non-singlet sector $\gamma^{\eta}_{NS}(n)$ are the same as in the spin-averaged case. In the $\overline{\mathrm{MS}}$ scheme, they are given by[38]

$$\begin{aligned}
\gamma^{(1)\ \eta}_{NS}(n) = \quad & C_F^2 \quad \left[\frac{16S_1(n)(2n+1)}{n^2(n+1)^2} + 24S_2(n) + 64\tilde{S}(n,\eta) - 8S_3'(n/2,\eta) - 3 + \right. \\
& 16\left(2S_1(n) - \frac{1}{n+1}\right)(S_2(n) - S_2'(n/2,\eta)) - \\
& \left. 8\frac{3n^3+n^2-1+2\eta(2n^2+2n+1)}{n^3(n+1)^3}\right] + \\
& C_F C_A \quad \left[\frac{536}{9}S_1(n) - 8\left(2S_1(n) - \frac{1}{n(n+1)}\right)(2S_2(n) - S_2'(n/2,\eta)) - \right. \\
& \frac{88}{3}S_2(n) - 32\tilde{S}(n,\eta) + 4S_3'(n/2,\eta) - \frac{17}{3} - \\
& \left. \frac{\frac{4}{9}(151n^4+236n^3+88n^2+3n+18) - 8\eta(2n^2+2n+1)}{n^3(n+1)^3}\right] + \\
& C_F T_f \quad \left[-\frac{160}{9}S_1(n) + \frac{32}{3}S_2(n) + \frac{4}{3} + \frac{16}{9}\frac{11n^2+5n-3}{n^2(n+1)^2}\right] . \qquad \text{(B.20)}
\end{aligned}$$

Note that for $\eta = -1$, the first moment of the non-singlet anomalous dimension vanishes ($\gamma^{(1)\ \eta=-1}_{NS}(n=1) = 0$), therefore the matrix elements Δq_3 and Δq_8 are independent of Q^2 (the the flavor non-singlet axial current is conserved).

The NLO flavor singlet anomalous dimensions in the $\overline{\mathrm{MS}}$ scheme are given by[37]

$$\gamma^{(1)}_{qq}(n) = \gamma^{(1)\ \eta=-1}_{NS}(n) + 16C_F T_f\frac{n^4+2n^3+2n^2+5n+2}{n^3(n+1)^3} , \qquad \text{(B.21)}$$

where $\gamma^{(1)\ \eta=-1}_{NS}(n)$ are given by Eq. (B.20). Other elements of the two-loop anomalous dimension matrix are

$$\begin{aligned}
\gamma^{(1)}_{qG}(n) = \quad & 8C_F T_f \quad \left[2\frac{n-1}{n(n+1)}\left(S_2(n) - S_1^2(n)\right) + 4\frac{n-1}{n^2(n+1)}S_1(n) - \right. \\
& \left. \frac{5n^5+5n^4-10n^3-n^2+3n-2}{n^3(n+1)^3}\right] + \\
& 16C_A T_f \quad \left[\frac{n-1}{n(n+1)}\left(-S_2(n) + S_2'(n/2,-1) + S_1^2(n)\right) - \right. \\
& \left. \frac{4}{n(n+1)^2}S_1(n) - \frac{n^5+n^4-4n^3+3n^2-7n-2}{n^3(n+1)^3}\right] \qquad \text{(B.22)} \\
\gamma^{(1)}_{Gq}(n) = \quad & 32C_F T_f \quad \left[-\frac{n+2}{3n(n+1)}S_1(n) + \frac{5n^2+12n+4}{9n(n+1)^2} + \right] +
\end{aligned}$$

$$\begin{aligned}
& 4C_F^2 && \left[2\frac{n+2}{n(n+1)}\left(S_2(n)+S_1^2(n)\right)-2\frac{3n^2+7n+2}{n(n+1)^2}S_1(n)+\right. \\
& && \left.\frac{9n^5+30n^4+24n^3-7n^2-16n-4}{n^3(n+1)^3}\right]+ \\
& 8C_AC_F && \left[\frac{n+2}{n(n+1)}\left(-S_2(n)+S_2'(n/2,-1)-S_1^2(n)\right)+\right. \\
& && \frac{11n^2+22n+12}{3n^2(n+1)}S_1(n)- \\
& && \left.\frac{76n^5+271n^4+254n^3+41n^2+72n+36}{9n^3(n+1)^3}\right] && \text{(B.23)}
\end{aligned}$$

$$\begin{aligned}
\gamma_{GG}^{(1)}(n) = {} & 8C_FT_f && \left[\frac{n^6+3n^5+5n^4+n^3-8n^2+2n+4}{n^3(n+1)^3}\right]+ \\
& 32C_AT_f && \left[-\frac{5}{9}S_1(n)+\frac{3n^4+6n^3+16n^2+13n-3}{9n^2(n+1)^2}\right]+ \\
& 4C_A^2 && \left[-S_3'(n/2,-1)-4S_1(n)S_2'(n/2,-1)+8\tilde{S}(n,-1)+\right. \\
& && \frac{8}{n(n+1)}S_2'(n/2,-1)+ \\
& && 2\frac{67n^4+134n^3+67n^2+144n+72}{9n^2(n+1)^2}S_1(n)- && \text{(B.24)} \\
& && \left.\frac{48n^6+144n^5+469n^4+698n^3+7n^2+258n+144}{9n^3(n+1)^3}\right]
\end{aligned}$$

The finite sums $S_k(n)$, $S_k'(n/2,\eta)$, and $\tilde{S}(n,\eta)$ used in the expressions above are defined as[86,150]

$$S_k(n) \equiv \sum_{j=1}^{n}\frac{1}{j^k} \qquad \text{(B.25)}$$

$$\begin{aligned}
S_k'(n/2,\eta) &\equiv 2^{k-1}\sum_{j=1}^{n}\frac{1+(-)^j}{j^k} \\
&= \frac{1}{2}(1+\eta)S_k\left(\frac{n}{2}\right)+\frac{1}{2}(1-\eta)S_k\left(\frac{n-1}{2}\right) && \text{(B.26)}
\end{aligned}$$

$$\begin{aligned}
\tilde{S}(n,\eta) &\equiv \sum_{j=1}^{n}\frac{(-)^j}{j^2}S_1(j) \\
&= -\frac{5}{8}\zeta(3)+\eta\left[\frac{S_1(n)}{n^2}+\frac{\zeta(2)}{2}G(n)+\int_0^1 dx\ x^{n-1}\frac{\mathrm{Li}_2(x)}{1+x}\right], && \text{(B.27)}
\end{aligned}$$

where $G(n) \equiv \psi\left(\frac{n+1}{2}\right)-\psi\left(\frac{n}{2}\right)$, $\mathrm{Li}_2(x) = -\int_0^x dz\ \ln(1-z)/z$ is the Dilogarithm function, and $\eta = \pm 1$ for the non-singlet anomalous dimensions $\gamma_{NS}^{(1)\ \eta=\pm1}(n)$, and

$\eta = -1$ for the flavor singlet anomalous dimensions $\gamma_{ij}^{(1)}$.

The analytical continuations of the finite sums for complex n, required for the inverse Mellin transform, are given by[150]

$$S_1(n) = \gamma_E + \psi(n+1)\,, \quad \gamma_E = 0.577216 \tag{B.28}$$

$$S_2(n) = \zeta(2) - \psi'(n+1)\,, \quad \zeta(2) = \pi^2/6 \tag{B.29}$$

$$S_3(n) = \zeta(3) + \psi''(n+1)\,, \quad \zeta(3) = 1.202057\,. \tag{B.30}$$

The functions $\psi^{(k)}(n) = d^{(k+1)} \ln\Gamma(n)/dn^{(k+1)}$ can be sufficiently accurately expressed by the following asymptotic sums valid for $Re\ n \geq 10$[150]:

$$\psi(n) \approx \ln(n) - \frac{1}{2n} - \frac{1}{12n^2} + \frac{1}{120n^4} - \frac{1}{256n^6} \tag{B.31}$$

$$\psi' \approx \frac{1}{n} + \frac{1}{2n^2} + \frac{1}{6n^3} - \frac{1}{30n^5} + \frac{1}{42n^7} - \frac{1}{30n^9} \tag{B.32}$$

$$\psi'' \approx -\frac{1}{n^2} - \frac{1}{n^3} - \frac{1}{2n^4} + \frac{1}{6n^6} - \frac{1}{6n^8} + \frac{3}{10n^{10}} - \frac{5}{6n^{12}}\,. \tag{B.33}$$

For $Re\ n < 10$, a recursion relation is used:

$$\psi^{(k)}(n+1) = \psi^{(k)}(n) + \frac{(-)^k\, k!}{n^{k+1}}\,. \tag{B.34}$$

Furthermore, the integral in Eq. (B.27) involving the Dilogarithm can be approximated by[150]

$$\int_0^1 dx\ x^{n-1} \frac{\mathrm{Li}_2(x)}{1+x} \approx \frac{1.010}{n+1} - \frac{0.846}{n+2} + \frac{1.155}{n+3} - \frac{1.074}{n+4} + \frac{0.550}{n+5}\,. \tag{B.35}$$

The evolution and fitting code was optimized for speed. The most time-consuming part was evaluation of the anomalous dimensions. Fortunately, since we are not varying the strong coupling constant in the fit, it only has to be done once for every point n used in the integration (the points in the quadrature formula are fixed). The matrices used in the singlet evolution (Eq. (B.11)) are calculated once for every number of flavors f. The moments of the initial parton distributions are calculated every time a parameter of the fit changes. One fit with 8 free parameters

(149 data points in the range $0.005 \leq x \leq 0.75$ and $0.95\ \mathrm{GeV}^2 \leq Q^2 \leq 58\ \mathrm{GeV}^2$) typically takes 3–4 min on a DEC Alpha 600 5/266 computer (that corresponds to 800-1000 iterations in MINUIT[156]).

We tested our code against the parameterizations of Ref. [86]. Using the "standard" NLO parameterization at initial $Q_0^2 = 0.34\ \mathrm{GeV}^2$, we evolved the GRSV[86] partons to $Q^2 = 100\ \mathrm{GeV}^2$ and compared with the output of the code provided by one of the authors.[159] The comparison is shown in Fig. B.2; two codes are in perfect agreement. In addition, we directly integrated the leading order DGLAP equations in Bjorken space evolving the structure functions by small steps in Q^2,[83,84] and found that the direct technique gave results very close to the Mellin evolution code.

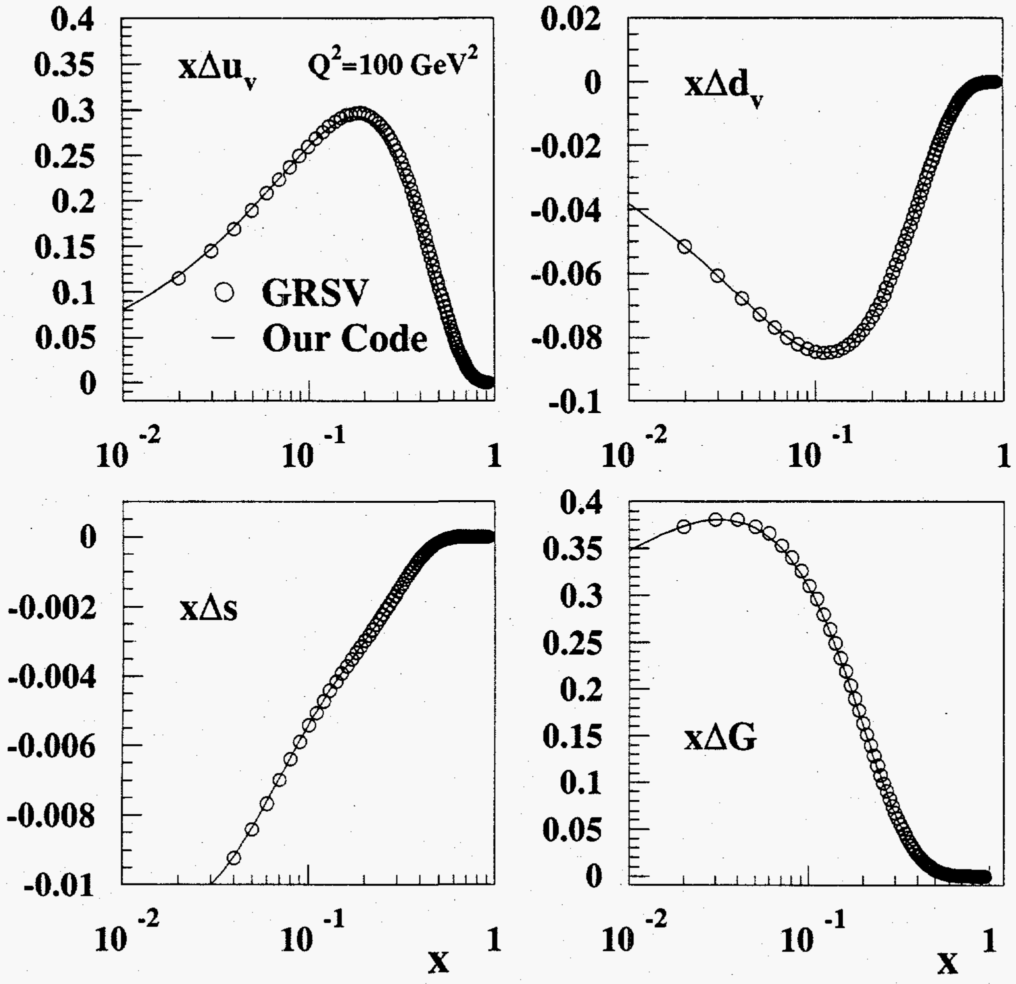

Fig. B.2. The parton distributions evolved from $Q_0^2 = 0.34$ GeV^2 to $Q^2 = 100$ GeV^2 are compared to the output of the GRSV code.[86,159]

APPENDIX C

RESULTS OF THE CALTECH ANALYSIS

The results for the structure functions and the photon-nucleon asymmetries, averaged between the two analyses, were given Chapter 4. For completeness, we will summarize here the results of the Caltech analysis.

Table C.1. The spin dependent structure function g_1^n and the photon-nucleon asymmetry A_1^n.

$\langle x \rangle$	$\langle Q^2 \rangle$ (GeV^2)	$g_1^n \pm$ stat. $\pm$ syst.	$A_1^n \pm$ stat. $\pm$ syst.
		2.75° spectrometer	
0.017	1.21	$-0.371 \pm 0.115 \pm 0.105$	$-0.061 \pm 0.019 \pm 0.017$
0.024	1.59	$-0.387 \pm 0.071 \pm 0.062$	$-0.082 \pm 0.015 \pm 0.014$
0.035	2.05	$-0.310 \pm 0.061 \pm 0.038$	$-0.083 \pm 0.018 \pm 0.012$
0.049	2.57	$-0.201 \pm 0.041 \pm 0.021$	$-0.084 \pm 0.016 \pm 0.009$
0.078	3.32	$-0.123 \pm 0.031 \pm 0.013$	$-0.081 \pm 0.019 \pm 0.010$
0.123	4.09	$-0.070 \pm 0.030 \pm 0.009$	$-0.081 \pm 0.031 \pm 0.010$
0.173	4.63	$-0.082 \pm 0.033 \pm 0.009$	$-0.123 \pm 0.052 \pm 0.016$
0.241	5.09	$-0.057 \pm 0.027 \pm 0.007$	$-0.096 \pm 0.075 \pm 0.019$
0.340	5.51	$-0.001 \pm 0.035 \pm 0.004$	$-0.256 \pm 0.197 \pm 0.071$
0.423	5.82	$0.024 \pm 0.059 \pm 0.006$	$0.133 \pm 0.606 \pm 0.034$
		5.5° spectrometer	
0.057	4.03	$0.234 \pm 0.280 \pm 0.036$	$0.047 \pm 0.118 \pm 0.012$
0.084	5.47	$-0.149 \pm 0.029 \pm 0.019$	$-0.103 \pm 0.017 \pm 0.013$
0.123	7.23	$-0.112 \pm 0.016 \pm 0.012$	$-0.107 \pm 0.015 \pm 0.012$
0.172	8.94	$-0.053 \pm 0.015 \pm 0.007$	$-0.079 \pm 0.023 \pm 0.010$
0.242	10.71	$-0.039 \pm 0.011 \pm 0.005$	$-0.109 \pm 0.030 \pm 0.015$
0.342	12.55	$-0.011 \pm 0.012 \pm 0.004$	$-0.031 \pm 0.065 \pm 0.021$
0.442	13.83	$-0.012 \pm 0.011 \pm 0.003$	$-0.091 \pm 0.139 \pm 0.020$
0.564	15.00	$0.002 \pm 0.008 \pm 0.001$	$0.083 \pm 0.279 \pm 0.031$

Table C.2. The spin dependent structure function g_2^n and the photon-nucleon asymmetry A_2^n.

$\langle x \rangle$	$\langle Q^2 \rangle$ (GeV^2)	$g_2^n \pm$ stat. $\pm$ syst.	$A_2^n \pm$ stat. $\pm$ syst.
		2.75° spectrometer	
0.017	1.21	$6.523 \pm 15.214 \pm 2.145$	$0.030 \pm 0.074 \pm 0.010$
0.024	1.59	$-1.479 \pm 7.232 \pm 0.993$	$-0.015 \pm 0.056 \pm 0.008$
0.035	2.05	$-9.065 \pm 4.890 \pm 1.042$	$-0.122 \pm 0.064 \pm 0.014$
0.049	2.57	$4.559 \pm 2.504 \pm 0.540$	$0.098 \pm 0.056 \pm 0.012$
0.078	3.32	$1.520 \pm 1.330 \pm 0.254$	$0.068 \pm 0.065 \pm 0.013$
0.123	4.09	$1.033 \pm 0.952 \pm 0.229$	$0.107 \pm 0.106 \pm 0.026$
0.173	4.63	$0.097 \pm 0.794 \pm 0.145$	$0.003 \pm 0.176 \pm 0.032$
0.241	5.09	$-0.388 \pm 0.490 \pm 0.097$	$-0.207 \pm 0.229 \pm 0.046$
0.340	5.51	$0.787 \pm 0.442 \pm 0.197$	$0.919 \pm 0.522 \pm 0.161$
0.423	5.82	$0.050 \pm 0.580 \pm 0.020$	$0.177 \pm 1.414 \pm 0.041$
		5.5° spectrometer	
0.057	4.03	$43.265 \pm 31.639 \pm 4.648$	$0.997 \pm 0.727 \pm 0.107$
0.084	5.47	$4.362 \pm 2.377 \pm 0.455$	$0.173 \pm 0.098 \pm 0.018$
0.123	7.23	$0.459 \pm 0.987 \pm 0.199$	$0.028 \pm 0.079 \pm 0.016$
0.172	8.94	$0.214 \pm 0.711 \pm 0.150$	$0.025 \pm 0.110 \pm 0.023$
0.242	10.71	$0.362 \pm 0.396 \pm 0.094$	$0.107 \pm 0.132 \pm 0.030$
0.342	12.55	$-0.136 \pm 0.299 \pm 0.032$	$-0.128 \pm 0.263 \pm 0.028$
0.442	13.83	$-0.059 \pm 0.228 \pm 0.014$	$-0.157 \pm 0.506 \pm 0.029$
0.564	15.00	$-0.011 \pm 0.125 \pm 0.009$	$-0.062 \pm 0.904 \pm 0.059$

Table C.3. Results on A_1^n and g_1^n at the measured Q^2, along with g_1^n evaluated at $Q^2 = 5$ (GeV)^2 assuming that the ratio g_1^n/F_1^n scales with Q^2. The data of two spectrometers have been averaged.

x bin	$\langle x \rangle$	$\langle Q^2 \rangle$ GeV^2	g_1^n ± stat. ± syst.	A_1^n ± stat. ± syst.	g_1^n ± stat. ± syst. ($Q^2 = 5$ GeV^2)
0.014 – 0.02	0.017	1.2	$-0.371 \pm 0.115 \pm 0.105$	$-0.061 \pm 0.019 \pm 0.017$	$-0.524 \pm 0.163 \pm 0.149$
0.02 – 0.03	0.024	1.6	$-0.387 \pm 0.071 \pm 0.064$	$-0.082 \pm 0.015 \pm 0.014$	$-0.499 \pm 0.092 \pm 0.082$
0.03 – 0.04	0.035	2.0	$-0.310 \pm 0.061 \pm 0.040$	$-0.083 \pm 0.018 \pm 0.012$	$-0.369 \pm 0.073 \pm 0.047$
0.04 – 0.06	0.049	2.6	$-0.192 \pm 0.040 \pm 0.021$	$-0.082 \pm 0.016 \pm 0.009$	$-0.215 \pm 0.045 \pm 0.023$
0.06 – 0.10	0.081	4.5	$-0.137 \pm 0.021 \pm 0.016$	$-0.093 \pm 0.013 \pm 0.011$	$-0.140 \pm 0.021 \pm 0.016$
0.10 – 0.15	0.123	6.6	$-0.103 \pm 0.014 \pm 0.011$	$-0.102 \pm 0.014 \pm 0.011$	$-0.101 \pm 0.014 \pm 0.011$
0.15 – 0.20	0.173	8.2	$-0.058 \pm 0.014 \pm 0.007$	$-0.086 \pm 0.021 \pm 0.011$	$-0.057 \pm 0.014 \pm 0.007$
0.20 – 0.30	0.242	9.8	$-0.041 \pm 0.011 \pm 0.005$	$-0.107 \pm 0.027 \pm 0.016$	$-0.042 \pm 0.011 \pm 0.005$
0.30 – 0.40	0.342	11.7	$-0.010 \pm 0.011 \pm 0.004$	$-0.054 \pm 0.062 \pm 0.021$	$-0.011 \pm 0.012 \pm 0.005$
0.40 – 0.50	0.441	13.4	$-0.011 \pm 0.011 \pm 0.002$	$-0.080 \pm 0.136 \pm 0.019$	$-0.013 \pm 0.013 \pm 0.003$
0.50 – 0.70	0.564	15.0	$0.002 \pm 0.008 \pm 0.001$	$0.083 \pm 0.279 \pm 0.031$	$0.004 \pm 0.011 \pm 0.001$

REFERENCES

[1] E. D. Bloom *et al.*, *Phys. Rev. Lett.* **23** (1969) 930;
M. Breidenback *et al.*, *Phys. Rev. Lett.* **23** (1969) 935.

[2] CERN Courier, Volume 30, number 9 (December 1990) 1.

[3] R. P. Feynman, *Phys. Rev. Lett.* **23** (1969) 1415.

[4] J. D. Bjorken, *Phys. Rev.* **D1** (1970) 1376.

[5] J. D. Bjorken and E. A. Paschos, *Phys. Rev.* **185** (1969) 1975.

[6] The E80 Collaboration, M. J. Alguard *et al.*, *Phys. Rev. Lett.* **37** (1976) 1258, *Phys. Rev. Lett.* **37** (1976) 1261, *Phys. Rev. Lett.* **41** (1978) 70.

[7] G. Baum *et al.*, *Phys. Rev. Lett.* **51** (1983) 1135.

[8] The EMC Collaboration, J. Ashman *et al.*, *Phys. Lett.* **B206** (1988) 364, *Nucl. Phys.* **B328** (1990) 1;
V. Hughes *et al.*, *Phys. Lett.* **B212** (1988) 511.

[9] The E142 Collaboration, P. L. Anthony *et al.*, *Phys. Rev. Lett.* **71** (1993) 959; *Phys. Rev.* **D54** (1996) 6620.

[10] The E143 Collaboration, K. Abe *et al.*, *Phys. Rev. Lett.* **74** (1995) 346.

[11] The E143 Collaboration, K. Abe *et al.*, *Phys. Rev. Lett.* **75** (1995) 25.

[12] The SMC Collaboration, D. Adams *et al.*, *Phys. Lett.* **B329** (1994) 399.

[13] The SMC Collaboration, B. Adeva *et al.*, *Phys. Lett.* **B302** (1993) 533;
D. Adams *et al.*, *Phys. Lett.* **B357** (1995) 248;
CERN-PPE/97-008 (1997).

[14] The E154 Proposal, E. W. Hughes *et al.*, October 1993, unpublished.

[15] F. E. Close, *An Introduction to Quarks and Partons*, Academic Press (1979).

[16] E. Rutherford, *Phil. Mag.* **21** (1911) 669.

[17] T. Pussieux and R. Windmolders, in *Internal Spin Structure of the Nucleon*, ed. V. W. Hughes and C. Cavata, World Scientific (1995).

[18] E. Leader and E. Predazzi, *An Introduction to Gauge Theories and the New Physics*, Cambridge University Press (1985).

[19] D. J. Gross and F. Wilczek, *Phys. Rev.* **D9** (1974) 980.

[20] Review of Particle Properties, Particle Data Group (R. M. Barnett *et al.*), *Phys. Rev.* **D55** (1996) 1.

[21] M. Bourquin *et al.*, *Z. Phys.* **C21** (1983) 27.

[22] The E143 Collaboration, K. Abe *et al.*, *Phys. Rev. Lett.* **76** (1996) 587.

[23] The SMC Collaboration, B. Adeva *et al.*, *Phys. Lett.* **B336** (1994) 125.

[24] See, for example, R. L. Jaffe and A. Manohar, *Nucl. Phys.* **B337** (1990) 509; S. J. Brodsky, J. Ellis, and M. Karliner, *Phys. Lett.* **B206** (1988) 309.

[25] X. Ji, MIT-CTP-2517, hep-ph/9603249 (1996).

[26] J. D. Bjorken, *Phys. Rev.* **148** (1966) 1467; *Phys. Rev.* **D1** (1970) 1376.

[27] J. Kodaira *et al.*, *Phys. Rev.* **D20** (1979) 627, *Nucl. Phys.* **B159** (1979) 99.

[28] S. G. Gorishny and S. A. Larin, *Phys. Lett.* **B172** (1986) 109;
S. A. Larin and J. A. M. Vermaseren, *Phys. Lett.* **B259** (1991) 345.

[29] J. Ellis and R. Jaffe, *Phys. Rev.* **D9** (1974) 1444.

[30] J. Ellis and M. Karliner, *Phys. Lett.* **B313** (1993) 131.

[31] H. Burkhardt and W. N. Cottingham, *Ann. Phys.* **56** (1970) 453.

[32] B. L. Ioffe, V. A. Khoze and L. N. Lipatov, *Hard Processes*, **Vol.1** (North-Holland, Amsterdam, 1984).

[33] T. P. Cheng and W. K. Tung, *Phys. Rev. Lett.* **24** (1970) 851.

[34] J. B. Bronzan *et al.*, *Phys. Rev.* **157** (1967) 1448;
H. D. I. Abarbanel *et al.*, *Phys. Rev.* **160** (1967) 1239;
V. Singh, *Phys. Rev. Lett.* **18** (1967) 36;
A. Mueller and L. Trueman, *Phys. Rev.* **160** (1967) 1296.

[35] R. L. Jaffe and X. Ji, *Phys. Rev.* **D43** (1991) 724.

[36] S. Wandzura and F. Wilczek, *Phys. Lett.* **B172** (1977) 195.

[37] R. Mertig and W.L. van Neerven, *Z. Phys.* **C70** (1996) 637;
W. Vogelsang, *Phys. Rev.* **D54** (1996) 2023 and references therein.

[38] E. G. Floratos, C. Kounnas, and R. Lacaze, *Nucl. Phys.* **B192** (1981) 417.

[39] W. Furmanski and R. Petronzio, *Z. Phys.* **C11** (1982) 293.

[40] S. J. Brodsky and G. P. Lepage, *Proceedings of the 1979 SLAC Summer Instutute on Particle Physics*, SLAC (1979).

[41] V. N. Gribov and L. N. Lipatov, *Sov. J. Nucl. Phys.* **15** (1972) 438; *Sov. J. Nucl. Phys.* **15** (1972) 675.

[42] Yu. L. Dokshitzer, *Sov. Phys. JETP* **46** (1977) 461.

[43] G. Altarelli and G. Parisi, *Nucl. Phys.* **B126** (1977) 298.

[44] T. Gehrmann and W. J. Stirling, *Phys. Lett.* **B365** (1996) 347.

[45] S. D. Drell, B. Levy, and T. M. Yan, *Phys. Rev.* **187** (1969) 2159, *Phys. Rev.* **D1** (1970) 1035, *Phys. Rev.* **D1** (1970) 1617.

[46] S. J. Brodsky and G. P. Lepage, *Phys. Rev.* **D22** (1980) 2157 and references therein.

[47] R. Blankenbecler and S. J. Brodsky, *Phys. Rev.* **D10** (1974) 2973.

[48] The E155 Proposal, R. Arnold, J. McCarthy *et al.*, October 1993, unpublished.

[49] S. J. Brodsky, M. Burkardt, and I. Schmidt, *Nucl. Phys.* **B441** (1994) 197.

[50] R. Blankenbecler and S. J. Brodsky, Ref. [47];
J. F. Gunion, *Phys. Rev.* **D10** (1974) 242;
S. J. Brodsky and G. P. Lepage, Ref. [40].

[51] J. D. Bjorken, *Phys. Rev.* **D1** (1970) 1376.

[52] E. Bloom and F. Gilman, *Phys. Rev. Lett.* **25** (1970) 1140.

[53] A. Lung *et al.*, *Phys. Rev. Lett.* **70** (1993) 718.

[54] S. J. Brodsky and G. P. Lepage, in *Perturbative Quantum Chromodynamics*, Ed. by A. H. Muller, World Scientific (1989).

[55] S. J. Brodsky, P. Hoyer, A. H. Mueller, and W. Tang, *Nucl. Phys.* **B369** (1992) 519.

[56] A.V. Efremov and O.V. Teryaev, JINR-E2-88-287 (1988); *Phys. Lett.* **B240** (1990) 200.

[57] G. Altarelli and G. Ross, *Phys. Lett.* **B212** (1988) 391.

[58] R. D. Carlitz, J.D. Collins and A.H. Mueller, *Phys. Lett.* **B214** (1988) 229. See also the comments in R.L. Jaffe and A. Manohar, *Nucl. Phys.* **B337** (1990) 509.

[59] S. D. Bass and A. W. Thomas, *Prog. Part. Nucl. Phys.* **33** (1994) 449, preprint hep-ph/9310306 (1993).

[60] T. Gehrmann and W. J. Striling, *Z. Phys.* **C65** (1995) 461.

[61] G. T. Bodwin and J. Qiu, in *Proceedings of Polarized Collider Workshop*, University Park, PA, (1990);
G. T. Bodwin and J. Qiu, *Phys. Rev.* **D41** (1990) 2755.

[62] J. Chyla, *Phys. Rev.* **D48** (1993) 4385.

[63] R. D. Ball, S. Forte, and G. Ridolfi, *Phys. Lett.* **B378** (1996) 255.

[64] A. Donnachie and P.V. Landshoff, *Phys. Lett.* **B296** (1992) 227.

[65] R. L. Heimann, *Nucl. Phys.* **B64** (1973) 429.

[66] M. Anselmino, A. Efremov, and E. Leader, *Phys. Rep.* **261** (1995) 1.

[67] J. Kuti, preprint MIT CTP #234 (1971);
J. Kuti, in *Internal Spin Structure of the Nucleon*, ed. V. W. Hughes and C. Cavata, World Scientific (1995).

[68] F. E. Close and R. G. Roberts, *Phys. Rev. Lett.* **60** (1988) 1471.

[69] R. D. Ball and S. Forte, *Phys. Lett.* **B335** (1994) 77.

[70] S. D. Bass and P. V. Landshoff, *Phys. Lett.* **B336** (1994) 537.

[71] J. Bartels, B. I. Ermolaev, and M. G. Ryskin, *Z. Phys.* **C70** (1996) 273; preprint DESY-96-025 (1996).

[72] J. L. Friar *et al.*, *Phys. Rev.* **C42** (1990) 2310.

[73] C. Coffi degli Atti *et al.*, *Phys. Rev.* **C48** (1993) 968.

[74] J. Aubert *et al.*, *Phys. Lett.* **B123** (1983) 275.

[75] M. Borghini, *Phys. Rev. Lett.* **20** (1968) 419.

[76] G. G. Petratos *et al.*, Report No. SLAC-PUB-5678 (1991), unpublished.

[77] The E143 Collaboration, K. Abe *et al.*, *Phys. Lett.* **B364** (1995) 61.

[78] J. Ellis and M. Karliner, *Phys. Lett.* **B341** (1995) 397.

[79] L. W. Whitlow *et al.*, *Phys. Lett.* **B250** (1990) 193; S. Dasu *et al.*, *Phys. Rev.* **D49** (1994) 5641.

[80] The HERMES Proposal, K. Coulter *et al.*, DESY/PRC **90-1** (1990);
M. Veltri *et al.*, Proc. Physics at HERA, Vol. 1, **447** (1991);
the HERMES Collaboration, *Technical Design Report*, July 1993.

[81] A. Simon, Proc. 12th Int. Symposium on High Energy Spin Physics, SPIN '96, Amsterdam (1996), to be published in the proceedings.

[82] J. Ellis and M. Karliner, preprint CERN-TH/95-279, hep-ph/9510402.

[83] G. Altarelli, P. Nason, and G. Ridolfi, *Phys. Lett.* **B320** (1994) 152; *ERRATUM-ibid.* **B325** (1994) 538.

[84] C. Bourrely *et al.*, preprint CPT-96-PE-3327, hep-ph/9604204.

[85] M. Gluck, E. Reya, and W. Vogelsang, *Phys. Lett.* **B359** (1995) 201.

[86] M. Gluck *et al.*, *Phys. Rev.* **D53** (1996) 4775.

[87] T. Gehrmann and W. J. Stirling, *Phys. Rev.* **D53** (1996) 6100.

[88] R. Alley *et al.*, *Nucl. Instrum. Methods* **A365** (1995) 1.

[89] M. Woods, Report No. SLAC-PUB-7320 (1996), unpublished.

[90] R. A. Erickson, E154 collaboration meeting, March 1996, unpublished.

[91] H. R. Band *et al.*, E154 Tech. Note # 40 (1996), unpublished.

[92] C. C. Young, E154 technical note # 35, unpublished.

[93] C. Møller, *Ann. Phys.* **14** (1932) 532;
J. Arrington *et al.*, *Nucl. Instrum. and Meth.* **A311** (1992) 39.

[94] H. R. Band, *AIP Conf. Proc.* **343** (1994) 245.

[95] H. R. Band and R. Prepost, E143 Technical Note # 110 (1996), unpublished.

[96] G. G. Scott and H. W. Sturner, *Phys. Rev.* **184** (1969) 490.

[97] L. G. Levchuk, *Nucl. Instrum. Methods* **A345** (1994) 496.

[98] H. Middleton, Ph. D. thesis, Princeton University (1994), unpublished.

[99] W. Happer, *Rev. Mod. Phys.* **44** (1972) 169.

[100] T. E. Chupp *et al.*, *Phys. Rev.* **C36** (1987) 2244.

[101] K. D. Bonin, T. D. Walker, and W. Happer, *Phys. Rev.* **A37** (1988) 2877; K. P. Coulter *et al.*, *Nucl. Instrum. Methods* **A276** (1989) 29.

[102] M. V. Romalis, E154 Technical Note # 34 (1996), unpublished.

[103] M. V. Romalis and T. B. Smith, E154 Technical Note (1996), unpublished.

[104] A. Abragam, Principles of Nuclear Magnetism (Oxford University Press, New York, 1961).

[105] N. R. Newbury *et al.*, *Phys. Rev.* **A48** (1993) 558; A. S. Barton *et al.*, *Phys. Rev.* **A49** (1994) 2766.

[106] M. V. Romalis, E154 collaboration meeting, March 1996, unpublished.

[107] G. G. Petratos, Report No. SLAC/ESA-2/93 (1993), unpublished.

[108] R. Arnold *et al.*, Report No. SLAC/ESA-4/93 (1993), unpublished.

[109] K. L. Brown, Report No. SLAC-REP-75 (1982), unpublished.

[110] J. A. Dunne, Pre-thesis project, American University, Washington, D.C. (1994), unpublished.

[111] The ASP collaboration, N. A. Roe *et al.*, *Phys. Rev.* **D41** (1990) 17.

[112] P. L Anthony and Z. M. Szalata, Report No. SLAC-PUB-7201 (1996), unpublished.

[113] J. Wang, E154 collaboration meeting, May 1996, unpublished.

[114] P. Zyla, private communication.

[115] L. Sorrell, E154 technical note # 25 (1995), unpublished.

[116] S. Incerti, E154 technical note # 30 (1996), unpublished.

[117] S. Incerti and Y. Terrien, E154 technical note # 22 (1995), unpublished.

[118] V. Breton *et al.*, *Nucl. Instrum. Methods* **A362** (1995) 478.

[119] N. V. Rabin, *Instrum. Exp. Tech.* **35** (1992) 947.

[120] Yu. Bushnin *et al.*, *Nucl. Instrum. Methods* **106** (1973) 493;
G. A. Akodopyanov *et al.*, *Nucl. Instrum. Methods* **140** (1977) 441;
F. Blanchi *et al.*, *Nucl. Instrum. Methods* **A279** (1981) 473.

[121] S. Incerti, E154 technical note # 31 (1996), unpublished.

[122] D. Kawall, Ph. D. thesis, Stanford (1995), unpublished.

[123] P. Zyla, E154 collaboration meeting, May 1996, unpublished.

[124] Yu. Kolomensky, E154 technical note # 26 (1996), unpublished.

[125] M. Olson, private communication.

[126] J. Dunne, Ph. D. thesis, American University (1995), unpublished.

[127] Yu. Kolomensky, E154 collaboration meeting, May 1996, unpublished.

[128] P. Zyla and T. Averett, E154 technical note # 43 (1996), unpublished.

[129] M. Arneodo *et al.*, *Phys. Lett.* **B364** (1995) 107.

[130] J. Gomez *et al.*, *Phys. Rev.* **D49** (1994) 4348.

[131] G. I. Smirnov, *Phys. Lett.* **B364** (1995) 87.

[132] M. Romalis, E154 technical note # 34 (1996), unpublished.

[133] I. V. Akushevich and N. M. Shumeiko, *J. Phys.* **G20** (1994) 513.

[134] I. V. Akushevich, N. M. Shumeiko and A. E. Tolkachev, POLRAD 1.5 (1996), unpublished.

[135] L. M. Stuart, private communication.

[136] D. Y. Bardin and N. M. Shumeiko, *Nucl. Phys.* **B127** (1977) 242.

[137] N. Dombey, *Rev. Mod. Phys.* **41** (1969) 236;
B. Blankleider and R. M. Woloshyn, *Phys. Rev.* **C29** (1984) 538.

[138] L. W. Mo and Y. S. Tsai, *Rev. Mod. Phys.* **41** (1969) 205;
Y. S. Tsai, SLAC-PUB-848 (1971).

[139] M. Romalis and Yu. Kolomensky, E154 technical note (1997), unpublished.

[140] D. Reyna, E154 technical note (1997), unpublished.

[141] Yu. Kolomensky and F. Sabatié, E154 technical note # 44 (1996), unpublished.

[142] F. Sabatié, E154 technical note (1996), unpublished.

[143] S. Inserti and V. Breton, E154 technical note # 36 (1996), unpublished.

[144] A. D. Martin, R. G. Roberts, and W. J. Stirling, *Phys. Lett.* **B387** (1996) 419.

[145] M. Gluck, E. Reya, and A. Vogt, *Z. Phys.* **C67** (1995) 433.

[146] J. Botts *et al.*, *Phys. Lett.* **B304** (1993) 159.

[147] T. Gehrmann and W. J. Stirling, *Phys. Rev.* **D53** (1996) 6100.

[148] H. Georgi and H. D. Politzer, *Phys. Rev.* **D9** (1974) 416;
D. J. Gross and F. Wilczek, *Phys. Rev.* **D9** (1974) 980.

[149] M. Lacombe *et al.*, *Phys. Rev.* **C21** (1980) 861;
M. J. Zuilhof and J. A. Tjon, *Phys. Rev.* **C22** (1980) 2369;
R. R. Machleid *et al.*, *Phys. Rep.* **149** (1987) 1.

[150] M. Gluck, E. Reya, and A. Vogt, *Z. Phys.* **C48** (1990) 471.

[151] G. t'Hooft and M. Veltman, *Nucl. Phys.* **B44** (1972) 189.

[152] R. Brock *et al.*, *Handbook of perturbative QCD*, *Rev. Mod. Phys.* **67** (1995) 157.

[153] S. J. Brodsky and H. J. Lu, *Phys. Rev.* **D51** (1995) 3652, and references therein.

[154] J. Kodaira, *Nucl. Phys.* **B165** (1980) 129.

[155] P. Ratcliffe, *Phys. Lett.* **B192** (1987) 309.

[156] CERN Application Software Group, *CERN Program Library Long Writeup* **D506** (1992) .

[157] See for example C. Pascaud and F. Zomer, Preprint LAL 95-05 (1995).

[158] S. Forte and G. Ridolfi, private communication.

[159] W. Vogelsang, private communication.

[160] M. A. Ahmed and G. G. Ross, *Phys. Lett.* **B56** (1975) 385;
M. B. Einhorn and J. Soffer, *Nucl. Phys.* **B74** (1986) 714.

[161] R. D. Ball, S. Forte, and G. Ridolfi, *Nucl. Phys.* **B444** (1996) 287.

[162] J. Blümlein, S. Riemersma, and A. Vogt, preprint DESY-96-131 (1996);
Nucl. Phys. Proc. Suppl. **51C** (1996) 30.

[163] D. Graudenz, M. Hampel, A. Vogt, and C. Berger, *Z. Phys.* **C70** (1996) 77.

[164] CERN Application Software Group, *CERN Program Library Short Writeup* **D107** (1992) .